공학박사 학위논문

Measurement Method for Suspended Sediment Concentration in Rivers Using High-Resolution Hyperspectral Imagery

고해상도 초분광영상을 활용한 하천 부유사농도 계측기법 개발

2022년 8월

서울대학교 대학원

건설환경공학부

권시윤

Measurement Method for Suspended Sediment Concentration in Rivers Using High-Resolution Hyperspectral Imagery

고해상도 초분광영상을 활용한 하천 부유사농도 계측기법 개발

지도교수 서 일 원

이 논문을 공학박사 학위논문으로 제출함

2022년 4월

서울대학교 대학원

건설환경공학부

권 시 윤

권시윤의 공학박사 학위논문을 인준함

2022년 6월

위원장 ____________________ (인)

부위원장 ____________________ (인)

위원 ____________________ (인)

위원 ____________________ (인)

위원 ____________________ (인)

Abstract of dissertation

Measurement Method for Suspended Sediment Concentration in Rivers Using High-Resolution Hyperspectral Imagery

By

Siyoon Kwon

Doctor of Philosophy in Civil and Environmental Engineering

Seoul National University

Professor Il Won Seo, Advisor

The conventional measurement method of suspended sediment concentration (SSC) in the riverine system is labor-intensive and time-consuming since it has been conducted using the sampling-based direct measurement method. For this reason, it is challenging to collect high-resolution datasets of SSC in rivers. In order to overcome this limitation, remote

sensing-based techniques using multi- or hyper-spectral images from satellites or UAVs have been recently carried out to obtain high-resolution SSC distributions in water environments. However, suspended sediment in rivers is more dynamic and spatially heterogeneous than those in other fields. Moreover, the sediment and streambed properties have strong regional characteristics depending on the river type; thus, only models suitable for a specific period and region have been developed owing to the increased spectral variability of the water arising from various types of suspended matter in the water and the heterogeneous streambed properties.

Therefore, to overcome the limitations of the existing monitoring system, this study proposed a robust hyperspectral imagery-based SSC measurement method, termed cluster-based machine learning regression with optical variability (CMR-OV). This method dealt with the spectral variability problem by combining hyperspectral clustering and machine learning regression with the Gaussian mixture model (GMM) and Random forest (RF) regression. The hyperspectral clustering separated the complex dataset into several homogeneous datasets according to spectral characteristics. Then, the machine learning regressors corresponding to clustered datasets were built to construct the relationship between the hyperspectral spectrum and SSC.

The development and validation of the proposed method were carried out through the following processes: 1) analysis of confounding factors in the spectral variability through experimental studies, 2) selection of an optimal regression model and validation of hyperspectral clustering, and 3) evaluation of field applicability. In the experimental studies, the intrinsic hyperspectral spectra of suspended sediment were collected in a completely mixed state after removing the bottom reflection using a horizontal rotating cylinder. Then, hyperspectral data on various sediment properties (particle size and mineral contents) and river bed properties (sand and vegetation) were collected from sediment tracer experiments in field-scale open channels under different hydraulic conditions and compared with intrinsic hyperspectral spectra. Consequently, the change of the hyperspectral spectrum was different according to the sediment type and particle size distribution. In addition, under the shallow water depth condition of 1 m or less, the shape of the hyperspectral spectrum changed significantly depending on the bed type due to the bottom reflectance. The bottom reflectance substantially affected the hyperspectral spectrum even when the high SSC was distributed.

As a result of combining the GMM and RF regression with building a relationship between the SSC and hyperspectral data reflecting the spectral variability, the accuracy was substantially improved compared to the other methods. In particular, even when nonlinearity is considered based on the existing optimal band ratio analysis (OBRA) method, spectral variability could not be reflected due to the limitation of considering only a narrow wavelength range. On the other hand, CMR-OV showed high accuracy while considering a wide range of wavelengths with clusters having distinct spectral characteristics.

Finally, the CMR-OV was applied to the straight and meandering reaches of the Hwang River and the confluence of the Nakdong and Hwang Rivers in South Korea to assess field applicability. There was a remarkable improvement in the accuracy and precision of SSC mapping under various river conditions compared to the existing models, and CMR-OV showed robust performance even with non-calibrated datasets. At the river confluence, the mixing pattern between the main river and tributary was apparently retrieved from CMR-OV under optically complex conditions. Compared to the non-clustered model, hyperspectral clustering played a primary role in improving the performance by separating the water bodies originating from both rivers. It was also possible to quantitatively evaluate the complicated mixing pattern in detail compared to the existing point measurement. Therefore, it is expected that the accuracy and efficiency of river investigation will be significantly improved through the SSC measurement method presented in this study.

Keywords: river suspended sediment measurement, remote sensing, hyperspectral imagery, spectral variability, machine learning, spatial distribution mapping

Student number: 2018-28430

Table of contents

Abstract of dissertation i

List of figures ix

List of tables xvii

List of abbreviations xix

List of symbols xxii

1. Introduction 1

2. Theoretical research 13

2.1.1 Pre-processing of hyperspectral image (HSI) 19

2.1.2 Optical characteristics of suspended sediment in rivers 28

2.1.2.1 Theory of solar radiation transfer in rivers 28

2.1.2.2 Heterogeneity of sediment properties 33

2.1.2.3 Effects of bottom reflectance 38

2.1.2.4 Vertical distribution of suspended sediment 41

2.1.3 Retrieval of suspended sediment from remote sensing data 46

2.1.3.1 Remote sensing-based regression approach 46

2.1.3.2 Clustering of remote sensing data 52

2.2 Mapping of suspended sediment concentration in rivers 56

2.2.1 Traditional method for spatial measurement 56

2.2.2 Spatial measurement at river confluences 57

2.2.2.1 Dynamics of flow and mixing at river confluences 57

2.2.2.2 Field experiments in river confluences.................................. 64

3. Experimental studies 68
3.1 Experimental cases 68
3.2 Laboratory experiment 74
3.2.1 Experimental setup.. 74
3.2.2 Experimental method.. 78
3.3 Field-scale experiments in River Experiment Center.......................... 83
3.3.1 Experiments in the straight channel... 83
3.3.2 Experiments in the meandering channel 96
3.4 Field survey 116
3.4.1 Study area and field measurement 116
3.4.2 Hydraulic and sediment data in rivers with simple geometry...... 122
3.4.3 Hydraulic and sediment data in river confluences...................... 126
3.5 Analysis of hyperspectral data of suspended sediment...................... 141
3.5.1 Hyperspectral data of laboratory experiment.............................. 142
3.5.2 Hyperspectral data of field-scale experiments............................ 146
3.5.2.1 Effect of bottom reflectance 146
3.5.2.2 Principal component analysis of the effect of suspended sediment properties.. 154

4. Development of suspended sediment concentration estimator using UAV-based hyperspectral imagery 164
4.1 Outline of Cluster-based Machine learning Regression with Optical Variability (CMR-OV).. 164
4.2 Pre-processing of hyperspectral images 168
4.3 Regression models and clustering technique..................................... 173
4.3.1 Index-based regression models 173
4.3.2 Machine learning regression models... 175

4.3.3 Relevant band selection 183
4.3.4 Gaussian mixture model for clustering 185
4.3.5 Performance criteria 188
4.4 Model development and evaluation 189
4.4.1 Comparison of regression models 189
4.4.1.1 OBRA-based explicit models 189
4.4.1.2 Machine learning-based implicit models 194
4.4.2 Assessment of hyperspectral clustering 200
4.4.3 Spatio-temporal SSC_V mapping using CMR-OV 215

5. Evaluation of field applicability of CMR-OV 225
5.1 Outline of field applicability test 225
5.2 Cross-applicability validation of CMR-OV 227
5.3 Assessment of field applicability in rivers with simple geometry 234
5.4 Assessment of field applicability in river confluences 241
5.4.1 Classification of river regions using hyperspectral clustering 241
5.4.2 Retrievals of SSC_V map 258
5.4.3 Mixing pattern extraction from SSCv map 271

6. Conclusions and future study 274
6.1 Conclusions 274
6.2 Future directions 278

Reference 280

Appendix 308
Appendix A. Breakthrough curve (BTC) analysis 308
Appendix B. Experimental data 310
Appendix B. 1. BTCs of in-situ measured SSC from field-scale experiments 310

Appendix B. 2. Dataset of spectra from hyperspectral images and corresponding SSC in rivers 330
Appendix C. CMR-OV code 331

국문초록 337

List of figures

Fig. 1. 1. Study overview..12
Fig. 2. 1. Flowchart of a remote sensing technique for measurement of suspended sediment. 15
Fig. 2. 2. Types of UAV-based HSI acquisition...16
Fig. 2. 3. Schematic diagram of hyperspectral regression model for SSC measurement. 18
Fig. 2. 4. Field of view (FOV) projection of UAV-mounted camera and its spatial shifts of the frame. 22
Fig. 2. 5. Schematic diagram of radiometric correction using ELM. 24
Fig. 2. 6. Noise in HSI due to surface reflection and its removal with filtering. 27
Fig. 2. 7. Solar radiation transfer in water environments (modified from Beak et al., 2019). 30
Fig. 2. 8. Reflectance calculated from simplified radiative transfer equation, Eq. (2.2), according to water depth; (a) sediment bottom and (b) Macrophyte (vegetation) bottom..40
Fig. 2. 9. Mechanics of vertical transport of suspended sediment in rivers. ...42
Fig. 2. 10. Variation of SSC along with the flow depth (revised from Rouse (1937)). 45
Fig. 2. 11. Remote sensing reflectance (Rrs) by clear water (blue) and water with chlorophyll (green), CDOM (navy), and sediment (brown) (revised from Hafeez et al. (2019))..47
Fig. 2. 12. Flowchart of hyperspectral clustering...54
Fig. 2 13. Spatial distribution of SSC at large river confluences (revised from Jung et al. (2019)). 62
Fig. 2. 14. Eddy dynamics at large river confluences (revised from Jirika and

Uijttewaal (2004)): (a) wake mode; (b) Kelvin-Helmholz mode; (c) vertical eddy generation. 63
Fig. 3. 1 Experimental setting in the laboratory for (a) concentration, (b) PSD, and (c) density of sediment sample. 72
Fig. 3. 2. Comparison of SSC_W measured based on the dry weight of each sample and SSC_V measured using LISST-200X: (a) QS1, (b) YL1, and (c) YL2. 73
Fig. 3. 3. Experimental setup of Exp. 1; (a) overview, (b) apparatus of rotating lateral cylinder, (c) photo of experimental setup.....................................77
Fig. 3. 4. Spatially averaged hyperspectral spectrum of QS2: (a) points extracted for spatial average; (b) spatially averaged hyperspectral spectrum. 79
Fig. 3. 5. (a) RGB images and (b) spectral profiles according to SSC_W value in Exp. 1. 81
Fig. 3. 6. (a) Experimental set-up in REC channel of which water is supplied from nearby Nakdong River; (b) Injection point and measurement section of Exp. 2-1 in the experimental channel; (c) picture of sediment injection scene; (d) detailed configuration of the observation point of Exp. 2-1....86
Fig. 3. 7. PSD of the suspended sediment at the maximum SSC_V measured in Exp. 2-1; (a), (c), and (e) represent PSD sampled near the water surface; (b), (d), and (f) represent PSD sampled near the riverbed. 91
Fig. 3. 8. BTCs of In-situ measured SSC_V: (a) quartz sand, (b) yellow less, (c) mixture, and (d) their RGB images. 93
Fig. 3. 9. (a) Bottom types, Injection Point (I.P), and measurement section of concentration and flow in Exp. 2-2; (b) in-situ measurements of SSC_V and flow in Section 2; (c) in-situ measurements of SSC_V in Sections 1 and 3; (d) channel Bottom covered by vegetation and (e) natural sediment. 98
Fig. 3. 10 Hydraulic conditions in each section: Cross-sectional averaged

velocity and water depth in (a) Cases 2-2-1 ~ 2-2-3 and (b) Cases 2-2-4 ~ 2-2-7. 104
Fig. 3. 11. SCI in each section before and after removing vegetation at Sec. C2. 105
Fig. 3. 12. BTCs of in-situ measured SSC_V (vegetated bottom): (a) Case 2-2-1, (b) Case 2-2-2, and (c) Case 2-2-3. 108
Fig. 3. 13. BTCs of in-situ measured SSC_V for sand bottom: (a) Case 2-2-4, (b) Case 2-2-5, (c) Case 2-2-6, and (d) Case 2-2-7. 109
Fig. 3. 14. Cloud images of quartz sand and yellow loess captured using an RGB camera mounted on a drone. 110
Fig. 3. 15. Standard deviation and skewness of BTCs measured in each case. 113
Fig. 3. 16. PSDs at the maximum SSC_V value at Exp. 2-2-vegetation (a and b) and Exp. 2-2-sand (c and d). 115
Fig. 3. 17. Location of survey areas at the Nakdong and Hwang Rivers. 119
Fig. 3. 18. Flow discharge at Hapcheon-Changnyung dam and Hwang River bridge stations, and date of field surveys. 121
Fig. 3. 19. RGB images of the field campaign area of (a) Exp. 3-1 and (b) 3-2 in Hwang River captured by drone. 123
Fig. 3. 20. Measured datasets in Exp 3-1: (a) depth-averaged water depth and velocity; (b) surface SSC_V; (c) vertical SSC_V profile. 124
Fig. 3. 21. The measured distribution of (a) H and (b) SSC_V in Exp. 3-2. 125
Fig. 3. 22 RGB images of the near-field of confluence between Nakdong and Hwang Rivers captured by drone in Exp. 4-1~4-3. 129
Fig. 3. 23. Flow measurement results at nine cross-sections upstream and downstream of the confluence of Nakdong and Hwnag Rivers in Exp. 4-1 (left bank on the right hand)..134
Fig. 3. 24. Vertical (a) SSC_V and (b) PSD profiles measured using LISST at NR5 in Exp. 4-1; y denotes the distance from the left bank. 136

Fig. 3. 25. Flow measurement results at nine cross-sections upstream and downstream of the confluence of Nakdong and Hwnag Rivers in Exp. 4-3 (left bank on the right hand)...138
Fig. 3. 26. Vertical (a) SSC_V and (b) PSD profiles measured using LISST at NR5 in Exp. 4-3; y denotes the distance from the left bank. 140
Fig. 3. 27. Hyperspectral spectrum according to SSC_W under non-bottom reflectance condition (Exp. 1): (a) QS 1, (b)QS 2, (c) YL 1, and (d) YL 2. 143
Fig. 3. 28. R^2 distribution of OBRA with a single-band ratio under non-bottom reflectance condition: (a) QS 1, (b)QS 2, (c) YL 1, and (d) YL 2..........145
Fig. 3. 29. Acquired hyperspectral spectrum at the corresponding point of SSC_V in-situ measurement: (a) Quartz sand, (b) Yellow loess, (c) Mixture...148
Fig. 3. 30. Results of OBRA with a single-band ratio under a constant bottom reflectance condition: (a) QS 1, (b) YL 1, and (c) mixture. 149
Fig. 3. 31. Hyperspectral spectrum collected in background water without sediment injection at each section of Exp. 2-2: (a) vegetation bottom, (b) sand bottom. (c) comparison by bottom type in Sec. C2; shaded area indicates the standard deviation of the time-averaged spectrum. 152
Fig. 3. 32. Hyperspectral spectrum according to SSCv at Sec. C2 of Exp. 2-2 with natural sand (a, c, and e) and vegetated bottom (b, d, and f). 153
Fig. 3. 33. Hyperspectral spectrum under constant bottom condition (Exp. 2-1) in the space of the principal component (PC) 1 and 2. 157
Fig. 3. 34. The comparison of RGB image, PC 1, and PC 2: (a) Case 2-1-1 (Quartz sand), (b) Case 2-1-2 (Yellow loess), (c) Case 2-1-3 (Quartz sand+ Yellow loess). 159
Fig. 3. 35. Hyperspectral spectrum in the space of the PCs 1 and 2 for Exp. 2-2: (a) quartz sand, (b) yellow loess, and (c) mixture.............................161
Fig. 4. 1. Flowchart of CMR-OV with two modules: real-time updating and

application. 166
Fig. 4. 2. Flowchart of the process of developing multiple estimators based on three main algorithms: RFE, MLR, and GMM. 167
Fig. 4. 3. Times series data of (a) radiance, (b) normalized reflectance, and (c) filtered reflectance in the 650 nm wavelength 172
Fig. 4. 4. Structure of single decision tree for HSI-based SSC estimation.... 178
Fig. 4. 5. Training and prediction processes in RF. 180
Fig. 4. 6. Flowchart of selecting relevant spectral bands using RFE 184
Fig. 4. 7. Comparison of in-situ measure SSCv and remote sensed SSCv from linear regression (LR) and symbolic regression (SR); The independent variables are (a) single band ratio and (b) normalized difference ratio. 192
Fig. 4. 8. (a) Results of RFE and optimal point of RF and SVR; Frequency of a selected band from RFE according to wavelength: (b) RF, (c) SVR. .195
Fig. 4. 9. Comparison of in-situ measured SSC and remote sensed SSC from RF and SVR. 198
Fig. 4. 10. Relative band importance calculated using RFE according to cluster type in Exp. 2-1 (constant bottom condition). 203
Fig. 4. 11. Result of the clustered dataset (Exp. 2-1) in the PCs domain. 204
Fig. 4. 12. Comparison of in-situ measured SSC_V and predicted SSC_V (a) before and (b) after clustering. 207
Fig. 4. 13. Relative band importance calculated by RFE according to the cluster type in Exp. 2-2. 210
Fig. 4. 14. Hyperspectral spectrum of (a) Cluster 1 and (b) Cluster 2, with the mean of the spectrum indicated as a bold line and the standard deviation as shade; (c) boxplot of physical factors according to the cluster type: sediment type, bottom type, d_{50}, the fraction of clay, silt and sand, and temperature. 214
Fig. 4. 15. Spatiotemporal SSCv distribution retrieved from CMR-OV in Exp. 2-1: (a) quartz sand, (b) yellow loess, and (c) mixture. 217

Fig. 4. 16. Comparison of in-situ measured BTC of SSC_V and retrieved BTC of SSC_V using CMR-OV with training data set and test data set: (a) quartz sand, (b) yellow loess, (c) mixture. 220
Fig. 4. 17. Spatiotemporal SSC_V distribution retrieved from CMR-OV in Exp. 2-2: (a and b) quartz sand, (c and d) fine yellow loess. 223
Fig. 4. 18. Spatiotemporal SSC_V distribution retrieved from CMR-OV in Exp. 2-2: (a and b) coarse yellow loess, (c and b) mixture. 224
Fig. 5. 1. Comparison between in-situ measurement and prediction of local learning and merged learning. 229
Fig. 5. 2. Relative band importance from CMR-OV by merged learning. 230
Fig. 5. 3. Shuffled dataset of 5 folds cross-validation; training dataset is in black, and test dataset is in white. 232
Fig. 5. 4. Cross-validation results according to the number of clusters: (a) training score and a test score of R^2, (b) test score of RMSE, and (c) learning rate. 233
Fig. 5. 5. Comparison of in-situ measured time-averaged SSCv and SSCv estimated using (a) CMR-OV and (b) explicit model (SR 2) in Exp. 4-1. 235
Fig. 5. 6. Spatial SSCv distributions in Exp. 3-1 retrieved using (a) CMR and (b) explicit model (SR 2). 236
Fig. 5. 7. Comparison of in-situ measured time-averaged SSCv and SSCv estimated using (a) CMR-OV and (b) explicit model (SR 2) in Exp. 3-1. 239
Fig. 5. 8. Spatial SSCv distributions in Exp. 3-2 retrieved using (a) CMR and (b) explicit model (SR 2). 240
Fig. 5. 9. (a) Cluster mapping result of HSI acquired in Exp. 4-1 and averaged hyperspectral spectrum of (b) Cluster 1 and (c) Cluster 2. 243
Fig. 5. 10. PCA results of Survey 1: (a) Hyperspectral spectrum in PC 1 - PC 2 domain and (b) histogram of PC 1. 244

Fig. 5. 11. Sediment-water quality parameters of hyperspectral clusters in Exp. 4-1. 246
Fig. 5. 12. Comparison between hyperspectral clustering and in-situ measured clustering. 247
Fig. 5. 13. (a) Cluster mapping result of HSI acquired in Exp. 4-2 and averaged hyperspectral spectrum of (b) Cluster 1, (c) Cluster 2, and (c) Cluster 3. 249
Fig. 5. 14. PCA results of Exp.4.2: (a) Hyperspectral spectrum in PC 1 - PC 2 domain and (b) histogram of PC 1. 251
Fig. 5. 15. Sediment-water quality parameters of hyperspectral clusters in Exp. 4-2. 252
Fig. 5. 16. (a) Cluster mapping result of HSI acquired in Exp. 4-3 and averaged hyperspectral spectrum of (b) Cluster 1 and (c) Cluster 2. 255
Fig. 5. 17. PCA results of Exp.4-2: (a) Hyperspectral spectrum in PC 1 - PC 2 domain and (b) histogram of PC 1. 256
Fig. 5. 18. Sediment-water quality parameters of hyperspectral clusters in Exp. 4-3. 257
Fig. 5. 19. Comparison of SSC_V mapping results of Survey 1: (a) CMR-OV and (b) single RF. 259
Fig. 5. 20. In-situ measurement-based mapping results of Exp. 4-1: (a) raw SSC_V data, (b) interpolated SSC_V data, and (c) interpolated turbidity data. 260
Fig. 5. 21. Comparison of depth-averaged SSCv and estimated SSCv along with the transverse distance from the left bank at NR5 section in Exp. 4-1. 262
Fig. 5. 22. Comparison of in-situ measured SSCv and estimated SSCv along with the transverse distance from the left bank in the NR5 section in Exp. 4-2. 264
Fig. 5. 23. Comparison of SSCv mapping results of Exp. 4-2: (a) CMR-OV

and (b) single RF..265
Fig. 5. 24. Comparison of depth-averaged in-situ measured SSCv and estimated SSCv along with the transverse distance from the left bank at NR3 section in Exp. 4-3..268
Fig. 5. 25. SSCv mapping results from CMR-OV in Exp. 4-3.....................269
Fig. 5. 26. In-situ measurement-based mapping results of Exp. 4-3: (a) raw turbidity data and (b) interpolated turbidity data. 270
Fig. 5. 27. Mixing metric distribution along with longitudinal distance normalized by upstream width (X_L/W_0): (a) Exp. 4-1 and (b) Exp. 4-3. 273

List of tables

Table 2. 1. HSI pre-processing methods used in previous studies using UAV-borne hyperspectral images.......20
Table 2. 2. Variables to estimate the optical properties and the related properties of the sediment.......37
Table 2. 3. Regression models for remote sensing-based SSC measurement .48
Table 2. 4. Comparison of clustering methods.......55
Table 2. 5. Summary of field experiments of previous studies in river confluences. 66
Table 3. 1. Properties of the sediment used in the experiments; a dominant fraction value of each sediment are bolded in the shaded column.......70
Table 3. 2. Summary of experimental studies: lab-scale and field-scale experiments.......71
Table 3. 3. Experimental cases and properties of sediment used in each case. 82
Table 3. 4. Sediment injection condition in Exp. 2-1.......85
Table 3. 5. Description of SSC_V curves from Exp. 2-1. 95
Table 3. 6. Sediment injection condition in Exp. 2-2.......99
Table 3. 7. Results of hydraulic measurements in Exp. 2-2. 103
Table 3. 8 Description of SSC_V curves from Exp. 2-2: Case 2-2-1 ~ 2-2-3..111
Table 3. 9 Description of SSC_V curves from Exp. 2-2: Case 2-2-4 ~ 2-2-7..112
Table 3. 10. Summary of field surveys.......120
Table 3. 11 Characteristic parameters of Nakdong and Hwang Rivers during Exps. 4-1 ~ 4-3.......128
Table 3. 12. Summary of hyperspectral datasets of suspended sediment collected in lab-scale and field-scale experiments.......141
Table 3. 13. Correlation between principal component 1 (PC 1) and sediment

properties for Exp. 2-1. 158
Table 3. 14. Correlation between PCs and physical variables for Exp. 2-2; the highlighted panels indicate an absolute value of correlation over 0.5. ..163
Table 4. 1. Statistical properties of training and test dataset. 190
Table 4. 2. Equations of index-based explicit regression models and their independent variable with optimal wavelength. 193
Table 4. 3. Validation results of separately trained models according to sediment type of Exp. 2-1. 199
Table 4. 4. Evaluation of RF according to number of clusters in Exp. 2-1; the values of highest accuracy are bolded..202
Table 4. 5. Wavelength of selected bands in each cluster.............................202
Table 4. 6. Evaluation of RF according to the number of clusters in Exp. 2-2; the values of highest accuracy are bolded...206
Table 4. 7. Wavelength of selected bands in each cluster and the non-clustered dataset. 209
Table 4. 8. Physical variables of each cluster and differences in each variable as measured by the Mann-Whitney U test; sand and vegetated bottom were indexed as 0 and 1, respectively. 213
Table 4. 9. Evaluation of estimated BTC from CMR-OV according to parts of BTC..219
Table 5. 1. Summary of datasets for field applicability test. 226

List of abbreviations

ADCP	Acoustic Doppler current profiler
ADV	Acoustic Doppler velocimeter
AOPs	Apparent Optical Properties
BTC	Breakthrough curve
CHZ	Confluence hydrodynamic zone
CMR-OV	Cluster-based machine learning regression with optical variability
EC	Electronic conductivity
ELM	Empirical line method
FOV	Field of view
GMM	Gaussian mixture model
HIS	Hyperspectral image
IOPs	Inherent optical properties
IP	Injection point
KH	Kelvin-Helmholtz
LISST	Laser in-situ scattering transmissometers
LR	Linear regression
LSPIV	Large scale particle image velocimetry
MAPE	Mean absolute percentage error

MLR	Machine learning regression
MSE	Mean square error
NIR	Near-infrared
NUC	Nonuniformity corrections
OBRA	Optimal band ratio analysi
PC	Principal component
PCA	Principal component analysis
PDF	Probability density function
POS	Position and orientation system
PSD	Particle size distribution
REC	River Experimental Center
RF	Random forest
RFE	Recursive feature elimination
RFECV	Recursive feature elimination cross-validation
RMSE	Root mean square error
RMSEP	Root mean square error percentage
RTK-GPS	Real-time kinematic-global positioning system
SAVGOL	Savitzky-Golay
SCI	Secondary current intensity
SMA	Spectral mixing analysis
SR	Symbolic regression
SSC	Suspended sediment concentration

SVM	Support vector machine
SVR	Support vector regression
TSE	Total error score
UAV	Unmanned aerial vehicle
VIS	Visible

List of symbols

Latin Uppercase

C	Concentration
DN	Digital number
E_d	Irradiance
Fr_d	Densimetric Froude number
G'	Coefficient defined as the relative contribution of the scattering to the vertical attenuation of the irradiance
H	Water depth
H_c	Cross-sectional averaged water depth
I_i	Relative importance of *i*th spectral band
J	Number of clusters
K	Attenuation coefficient
$KURT$	Kurtosis
L	Radiance
L_b	Upwelling radiance from the bed
L_c	Backscattered radiance from the water body
L_p	Upwelling path radiance from the atmosphere
L_s	Upwelling radiance from the interface between the atmosphere and the water body

L_u	Total radiance recorded at the sensor
MR	Flow momentum ratio
$N(d)$	PSD representing the number of particles having size d
N_{mix}	Gaussian mixture probability density function
N_k	Gaussian distribution of *kth* cluster
NT	Number of decision tree in Random forest model
P	Rouse number
Q	Discharge
$\overline{Q_a}$	efficiency factors for absorbance
$\overline{Q_{bb}}$	efficiency factors for backscattering
QR	Discharge ratio
R	Reflectance
R_∞	Reflectance of the infinitely deep water column
R_{rs}	Remote sensing reflectance
$SKNS$	Skewness
SSC_V	Volumetric concentration of suspended sediment
SSC_W	Weight concentration of suspended sediment
T	Water temperature
U	Depth-averaged streamwise velocity
U_*	Reach-averaged shear velocity
U_c	cross-sectional averaged velocity

UR	Mean flow velocity ratio
W	Channel width
W_0	Upstream channel width
X	Independent variable
X_L	Longitudinal distance

Latin Lowercase

a	Absorption coefficient
a_{ss}	Absorption coefficient of suspended sediment
a_{tot}	Total absorption coefficient
b_b	Backscattering coefficient
b_{bss}	Backscattering coefficient of suspended sediment
b_{tot}	Total backscattering coefficient
c	Time-averaged concentration
c'	Fluctuations of concentration
c_f	Quadratic-law friction coefficient
d	Particle size
d_{50}	Median particle size
g	Gravitational acceleration
i	Index of data

j	Dummy variable
k	Order
l	Log likelihood
$loss$	Loss function
m_k	k_{th} degree temporal moment
$\dot{m}$	Mass flux
n	Number of the transverse measurement points
t	Time
$\overline{t}$	Centroid time
u	Streamwise velocity
u_n'	Deviation of the spanwise velocity
w	Vertical velocity
w_s	Settling velocity
$\hat{y}_i$	Predicted suspended sediment concentration
y_i	In-situ measured suspended sediment concentration
z	Vertical direction

Greek Uppercase

Γ	Penalty factor
$\Delta\rho^*$	Relative density difference

$\Delta\rho_{ssc}$	Effect of suspended sediment on water density
Σ	Covariance matrix

Greek Lowercase

β	Ratio of momentum diffusivity and turbulent diffusion coefficient
γ	Responsibility
ε	Deviation
θ	Parameter subset of Gaussian mixture model
κ	Von Kármán constant
λ	Wavelength
μ	Mean
ν	Momentum diffusivity coefficient
ξ	Slack variable
π_k	Mixture coefficient
ρ	Density
ρ_b	Bottom albedo
σ	Standard deviation
σ_{nyz}	Mixing metric

σ_{nz} Standard deviation of SSC for the downstream cross-sections

Ψ Shape factor

ω Weight of spectral band

1. Introduction

1.1 Background and necessities of study

In rivers, the dynamics of suspended sediment exert a significant impact on river morphology and the ecosystem; they also affect flow and transport behaviors of pollutants (Kabir and Ahmari, 2020; Leite Ribeiro et al., 2012; Umar et al., 2018a). To improve our understanding of the suspended sediment transport mechanisms in riverine system, high-resolution spatio-temporal data of the suspended sediment are required for analysis of the complex interactions between suspended sediments and the hydraulic and environmental factors such as river discharge, velocity, and water quality variables (Vercruysse et al., 2017). In the conventional method, measurement of the suspended sediment concentration (SSC) relied on in-situ measurements based on the sampling of the river water. This in-situ measurement approach is highly labor-intensive and time-consuming, and it provides low-resolution temporal and spatial datasets (Qu et al., 2016). Laser-diffraction-based optical sensors and turbidity sensors have frequently been used as alternatives of the conventional method, to obtain high-resolution temporal SSC data using high measurement frequency (Haun et al., 2013; Lokhov et al., 2020; Pedocchi and García, 2006; Pomázi and Baranya, 2020). These sensors can semi-automatically provide sufficient temporal data and trends after calibration with point samples; however, the labor costs are high for producing high-spatial-resolution data because these sensors only provide point measurements (Pomázi and Baranya, 2020; Rai and Kumar, 2015). Acoustics-based SSC measurements are an alternative to these point-based measurement methods; they are obtained using an acoustic Doppler current profiler (ADCP) to determine the cross-sectional distribution of suspended sediment (Simmons et al., 2020; Son et al., 2021; Wosiacki et al., 2021). Despite this distinct advantage over other methods, ADCP is limited in differentiating the change between SSC and the particle size distribution (PSD) of the suspended sediment, because single or multiple frequencies should be selected for use in ADCP (Aggarwal et al., 2011). Therefore, the error increases with variations in PSD; the ADCP data are accurate in a limited PSD range depending on the specific frequencies in the ADCP (Thorne and Hanes, 2002; Thorne and Hurther, 2014).

In recent years, with the advances in image processing techniques, numerous studies have used remote sensing approaches to retrieve high-resolution spatial data on the quality of large bodies of water from multispectral or hyperspectral satellite images (Arisanty and Nur Saputra, 2017; Caballero et al., 2018; Dekker, 1993; Dekker et al., 2001; Dethier et al., 2020; Ismail et al., 2019; Kabir and Ahmari, 2020; Ross et al., 2019; Topp et al., 2020; Umar et al., 2018a). The principle underlying the remote sensing SSC measurement in aquatic environments is based on the optical characteristics of sunlight, which is absorbed intensively in the water body. By sensing the sunlight intensity, the spectral signals of solar radiation at visible (VIS) and near-infrared (NIR) wavelengths can be captured by multispectral or hyperspectral cameras (Dethier et al., 2020; Fonstad and Marcus, 2005; Kwon et al., 2020; Wei et al., 2019). These spectral signals of solar radiation are recorded as the radiance of discrete spectral bands with respect to wavelength. The VIS and NIR regions are the most relevant spectral band when using this feature of the remote sensing technique; they best represent SSC based on the correlation between SSC and the radiance of the bands. To identify the relationship between SSC and the relevant spectral bands, many researchers applied simple regression models, including linear, exponential, polynomial, and log-linear models (Doxaran et al., 2003; Islam et al., 2001; Liu et al., 2017; Ma and Dai, 2005; Pereira et al., 2019; Schiebe et al., 1992; Shen et al., 2010; Topliss et al., 1990; C. Wang et al., 2017; F. Wang et al., 2009; J.-J. Wang et al., 2009). Additionally, machine learning approaches were applied to improve the accuracy of the regression model with more diverse spectral bands, effectively resolving the nonlinearity between the input spectral values and the target SSC values (Peterson et al., 2018; Umar et al., 2018).

In terms of the water bodies, most remote-sensing studies were conducted in marine and coastal environments because it is possible to acquire sufficient amount of relevant spatial data from satellite images, and the effect of bottom reflectance is less pronounced in marine and coastal areas than in the shallow water bodies of rivers. Due to the relative narrowness of rivers, remote sensing-based SSC measurements have rarely been applied to riverine systems (Pham et al., 2018). The recently launched Sentinel-2 and Sentinel-3 satellites have improved the spatial resolution of available images by up to 5–10 m; however, coarse spectral resolution, which has a bandwidth of 60–80 nm, is still a crucial shortcoming of satellite-based remote sensing for the measurement of water quality and SSC in rivers (Dekker, 1993; Kwon et al., 2022a, 2020). To overcome this limitation, UAV (unmanned aerial vehicle)-based hyperspectral remote sensing was carried out to measure water depth, algal blooms, and cyanobacteria concentration with higher spatio-temporal resolution and a narrower spectral band width than those provided by multispectral sensors (Kwon et al., 2020; Legleiter et al., 2019; Legleiter and Harrison, 2019; Pyo et al., 2020a). However, the research on the hyperspectral measurement of SSC in rivers is currently insufficient due to the regional characteristics of suspended sediment and stream bed (Dethier et al., 2020; Gebreslassie et al., 2020; Kabir and Ahmari, 2020; Kwon et al., 2021b). Especially in shallow waters, the variety of stream bed types makes the hyperspectral measurement of SSC even more challenging since it is influenced by bottom reflectance.

Earlier studies mainly focused on improving the prediction accuracy in the specific study areas where the relationship between suspended sediment and optical properties of spectral bands is relatively apparent. However, the main wavelengths of the spectral bands involved in the regression equations were spread over a relatively wide range according to the trained area (Pereira et al., 2019). This regionality occurred because the optical characteristics of suspended sediment vary significantly according to the particle size, mineral content, sediment color of the suspended sediment, and stream bed types. These variables are collectively referred to as the spectral variability of suspended sediment (Kabir and Ahmari, 2020; Volpe et al., 2011). Therefore, it is highly challenging to use the existing methods in optically complex rivers, such as river confluences where sediment characteristics, water quality, and bathymetry vary to a great extent.

To account for the spectral variability of suspended sediment, several empirical and semi-empirical models were developed (Bhargava and Mariam, 1990; Gebreslassie et al., 2020; Kabir and Ahmari, 2020; Qu et al., 2016). Among them, a semi-empirical model, spectral mixing analysis (SMA), showed relatively accurate performance irrespective of the spectral variability of suspended sediment (Gebreslassie et al., 2020; Qu et al., 2016). This model can be developed from laboratory analysis to obtain the individual spectrum of constituents, including clean water and dry sediment. The spectral mixing abundance of each constituent can be estimated by decomposing the measured spectrum of river waters based on SMA. The spectral mixing abundance is finally used as the independent variable of the SSC regression model. However, this model did not consider the bottom effect and has limitations in extending to the spatial mapping of SSC because it can be validated and applied only at the points where river water is sampled. Furthermore, a number of suspended sediment samples are required to represent the sediment characteristics of the target river adequately. It is also difficult to consider the suspended sediment as a single constituent if the sediment properties have a bimodal distribution of particle size or varied mineral contents. To develop an empirical model, Kabir and Ahmari (2020) established log-linear regression equations according to sediment color using an RGB camera-based laboratory experiment. They developed practical and accurate models and insisted on the necessity for classification of the SSC estimator according to suspended sediment variability. However, this model had limitations; the amount of available data was inadequate, and the performance in the field was relatively poor due to the discrepancy between the PSDs of suspended sediment samples used in model development and those used in the model application.

Accounting for spectral variability is the most challenging factor in achieving a robust SSC estimator based on remote sensing technique (Dethier et al., 2020; Kwon et al., 2022b, 2022a). Therefore, the key objective of this study was to develop a UAV-based hyperspectral technique that maximizes the accuracy of SSC estimation through understanding the confounding factors of spectral variability. Through this advancement in SSC estimation in rivers, the UAV-based hyperspectral technique could retrieve the high-resolution spatial distribution of SSC in various river conditions. Moreover, it could be used in the problems requiring high-resolution data, such as sediment mixing problems in river confluences, and it could give substantial insights into the physical process of suspended sediment in rivers.

1.2 Objectives and scopes

The primary objective of this study was to develop a robust measurement method for suspended sediment concentration (SSC) using UAV-based hyperspectral imagery and retrieve the spatial distribution of SSC in various field conditions in the riverine system. This main objective was achieved by following three tasks: (1) Experimental studies (Chapter 3); (2) Development of SSC measurement method using UAV-based hyperspectral imagery (Chapter 4); (3) Evaluation of field applicability of developed method (Chapter 5).

In the first task, a laboratory experiment, field-scale experiments, and field surveys were conducted to figure out the spectral variability of suspended sediment (sediment properties, streambed properties, and vertical mixing state of suspended sediment) under various hydro-geomorphic conditions. The first experiment was conducted using the rotating horizontal cylinder in the laboratory. It was set to observe intrinsic optical properties of suspended sediment in a completely mixed state with non-bottom reflectance. Two field-scale experiments were conducted in which various types of sediment were injected in field-scale straight and meandering channels. In these experiments, spatiotemporal hyperspectral images and the corresponding time-series of in-situ measured SSC data were obtained in each case. Based on these experimental datasets, the confounding factors of spectral variability were investigated by comparing the various spectra from hyperspectral images with each other and through principal component analysis (PCA). In addition, five field surveys were carried out in natural rivers of straight reach, meandering reach, and river confluence. In these surveys, both point data of in-situ measured SSC and spatially scanned hyperspectral images from UAVs were collected for the field applicability validation of the model in Chapter 5.

In the second task, a robust machine learning regression framework for SSC estimation was proposed using hyperspectral imagery obtained from UAVs. This novel method, named the cluster-based machine learning regression with optical variability (CMR-OV), consists of three main algorithms: data clustering using Gaussian mixture model (GMM), spectral band selection using recursive feature elimination (RFE), and machine learning regression (MLR) for the relation between hyperspectral spectrum and SSC. Using GMM clustering, the hyperspectral datasets were clustered according to spectral similarity. Separate MLR models were built for every cluster, using corresponding spectral bands selected by RFE. The proposed framework aims to make remote sensing of SSC possible even in optically complex rivers using a wide range of spectral data from various experiments.

In the third task, the field applicability of the proposed model (CMR-OV) was evaluated in two types of testbeds: (1) a shallow river with a single spectral characteristic of river water with a strong bottom effect and (2) a river confluence with two complex spectral characteristics from confluent flows. Remote sensing in shallow waters is challenging owing to the substantial bottom effect; therefore, this study evaluated how CMR-OV controls the bottom effect in a shallow river. The river confluences usually have optically complex conditions since river flow, bathymetry, and mixing characteristics vary rapidly. Therefore, the performance of CMR-OV in controlling the spectral variability was evaluated in a river confluence. Based on the feature of each testbed, the evaluations were focused on four aspects: (1) Cross-applicability; (2) Uncalibrated dataset applicability; (3) Classification of river regions using hyperspectral clustering; (4) Reproducibility of mapping SSC distribution. The objective of the first evaluation was to assess the uncertainty of trained CMR-OV in various rivers. In this process, the accuracy of merged learning using the combined dataset of all field-scale experiments and field surveys was compared with local learning. Subsequently, 5-folds cross-validation was conducted based on merged learning to assess the cross-applicability. Secondly, the applicability in uncalibrated datasets was evaluated using independent datasets in natural rivers. Locality of estimator was the most critical limitation in previous studies; therefore, how much of that limitation can be overcome was evaluated using this assessment. The third evaluation was performed to verify whether CMR-OV can distinguish a tributary and mainstream in a confluence using just hyperspectral imagery. For this, the optical characteristics of river confluences were analyzed based on hyperspectral clustering by comparing water quality and hydrodynamic conditions of each dataset. Finally, the trained CMR-OV model was assessed for accurately reproducing the spatial distributions under independent conditions and retrieval of high-resolution SSC distributions under varying hydrodynamic and morphological conditions in each testbed.

Based on the three tasks mentioned above, the final objectives of this study were as follows: (i) evaluating confounding factors of hyperspectral imagery-based SSC estimation; (ii) developing a robust algorithm to retrieve spatial distribution of suspended sediment concentration in optically complex rivers; (iii) evaluating field-applicability of UAV-based hyperspectral approach in various field conditions. Achieving these objectives could enhance the competence to measure SSC and analyze the physical process of suspended sediment in rivers by overcoming the disadvantages of conventional analysis methods. An outline of this research structure was summarized in Fig. 1.1.

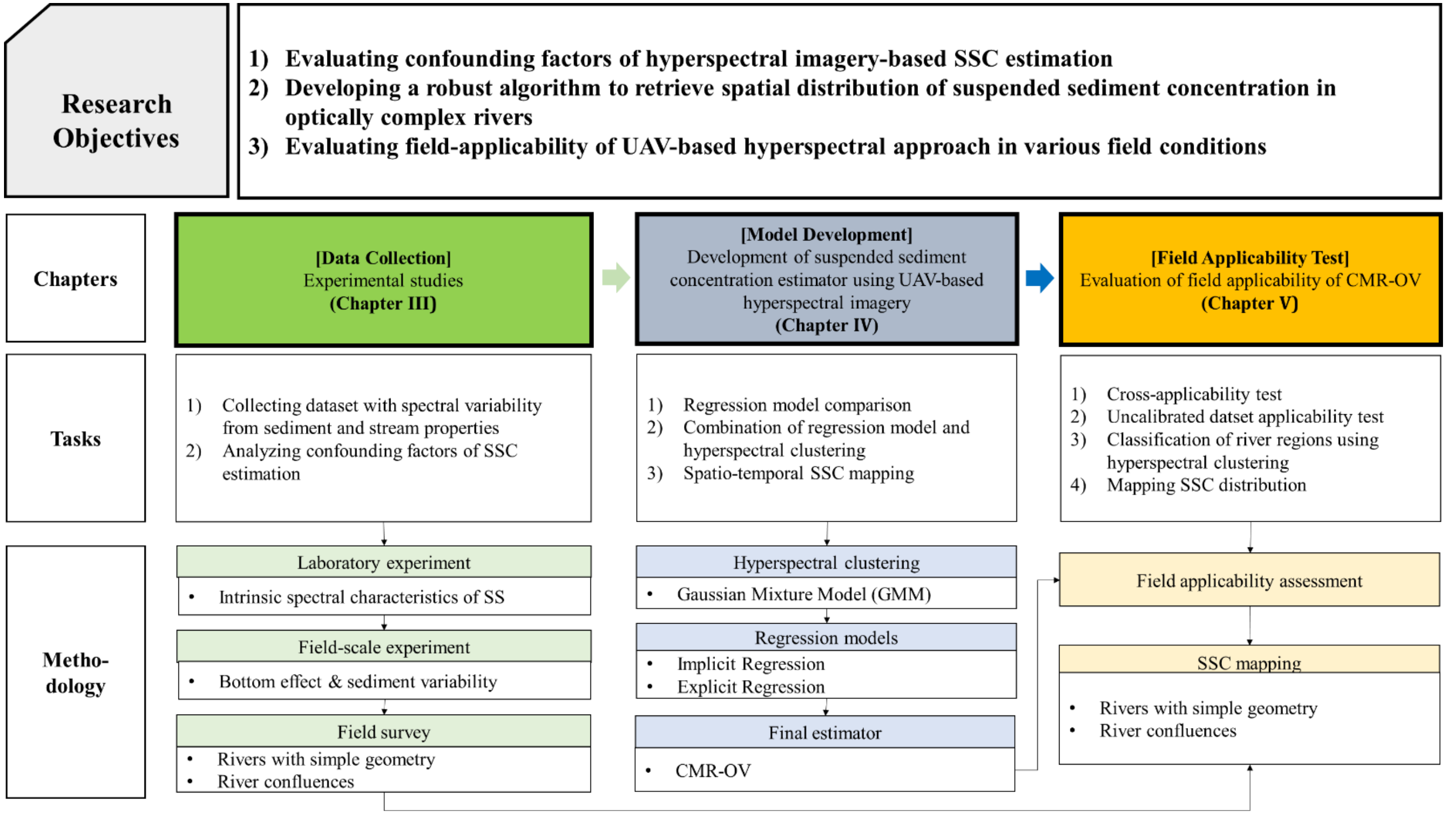

Fig. 1. 1. Study overview.

2. Theoretical research

2.1 Remote sensing technique for measurement of suspended sediment

Developing remote sensing technique for suspended sediment in rivers using UAV-based hyperspectral images (HSI) consists of three main processes: (1) data acquisition, (2) preprocessing of HSI, and (3) regression model development (Fig. 2.1). In data acquisition, in-situ measured values of SSC are required as a reference value. HSIs can be obtained by two types, hovering and spatial scanning, according to the data format, as shown in Fig. 2.2. By hovering UAVs over the cross-section of interest, the spatiotemporal image in the cross-section can be obtained, as shown in Fig. 2.2 (a). To acquire HSI covering a large area, multiple strips are obtained by scanning the space (Fig. 2.2 (b)), and then spatial information of a large area is obtained by co-registering them using coordinates of geo-reference points on the ground. The essential principle in developing a remote sensing-based estimator is to construct a regression model by finding the relationship between the physical quantity of the target variable and the spectral band in the hyperspectral spectrum that responds to its optical characteristics. Accordingly, the in-situ measured SSC dataset is required with corresponding HSIs. Before developing a regression model, the HSI needs to be preprocessed to extract the spectral bands in the hyperspectral spectrum under identical conditions. First of all, it is necessary to standardize the HSI taken under different conditions (radiometric correction) and to remove noise such as surface reflection (noise filtering). Then, the geometric distortion due to the gap between the field of view (FOV) of the camera and its recorded coordinates of each pixel must be corrected using geo-reference points (geometric correction).

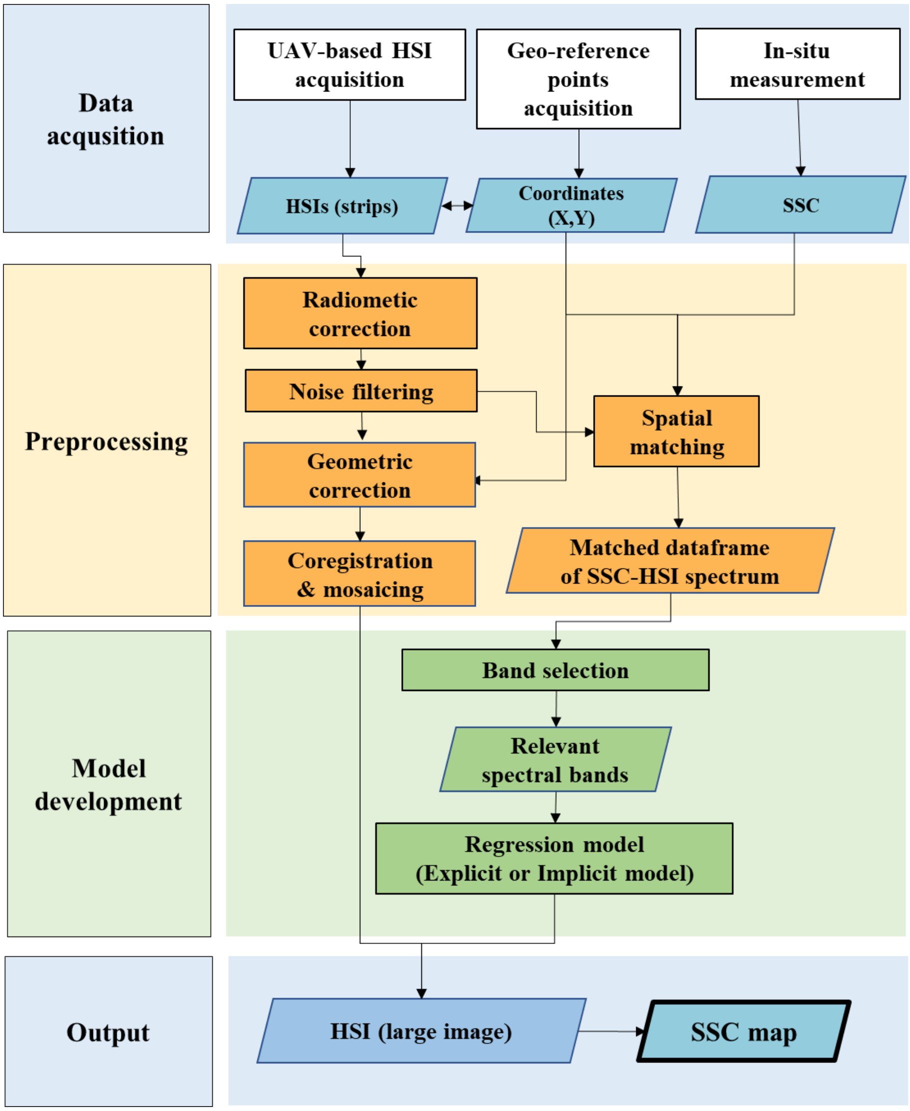

Fig. 2. 1. Flowchart of a remote sensing technique for measurement of suspended sediment.

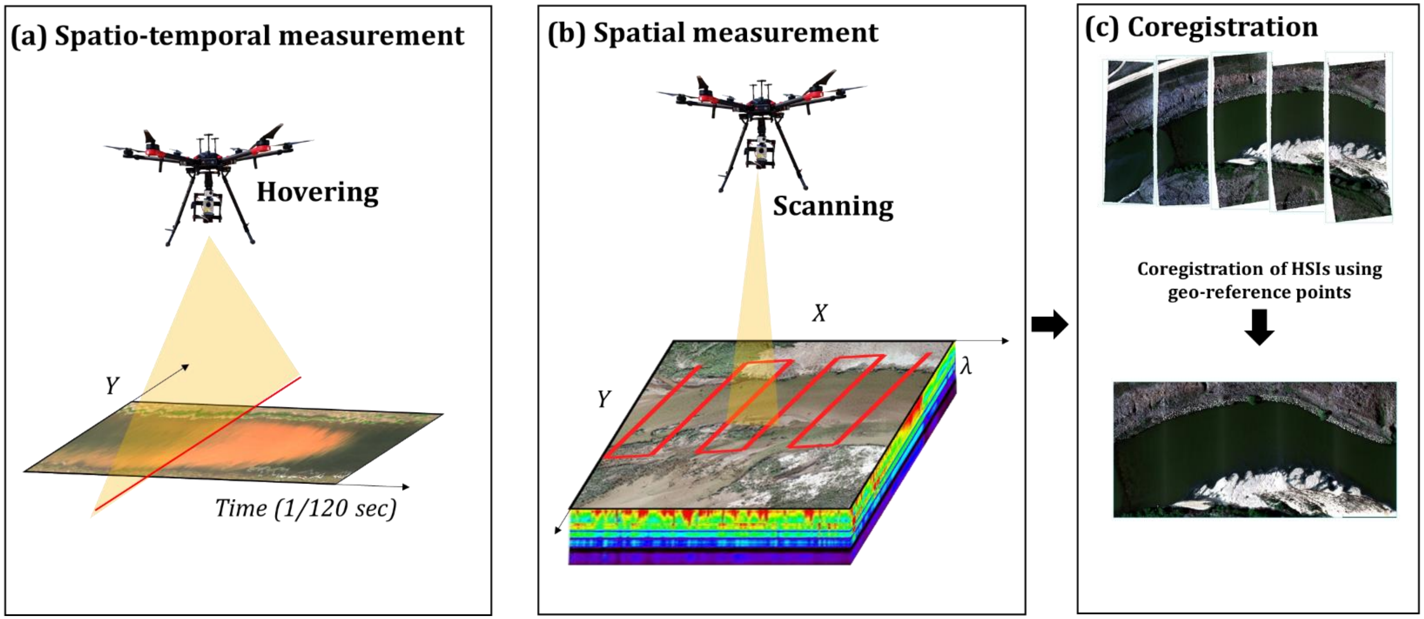

Fig. 2. 2. Types of UAV-based HSI acquisition.

After preprocessing, the regression model can be developed using an in-situ measured SSC dataset and corresponding hyperspectral spectrum as dependent and independent variables (Fig. 2.3). In this process, band selection can enhance the model accuracy by selecting relevant bands because the hyperspectral spectrum has several redundant bands with the suspended sediment. In addition, the form of the regression model is vital to the accuracy. Therefore, finding the optimal form of the model is required according to the given dataset. The finally constructed regression model can retrieve the high-resolution SSC map using preprocessed HSI (Fig. 2.3). However, the uncertainty of this method increases in optically complex conditions due to the variety of suspended sediment and river conditions. Moreover, applying the model to uncalibrated areas is challenging because of the high locality. Based on this knowledge of the general remote sensing approach, the general process of building the SSC remote sensing estimator is described in the following sections of Chapter 2. Further, a novel method to overcome the general method is proposed in Chapter 3.

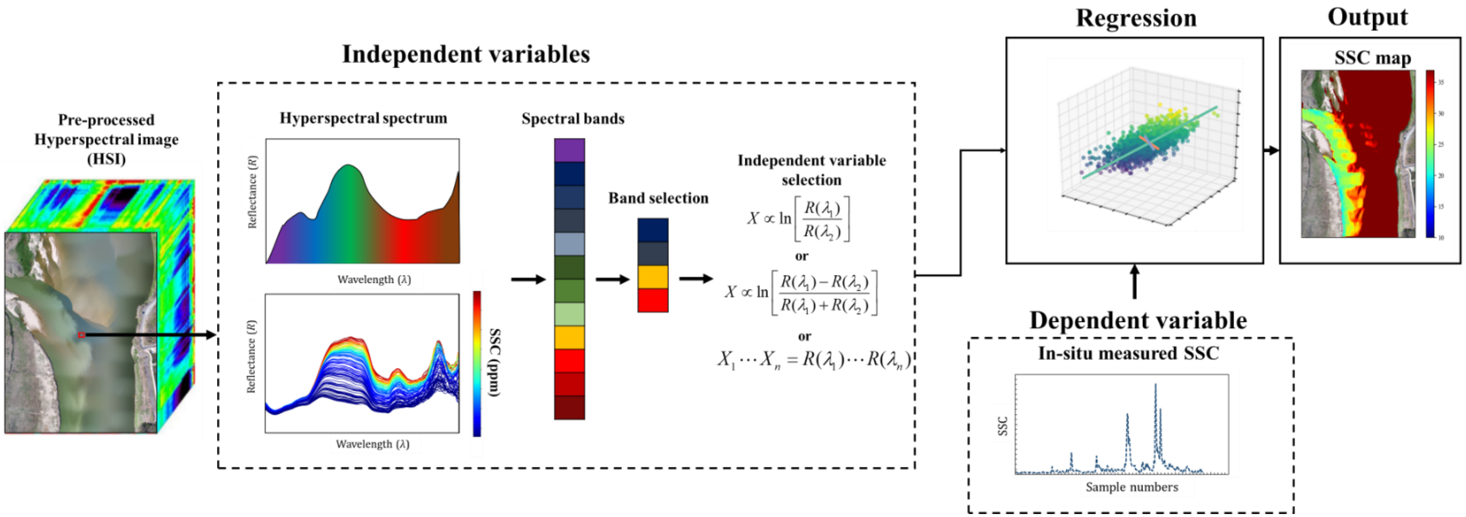

Fig. 2. 3. Schematic diagram of hyperspectral regression model for SSC measurement.

2.1.1 Pre-processing of hyperspectral image (HSI)

UAV-based hyperspectral images need a different and more complicated pre-processing than satellite-based multispectral images due to the low acquisition height, inconstant movement of the UAVs, and the strong influence of the illumination according to camera angle. Existing software for processing UAV-based RGB images is often not applicable for hyperspectral images since most hyperspectral cameras are line scanning type-based push-broom sensors (Barreto et al., 2019; Fowler, 2014). Therefore, the preprocessing technique for UAV-borne RGB images can also not handle the size and especially the data format of hyperspectral imagery. Considering these characteristics of hyperspectral image (HSI), preprocessing for UAV-borne HSI analysis consists of three main steps as follows: (1) geometric correction, (2) radiometric correction, and (3) noise filtering. The methods of HSI preprocessing in recent studies based on the UAV platform are summarized in Table 2.1.

Table 2. 1. HSI pre-processing methods used in previous studies using UAV-borne hyperspectral images.

Reference	Geometric correction	Radiometric correction	Noise filtering	Target
Jakob et al. (2016)	Georeferencing with RGB image	Rikola software, Empirical line method using tarps	SAVGOL	Mineral Exploration
Legleiter et al. (2019)	Georeferencing with kinematic GPS	Empirical line method using tarps	-	Water depth (River)
Kwon et al. (2020)	Georeferencing with kinematic GPS	Empirical line method using tarps	SAVGOL, Wiener2	Agal bloom (Lake)
Gai et al. (2020)	Georeferencing with kinematic GPS	FLAASH (ENVI)	SAVGOL	Chl-a (Coastal)
Booysen et al. (2021)	Georeferencing with RGB image	Rikola software, Empirical line method using tarps	SAVGOL	Rare earth elements
Wei et al. (2021)	Georeferencing with ground measured points	Ground measured spectra based empirical line method	-	Suspended sediment (Lake, River)

The geometric correction is necessary to acquire spatially precise images since the UAV-mounted sensor moves slightly during flight, causing spatial shifts, as shown in Fig. 2.4 (Jaud et al., 2018). The geometric correction matches the HSI and the corresponding coordinates with the orientation system (POS) (Wei et al., 2019). From both HSI and POS, the coordinate system was transformed to establish the correspondence between the image pixels and the coordinates of the geo-reference points. The data of geo-reference points can be obtained by ground GPS at discrete points (Wei et al., 2019) or the RGB orthophoto measured by RTK-GPS mounted drone (Booysen et al., 2020; Jakob et al., 2017). After the geo-referencing, corrected images can be coregistered to make an entire image. The overlapping area of images is accordingly mosaicked without additional ground control points.

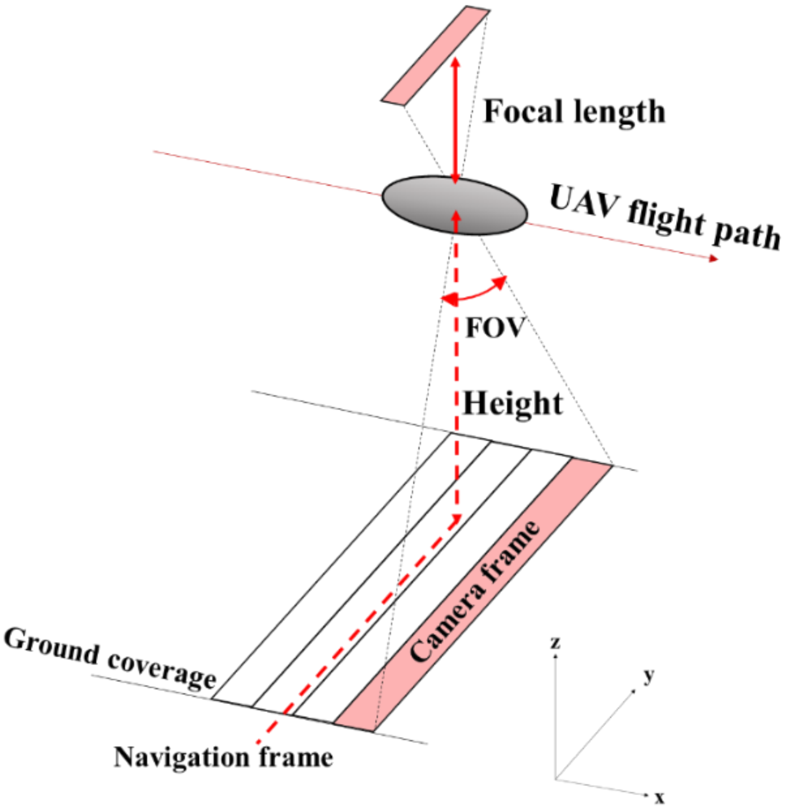

Fig. 2. 4. Field of view (FOV) projection of UAV-mounted camera and its spatial shifts of the frame.

Concurrently, a radiometric correction is needed to convert a digital number (*DN*), which stores the radiance as an integer on the hyperspectral camera, to relative reflectance. Since the radiance recorded in the hyperspectral camera did not coincide with the actual energy emitted or reflected by the surface due to the azimuth angle and elevation of the sun, a radiometric correction is needed to normalize the images, as shown in Fig. 2.5. For this correction, *DN* should be first converted to radiance by gain and offset of each pixel. These gain and offset values are typically retrieved from the metadata from the hyperspectral sensor. After this conversion, the radiance can finally be converted to relative reflectance using the empirical line method (ELM) based on the reference reflectance values (Smith and Milton, 1999). The reference reflectance values for calibration are usually obtained using the calibration tarps, which offer the Lambertian reflectance, as shown in Fig. 2.5. The Lambertian reflectance denotes the isotropic reflected light intensity, which serves as a reference for radiometric correction regardless of the camera angle (Baek et al., 2019). The spectrometer can also measure the reference value of reflectance through ground point measurement of reflectance (Wei et al., 2019). Therefore, the normalized HSI provides the enhanced interpretability and quality of the hyperspectral data (Jeon et al., 2019; Kim et al., 2020; Kwon et al., 2020; Legleiter et al., 2019; Meyer et al., 1993).

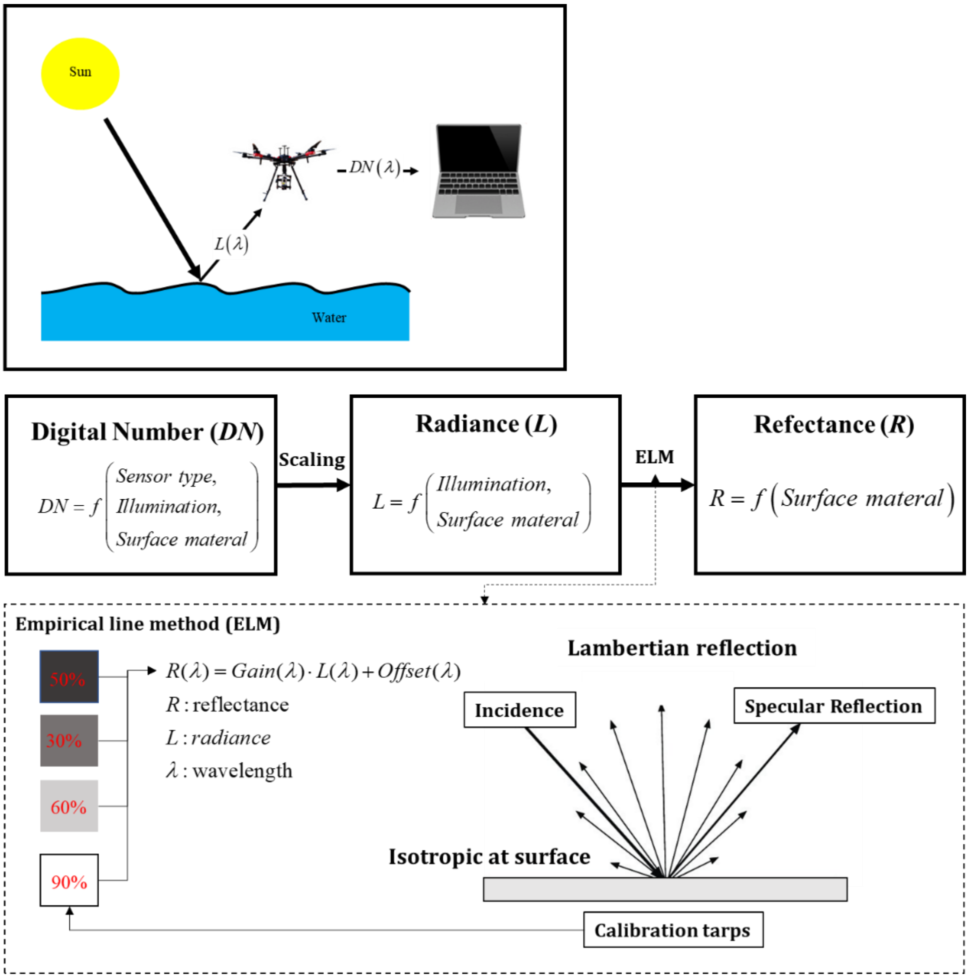

Fig. 2. 5. Schematic diagram of radiometric correction using ELM.

On the other hand, HSI usually includes noise, which usually arises from sensor sensitivity, sun glint, and solar conditions (e.g., cloud coverage) (Mishra et al., 2019; Zeng et al., 2017). When capturing the HSI in rivers, surface reflection usually occurs from irregular water surfaces owing to turbulence or at a point where the water surface changes rapidly. In addition, suspended substances or bubbles on the water surface induce the water surface reflection. In these cases, the back-scattered radiance from the water column from reaching the sensor can be disturbed by substantial surface radiance, as shown in Fig. 2.6. When the surface reflection occurs, the measured radiance shows a shape similar to the spectrum of sunlight, as illustrated in Fig. 2.6. This radiance spectrum has high values and is entirely different from the spectral characteristics of the water column; thus, preprocessing of this signal is necessary. Therefore, the de-nosing of HSI is essential for spectral analysis. Two ordinary filters for this process are Savitzky-Golay (SAVGOL) filter and the median filter (Eon and Bachmann, 2021; Kwon et al., 2020; Mishra et al., 2019; Okyay et al., 2016). SAVGOL uses different polynomial functions to smooth signals using a window-based technique (Savitzky and Golay, 1964). Median filtering is also a window-based filter, replacing each measured value with the median value of the data inside the window. These filtering methods can be used independently for each hyperspectral spectrum of a pixel in the HSI. Nevertheless, if the noise level is too high, these filters need to determine the optimum window size for filtering, but it is a user-dependent parameter. Further, the spectral profile can be deformed if the noise is present in subsequent wavelengths.

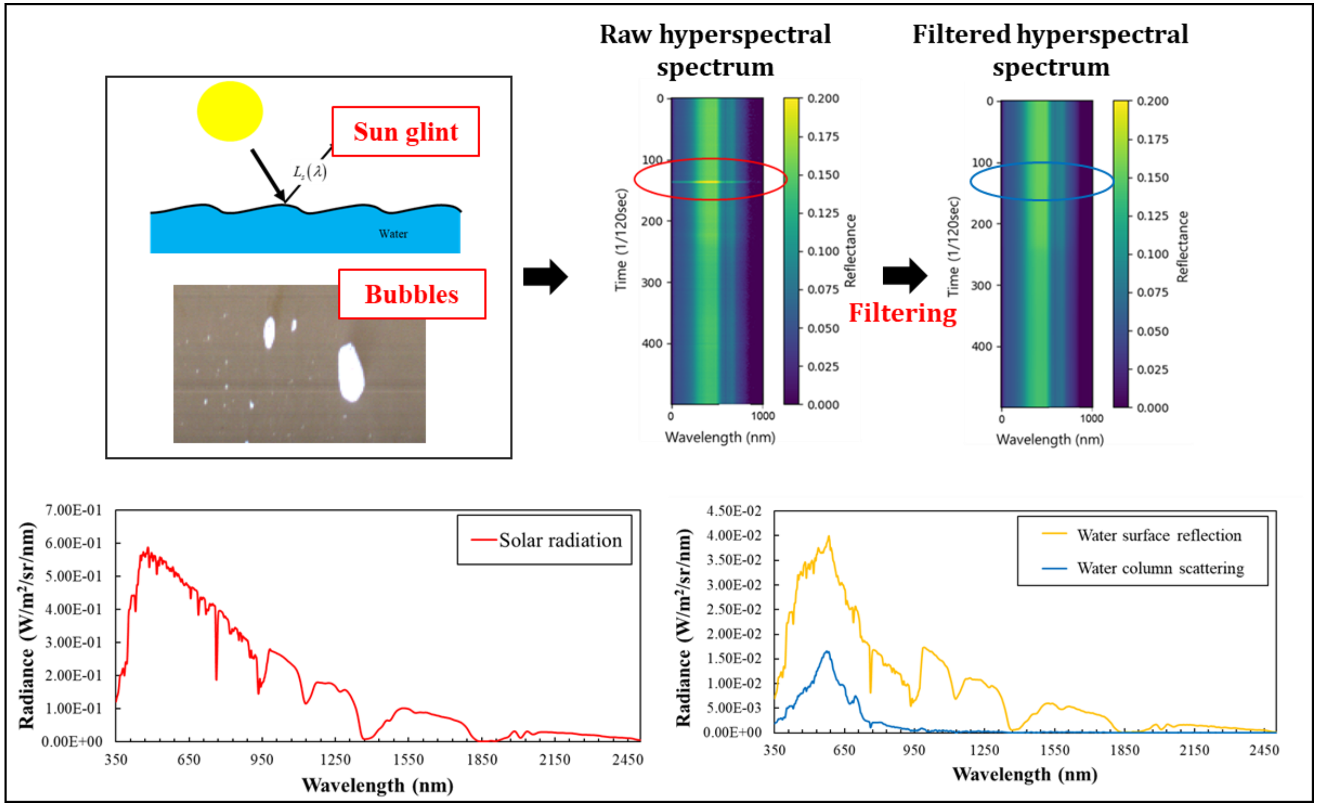

Fig. 2. 6. Noise in HSI due to surface reflection and its removal with filtering.

2.1.2 Optical characteristics of suspended sediment in rivers

2.1.2.1 Theory of solar radiation transfer in rivers

The principle of detecting the scattering feature of the suspended sediment as radiance and converting it into concentration is physically clear, but the radiance detected by the hyperspectral camera consist of complex signals. In addition, the scattered radiance is significantly affected by the variability of sediment and stream properties, and it is essential to understand the spectral variability by clarifying this principle. Therefore, in this chapter, the optical characteristics of rivers and suspended sediment are discussed.

The total radiance recorded at each pixel in the hyperspectral image of the water environment consists of four major sub-radiance: upwelling radiance from the bed (L_b), backscattered radiance from the water body (L_c), upwelling radiance from the interface between the atmosphere and the water body (L_s), and upwelling path radiance from the atmosphere (L_p) (Fig. 2.11) (Baek et al., 2019; Niroumand-Jadidi et al., 2018; Legleiter et al., 2004). Among these components, L_p can be removed by atmospheric correction or minimized by low-altitude flights of UAVs. L_s is influenced by roughness and sun glittering from the water surface; it is usually assumed to be negligible or removed by glint removal algorithms (Legleiter et al., 2017; Overstreet and Legleiter, 2017). L_c is influenced by the inherent optical properties (IOPs) of constituents in the water column, in which IOPs are independent optical properties with the illumination (i.e., backscattering (b_b) and absorption (a) coefficient) (Fan et al., 2015; Olmanson et al., 2013; Pinet et al., 2017; Wong et al., 2019). The water properties and constituents in the water column, including suspended sediment, determine these IOPs, especially b_b and a, as shown in Fig. 2.7. However, radiance is Apparent Optical Properties (AOPs), which are dependent on illumination conditions. Therefore, the relation between radiance and suspended sediment is significantly complex. This relation can be theoretically understood from the radiative transfer theory, which connects radiance and IOPs (Mobley, 1999).

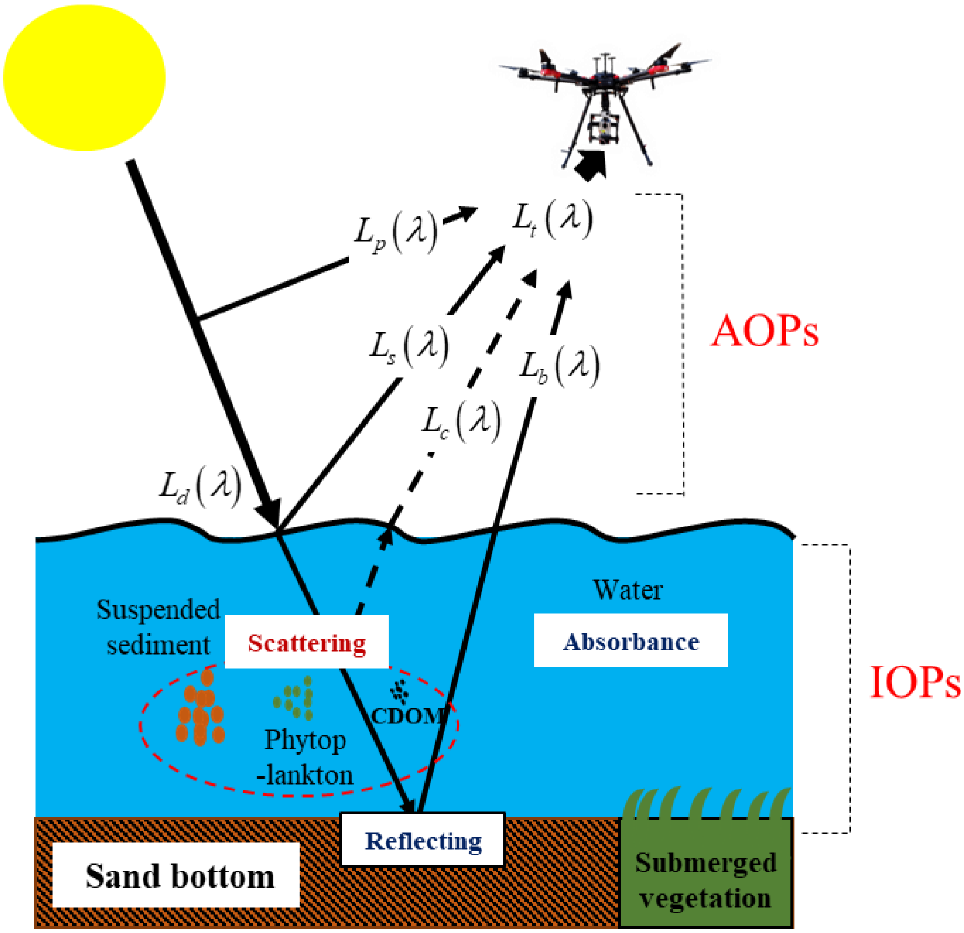

Fig. 2. 7. Solar radiation transfer in water environments (modified from Beak et al., 2019).

Since L_c is highly related to the suspended sediment, SSC can be inversely converted from the L_c using radiative transfer theory with backscattering and absorption coefficients of suspended sediment (Lee et al., 2002). However, L_c cannot be measured separably from L_b in hyperspectral images in shallow waters, which usually interferes with measuring intrinsic L_c value. To overcome such limitation, L_c and L_b signals are interpreted in connection with the analytical or semi-analytical method based on radiative transfer theory (Eqs. 2.1 and 2.2) (Lee et al., 1999; Pinet et al., 2017; Volpe et al., 2011).

$$R_{rs}(\lambda) = \frac{L_u(\lambda)}{E_d(\lambda)} \tag{2.1}$$

$$\frac{L_u(\lambda)}{E_d(\lambda)} = R_\infty(\lambda)(1 - e^{-K(\lambda)H}) + \frac{\rho_b}{\pi} e^{-\kappa(\lambda)H} \tag{2.2}$$

where R_{rs} denotes the remote sensing reflectance, L_u is the total radiance recorded at the sensor, λ denotes wavelength, E_d is irradiance, R_∞ is the reflectance of the infinitely deep water column, h is water column depth, $K(\lambda)$ is attenuation coefficient, ρ_b is bottom albedo, which is distinctive properties according to bottom type. This equation indicates that the water column radiance, the first term on the right hand, is exponentially increasing with the $K(\lambda)$ and *H,* and it has a maximum value when the water depth is infinitely deep ($R_{rs}(\lambda) = R_{\infty}(\lambda)$). The relation between both confounding optical variables, R_{∞} and $K(\lambda)$, and suspended sediment is described in Chapter 2.1.2.2. The second term in the right hand is bottom reflectance, which is also a function of $K(\lambda)$ and *h*. Differently from water column reflectance, the bottom reflectance exponentially decreases as *h* increases with the ρ_b as the maximum value. The effect of bottom reflectance on total reflectance measured at the sensor is elaborated in Chapter 2.1.2.3.

Although this physics-based approach has the advantage of being robust even when using a small number of data, it requires prior information about the IOPs of water constituents and bottom albedo (Niroumand-Jadidi et al., 2019a). Moreover, the IOPs and bottom albedo are challenging to measure since they vary considerably according to the variety of suspended sediment and bottom characteristics in the water environments (Pinet et al., 2017).

In this study, three confounding factors that influence the spectral variability of suspended sediment in rivers were investigated in detail. The first factor is the heterogeneity of sediment properties (i.e., particle size distribution, mineral characteristics, and particle density). This factor varies L_c in Eq. 2.2 since the sediment properties change the backscattering coefficient (b_b) and absorbance coefficient (a) of the water column. Therefore, the optimal wavelength of suspended sediment is hard to be selected if various suspended sediment exists in the water column (Volpe et al., 2011). The second factor is a variety of bottom properties, which determine the L_b in Eq. 2.1. Especially in shallow waters, suspended sediment retrievals are challenging since the bottom signal critically disturbs the intrinsic signal of suspended sediment. Therefore, almost all previous studies did not account for the effect of bottom properties on suspended sediment retrievals since they mainly used low-resolution satellite images. Lastly, the third factor is the dynamic vertical profile of suspended sediment. Because of the non-uniform profile of suspended sediment in the vertical direction in the water bodies, the amount of light that passes through the water column is inconsistent with the same depth-averaged SSC. These three factors are detailed in the following Chapters 2.1.2.2~2.1.2.4, respectively.

2.1.2.2 Heterogeneity of sediment properties

Solar radiation, scattered by suspended sediment in the water column, depends on sediment properties (volume and particle size) and refractive index relative to water, which depends on the mineral characteristics of sediment (Liu et al., 2020; Pinet et al., 2017). Since particle size of suspended sediment is relatively larger than the wavelength of the visible range (500-700 nm) to Near-

Infra Red (NIR) (700-1000 nm), the Mie scattering theory has been used in many previous studies to calculate the IOPs and AOPs of turbid waters (Doxaran et al., 2009; Woźniak and Stramski, 2004). Based on the hypothesis of homogeneous spherical particles in Mie scattering theory, the Mie scattering-based model was proposed to calculate both backscattering coefficient ($b_{b_{SS}}$) and absorbance coefficient (a_{SS}) of suspended sediment (de Rooij and van der Stap, 1984). This model can compute the IOPs of suspended sediment populations considering PSD. In specific, the PSD in this model assumed power-law PSD to calculate both b_{bSSC} and a_{NAP}, as follows:

$$b_{b_{SS}} = \frac{3\overline{Q_{bb}}}{2\rho_{ss}} \int_{D_{\min}}^{D_{\max}} N(D) D^2 dD \left(\int_{D_{\min}}^{D_{\max}} N(D) D^3 dD \right)^{-1} \tag{2.3}$$

$$a_{SS} = \frac{3\overline{Q_a}}{2\rho_{ss}} \int_{d_{\min}}^{d_{\max}} N(d) d^2 dd \left(\int_{d_{\min}}^{d_{\max}} N(d) D^3 dd \right)^{-1} \tag{2.4}$$

$$N(d) = SSC_V \times d^{-J} \tag{2.5}$$

where $\overline{Q_{bb}}$ and $\overline{Q_a}$ are efficiency factors for backscattering and absorbance, respectively, N is the PSD representing the number of particles having size d, SSC_v is the volume concentration of suspended sediment, J is Junge's exponent, and ρ_{ss} is particle density. The efficiency factors ($\overline{Q_{bb}}$ and $\overline{Q_a}$) offer the amount of incident light backscattered and absorbed, which are intrinsic values according to the mineralogy of suspended sediment. The effect of particle size and density is also accounted for by integrated PSD and particle density in Eq. 2.4 and 2.5.

Therefore, five variables are needed to calculate the $b_{b_{SS}}$ and a_{SS}, and all of these variables can be determined by the sediment properties, as described in Table 2.2. Moreover, the reflectance of infinitely deep water column (R_∞) and downward diffuse attenuation coefficient (K_d) are calculated from $b_{b_{SS}}$ and a_{SS} using the following equations (Lee et al., 1999; Mobley, 1999; Pinet et al., 2017):

$$R_\infty(\lambda) = 0.33\frac{b_b(\lambda)}{a(\lambda)+b_b(\lambda)} \tag{2.6}$$

$$K_d = \sqrt{a_{TOT}^2 + (G' \times a_{TOT} \times b_{TOT})} \tag{2.7}$$

where a_{TOT} and b_{TOT} represent total absorbance and scattering coefficient including suspended sediment and other particles, as illustrated in Fig. 2.7; G' is a coefficient defined as the relative contribution of the scattering to the vertical attenuation of the irradiance, and its range is from 0.233 to 0.264 (Kirk, 1994).

From this relationship between AOPs and IOPs, it can be seen that backscattered reflectance in the simplified radiative transfer equation (Eq. 2.2), $R_{\infty}(\lambda)(1-e^{-K(\lambda)H})$, is apparently related to sediment properties. Moreover, the spectral variability caused by suspended sediment properties is inevitable in rivers, and thus the contribution of the effect of heterogeneity of sediment properties must be necessarily investigated in respect to hyperspectral image-based passive remote sensing.

Table 2. 2. Variables to estimate the optical properties and the related properties of the sediment.

Symbol	Description	Related properties
$\overline{Q_a}$	Absorption efficiency factor	Mineralogy
$\overline{Q_{bb}}$	Backscattering efficiency factor	Mineralogy
ρ_{ss}	Particle density	Sediment density
d	Particle size	Sediment particle size
$N(d)$	Particle size distribution	Sediment particle size distribution

2.1.2.3 Effects of bottom reflectance

Since most studies of SSC estimation using remote sensing data were conducted by satellite images, remote sensing techniques for SSC were developed primarily for large and deep water environments, such as coastal waters (Jiang et al., 2021; Koestner et al., 2020; Spyrakos et al., 2018; Zhang et al., 2020), eustray (Doxaran et al., 2003; Islam et al., 2001; Shen et al., 2010), and large rivers (Kilham et al., 2012; Peterson et al., 2018; Umar et al., 2018). Therefore, despite the successful application of remote sensing models for SSC measurement in these areas, the contribution of bottom reflectance was not considered actively owing to its nonsignificant contribution in deep water environments.

Recently, the use of a UAV-mounted hyperspectral camera for monitoring water quality parameters has been explored. This system provides spatio-temporally high-resolution hyperspectral images for shallow water analysis with radiance values in a wide range of wavelengths, even though this system has been used extensively in bathymetry retrievals of shallow waters with the advantage of satisfactory resolution (Kim et al., 2019; Legleiter and Harrison, 2019). Contrary to bathymetry retrievals, applying this system to suspended sediment retrievals in shallow waters is challenging because the bottom signal critically disturbs the intrinsic signal of suspended sediment. Therefore, the precisely optimal wavelength of suspended sediment is disturbed by the bottom types (Volpe et al., 2011).

In the simplified radiative equation (Eq. 2.2), the bottom reflectance is expressed as $\frac{\rho_b}{\pi} e^{-K(\lambda)h}$. This term reveals that the bottom reflectance exponentially decreases according to water depth *H*, while the backscattered reflectance increases exponentially with increasing water depth, as described in Section 2.1.2.1. Fig. 2.14 shows the effect of water depth on total, water column, and bottom reflectance in 550 nm calculated by Eq. 2.2. For calculation with a reasonable range of each parameter, it was assumed that $K(550nm) = 1m^{-1}$ and $R_{\infty}(550nm) = 0.5$, which is adapted by the values included in the range suggested by Albert and Mobley (2003). For the bottom albedo in this equation, the value corresponding to the sediment and vegetation in 550 nm was used to compare the effect of the bottom type difference. This figure reveals that bottom and water column reflectance are changing dramatically with water depth where the water depth is smaller than 2 m. Furthermore, the bottom reflectance shows different values in this sensitive range according to bottom types. In this respect, the varying water depth and variety of bottom properties increase the spectral variability, especially in shallow waters such as small to medium rivers (Niroumand-Jadidi et al., 2019b).

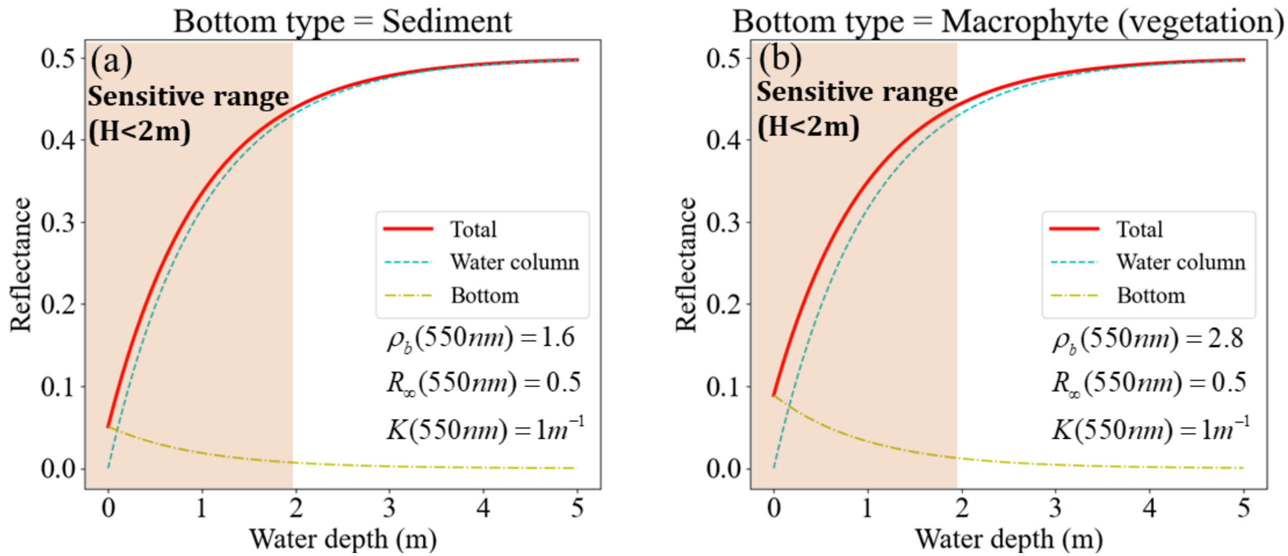

Fig. 2. 8. Reflectance calculated from simplified radiative transfer equation, Eq. (2.2), according to water depth; (a) sediment bottom and (b) Macrophyte (vegetation) bottom.

2.1.2.4 Vertical distribution of suspended sediment

The vertical distribution of suspended sediment concentration in rivers is non-uniform due to the interaction between turbulent diffusion and sediment settling in the water column. As shown in Fig. 2.15, the vertical advection-diffusion equation under steady flow is expressed as follows:

$$w_s \frac{\partial C}{\partial z} + \frac{\partial}{\partial z}\left(\varepsilon_z \frac{\partial C}{\partial z} \right) = 0 \tag{2.8}$$

where C is concentration, w_s is settling velocity of suspended sediment, ε_z is the vertical turbulent diffusion coefficient, z denotes vertical direction. In this equation, the first term is the settling mass flux, and the second term is the rate of upward concentration diffusion caused by turbulent mixing.

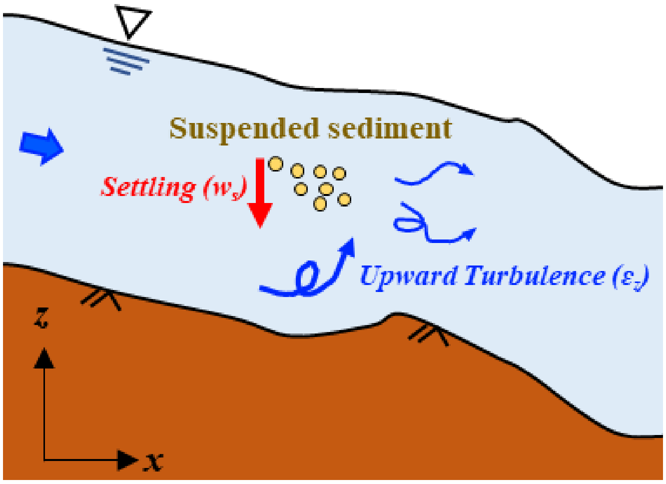

Fig. 2. 9. Mechanics of vertical transport of suspended sediment in rivers.

where β is the ratio of ε_z and ν, κ is the Von Kármán constant, u_* is shear velocity, and *h* is local water depth. From this expression and Eq. 2.7, Rouse (1937) derived an equation for the vertical profile of suspended sediment concentration at a distance *z* from the bed as follows:

$$\frac{C(z)}{C(z_x)} = \left(\frac{z_x}{z} \times \frac{h-z}{h-z_x} \right)^P \tag{2.10}$$

where z_x is the reference distance, $P = w_s / \beta \kappa u_*$ is referred to as the Rouse number, which indicates the ratio of the lift force from turbulent diffusion and downward gravity force.

In the Rouse equation, the vertical SSC distribution is determined by *P* as a shape factor. Fig 2.10 shows the variation of vertical SSC distribution according to *P*. As shown in this figure, the variation of SSC with the water depth is more profound for the higher value of *P* (Rouse, 1937). For the high value of *P* (large particles), SSC is higher near the river bottom and is monotonically decreasing as *z* increases approaching the water surface, whereas SSC distribution is almost uniform for the low value of *P* (small particles). While the variables related to turbulent diffusion in *P* are dominantly determined by flow and channel conditions, the w_s strongly depends on the particle size of suspended sediment. Therefore, the P is heterogeneously distributed in the river since the various PSDs in rivers induce separation between particles with significantly different settling velocities. In terms of solar radiation transfer in the river, this variability of the SSC vertical profile causes spectral variability. Even with the same depth-averaged SSC, the different profile of SSC influences how much light can pass through the water column.

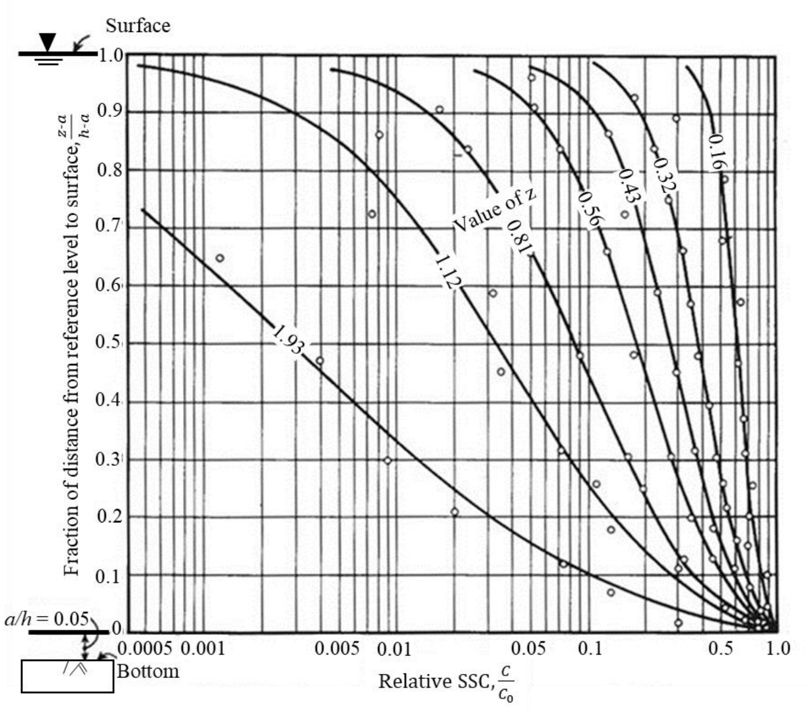

Fig. 2. 10. Variation of SSC along with the flow depth (revised from Rouse (1937)).

2.1.3 Retrieval of suspended sediment from remote sensing data

2.1.3.1 Remote sensing-based regression approach

Remote sensing of suspended sediment depends on the absorption of incoming solar energy by the water column. Suspended sediment in water reflects this energy more strongly than pure water, particularly in the VIS and NIR wavelengths (Bhargava and Mariam, 1991; Z. M. Chen et al., 1991; Dethier et al., 2020; Novo et al., 1989) (Fig. 2. 11). Based on this premise, many studies tried to clarify empirical relationships between reflectance and SSC using spectral bands in the VIS and NIR wavelengths. Developing this relationship requires a dataset including in situ SSC measurements and corresponding reflectance data of river pixels. However, finding relevant spectral bands among the wavelength range of hyperspectral imagery is crucial to developing pertinent regression models in the study area. The most widely used band selection method in remote sensing of the water environment is optimal band ratio analysis (OBRA), which determines the relevant bands by searching the band ratio with the highest correlation coefficient with SSC (Legleiter, 2021; Legleiter et al., 2019, 2004; Montanher et al., 2014). Most earlier researchers developed simple regression models, such as linear, exponential, polynomial, and log-linear models, using optimal band ratio or most correlated single band with SSC as an independent variable (Table 2.3).

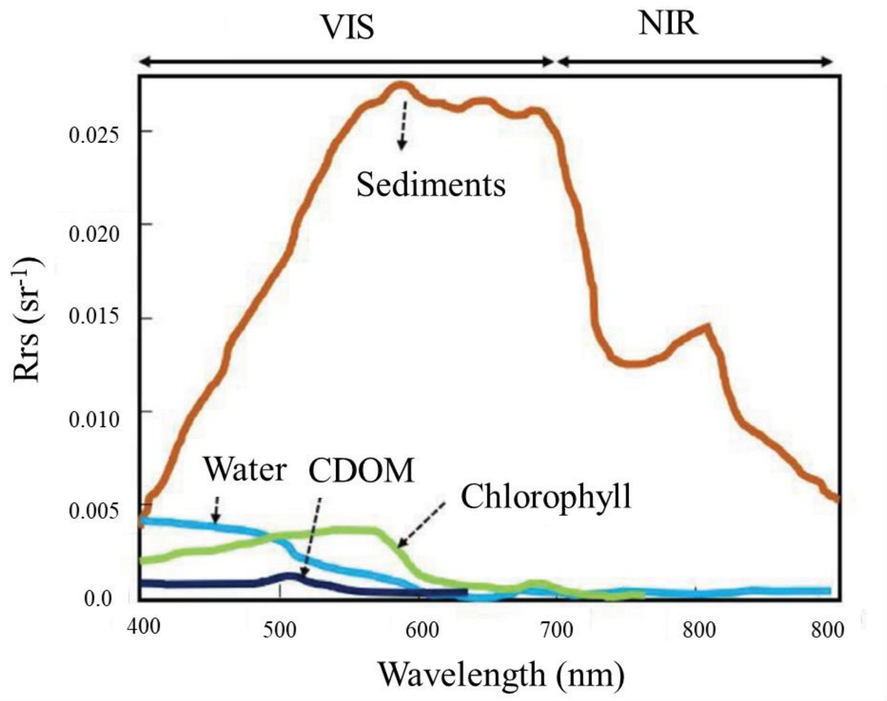

Fig. 2. 11. Remote sensing reflectance (Rrs) by clear water (blue) and water with chlorophyll (green), CDOM (navy), and sediment (brown) (revised from Hafeez et al. (2019)).

Table 2. 3. Regression models for remote sensing-based SSC measurement

Author	Sensor	Model	Band selection	*X*	Wavelength	Site	Remarks
Islam et al. (2001)	Satellite MODIS	$SSC = 69.39X - 201$	Correlation	$R(\lambda 1)$	λ 1: 449–479 nm	Lake	Explicit model using single spectral band
Doxaran et al. (2003)	Satellite SPOT	$SSC = 27.423\exp(0.0279X)$	OBRA	$\log\left(\frac{R(\lambda 1)}{R(\lambda 2)}\right)$	λ1: 500–590 nm λ2: 790–790 nm	Estray	Explicit model using band ratio
Doxaran et al. (2003)	Satellite Landsat	$SSC = 29.022\exp\left(0.0335X\right)$	OBRA	$\log\left(\frac{R(\lambda 1)}{R(\lambda 2)}\right)$	λ1: 555 nm λ2: 865 nm	Estray	Explicit model using band ratio
Doxaran et al. (2003)	Satellite SPOT	$SSC = 18.895\exp\left(0.0322X\right)$	Correlation	$R(\lambda 1)$	λ1: 841-876 nm	Estray	Explicit model using single spectral band
Doxaran et al. (2003)	Satellite Landsat	$SSC = 26.083\exp\left(0.0326X\right)$	OBRA	$\log\left(\frac{R(\lambda 1)}{R(\lambda 2)}\right)$	λ1: 555 nm λ2: 865 nm	Estray	Explicit model using band ratio
Islam et al. (2003)	Satellite Landsat TM	$SSC = 16.826 - 5.2369X$	OBRA	$\log\left(\frac{R(\lambda 1)}{R(\lambda 2)}\right)$	λ1: 450–520 nm λ2: 520–600 nm	Estray	Explicit model using band ratio
Chu et al. (2009)	Satellite MODIS	$SSC = 10^{\left(\frac{X-1.6}{7.5}\right)}$	Correlation	$R(\lambda 1)$	λ1: 620–670 nm	Lake	Explicit model using single spectral band
Wang et al. (2009)	Satellite MODIS	$SSC = \exp(43.23X + 1.37)$	Correlation	$R(\lambda 1)$	λ1: 841–876 nm	Estray	Explicit model using single spectral band
Fang et al. (2010)	Satellite EO-1 AL1	$SSC = -1229.5X + 53.795$	Correlation	$R(\lambda 1)$	λ1: 549 nm	Estray	Explicit model using single spectral band
Wang and Lu (2010)	Satellite MODIS	$SSC = \exp\left(4.177 + 0.262X\right)$	OBRA	$\log\left(\frac{R(\lambda 1)}{R(\lambda 2)}\right)$	λ1: 841–876 nm λ2: 1230–1250 nm	Lake	Explicit model using band ratio

Table 2. 3. Regression models for remote sensing-based SSC measurement (continued).

Author	Sensor	Model	Band selection	*X*	Wavelength	Site	Remarks
Wang et al. (2010)	Satellite MODIS	$SSC = -23.03 + 60.24X$	OBRA	$\log\left(\frac{R(\lambda 1)}{R(\lambda 2)}\right)$	λ1: 841–876 nm λ2: 1230–1250 nm	Lake	Explicit model using band ratio
Wang et al. (2010)	Satellite Landsat	$SSC = \exp(4.177 + 0.262X)$	Correlation	$R(\lambda 1)$	λ 1: 800-1100 nm	Lake	Explicit model using single spectral band
Espinoza Villar (2013)	Satellite MODIS	$SSC = 1020X^{2.94}$	Model validation result	$\log\left(\frac{R(\lambda 1)}{R(\lambda 2)}\right)$	λ1: 620–670 nm λ2: 841–876 nm	River	Explicit model using band ratio
Montanher et al. (2014)	Satellite Landsat TM	$SSC = aX + b$	Correlation	$R(\lambda 1)$	λ 1: 1550-1750 nm	River	Multiple explicit equations according to water types
Liu et al. (2017)	Satellite Sentinel-2	$SSC = 2950X^{1.357}$	Model validation result	$R(\lambda 1)$	λ 1: 773-793 nm	Lake	Explicit model using single spectral band
Wang et al. (2017)	Satellite Landsat TM	$SSC = 245287X^2 - 585.92X + 27.599$	Reference	$R(\lambda 1)$	λ 1: 760-900 nm	Estray	Explicit model using single spectral band
Umar et al. (2018)	Satellite Landsat TM	Random Forest (RF)	Model validation result	$R(\lambda 1)\cdots R(\lambda 7)$	λ 1 ~ λ 7: 450–2350 nm	River	Implicit model (machine learning regression)
Wei et al. (2019)	UAV-mounted HSI camera	Support Vector Regression (SVR)	-	$R(\lambda 1)\cdots R(\lambda 150)$	λ 1 ~ 150: 400–1000 nm	Lake, River	Implicit model (machine learning regression)
Kabir et al. (2020)	UAV-mounted RGB camera	$\ln(SSC) = aX + b$	-	$R(\lambda 1)$	λ 1: 600 nm	River	Multiple explicit equations according to sediment colors

Among these studies, Liu et al. (2017) developed exponential and power-law equations for SSC retrievals using reflectance of a single band from a multispectral satellite image in a lake. This study suggested the optimal equation and spectral band by comparing two equation types and each of the nine spectral bands in the multispectral image as an independent variable. Wang et al. (2017) proposed a quadratic model using the ratio of logarithmic transformed red band and NIR band using satellite images in estuaries and coasts. Also, Espinoza Villar (2013) used the ratio of red band and NIR as an independent variable of a power-law equation to map the SSC distribution in large rivers. Montanher et al. (2014) compared the reflectance of a single band and the ratio of reflectance of the spectral bands as an independent input variable for the linear regression model to estimate the SSC in rivers. While these simple regression models have the advantage that they can develop explicit equations, they have the disadvantage that only a narrow wavelength range can be utilized.

In recent years, Machine Learning Regression (MLR) has been applied to overcome the limitation of the explicit models. Various MLR models (a decision tree model-based model, a mathematical function-based nonlinear model, and a neuron-based deep learning model) have been used to solve complex problems in water environments (Ardabili et al., 2020; Kwon et al., 2021a; Pyo et al., 2020c; Stanev et al., 2018; Yao et al., 2008; Yaseen et al., 2019). These models made it possible to solve the nonlinear relation between independent and dependent variables that could not be solved by conventional regression methods. Although MLR is an implicit model which cannot clarify the algebraic relationship between reflectance and SSC, this approach has apparent advantages: (1) modeling of a non-linear relationship between reflectance and SSC; (2) suitability for high dimensional data processing; (3) featurization of spectral bands in the wide range of wavelength.

Umar et al. (2018) developed Random Forest (RF) regressor using multispectral satellite images in the confluence of large rivers. This model successfully retrieved the spatial distribution of SSC and captured the dynamic mixing process of suspended sediment in this complex area. Wei et al. (2019) first applied the UAV-borne hyperspectral image to estimate SSC in the lake and shallow river. Since the hyperspectral image used in their study contains 150 spectral bands in 400 – 1,000 nm, it has dealt with much higher-dimensional data than existing satellite-based studies. These high-dimensional data were featured through the Support Vector Regression (SVR) model, and their model showed accurate performance in both lake and river. However, the effect of bottom reflectance reduced the accuracy of their model in shallow waters.

Despite the successful estimation of SSC in previous studies, the wavelength range of selected spectral bands was distributed widely according to the study area. Kwon et al. (2021a) validated several models from previous studies in the Nakdong River, and they revealed that exixting empirical equations have a limitation on the transferability to the uncalibrated areas, which have heterogeneous spectral characteristics of water environments. Despite the successful attempts of the remote sensing approach, few studies have addressed the cause of locality; therefore, the globally applicable remote sensing technique for suspended sediment is insufficient.

2.1.3.2 Clustering of remote sensing data

As described in Section 2.1.2, spectral variability in the water column induces the heterogeneous relationship between SSC and the spectrum of reflectance. In this study, to improve the SSC estimator and understanding of spectral variability, the clustering approach was applied by grouping the SSC-reflectance dataset with optically homogeneous clusters. Cluster analysis using hyperspectral images can classify spectral clusters based on abundant spectral information. Moreover, this approach can analyze their physical properties through the relationship between the spectral characteristics and the physical variables, as depicted in Fig. 2.12. The clustering method is included in the unsupervised machine learning model. It can group the datasets based on the similarity standard and be categorized into several algorithms according to the similarity standard (Ni et al., 2020; Patel and Kushwaha, 2020; Zhou et al., 2018). The most widely used clustering algorithms are K-means clustering and hierarchical clustering. K-means clustering needs to determine a specified number of clusters before clustering, and then it can find the mutually exclusive cluster of spherical shape based on Euclidian distance (Q. Wang et al., 2017). Hierarchical clustering is a method of clustering based on Euclidian distance. This method searches a hierarchy of clusters without a pre-specified number of clusters. However, it is high time-consuming and has difficulty with space complexity (Wu et al., 2021). Unlike the above two methods, Gaussian Mixture Model (GMM) is based on probability density rather than the Euclidian distance of each data. The GMM describes each cluster as a separate Gaussian distribution, so the probability of belonging to each cluster can be estimated. This algorithm can cluster the overlapping data, which is not statistically apparent (Herms et al., 2021; Ni et al., 2020; Zhou et al., 2018). Due to such characteristics, GMM is robust to outliers and can find random shape clusters. The advantage and disadvantages of these clustering algorithms are summarized in Table 2.4, and the process of hyperspectral clustering is elaborated in Chapter 3.

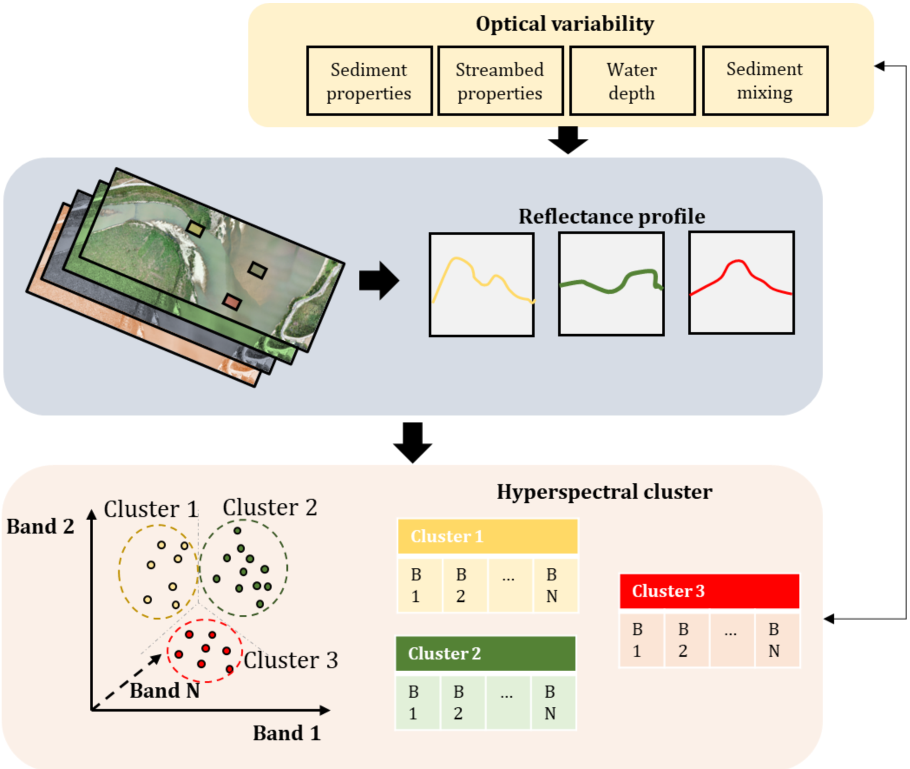

Fig. 2. 12. Flowchart of hyperspectral clustering.

Table 2. 4. Comparison of clustering methods.

	Advantage	Disadvantage
K-means	Based on Euclidian distance, an efficient and less complex method	Non-robust to the outlier, challenging to find the non-convex shape
Hierarchical clustering	Based on Euclidian distance, good visualization, no need to specify the number of clusters in advance	Non-robust to the outlier, time-consuming
GMM	Robustness to outlier (can find random shape cluster), probabilistic framework, the best result for overlapped datasets	Need large datasets, hard to estimate the number of clusters

2.2 Mapping of suspended sediment concentration in rivers

2.2.1 Traditional method for spatial measurement

The spatial distribution of SSC in rivers has not been thoroughly measured owing to the limitation of the measurement method. Among the conventional measuring techniques, the manual collection of samples using a water sampler was widely used to measure suspended sediment (Edwards and Glysson, 1999; Latosinski et al., 2014; Yang and Julien, 2019). To apply this method in large rivers, the spatial distribution measurement has relied on the possibility of deploying reel-mounted water samplers on a bridge, cableway, and boat due to their non-wadeable condition (Umar et al., 2018). Even though this sampling method is the most accurate measurement method, it is labor-intensive and time-consuming and requires measuring the dry weight of the sediment in the laboratory. Therefore, in recent years, the ADCP-based cross-sectional measurement has been used as an alternative method to collect datasets of spatial distribution, despite relatively high uncertainty. This method is more suitable for obtaining spatial distribution than the sampling method because it is possible to obtain high-resolution data by making the boat path dense and converting the data into a continuous spatial distribution using an interpolation technique (Kwak et al., 2020; Son et al., 2021). However, the movement of the boat usually disturbed the suspended sediment distribution, and the interpolated data is not sufficiently reliable.

All such methods enable the collection of accurate SSC data within individual points and cross-sections at a specific time. Nevertheless, such methods are still insufficient to analyze the complex mixing processes of suspended sediment in the complex river system, which requires high-resolution data. In terms of mixing analysis, the suspended sediment which moves with the flow in rivers can be used as the most natural and efficient alternative tracers to observe river mixing without the need for artificial tracer injection. Therefore, the remote sensing-based SSC measurement technique can be an ideal platform to analyze the mixing dynamics with a large spatio-temporal scale, even though it focuses on measuring the surface concentration. The hyperspectral imagery-based SSC measurement in this study is suitable for measuring high-resolution SSC distribution; thus, it is expected to give substantial insight into exploring complex mixing processes in river systems.

2.2.2 Spatial measurement at river confluences

2.2.2.1 Dynamics of flow and mixing at river confluences

River confluences are the most representative area where the complex spatial distribution of suspended sediment occurs because considerable changes are generated by the convergence of flows from the tributary into the main river (Fig. 2.13). These tributary flows commonly have different discharges, momentums, velocities, and bottom elevations from those of the main river; thus, the turbulent mixing, exchange of momentum, and mixing of suspended matters (e.g., suspended sediment, pollutant, algal bloom) occur with various patterns at the near-field of confluence, named the confluence hydrodynamic zone (CHZ) as depicted in Fig. 2.14 (Constantinescu et al., 2012; Konsoer and Rhoads, 2014; Rhoads and Johnson, 2018; Rhoads and Kenworthy, 1995; Sukhodolov et al., 2017; Yuan et al., 2021, 2019; Zinger et al., 2013). In this figure, the mixing process can be divided into three stages: near-field mixing, intermediate-field mixing, and far-field mixing. Among these regions, mixing processes in the near field or CHZ are the most complex and dynamic, and shear interface and helical motions in CHZ significantly affect the mixing mechanisms of suspended sediment downstream of the CHZ, especially the intermediate field (Fig. 2.14).

The velocity field in river confluences is highly complex when the two flows from the main river and tributary are merged. In order to understand the effects of the hydrodynamics of flow on the mixing process in river confluences, the hydrodynamic features in confluences are important since it has disparate features compared to general rivers. In analyzing the dynamics of flow in the river confluence, Best et al. (1987) proposed six hydrodynamic features: stagnation zone, flow deflection zone, flow separation zone, maximum velocity, flow recovery, and shear layers. These features of confluences vary according to physical variables of confluences: *W/H*, confluence angle (α), momentum ratio (*MR*), discharge ratio (*QR*), velocity ratio (*VR*), and bed discordance (Horna-Munoz et al., 2020; Lewis et al., 2020; Rhoads and Kenworthy, 1995). Despite several field studies on many confluences, the relationship between these variables and hydrodynamic features of confluence has not been thoroughly clarified because its variability (Pouchoulin et al., 2020).

Within the near-field (CHZ) of confluences, the helical motion, including secondary currents, is abruptly produced by confluent flows and channel curvature, as illustrated in Figs. 2.13–2.14 (Lewis et al., 2020; Rhoads and Johnson, 2018). This abnormal flow induces various patterns of the shear layer, which controls the mixing in the near field by producing strong large-scale and turbulent eddy at the interface of confluent flows (Cheng and Constantinescu, 2020; Penney et al., 2020). The mixing layer is generated when confluent flows with different SSC are entrained into this shear layer. The types of the shear layer in near-field can be classified into wake mode and Kelvin-Helmholtz (KH) mode according to *VR* and *MR*, as shown in Fig. 2.15 (Cheng and Constantinescu, 2021; Constantinescu et al., 2012; Gualtieri et al., 2019; White and Helfrich, 2013). In this figure, U_1 and U_2 are the streamwise velocity of tributary and main rivers, respectively. The wake mode is developed when the confluent flow has a similar velocity or momentum to those of the main river ($VR \approx 1$ or $MR \approx 1$). In this mode, the turbulent wake is developed behind the stagnation zone shown in Fig. 2.14. This wake induces negative velocities associated with vortex shedding of two counter-rotating horizontal eddies within the shear layer. Two shear layers are developed due to velocity deficit from the convergence of two boundary layers of the confluent flows. Then, the shear layer dissipates downstream, where the velocity deficit disappears. Contrarily, KH mode is developed with co-rotating horizontal eddy if the momentum or velocity of confluent flows has considerably different values from those of the main river. With vortex pairing, the shear layer of KH mode usually has a larger length scale of width than the wake mode (Cheng and Constantinescu, 2021; Constantinescu et al., 2014, 2012; Gualtieri et al., 2019).

Although the growth of the shear layer enhances the lateral mixing in the near field, the shear layer is rapidly dissipated owing to the effect of form roughness by large river bed forms such as dunes and riffles, especially at the large and shallow confluences (W/H>100) (Constantinescu et al., 2014; Gualtieri et al., 2019; Uijttewaal and Booij, 2000). In large and shallow confluences, the eddy is hard to grow in a vertical direction since the length scale is limited to water depth, as shown in Fig. 2.14 (c). On the contrary, the horizontal eddy is less affected by the boundary, so the transverse mixing is more dynamic even in the near field at the confluences. The strong eddy caused by the advective lateral momentum is much larger than the turbulent eddy in the transverse direction, which was proven by the numerical model and experiment results (Cheng and Constantinescu, 2020; Constantinescu et al., 2012; Lewis et al., 2020; Lewis and Rhoads, 2015; Rhoads and Sukhodolov, 2008). It means that the dispersion from secondary current is pronounced at the near field of confluences. However, confluence mechanisms are so complex that each has very different characteristics. Confluence angle, density differences, and bed discordance affect confluence mechanisms. Due to difficulty obtaining high-resolution flow and SSC observations, there is still a considerable lack of information on the mixing process and hydrodynamic mechanism in confluences.

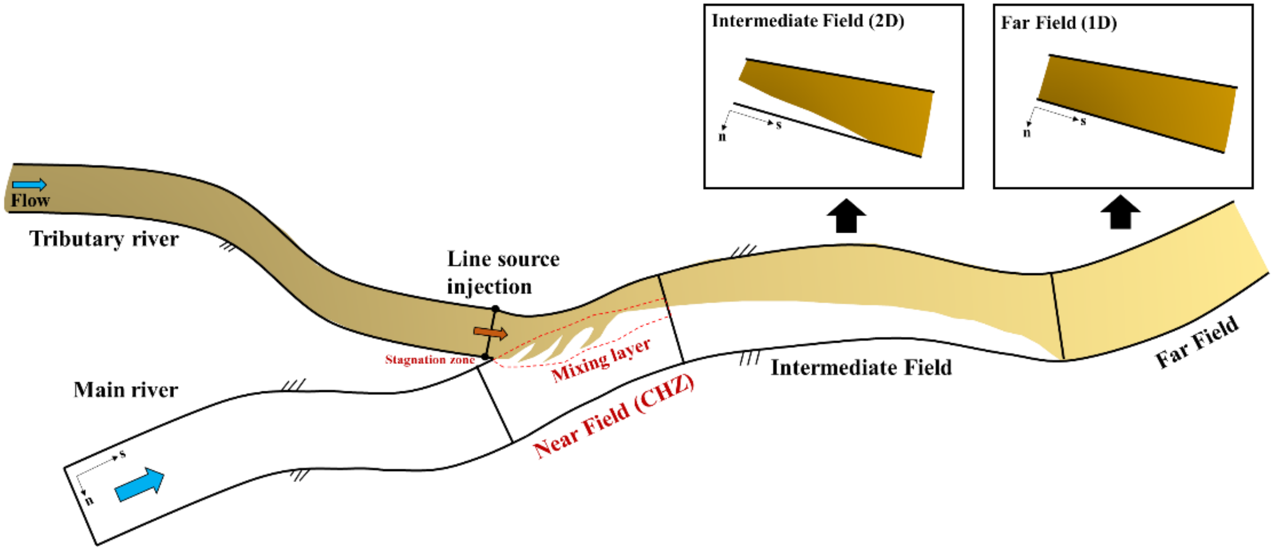

Fig. 2 13. Spatial distribution of SSC at large river confluences (revised from Jung et al. (2019)).

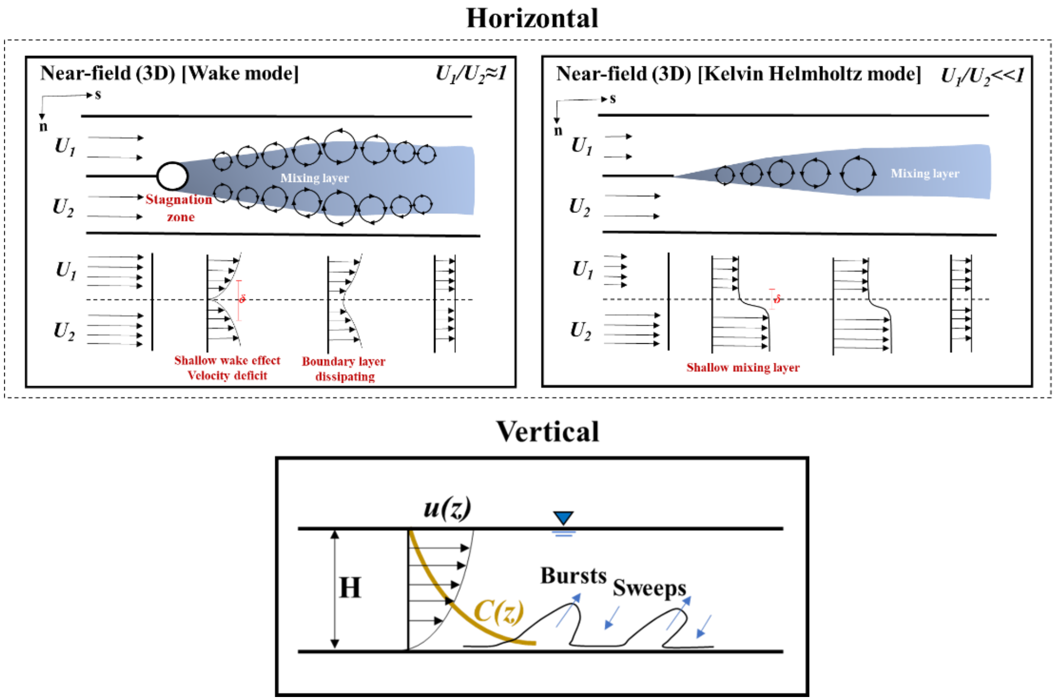

Fig. 2. 14. Eddy dynamics at large river confluences (revised from Jirika and Uijttewaal (2004)): (a) wake mode; (b) Kelvin-Helmholz mode; (c) vertical eddy generation.

2.2.2.2 Field experiments in river confluences

The dynamics of flow and suspended sediment in river confluences have been studied experimentally in various ways, as described in Table 2.5. This table shows that most studies were undertaken in small-to-medium rivers, where the width to depth ratio (W/H) is less than 50, and spatial measurement of flow and suspended sediment has not been conducted owing to the limitations of measurement techniques. In these rivers, spatial measurement of the CHZ region is mainly conducted using three-dimensional numerical models or large-scale particle image velocimetry (LSPIV) measurements due to the expensive computational load (Constantinescu et al., 2012; Lewis and Rhoads, 2018; Sabrina et al., 2021). However, in more recent years, using the ADCP, many studies have measured hydrodynamic features in CHZ of large rivers in detail (Gualtieri et al., 2018; Yuan et al., 2021). The results of these studies demonstrated that hydrodynamics and sediment mixing in large rivers with a W/H larger than 100 are more affected by form roughness than in small rivers. Therefore, secondary currents quickly dissipated, showing completely different phenomena with small-to-medium river confluences.

Table 2.5 shows that SSC measurements were conducted using ADCP or remote sensing by satellite. Gualtieri et al. (2018) measured SSC at several points in the Negro and Solimo˜es Rivers in Brazil. However, the number of SSC data is insufficient to analyze the spatially mixing of suspended sediment with flow characteristics. Using the backscatter intensity signal of ADCP as a surrogate for suspended sediment concentration, several studies conducted cross-sectional measurements by mounting ADCP on a moving boat at large confluences (Son et al., 2021; Szupiany et al., 2009; Yuan et al., 2021). Although this method can efficiently measure many SSC data with water depth and velocity profiles, it also has a relatively low resolution to quantify the mixing patterns and rates accurately. Umar et al. (2018) measured detailed information on spatial distributions of SSC using satellite remote sensing in the Mississippi and Missouri Rivers in the USA. However, the spatial resolution of multispectral satellite imagery is not enough to capture detailed mixing patterns of suspended sediment, as described in Chapter 2.1.2. Thus, the mixing of suspended sediment at river confluences has not been widely studied owing to the lack of a high-resolution SSC dataset.

Table 2. 5. Summary of field experiments of previous studies in river confluences.

Reference	Site	***W*** **(m)**	***W/H***	**QR**	**SSC measurement**	**Spatial measurement**
Rhoads and Kenworthy (1995, 1998)	Kaskaskia River and Copper Slough, Illinois, USA	**8–12**	**44.74, 24.28**	0.47	-	-
Sukhodolov and Rhoads (2001)	Kaskaskia River and Copper Slough, Illinois, USA + Saline and Salt Fork	**8–15**	**16-30**	0.25-1.18	-	
Rhoads and Sukhodolov (2004)	Kaskaskia River and Copper Slough, Illinois, USA	**8–12**	**44.74, 24.28**	0.47	-	-
Boyer et al. (2006)	Bayonne and Berthier Rivers, Quebec, Canada	**8–10**	**8–10**	-	-	-
Parsons et al. (2007)	Confluence-diffluence in Río Paraná, Argentina	**600-1,000**	**38.99, 84.91**	0.2,0.5	-	-
Rhoads and Sukhodolov (2008)	Kaskaskia River and Copper Slough, Illinois, USA	**8–12**	**44.74, 24.28**	0.47	-	-
Szupiany et al. (2009)	Confluence-diffluence in Río Paraná, Argentina	**600-1,000**	**38.99, 84.91**	0.2,0.5	ADCP	-
Constantinescu et al. (2012)	Kaskaskia River and Copper Slough, Illinois, USA	**8–12**	**44.74, 24.28**	0.47, 0.95		3D modeling
Ramón et al. (2013)	Ebro and Segre Rivers, Spain	**400**	**57**	0.13-0.40	-	-
Konsoer and Rhoads (2014)	Wabash and Ohio River, Wabash and Vermilion River, Indiana, USA	**500-675**	**68.7**	0.12-1.02	-	Cross-sectional analysis
Baranya et al. (2015)	Mosoni-Duna and River Rába, Hungary Ebro and Segre Rivers, Spain	**40-60**	-	0.12-1.02	-	3D Modeling
Riley et al. (2015)	Wabash and Ohio River, Wabash and Vermilion River, Indiana, USA	**500-675**	**68.7**	0.12-1.02	-	-

Table 2. 5. Summary of field experiments of previous studies in river confluences (continued).

Reference	Site	W (m)	W/H	QR	SSC measurement	Spatial measurement
Lewis and Rhoads (2015, 2018)	Kaskaskia River and Copper Slough, Illinois, USA + Saline and Salt Fork	**8–15**	**16-30**	0.25-1.18	-	LSPIV
Sukhodolov et al. (2017)	Ledra River and Torrente Sorgive die Bars, Italy	**10–17**	**13.75**	0.57	-	-
Pouchoulin et al. (2020)	Rhône and Saône Rivers, France	**270-275**	**29.69**	0.56-0.90		
Umar et al. (2018)	Mississippi and Missouri rivers, USA	**1,000**	**-**	0.4, 1.1	Satellite	Satellite
Gualtieri et al. (2018)	Negro and Solimo˜es Rivers	**2,347-3,134**	**56-115**	0.6	Sampling	-
Gualtieri et al. (2019)	Negro and Solimo˜es Rivers	**2,830**	**115.98, 58.42**	0.39, 0.32	-	Moving boat
Son et al. (2021)	Nakong and Hwang Rivers, South Korea	**305.7-317.8**	**44.75-47.9**	0.08-0.14	ADCP	Moving boat
Yuan et al. (2021)	Yangtze and Poyang Lake, China	**1,133, 1,930**	**129, 189**	0.2, 0.5	ADCP	Moving boat

3. Experimental studies

3.1 Experimental cases

In this study, a laboratory experiment (Exp. 1) and field-scale experiments (Exps. 2-1 and 2-2) were conducted to understand the spectral characteristics of suspended sediment and confounding factors inducing spectral variability. The laboratory experiment aimed to observe the intrinsic optical properties of suspended sediment in a completely mixed state with non-bottom reflectance. Field-scale experiments were conducted to evaluate the optical properties of suspended sediment under optically complex states. In the field-scale experiments, volumetric suspended sediment concentration (SSCv) was measured using a laser diffraction sensor. The hyperspectral images were collected using the UAV-mounted hyperspectral camera; this was performed through tracer tests with three types of sediments in a field-scale open channel. The characteristics of the optical variability of suspended sediment were investigated according to sediment properties, bottom types, background turbidity, and water depth.

In laboratory and field-scale experiments, experimental cases were mainly determined based on the types of sediment, channel bottom, and turbidity of the water flowing in the channel (Table 3.1). For both experiments, two different sediments were selected as the sample sediment: quartz sand and yellow loess. Further, two types of quartz sand and yellow loess with different densities and particle sizes were used in each experiment (Table 3.2). The density of the sediment samples used in lab-scale (Exp. 1) and field-scale experiments (Exp. 2-1, 2-2) was calculated from both the SSC_V measured by laser in-situ scattering transmissometers (LISST-200X by Sequoia Scientific Inc., USA) and the weight concentration of suspended sediment (SSC_W) measured through dry weight measurement (Fig. 3.1). In this procedure, distilled water was placed in a 1 L beaker, and the amount of the sample was increased when using LISST-200X. The full path flow-through chamber was utilized to circulate water and pass through the LISST-200X. Each concentration was measured for 1 min, and the mean concentration was used to calculate the density of each sediment. The PSD was measured using LISST-200X during this procedure. The density of each sediment is shown in Fig. 3.2, and the measured PSD of each sediment is described in Table 3.2. The mean of the volume concentration and weight concentration resulted in a high R^2 value, although the standard deviation of each volume concentration was relatively high. In addition, each sediment had apparently different density and PSD.

Table 3. 1. Properties of the sediment used in the experiments; a dominant fraction value of each sediment is indicated in bold in the shaded column.

Sediment type	Mineral contents	ρ_s (g/cm^3)	d_{50} (μm)	Fraction (%)		
				Clay (d < 4 μm)	Silt (4 μm < d < 62 μm)	Sand (62 μm < d)
QS 1	Quartz sand	2.36	140	0.35	3.43	**96.2**
QS 2		2.46	165	0.31	2.14	**97.5**
YL 1		1.23	16.3	18.9	**80.6**	0.44
YL 2		1.79	37.2	7.91	**60.8**	31.3

Table 3. 2. Summary of experimental studies: lab-scale and field-scale experiments.

Type	Exp.	Channel type	Sediment type (*n*)	Bottom type	Water depth (m)	SSC range	Background water quality			Description
							Turbidity (FNU)	Qhl-a (RFU)	EC (μS/㎝)	
Lab-scale	Exp. 1	Rotating horizontal cylinder	QS1 (1), QS2 (1), YL1 (1), YL2 (1) (4 cases)	99% absorbance film	0.6	0~1333.3 mg/L	0	0	0	Various sediment properties, non-bottom reflectance
Field-scale	Exp. 2-1	Straight channel	QS1 (1), QS2 (1), mixture (1) (3 cases)	Sand	0.8	32.12 ~270.92 μL/L	60	0.60	150.2	Various sediment properties, high turbidity
	Exp. 2-2	Meandering channel	QS1 (2), YL1 (2), YL2 (1), mixture (2) (7 cases)	Sand, vegetation	0.8	10.59 ~317.63 μL/L	0.1	0.01	160.5	Various sediment properties, low turbidity, bottom type, heterogeneous mixing

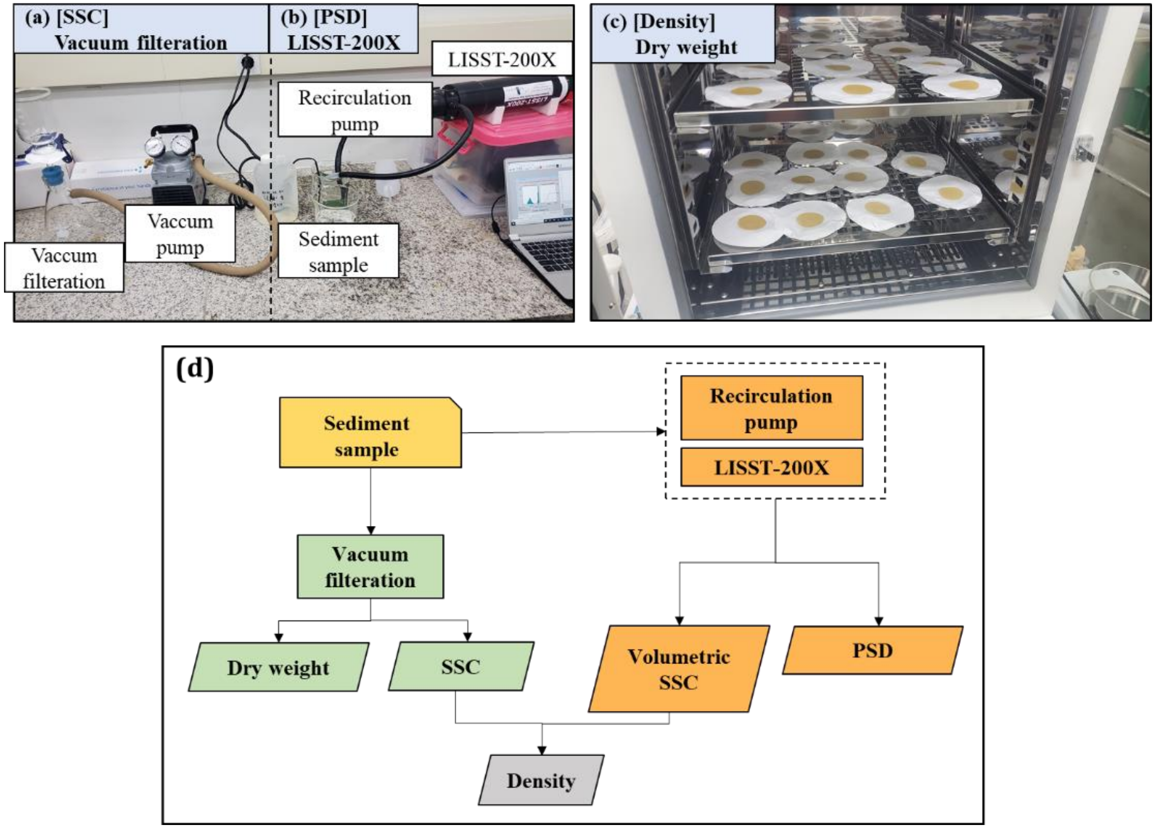

Fig. 3. 1 Experimental setting in the laboratory for (a) concentration, (b) PSD, and (c) density of sediment sample.

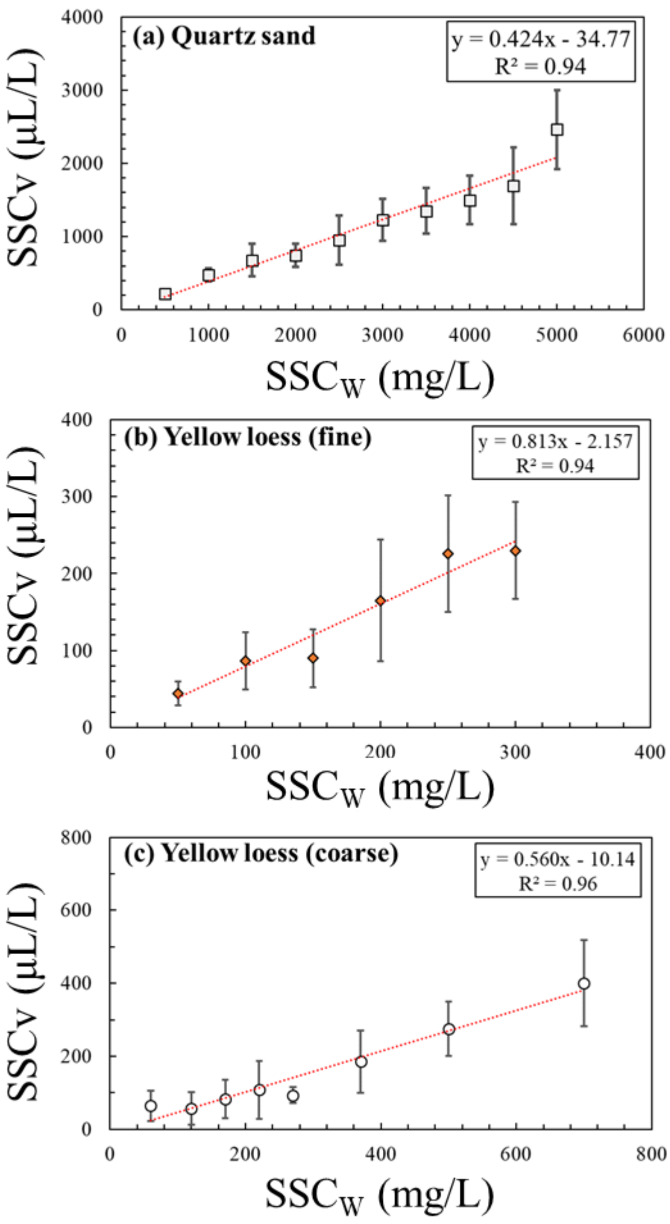

Fig. 3. 2. Comparison of SSC_W measured based on the dry weight of each sample and SSC_V measured using LISST-200X: (a) QS1, (b) YL1, and (c) YL2.

Using Principal Component Analysis (PCA) and clustering analysis with experimental datasets, this study quantitatively detailed the most confounding factors of optical variability of SSC, such as sediment properties (mineral contents, particle size, density), background turbidity, water depth, and bottom substrate, as detailed in Chapter 2.1.2. The experimental dataset was used to develop CMR-OV. The summary of each experiment and related impact variables are described in Table 3.2, and each experiment is described in detail, in the following subchapters (Chap. 3.2.1 and 3.2.2).

3.2 Laboratory experiment

3.2.1 Experimental setup

The primary approach to obtaining the relation between SSC and corresponding spectral signals is based on calibration between field samples and the spectrum obtained using a spectrometer. The measurement of intrinsic spectral properties is limited in a field experiment and involves high costs; therefore, laboratory-scale studies were performed through capturing the spectra of an opened water tank where the SSC varies (Chen et al., 1991; Choubey, 1994; Tolk et al., 2000; Kabir and Ahmari, 2020). The water tank-based studies set uniformly mixed conditions of suspended sediment using pumps and pipe systems (Tolk et al., 2000; Kabir and Ahmari, 2020). The pump system resuspends the sediment particles; however, the streamlines cannot cover the overall tank volume. If the mean particle size of sediment is large, it has a concise characteristic time scale for a particle to re-enter the turbulence region of the pump jet. Therefore, SSC over the water tank may vary unless the perforated pipe system is sufficiently dense to induce complete mixing. In addition, the water surface glittering may influence the measured spectrum when the water tank is open. Therefore, in this study, a more strictly controllable experimental setting was devised to determine the relationship between SCC and corresponding spectral signals. This experimental setting reduces the external uncertainty in measuring the suspended sediment's scattering intensity and guarantees uniform mixing and non-bottom effect conditions.

The hardware of the experimental setting consists of a rotating horizontal cylinder, halogen light sources, and measurement devices (Fig. 3.3). The cylinder (20.25 L) is connected to the angular frequency adjustable motor. Water and sediment are filled via three holes on the curved face of the cylinder. All faces of the cylinder can be detached. The curved face and the other side wall connected to the motor of the drum are black-coated, and the upper side opposite to the motor is transparent; 99% absorption film (Acktar light absorbent foil) was attached at the bottom of the drum, to prevent bottom reflection. The diagram of the horizontal agitator is illustrated in Fig. 3.3 (a). Halogen lamps, which provide almost constant illumination with a wide spectral range, were used during the experiment since illumination stability and spectral range of light sources were key factors in this experiment. Two halogen lamps were installed at 45 degrees to the drum's axis and 90 degrees to each halogen lamp to eliminate the shadow effect. Fig. 3.3 (b) and (c) show the apparatus and the experimental system. For spectral measurement, including radiance and reflectance, a hyperspectral camera (Corning microHSI 410 SHARK), which is a push-broom type sensor with a size of 13.6 × 8.7 × 7.0 cm and a weight of 680 g, was used. This sensor covers the 400–1000 nm spectral range with 150 spectral bands and 682 spatial pixels per line. This sensor spatially records the light entering through the prism by arranging multiple optical sensors linearly (Fowler, 2014). In addition, a point spectrometer (SR-2500 by Spectral evolution, USA) was used to measure a more precise and comprehensive range of radiance spectrum. This spectrometer covers the 350–2,500 nm spectral range in 1 nm increments with 2,151 spectral bands.

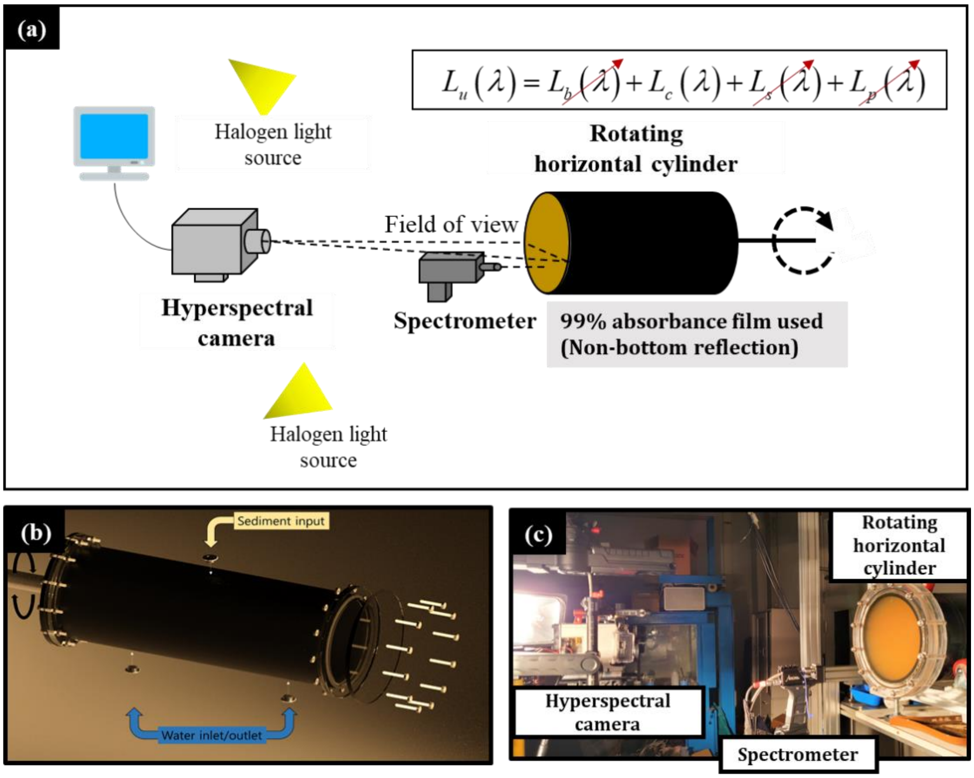

Fig. 3. 3. Experimental setup of Exp. 1; (a) overview, (b) apparatus of rotating lateral cylinder, (c) photo of experimental setup.

3.2.2 Experimental method

Input SSC_W was controlled by injecting a known amount of sediment into a cylinder with a known volume, where SSC_W was calculated as sediment mass divided by cylinder volume. When the mixing was completed, the reflectance spectrum was measured. For the calibration of the hyperspectral camera and point spectrometer, the Spectralon multi-step reflection target of 12, 25, 50, and 99% reflectance and 99% reflection targets were captured for every measurement. The empirical line method (ELM) was used to convert radiance *L* to reflectance *R* based on reference reflectance values from Spectralon, as follows:

$$R(\lambda) = Gain(\lambda) \cdot L(\lambda) + Offset(\lambda) \quad (3.1)$$

Before the experiment, the complete mixing was confirmed; the hyperspectral spectrum of values at uniformly distributed 9 points were spatially averaged (Fig. 3.4 (a)). Using the heaviest sediment particle (QS2), the test was conducted at a concentration of 222.22 ppm. The error range of spatial averaging was 2 to 7% from the standard deviation of hyperspectral spectra (shaded area in Fig. 3.4 (b)).

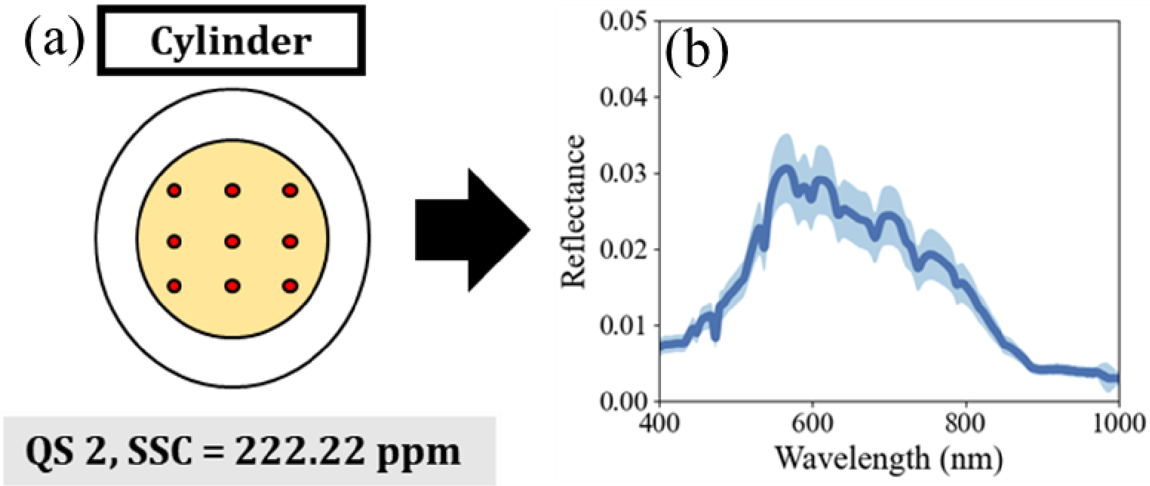

Fig. 3. 4. Spatially averaged hyperspectral spectrum of QS2: (a) points extracted for spatial average; (b) spatially averaged hyperspectral spectrum.

Fig. 3. 5 (a) shows an example of extracting RGB images of yellow loess according to SSC_W from a hyperspectral image acquired by a line scanning using a hyperspectral camera. The color of suspended sediment apparently became vivid with increasing SSC_W. Similarly, the reflectance values of the hyperspectral spectrum increased in the wavelength range of 400–1,000 nm in proportion to the SSC_W values (Fig. 3.5 (b)). However, at wavelengths above 1,000 nm, all the light was absorbed by the water column rather than being scattered by the suspended sediment. The bottom reflectance was completely removed; therefore, it was confirmed that the reflectance converged to almost zero when there was no suspended sediment in the clean tap water.

In this study, using the laboratory rotating cylinder, experimental cases were planned according to sediment types, based on the same sediment as the two quartz sand types and three yellow loess types above (Table. 3.1). The detailed description of each case is summarized in Table 3.3.

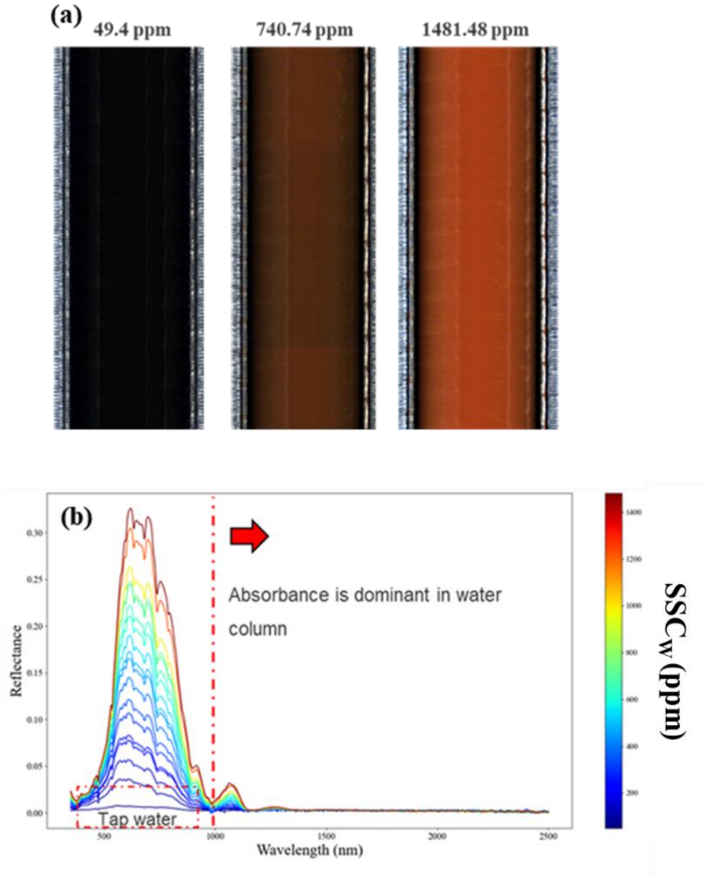

Fig. 3. 5. (a) RGB images and (b) spectral profiles according to SSC$_W$ value in Exp. 1.

Table 3. 3. Experimental cases and properties of sediment used in each case.

Case	Sediment type	d_{50} (µm)	Volume (L)	SSC_W range (ppm)	Measured variables
Case 1-1	YL 1	16.3	20.25	0~1333.3 (18 points)	Radiance (L), Reflectance (R), Temperature (T), Concentration (SSC_W), Particle size distribution (PSD)
Case 1-2	YL 2	37.2			
Case 1-3	QS 1	140			
Case 1-4	QS 2	165			

3.3 Field-scale experiments in River Experiment Center

3.3.1 Experiments in the straight channel

(1) Experimental site and channel

The optical property of the suspended sediment varies with the sediment properties (i.e., mineral content, density, PSD) and stream bed properties (Z. Chen et al., 1991; Dethier et al., 2020; Qu et al., 2016). Therefore, in this study, field-scale experiments were conducted to analyze the optical variability owing to sediment characteristics and bottom types of the stream bed, which are the confounding factors while evaluating the relation between SSC and hyperspectral reflectance; they lead to a large degree of uncertainty in remote sensing-based SSC estimation (Kwon et al., 2022b). For this objective, tracer tests were conducted with three types of sediment to obtain a dataset containing both hyperspectral images and in-situ measured SSC_V values, for the various sediment characteristics. The sediment tracers used in the experiment consisted of quartz sand, yellow loess, and a mixture of quartz sand and yellow loess (Table 3.4).

The experiments were conducted in the River Experimental Center (REC) of the Korea Institute of Civil Engineering and Building Technology (KICT), located in Andong, South Korea, as shown in Fig. 3.6 (a) (Kwon et al., 2022b). The Exp. 2-1 were performed in a straight channel with a river-scale trapezoidal section with a length of 500 m, top width of 11 m, depth of 2 m, and side slope of 1/2. The channel bed was covered by natural sand, and the side bank was covered by concrete blocks. The experimental water used in the channel was pumped in from the Nakdong River, located near the REC. Fig. 3.6 (b) shows the sediment injection point and measurement section in the experimental channel. The injection point was located at the center of the upstream bridge. At this point, using a mixer, sediment solution diluted with the river water was injected in a completely mixed state, as shown in Fig. 3.6 (c). It was injected underwater to minimize the effect of the drop in momentum of the initial sediment tracer injection.

Table 3. 4. Sediment injection condition in Exp. 2-1.

Case	Sediment type	Bottom type	Weight (kg)	Volume (L)	Discharge (m^3/s)	Width (m)	Mean depth (m)	Mean velocity (m/s)	Date
2-1-1	Quartz sand (QS 1)	Natural sand	40	127	2	5	0.9	0.44	10/7/2020
2-1-2	Yellow loess (YL 1)								
2-1-3	Mixture (QS 1 + YL 1)								

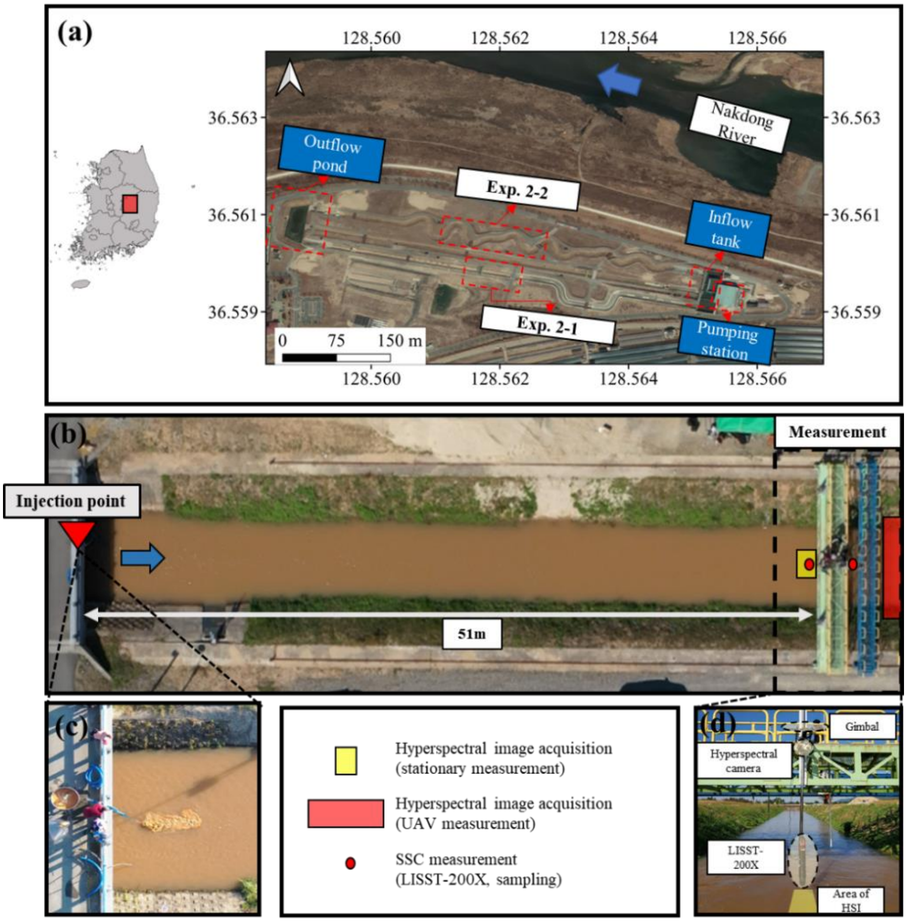

Fig. 3. 6. (a) Experimental set-up in REC channel of which water is supplied from nearby Nakdong River; (b) Injection point and measurement section of Exp. 2-1 in the experimental channel; (c) picture of sediment injection scene; (d) detailed configuration of the observation point of Exp. 2-1.

(2) Measurement technique and devices

In this experiment, two different measurement techniques were used to obtain both hyperspectral images and SSC_V values at the measurement sections: 1) fixed measurement; 2) moving measurement using UAV, as shown in Fig. 3.6 (d). First, using the fixed method, hyperspectral images were obtained at two locations, in front of and behind the bridge, via different techniques. Hyperspectral images were captured in front of the bridge in order to extract the ground-based hyperspectral spectrum of the corresponding pixels with the in-situ sensor. To minimize the effect of the atmosphere on the hyperspectral images, a push-broom line-scan type hyperspectral camera was installed at the center of the bridge, 1.85 m above the water surface, using a DJI Ronin 3-axis handheld gimbal. Second, for the images taken behind the bridge, spatial information, including the width of the channel, was obtained using a UAV (DJI Matrice 600 Pro)-mounted hyperspectral camera. These images were used to retrieve the spatio-temporal distribution of suspended sediment. For both measurements, the same hyperspectral camera (microHSI 410 SHARK) was used in the laboratory experiment study. The hyperspectral images of transverse lines over time were acquired by this sensor; therefore, the hyperspectral spectrum line was captured continuously as the water flowed while the sensor was fixed at the measurement section. Accordingly, the dimensions of the hyperspectral images obtained in this experiment were width *(y)* - time (t) - wavelength (λ).

For the in-situ SSC_V measurement, a LISST-200X, which measures particle size using light scattering based on underwater laser diffraction, was used to measure the SSCv, PSD, and temperature. The LISST-200X used in this study can measure a sufficient range of PSD and SSC_V: the PSD range consists of 36 bins that are distributed from 1 to 500 μm in logarithmic increments, while the range of SSC_V is from 0.5 to 700 ppm. This sensor was installed at the iron rod connected to the center of the bridge to measure the temporal concentration of suspended sediment, as shown in Fig. 3.6 (d). To obtain the concentration near the water surface and the bed, two LISST-200X devices were deployed at fixed depths of 0.675 and 0.225 m from the bed, which was 0.75 and 0.25 times the water depth. The sampling rate of both sensors was set to 0.67 Hz. The hydraulic data, including discharge and mean velocity, were obtained using the acoustic doppler current profiler (ADCP; River Surveyor S5 by SonTek, USA) at the measurement section. A water depth survey was conducted utilizing real-time kinematic-global positioning system (RTK-GPS; GRX1 by Sokkia, Japan).

(3) In-situ measured sediment characteristics

During the experimental period of the Exp. 2-1, the background turbidity was high enough to neglect the effect of bottom reflectance because the water was pumped in from the Nakdong River, which has high turbidity after a flood. The background PSD and the particle size of the sediment tracer in each case were under 0.2 mm; therefore, the PSD values ranging from 0.001 to 0.2 mm were considered. The range of PSD included four classes of sediment according to particle size: fine sand (range: 125–200 μm), very fine sand (range: 62–125 μm), silt (range: 4–62 μm), and clay (1–4 μm) (Merten et al., 2014; Wang et al., 2020).

The PSD at the maximum concentration in each case and the background water is illustrated in Fig. 3.7. The proportion of sand increased significantly near both the water surface and the river bed after the injection of quartz sand (Case 2-1-1) compared to that in the background water in which clay and silt were dominant, as shown in Fig. 3.7 (a) and (b). The relative frequency of sand was higher near the river bed than that near the water surface because quartz sand tends to settle to the bottom of a body of water. In the case of yellow loess (Case 2-1-2), the concentration of particles with the size of silt and very fine sand increased at the maximum overall particle concentration, as shown in Fig. 3.7 (c) and (d),. However, in this case, the variations in concentration near the water surface and river bed were similar, which implies that the settling velocity was not very high. For the mixture of quartz sand and yellow loess (Case 2-1-3), the relative frequency of silt and fine sand increased, similar to that in the yellow loess case (Case 2-1-2), as shown in Fig. 3.7 (e) and (f). The relative frequency of fine sand increased to a greater extent than that in Case 2-1-2 due to the effect of quartz sand. Similarly, the relative frequency of fine sand at the sampling depth of 0.25H was greater than the relative frequency of fine sand at the sampling depth of 0.75H owing to the settling property of quartz sand.

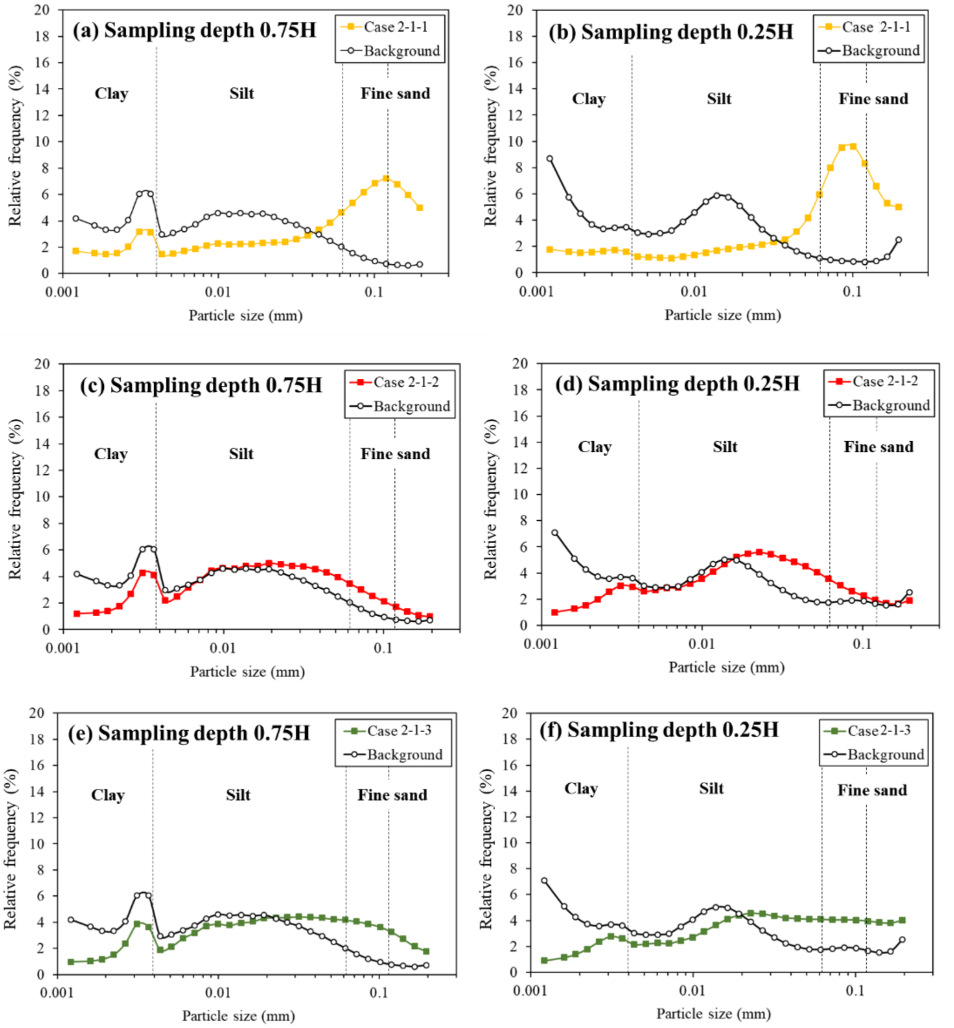

Fig. 3. 7. PSD of the suspended sediment at the maximum SSC_V measured in Exp. 2-1; (a), (c), and (e) represent PSD sampled near the water surface; (b), (d), and (f) represent PSD sampled near the riverbed.

Breakthrough curves (BTCs) of SSC_V measured at 0.75H and 0.25H of the three experimental cases are plotted in Fig. 3. 8 (a)–(c). The SSC_V for Case 2-1-1 was lower than that for Case 2-1-2 even though the same amount of mass was discharged at the injection point in all three cases. This could be attributed to the high fall velocity; the quartz sand in Case 2-1-1 settled down to the channel bed faster than the yellow loess in Case 2-1-2 when it was transported downstream of the injection point in the channel. The suspended sediment cloud images captured by the RGB camera (Fig. 3.8 (d)) clearly indicated this difference: the suspended sediment cloud of quartz sand in Case 2-1-1 is less vivid than the cloud of yellow loess in Case 2-1-2. A comparison of two BTCs of quartz sand in Case 1, shown in Fig. 3.8 (a), revealed that the concentration measured near the bed (0.25 H) was greater than that measured near the water surface (0.75 H). The mixture of quartz sand and yellow loess (Case 2-1-3) showed intermediate behavior between that in Cases 2-1-1 and 2-1-2.

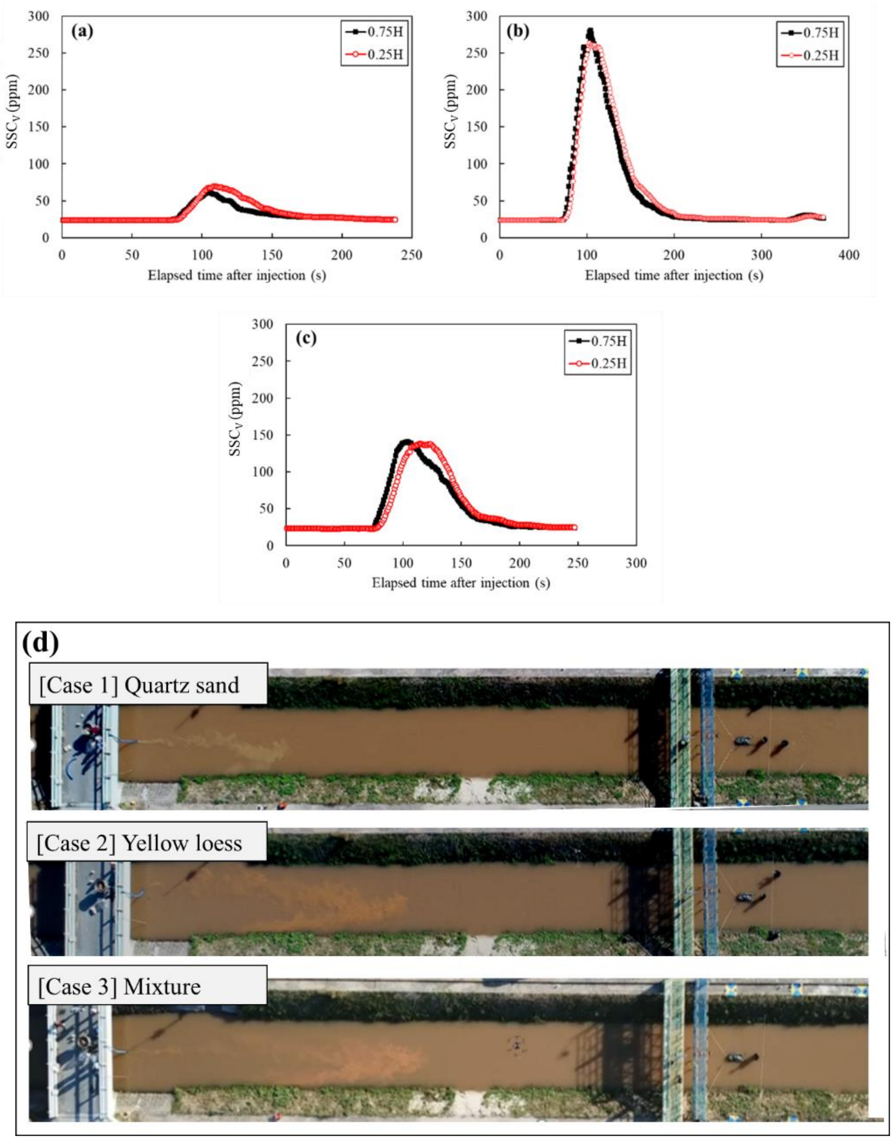

Fig. 3. 8. BTCs of In-situ measured SSC$_V$: (a) quartz sand, (b) yellow less, (c) mixture, and (d) their RGB images.

BTC features reveal the transport and mixing characteristics of the solute; the calculation process and description are elaborated in Appendix A. The BTC features of Exp. 2-1 are shown in Table. 3.5. The time ($\bar{t}$) to the centroid of BTC was almost the same in all three cases. Furthermore, the tail of the BTC (S_{tail}) was calculated using the power-law slope, which is used as a criterion of storage zone effect in rivers (Kwon et al., 2021b; Kim et al., 2021). In all three cases, the tail slopes were not persistent because the storage effects owing to the boundary irregularities in this prismatic straight channel were not significant compared to that in natural rivers. However, the quartz sand showed relatively high tail slopes and had high skewness compared to other sediment types. This result demonstrates that the residence time of suspended sediment depends on particle size due to its interaction with channel irregularities.

Table 3. 5. Description of SSC_V curves from Exp. 2-1.

	Measured depth	Centroid $\bar{t}$ (s)	σ_t	Skewness	Kurtosis	$\bar{C}$ (ppm)	C_p (ppm)	S_{tail}
Case 2-1-1 (quartz sand)	0.75H	182.4	43.20	1.211	0.855	32.57	59.87	-4.31
	0.25H	186.4	39.07	1.017	1.363	36.06	68.48	-5.12
Case 2-1-2 (yellow loess)	0.75H	171.5	33.30	0.816	0.429	113.2	280.0	-5.95
	0.25H	179.7	35.83	0.789	0.364	108.4	262.8	-5.34
Case 2-1-3 (mixture)	0.75H	174.5	33.19	0.608	0.035	65.02	140.7	-5.82
	0.25H	186.8	36.56	0.851	0.98	65.07	138.1	-6.25

3.3.2 Experiments in the meandering channel

(1) Experimental channel

The experimental channel of Exp. 2-2 is a field-scale meandering channel in the REC, as illustrated in Fig. 3.9 (a). This channel has a trapezoidal section of the natural river scale, length 500 m, top width 11 m, depth 2 m, and three reaches with varying sinuosities of 1.2, 1.5, and 1.7. In this channel, the experiment was performed in the reaches with 1.7 sinuosity and a length of 170 m, as shown in Fig. 3.9 (a) (Kwon et al., 2022a). The background water was relatively clean with low turbidity during the experiment, compared to that in Exp. 2-1 (Table 3.2). Therefore, the bottom reflectance contributed considerably to the hyperspectral spectrum in this experiment. To analyze this bottom effect, experiments were conducted for two bottom types: natural-sand-covered with approximately 0.1 m vegetation at the upper reach and a natural arid sand bed at the lower reach, as described in Fig. 3.9 (b). The vegetation in this channel grew naturally after rain; therefore, it was rooted strongly enough to maintain the flow. The sand bed reaches were set up by removing all vegetation before the experiments. In the experimental reach, we set up three sections (Sections C1–C3) for the measurement of suspended sediments, hyperspectral images, flow, and geometry; and four sections (Sections H1–H4) for the flow measurements only. The injection point (IP) of sediment particles was located at a concrete bridge 80 m upstream from Section C1. At the IP, the sediment particles were mixed using a specially designed mixer, which we injected underwater using a rubber hose (Kwon et al., 2022b).

The injected sediments of Exp. 2-2 consist of quartz sand (QS 1), yellow loess (YL 1 and YL 2), and a mixture of QS 1 and YL2. In order to analyze the effect of particle size on optical characteristics, two yellow loesses with different particle sizes were used in Cases 2-2-2 and 2-2-3, which were sieved to 75 μm and 250 μm size fractions, respectively. This enabled investigating the particle size effect with or without fine sand (75–250 μm) in these cases. All cases were performed under almost the same injection conditions except for the injected weight of quartz sand since the density of quartz sand is higher than that of yellow loess; 60 kg of quartz sand, which is 20 kg more than that of yellow loess, was injected (Table 3.6). In addition, the effect of bottom type on the hyperspectral spectrum was analyzed to remove the vegetation covering 6 m around section 2 after Case 2-2-4 ~ 6 to change the bottom type of Section 2 to a sediment bottom.

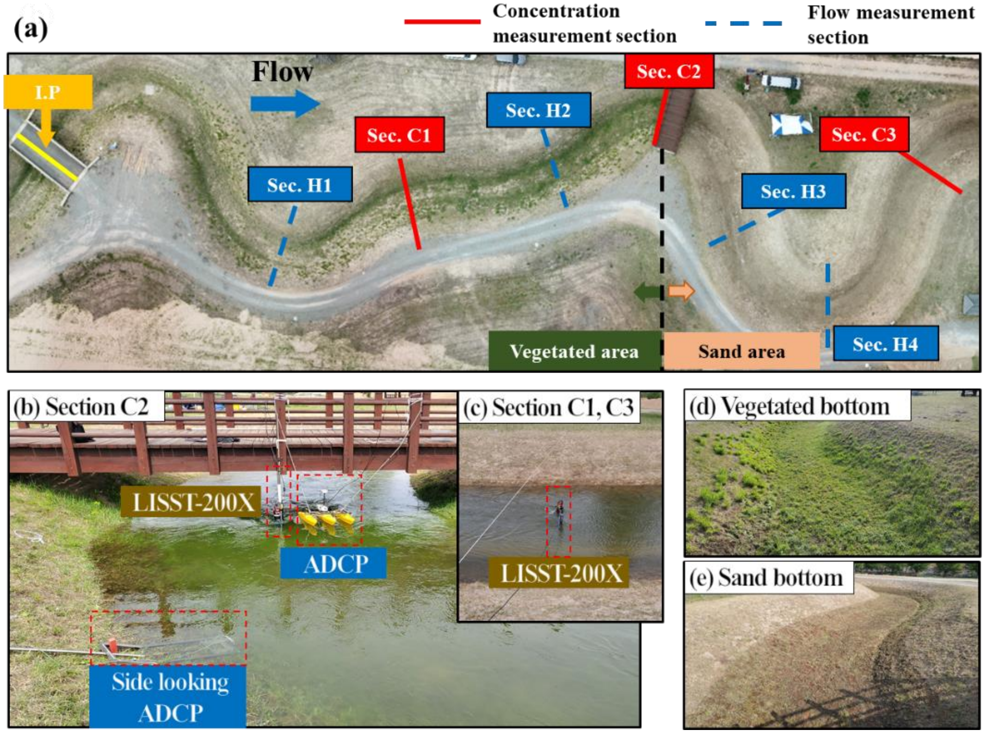

Fig. 3. 9. (a) Bottom types, Injection Point (I.P), and measurement section of concentration and flow in Exp. 2-2; (b) in-situ measurements of SSC_V and flow in Section 2; (c) in-situ measurements of SSC_V in Sections 1 and 3; (d) channel Bottom covered by vegetation and (e) natural sediment.

Table 3. 6. Sediment injection condition in Exp. 2-2.

Case	**Bottom type**	**Date**	**Sediment type**	**Sediment density (g/cm^3)**	**Weight (kg)**	**Volume (L)**	**Duration (s)**	**Injection rate (m^3/s)**
2-2-1	Vegetation	4/27/2021	QS 1	2.36	60	128	38	0.554
2-2-2			YL 1	1.23	40	127	34	0.744
2-2-3			Mixture (QS 1 + YL1)	-		127	33	0.767
2-2-4	Natural sand	4/28/2021	QS 1	2.36	60	127	38	0.666
2-2-5			YL 1	1.23	40	127	35	0.723
2-2-6			YL 2	1.79		127	32	0.791
2-2-7			Mixture (QS 1 + YL2)	-		127	34	0.744

(2) Measuring instrument

Two submersible laser-diffraction analyzers, LISST-200X, were used to measure SSC_V and PSD at two sections in both experiments. The LISST-200X was installed at the iron rod connected to the center of the bridge to measure the temporal variation of SSC_V in Section C2, as shown in Fig. 3.9 (a). Likewise, the second LISST-200X was installed at the center of Sections C1 and C3, connecting with a piled iron rod in the channel bed, as shown in Fig. 3.9 (b). These sensors should be submerged for at least 10 cm from the water surface. Therefore, they were deployed at a fixed depth of 0.75 times the total water depth from the river bed because the SSC_V near the water surface shows a high correlation with the hyperspectral images. The sampling rate of both sensors was set to 0.67 Hz. Simultaneously, two UAVs mounting hyperspectral cameras hovered to acquire hyperspectral images at 25 m above the water surface of all measurement sections with a sampling rate of 120 Hz. Hyperspectral images of transverse lines over time were acquired at each measurement section. The hydraulic data, including discharge, mean velocity, and water depth, were obtained using the ADCP (River Surveyor S5 by SonTek, USA) at the measurement section before each experiment.

(3) Hydraulic and sediment data

The results of hydraulic measurements in all experiments are summarized in Table 3.7. The mean water depths measured in each section ranged from 0.56–0.67 m, which is relatively shallow compared to the water depth range covered in previous studies. Therefore, the bottom effect is the crucial point of these experiments, which is a confounding factor that limits the retrieval of the SSC_V from hyperspectral images. During the experiment, the flow and water depth profiles were different in the vegetated and sand bottom area despite constant discharge conditions, as shown in Table 3.7. The vegetated bottom induced substantial bottom friction; therefore, the mean water depth of the vegetated area was deeper than that in the sand area.

Fig. 3.10 (a) and (b) show the cross-sectional averaged depth and flow velocity according to the longitudinal distance. In all cases, the water depth tends to decrease at the point where the vegetation section changes to the sand section. In addition, this decrease in water depth was clear in cases 2-2-1 ~ 2-2-3, where the entrance of the 1.7 meandering reaches (Sec. C2) was vegetated. The velocity instantaneously decreased at the entry point of the meandering section and increased through the meandering reaches. Such a meandering effect also can be quantified through secondary current intensity (SCI) in Eq. 3.2 (Seo et al., 2006).

$$SCI = \frac{1}{n}\sum_{i=1}^{n}\frac{\sqrt{\overline{\left(u_n'\right)^2}}}{U_c} \tag{3.2}$$

where n = number of the transverse measurement points, u_n' is the deviation of the spanwise velocity, U_c is the cross-sectional averaged velocity.

According to calculated SCI along with longitudinal direction (Fig. 3. 11), the secondary flow generated in the meandering section with 1.5 sinuosity was weakened, and then the secondary flow was substantially generated again at Sec. C2, which is the meandering entrance of 1.7 sinuosity reach. Particularly, the secondary flow was strongly generated when the Sec. C2 was sand bottom due to its relatively low bottom friction. Therefore, the hydraulic conditions in Sec C1–C3 were different owing to bottom friction and the meandering effect. This discrepancy in the hydraulic conditions in each section could induce various mixing conditions of the suspended sediment.

Table 3. 7. Results of hydraulic measurements in Exp. 2-2.

Case	Section	Distance (m)	Discharge (m^3/s)	Mean velocity (m/s)	Width (m)	Mean depth (m)	Slope	*SCI*	*Fr*
2-2-1 ~2-2-3	Sec. H1	47.75	2.37	0.62	5.8	0.66	0.0024	0.072	0.24
	Sec. C1	78.85	2.43	0.63	5.9	0.66	0.0024	0.067	0.25
	Sec. H2	99.15	2.50	0.67	5.7	0.65	0.0012	0.047	0.27
	Sec. C2	109.4	2.58	0.67	6.1	0.63	0.0016	0.054	0.27
	Sec. H3	128.2	2.22	0.57	6.1	0.64	0.0034	0.052	0.23
	Sec. H4	148.3	2.41	0.61	5.9	0.67	0.0036	0.068	0.24
	Sec. C3	170.0	2.28	0.56	6.0	0.68	0.0006	0.055	0.22
2-2-4 ~2-2-7	Sec. H1	47.75	2.33	0.63	5.8	0.63	0.0024	0.067	0.26
	Sec. C1	78.85	2.33	0.61	5.7	0.67	0.0024	0.077	0.24
	Sec. H2	99.15	2.56	0.65	5.7	0.69	0.0012	0.047	0.25
	Sec. C2	109.4	2.24	0.57	6.0	0.66	0.0016	0.083	0.22
	Sec. H3	128.2	2.25	0.57	6.0	0.66	0.0034	0.063	0.22
	Sec. H4	148.3	2.45	0.61	5.9	0.68	0.0036	0.071	0.24
	Sec. C3	170.0	2.57	0.61	6.0	0.70	0.0006	0.061	0.23

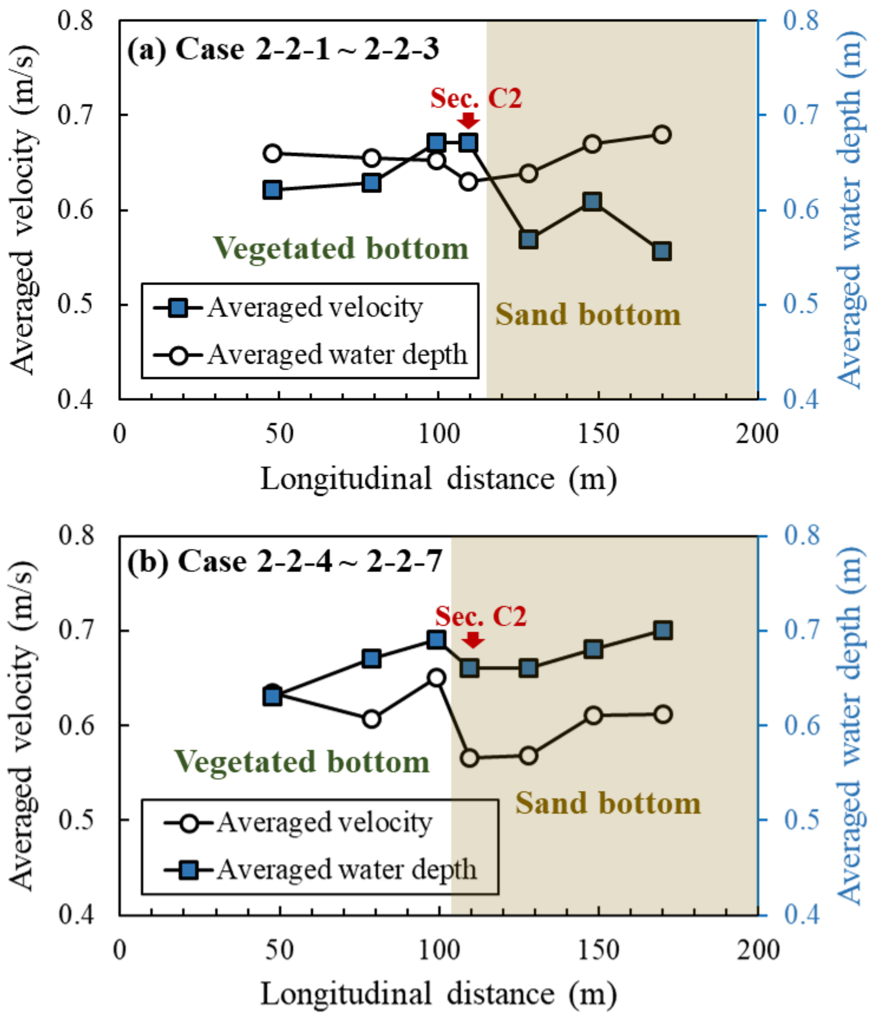

Fig. 3. 10 Hydraulic conditions in each section: Cross-sectional averaged velocity and water depth in (a) Cases 2-2-1 ~ 2-2-3 and (b) Cases 2-2-4 ~ 2-2-7.

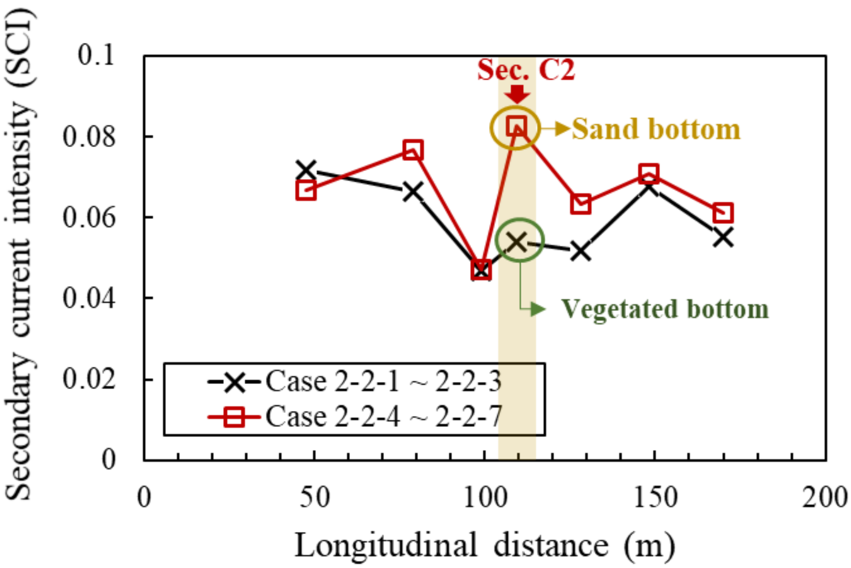

Fig. 3. 11. SCI in each section before and after removing vegetation at Sec. C2.

The BTCs of Exp. 2-2 observed using pulse injection are plotted as in Fig. 3.12 and 3.13. The features of each BTC are summarized in Tables 3.8 and 3.9. The BTC of each sediment type revealed different shapes owing to differences in density. The SSC_V of the quartz sand was lower than that of the yellow loess and mixture, although a larger amount of quartz sand was injected. This occurred due to the large density of quartz sand, which induces the sediment to settle more rapidly to the streambed. For this reason, the peak concentration (C_P) and mean concentration ($\overline{C}$) of quartz sand were lower than that of other sediments, as shown in Tables 3.8 and 3.9. This phenomenon was also shown in the RGB images acquired by drones, which demonstrated that the settling effect caused the low visibility of suspended sediment clouds of quartz sand, as shown in Fig. 3.14.

The BTCs required almost the same time to reach peak concentration and time to the centroid ($\overline{t}$) in the same section irrespective of sediment type, as shown in Tables 3.8 and 3.9. The BTCs were dispersed in the downstream sections, resulting in lower concentrations and longer durations. The standard deviation of BTCs linearly increased with the longitudinal distance, irrespective of the sediment type (Fig. 3.15). However, the skewness of quartz sand was different with yellow loess and mixture. This is because the particles of quartz sand were large and heavy, so they were substantially affected by the large friction of the vegetated bottom. BTC of quartz sand showed higher skewness than that of the non-vegetated case with strong secondary flow when the Sec. C2 was vegetated.

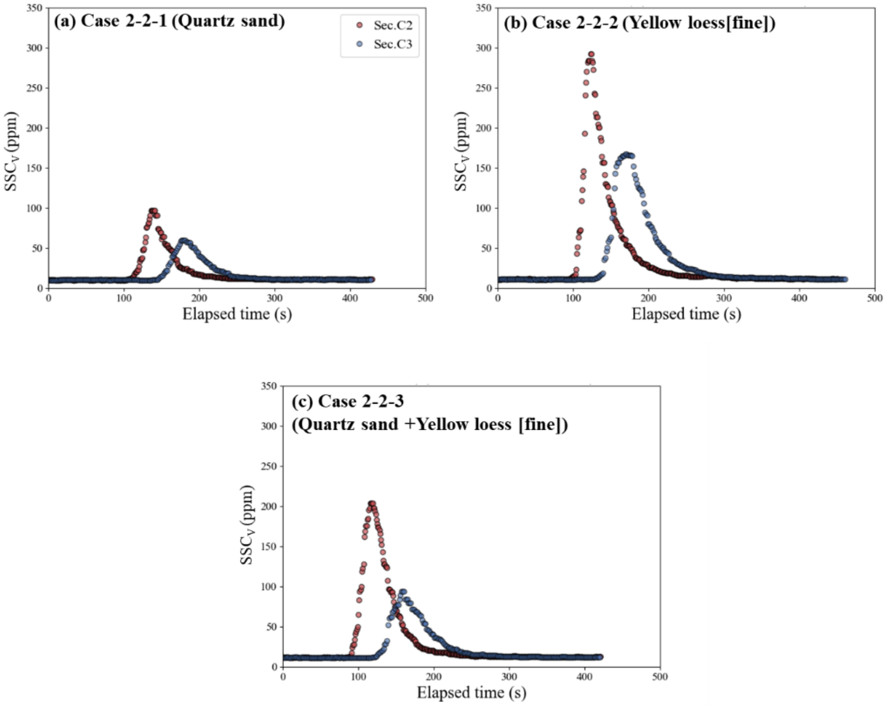

Fig. 3. 12. BTCs of in-situ measured SSC$_V$ (vegetated bottom): (a) Case 2-2-1, (b) Case 2-2-2, and (c) Case 2-2-3.

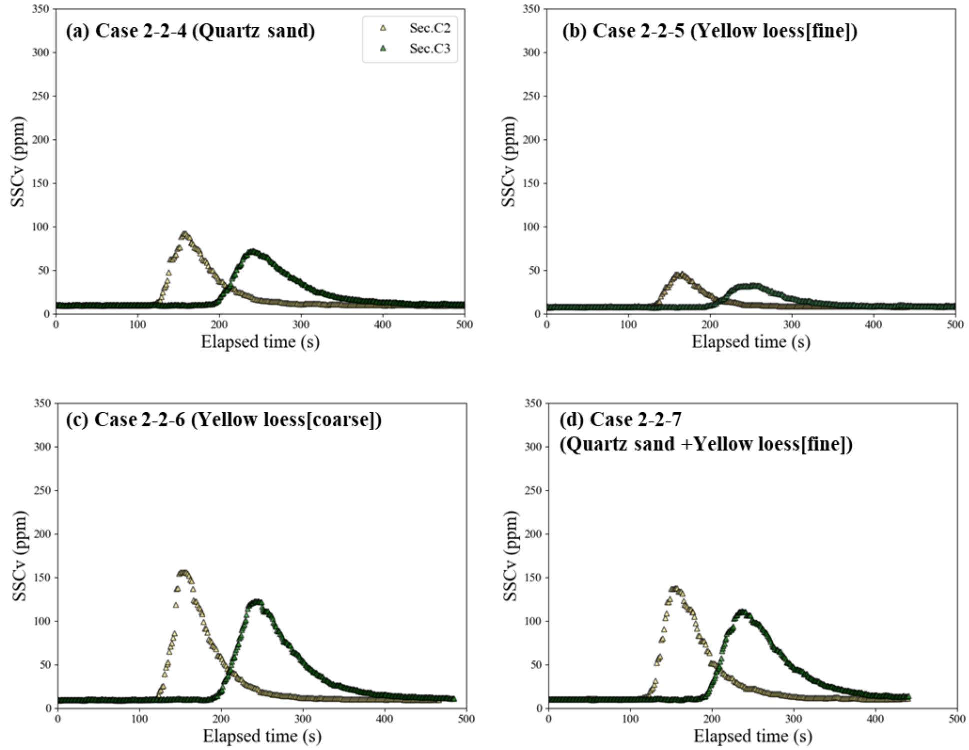

Fig. 3. 13. BTCs of in-situ measured SSC_V for sand bottom: (a) Case 2-2-4, (b) Case 2-2-5, (c) Case 2-2-6, and (d) Case 2-2-7.

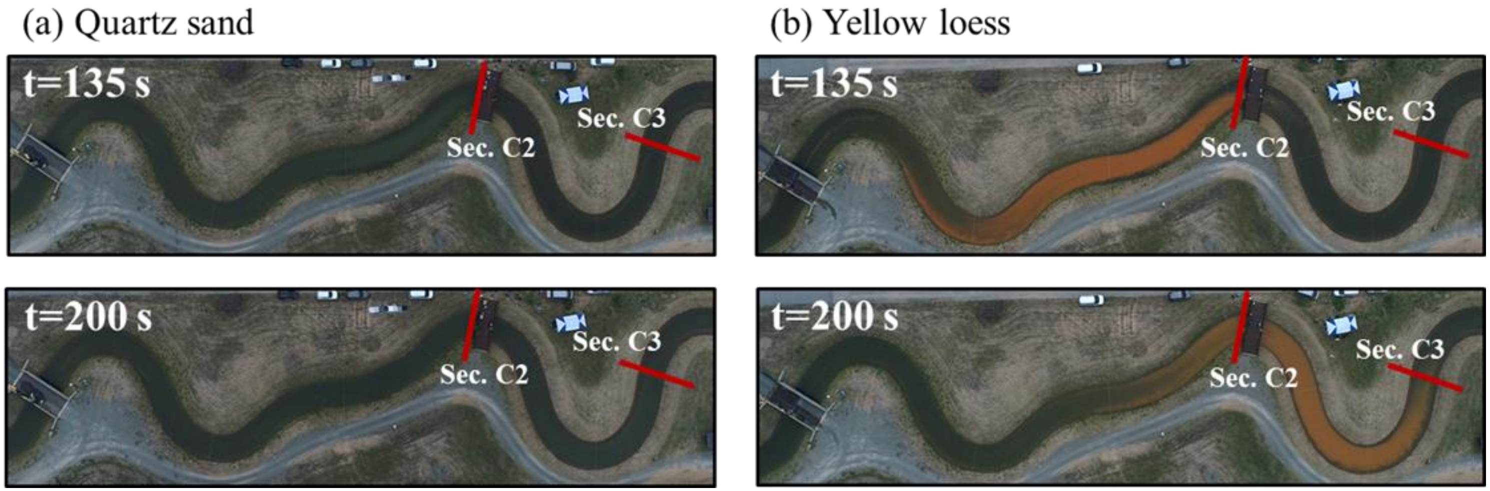

Fig. 3. 14. Cloud images of quartz sand and yellow loess captured using an RGB camera mounted on a drone.

Table 3. 8 Description of SSC_V curves from Exp. 2-2: Case 2-2-1 ~ 2-2-3.

Case	Section	Centroid $\bar{t}$ (s)	σ_t	Skewness	Kurtosis	$\bar{C}$ (ppm)	C_p (ppm)	S_{tail}
Case 2-2-1 (quartz sand)	Sec. C1	150.3	21.94	1.251	0.905	19.81	86.99	-7.18
	Sec. C2	193.2	23.93	1.875	-5.858	12.59	49.28	-8.07
Case 2-2-2 (yellow loess)	Sec. C1	137.9	22.49	1.235	0.58	66.93	280.79	-6.11
	Sec. C2	184.8	28.31	1.009	1.062	45.19	156.54	-7.01
Case 2-2-3 (mixture)	Sec. C2	129.8	22.55	1.062	1.604	45.94	192.04	-6.49
	Sec. C2	175	28.13	0.893	1.409	22.17	82.09	-6.86

Table 3. 9 Description of SSC_V curves from Exp. 2-2: Cases 2-2-4 ~ 2-2-7.

Case	Section	Centroid $\bar{t}$ (s)	σ_t	Skewness	Kurtosis	$\bar{C}$ (ppm)	C_p (ppm)	S_{tail}
Case 2-2-4 (quartz sand)	Sec. C2	177.1	27.82	1.23	0.18	8.280	38.15	-6.97
	Sec. C3	272.2	49.52	1.02	2.15	6.200	24.80	-5.91
Case 2-2-5 (fine yellow loess)	Sec. C2	173.4	29.42	0.91	0.86	37.74	146.4	-6.36
	Sec. C3	268.1	44.21	0.95	0.92	25.32	112.94	-6.55
Case 2-2-6 (coarse yellow loess)	Sec. C2	175.7	31.78	1.08	0.71	37.64	127.51	-5.82
	Sec. C3	264.9	44.41	0.98	0.76	25.71	100.53	-6.38
Case 2-2-7 (mixture)	Sec. C2	175.9	30.49	0.89	1.01	22.07	82.31	-6.19
	Sec. C3	268.8	45.84	0.87	1.18	14.82	62.22	-6.33

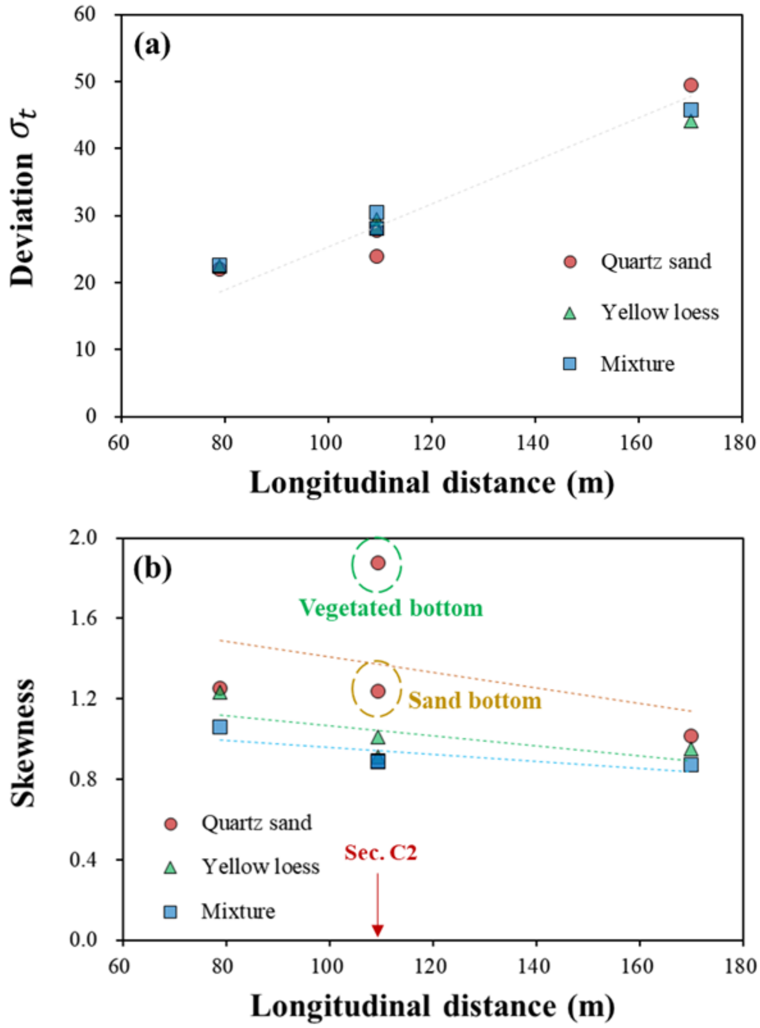

Fig. 3. 15. Standard deviation and skewness of BTCs measured in each case.

The PSDs at the maximum SSC_V of each experiment and background water are illustrated in Fig. 3.16, where the PSDs were determined according to sediment type regardless of transport distance and the bottom type. The quartz sand (Case 2-2-1 and 2-2-4) has sand-dominant PSD with a right-skewed distribution, while the yellow loess (Case 2-2-2, 2-2-3, and 2-2-4) has a bimodal distribution with the maximum in the range of silt. The two types of yellow loess (2-2-3 and 2-2-4) showed a considerable discrepancy in the particle size over 20 microns. Based on this difference in PSD with the same mineralogy, the effect of PSD on spectral characteristics can be investigated. In the PSD of the mixture (Case 2-2-3 and 2-2-7), the probability of fine sand was higher than that for yellow loess due to quartz sand. However, the mixture showed a similar tendency with yellow loess. This implied that the quartz sand settled faster than yellow loess due to its high density; therefore, the influence of the quartz sand disappeared rapidly.

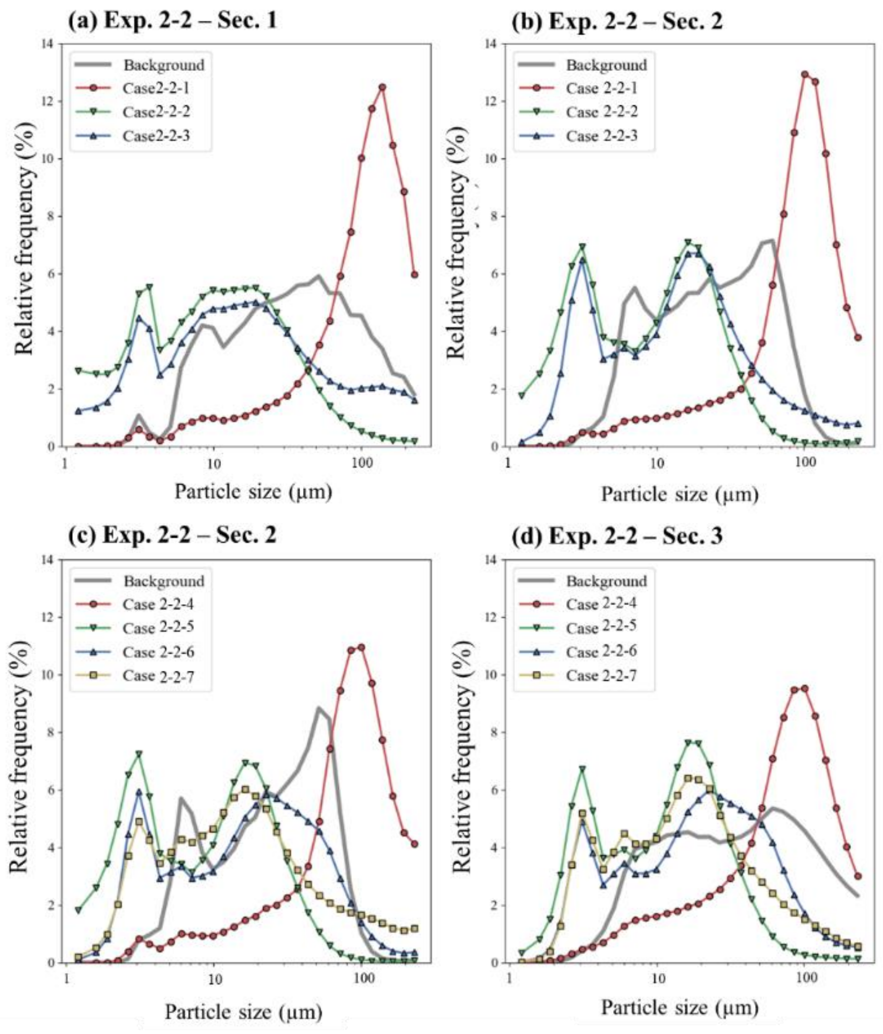

Fig. 3. 16. PSDs at the maximum SSC_V value at Exp. 2-2-vegetation (a and b) and Exp. 2-2-sand (c and d).

3.4 Field survey

3.4.1 Study area and field measurement

The field surveys were conducted to obtain the real river datasets for the evaluation of the applicability of CMR-OV to various field conditions (Table 3.10). Two study sites for assessment were selected: Hwang River; the confluence of Nakdong River and Hwang River in South Korea. The streambed substrates of both rivers are dominantly fine sand, so morphological change and sediment transport occurred in various ways. The total watershed area of the Nakdong River is 23,817 km^2, with a main channel length of 522 km. Hwang River is the main tributary of Nakdong River, with a length of 107.6 km and a total watershed area of 1,329 km^2. The confluence of both rivers is located in the lower reaches of the Nakong River, at about 7.5 km downstream of the Hapcheon-Changnyung dam (Fig. 3.16).

In the upstream and downstream reaches of the Hwang River, two surveys (Exp. 3-1 and 3-2) were conducted (Fig. 3.17). During Exp. 3-1, the SSC_V and PSD were measured for 1 minat 10 points in a shallow depth zone ($H < 1$m) using LISST-200X. Particularly, 4 points were measured up to the vertical SSC_V profiles. The velocity and water depth were measured at the same points of SSC_V measurements using an acoustic Doppler velocimeter (ADV; Flowtracker2 by Sontek, USA). In Exp. 3-2, horizontally dense profiles of suspended sediment, water quality, flow, and geometry were simultaneously measured at 49 points using sensors installed in a boat moving laterally across the river (Kwak et al., 2020). In specific, the profile of SSC_V and PSD near the water surface was measured using a LISST-200X and a reel attached to the side of a boat. Additional hydraulic data such as water depth and vertical flow velocity profile were obtained using the ADCP (River Surveyor M9 by SonTek, USA) and GPS device installed on the boat (Kwak et al., 2020; Son et al., 2021).

Three surveys (Exps. 4-1~4-3) were conducted at a near-field of river confluence, where dynamic mixing occurs owing to the varying confluent flows from both rivers, which converge on the right bank. All surveys were conducted during low flow conditions (Fig. 3.18). During these surveys, the suspended sediment and flow measurements were conducted using the same methods in Exp. 3-2. In addition, in Exps. 4-1 and 4-3, the vertical SSCv and PSD profiles were measured at 4 to 5 points in the downstream section of about 350 m after confluence. In Exp. 4-2, the overall water depth was very shallow; therefore, it was measured at about 0.3 m below the water surface. YSI 6600 EDS was utilized to measure water temperature and water quality data such as Qhl-a, turbidity, pH, and dissolved oxygen (DO). After all surveys, sampled suspended sediment at the measurement points was used to validate the SSCv measured by LISST-200X with SSCw. These samples were analyzed in the laboratory using the procedure to estimate density, as represented in Fig. 3.1.

In all field surveys, the HSIs were simultaneously acquired using the

UAV-mounted hyperspectral camera platform, as described in Chapter 3. The UAV platform was manipulated to scan in the river width direction to cover the entire target area in the surveys, while the hyperspectral images were acquired by hovering the drone in field-scale experiments. Several flight strips were designed, and the independently acquired strips of hyperspectral images were co-registered to obtain the hyperspectral images covering a large area. In this procedure, the geo-referenced points and RGB images were used to align HSIs strips accurately so that corresponding pixels of overlapped locations were geometrically integrated. The final co-registered images were pre-processed to be equitably utilized, as described in Chapter 2.2.

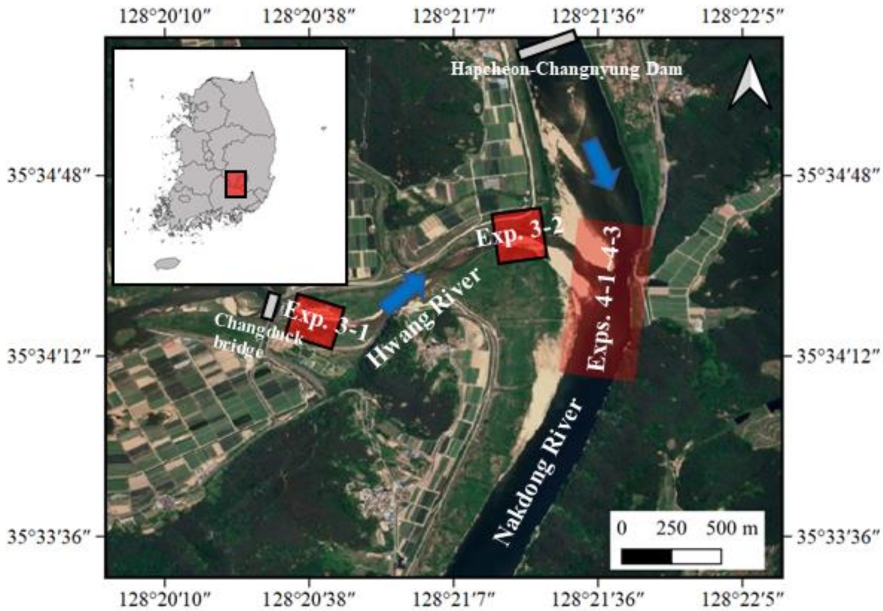

Fig. 3. 17. Location of survey areas at the Nakdong and Hwang Rivers.

Table 3. 10. Summary of field surveys.

Type	Experiment	Location	Survey date	SSC range (μL/L)	*d50* (μm)	Bottom type	Water depth (m)	Descriptions
Field (straight and meandering rivers)	Exp. 3-1	Hwang river (upstream)	03/29/2021	24.08 ~52.96	92.90	Sand	0.15~1.1	Shallow water depth; vertical SSC profiles were measured
	Exp. 3-2	Hwang river (downstream)	03/30/2021	22.52 ~30.32	81.52	Sand	0.6~2.6	Shallow water depth; horizontally dense surface SSC profiles were measured
Field (river confluences)	Exp. 4-1	Confluence of Nakdong and Hwang Rivers	03/30/2021	22.25 ~40.01	81.52, 167.47	Sand	0.6~3.7	Various water depth and sediment conditions; horizontally dense surface SSC profiles were measured; vertical SSC profiles were measured at the near-field of a confluence
	Exp. 4-2		10/07/2021	7.73 ~13.74	24.66, 26.67	Sand	0.5~2.5	Shallow water depth; horizontally dense surface SSC profiles were measured; vertical SSC profiles were measured at the near-field of a confluence
	Exp. 4-3		04/21/2022	5.99 ~24.04	50.36, 39.16	Sand	0.3~5.0	Vertical SSC profiles were measured at the near-field of a confluence

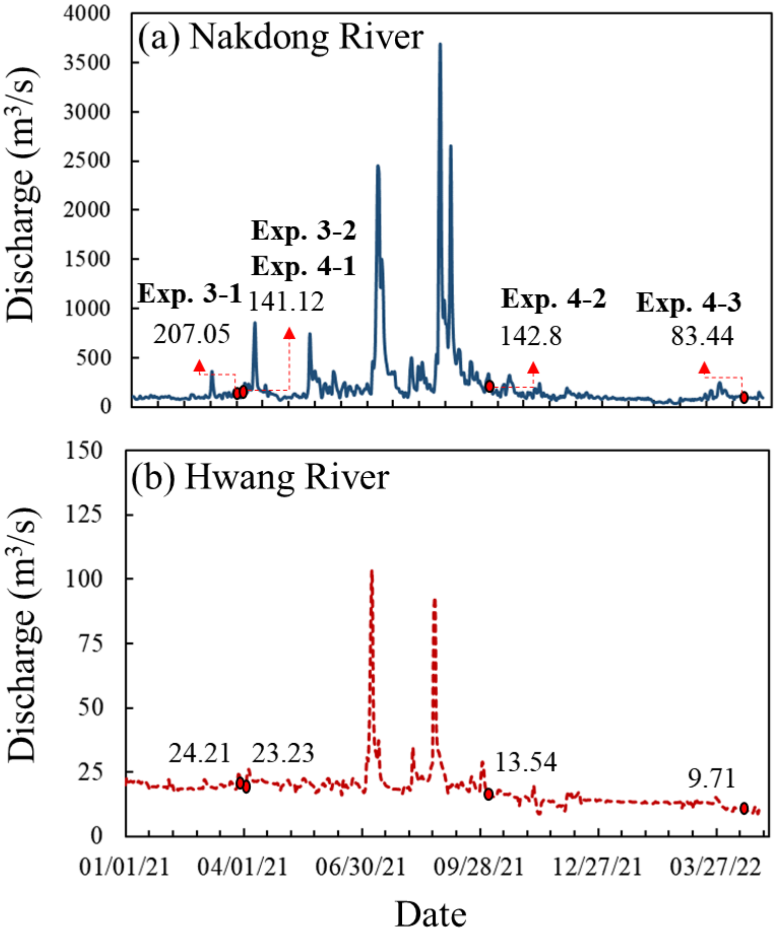

Fig. 3. 18. Flow discharge at Hapcheon-Changnyung dam and Hwang River bridge stations, and date of field surveys.

3.4.2 Hydraulic and sediment data in rivers with simple geometry

Fig. 3.19 shows the RGB images acquired using a drone and the in-situ measured points in Exp. 3-1 and 3-2. The survey area in Exp. 3-1 was located near the left bank. The water depth of in-situ measured points ranged between 0.15~0.6 m, as shown in Fig. 3.20 (a). Owing to the shallow depth, the dune at the riverbed can be seen in the RGB image. Fig. 3.20 (b) shows the SSC_V collected at each in-situ measurement point. The SSC_V was uniformly distributed; however, the SSC_V values at points 5 and 6 were relatively high with high standard deviations. It is inferred that the suspended sediment was resuspended temporarily at the riverbed near these points, not from the upstream. Fig. 3.20 (c) shows the vertical SSC_V profiles at points 1, 3, 7, and 10. The concentration tends to be higher toward the riverbed, except for point 10, as in the Rouse equation (Eq. 2.10).

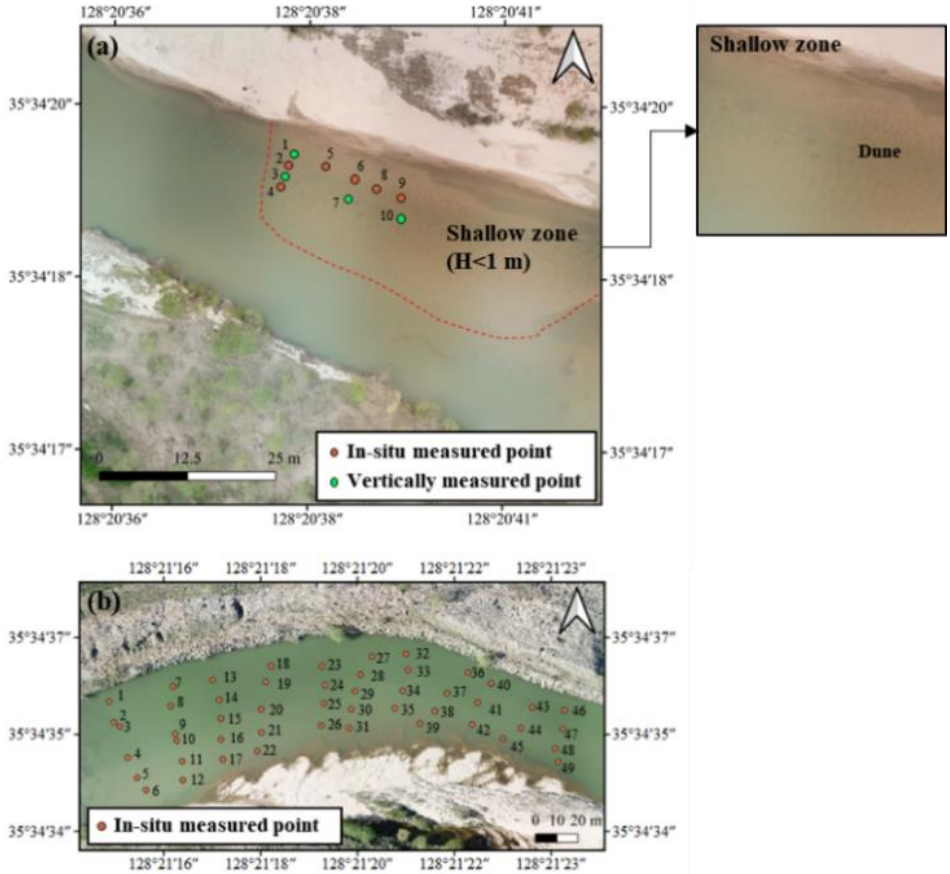

Fig. 3. 19. RGB images of the field campaign area of (a) Exp. 3-1 and (b) 3-2 in Hwang River captured by drone.

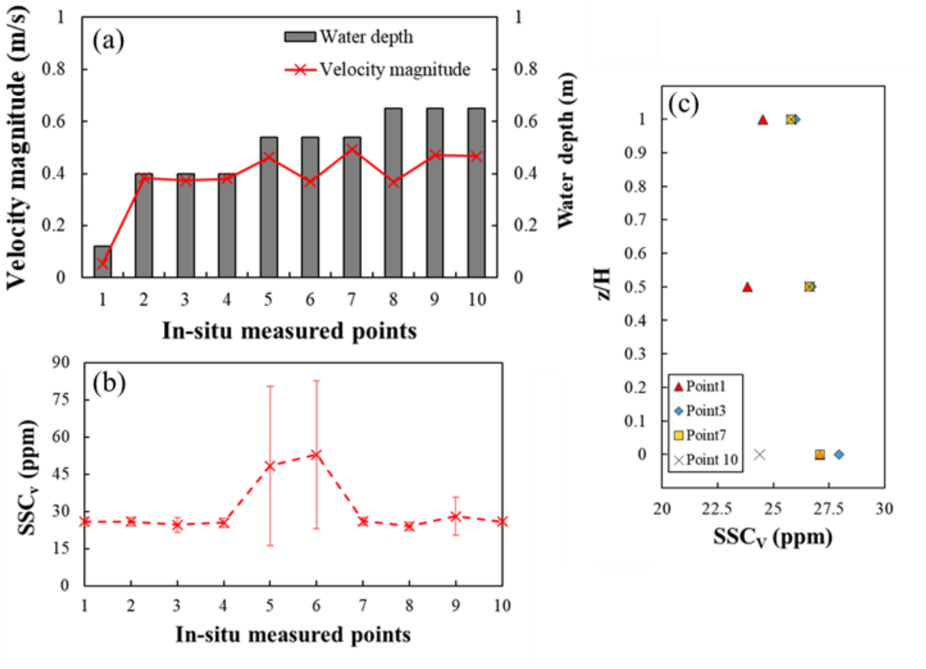

Fig. 3. 20. Measured datasets in Exp 3-1: (a) depth-averaged water depth and velocity; (b) surface SSC_V; (c) vertical SSC_V profile.

The water depth of the Exp. 3-2 ranged from 0.6 ~ 2.6 m (Fig. 3.21 (a)); however, most of the area was deeper than that in the field-scale experiment. The SSC_V was uniformly distributed at around 25 ppm (Fig. 3.21 (b)). Nevertheless, it was difficult to accurately predict SSC_V using hyperspectral images in this area because the water depth of the measurement points varied considerably. This difference in water depth caused a discrepancy in the effect of the bottom reflectance. This depth variation might cause significant uncertainty in remote sensing-based SSC prediction.

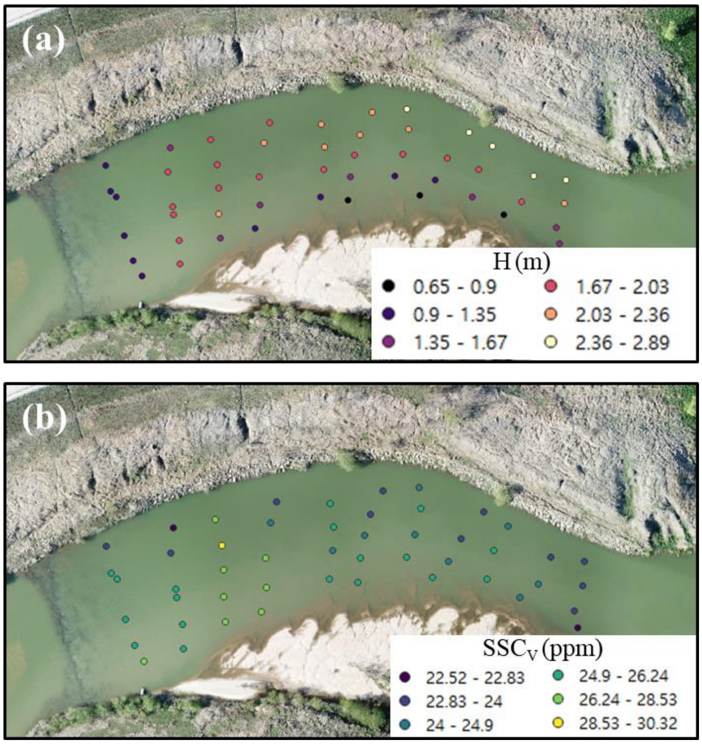

Fig. 3. 21. The measured distribution of (a) *H* and (b) SSC_V in Exp. 3-2.

3.4.3 Hydraulic and sediment data in river confluences

The Hapcheon-Changnyung dam was operated during Exp. 4-2, not during Exps. 4-1 and 4-3. Therefore, the velocity ratio (*UR*) and momentum ratio (*MR*) showed considerable discrepancies, while the discharge ratio (*QR*) of the three surveys was similar in a range between 0.1 to 0.198. This difference induced disparate hydrodynamic conditions in each survey, detailed in Table 3.11. Moreover, according to the flow classification at the river confluences covered in Section 2.2.2.1, Exp. 4-1 was inferred as a wake mode because the *UR* was close to unity. The sandbar at the stagnation zone separated the flow and induced the wake flow. Therefore, an irregular mixing layer can be seen in the case of Exp. 4-1 (Fig. 3.22 (a)). *UR* of Exp. 4-3 was 0.954; therefore, it was also classified as wake mode. However, the mixing layer was less irregular than that in Exp. 4-1 because the sandbar at the stagnation zone was submerged with deep water depth, and the mean velocities of both rivers were low at 0.133 and 0.127. Exp. 3-2 can be classified as KH mode owing to a low *UR* value of 0.36. The mixing layer was not seen in the photograph because of the low watercolor contrast in this survey (Fig. 3.22 (b)).

In terms of river scale, width over depth (*W/H*) ranged around 151, 90, and 167 in each survey. When the suspended sediment properties were compared among all surveys, the SSC_V contrast was strong in Exps. 4-1 and 4-3, which can be seen in the color of both rivers in the RGB image captured by the drone (DJI Mavic Pro2) (Fig. 3.22). There was an apparent contrast in the particle size of suspended sediment between Nakdong and Hwang Rivers. In Exp. 4-1, relatively large particles (d_{50} = 167.47 μm) were transported from the upstream Nakdong River; however, the particle size of Hwang River was relatively fine (d_{50} = 81.52 μm). The d_{50} of both rivers in Exp. 4-3 were different at 50.36 μm and 39.16 μm, respectively. However, in Exp. 4-2, the SSCv and d_{50} were relatively low compared to that in the other surveys. The mean SSCv values of Nakdong and Hwang Rivers were similar in Exp. 4-2; therefore, the color contrast was not captured in Exp. 4-2 (Fig. 3.22 (b)). The particle size was also similar at 24.66 and 26.67 μm in both the rivers.

Table 3. 11 Characteristic parameters of Nakdong and Hwang Rivers during Exps. 4-1 ~ 4-3.

	Exp. 4-1 (03/30/2021)		**Exp. 4-2 (10/06/2021)**		**Exp. 4-3 (04/21/2022)**	
Characteristic parameters	**Nakdong River**	**Hwang River**	**Nakdong River**	**Hwang River**	**Nakdong River**	**Hwang River**
Discharge, Q (m^3/s)	141.1	23.23	142.8	13.54	102.5	20.32
Mean velocity, U (m/s)	0.219	0.189	0.620	0.22	0.133	0.127
Width, W (m)	324	64.7	144	82.0	358	80.0
Mean depth, H (m)	2.13	1.9	1.6	0.75	2.2	2.0
W/H	151.88	34.05	90	109.33	166.65	40
Water temperature (℃)	14.9	13	24.17	22	16.71	16.73
Density, ρ (kg/m^3)	999.21	999.48	997.31	997.78	998.92	998.91
SSC_V (ppm)	37.36	26.34	9.14	9.07	20.69	15.3
d_{50} (µm)	167.47	81.52	24.66	26.67	50.36	39.16
Densiometric Froude number, Fr_d	6.67	-	13.37	-	31.66	-
Turbidity (NTU)	15.5	15.75	2.8	5.2	4.98	3.96
Chl-a (RFU)	2.49	1.12	2.44	4.18	1.60	1.54
Cyanobacteria cell count (cells/mL)	0	-	653	-	0	-
pH	8.30	7.44	7.3	8.0	8.81	8.80
Relative density difference, $\Delta\rho^*$	0.0002632		0.00047		0.0000068	
Confluence angle (°)	44.1		47		44.3	
Discharge ratio, QR	0.164		0.10		0.198	
Mean flow velocity ratio, UR	0.864		0.36		0.954	
Flow momentum ratio, MR	0.142		0.03		0.189	

(a) Exp. 4-1 (03/30/2021) **(b) Exp. 4-2 (10/06/2021)** **(c) Exp. 4-3 (04/21/2022)**

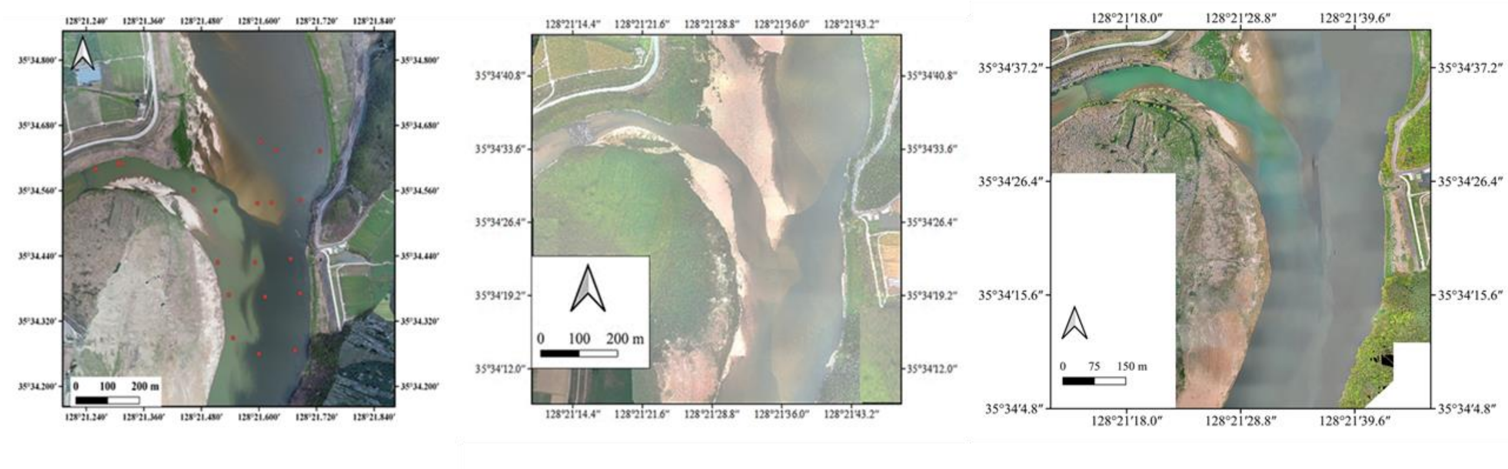

Fig. 3. 22 RGB images of the near-field of confluence between Nakdong and Hwang Rivers captured by drone in Exp. 4-1~4-3.

The density difference between the two rivers in the river confluence could be a critical factor for hydrodynamic conditions and mixing states because it can distort the interface between waters from the main river and tributary river (Gualtieri et al., 2019; Horna-Munoz et al., 2020; van Rooijen et al., 2020). In this study, water density was calculated from the measured water temperature and SSC. Eq. 3.3, proposed by Ford and Johnson (1983), was used to account for the effect of suspended sediment on water density.

$$\Delta\rho_{ssc} = SSC\left(1-\frac{1}{SG}\right)10^{-3} \tag{3.3}$$

where *SG* is the specific gravity of suspended sediment, and it was assumed as the standard value of quartz sand, which is 2.65. Based on the calculated water density, the relative density difference ($\Delta\rho^*$) was calculated by dividing the density difference between Nakdong and Hwang Rivers by the density of Nakdong River. The densiometric Froude number (Fr_d) was calculated using the relative density difference to investigate the contribution of inertial and buoyancy forces as follows:

$$Fr_d = U / (\Delta\rho^* gH)^{1/2} \tag{3.4}$$

where g denotes gravitational acceleration. $\Delta\rho^*$ is seasonally varied, ranging from O(10^{-5}) in winter to O(10^{-3}) in summer (Gualtieri et al., 2019, 2018). The densiometric Froude number represents that the inertial forces dominate when it is over-unity ($Fr_d \gg 1$) (Gualtieri et al., 2019; Horna-Munoz et al., 2020). Therefore, according to these criteria, the density contrast was relatively weak in all surveys.

The complex hydrodynamic conditions, including high turbulence levels and large-scale coherent structures from confluent flows (i.e., wake or Kelvin Helmholtz instability), substantially contribute to the transverse mixing in a river confluence (Biron et al., 2019; Constantinescu et al., 2016). Therefore, the flow characteristics were investigated using measured velocity profiles, along with the results of mixing analysis from CMR-OV, to understand the mixing pattern.

During all the surveys, the velocity fields and bathymetry profiles were measured at cross-sections using ADCP with the moving boat method, as detailed in Kwak et al. (2020). The VMT software was used to analyze and visualize this ADCP data (Parsons et al., 2013). The secondary flow vectors were calculated using the Rozovskii decomposition, which rotates individual verticals rather than the whole section (Rozovskii, 1957). From this decomposition, the primary velocity direction for each point can be precisely obtained as the depth-integrated flow vector. Accordingly, the secondary flows were efficiently calculated using the differences in depth-averaged vectors (Szupiany et al., 2009). The cross-sectional component of secondary flow was calculated in detail based on the divergence of the primary velocity vectors without distorting.

The Exps. 4-1 and 4-3 showed strong contrast of SSC and particle size of suspended sediment with different hydrodynamic conditions and mixing layer distribution. The vertical distribution of suspended sediment and flow fields in the near-field of the confluence were analyzed in detail. In Exp. 4-1, velocity fields and bathymetry profiles were measured and analyzed at eleven cross-sections (Fig. 3.23). Before confluence, the bathymetry was considerably distorted due to the sandbar near the stagnation zone in NR1 and 2. Accordingly, the main flow velocity developed near the left bank. In NR3, the two strong flows from Nakdong and Hwang Rivers merged behind the stagnation zone (sandbar), resulting in a velocity deficit owing to the wake effect. Therefore, the low-velocity zone was developed by merging both boundary layers of both flows. In NR4, a mixing interface was apparently formed between the two flows; this resulted in the development of two relatively strong helical motions in opposite directions between this interface. Afterward, the two streams combined strongly to form a dynamic mixing interface in NR 5 and 6. In NR 7, these secondary currents were dissipated gradually. The discordance in the right bank, where the flow injected from tributary eroded owing to the helical motion developed upstream. The flow tends to recover further downstream in NR 8 and NR 9.

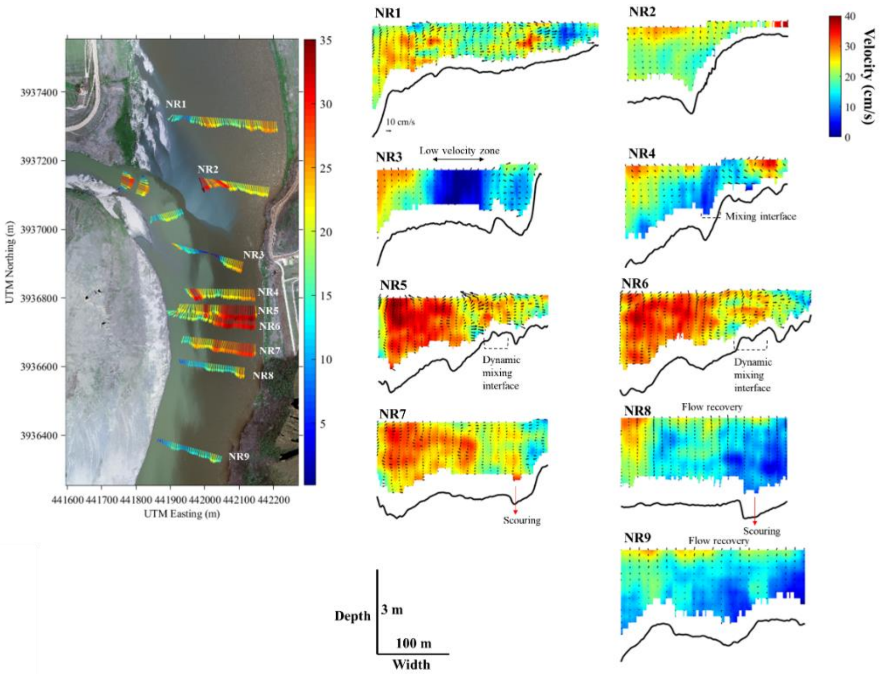

Fig. 3. 23. Flow measurement results at nine cross-sections upstream and downstream of the confluence of Nakdong and Hwnag Rivers in Exp. 4-1 (left bank on the right hand).

NR5 was the section where the flow and transverse mixing changed most abruptly. However, the vertical mixing in this section was weak compared to the transverse mixing, as shown in the vertical profiles of SSC along with the cross-section (Fig. 3.24). The vertical distribution of SSC_V was generally uniform except for the concentration near the river bed, which can be inferred as bed load. In addition, the fraction of fine clay (d < 2 μm) was highest near the right bank, which originated from the Hwang River. This clay was distributed throughout the water depth of the Hwang River with silt (d >20 μm); it was entrained into the Nakdong River after confluence. The waterbody near NR5 from the Nakdong River and Hwanggang River had completely different PSD near the mixing layer as a boundary after confluence. The suspended sediment was poorly mixed in this section; the heterogeneous PSDs near the mixing layer increased the spectral variability.

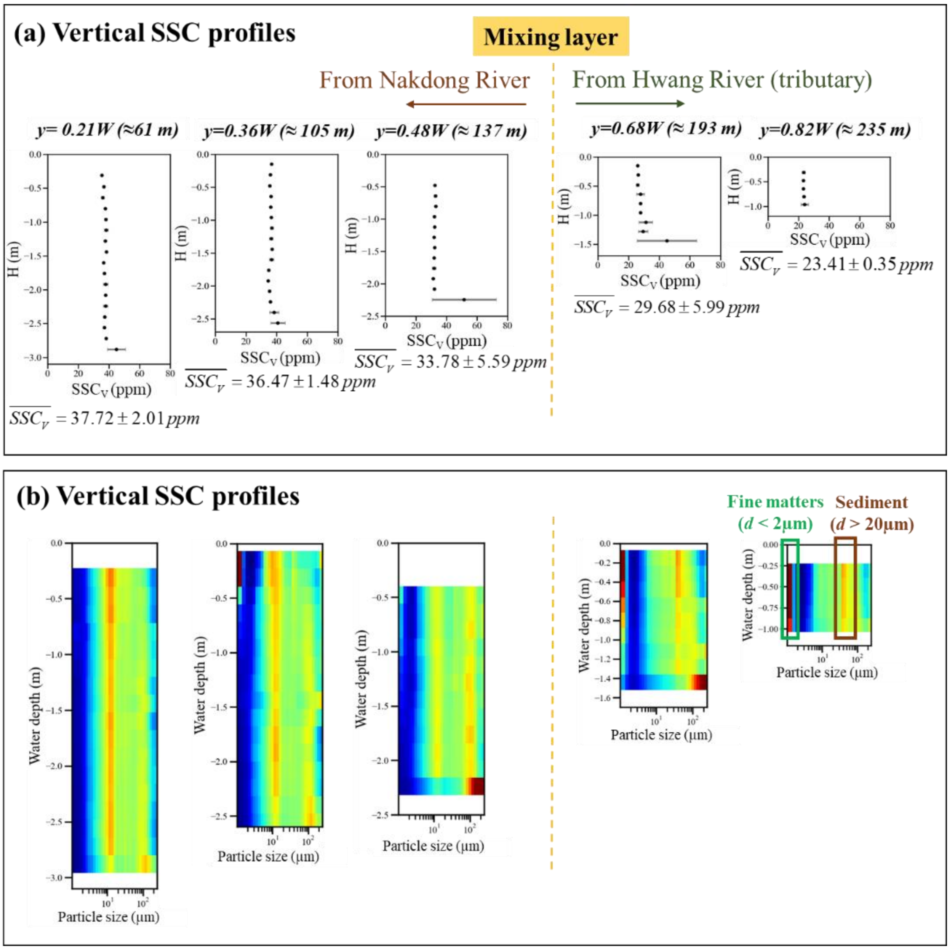

Fig. 3. 24. Vertical (a) SSC_V and (b) PSD profiles measured using LISST at NR5 in Exp. 4-1; *y* denotes the distance from the left bank.

In Exp. 4-3, the discharge was similar to that in Exp. 4-3; however, the velocity was slow, and the secondary flow was weaker (Fig. 3.25). Before confluence, the bathymetry was less distorted due to the sandbar near the stagnation zone in NR1 and 2. The sand bar area at the stagnation zone, which was very shallow in Exp. 4-1, was completely submerged in Exp. 4-3. The water depth of this area was approximately 2 m, as shown in the cross-sectional velocity distribution in NR 1 (Fig. 3.25). Afterward, the velocity deficit was generated when the two flows with similar velocity magnitude merged after the confluence (see NR 2 in Fig. 3.25). Nevertheless, the velocity deficit rapidly recovered at NR 3 (270 m downstream from the confluence point) due to the submerged sandbar and low velocity magnitude. The mixing interface was developed as shown in the cross-sectional velocity field of NR 3, but it was dissipated at NR 4 (downstream 450 m from the confluence point). Therefore, the wake in Exp. 4-3 developed weakly and then dissipated rapidly compared to that in Exp. 4-1; the two water bodies of different colors mixed rapidly, as shown in the photograph of Exp. 4-3 (Fig. 3.22 (c)).

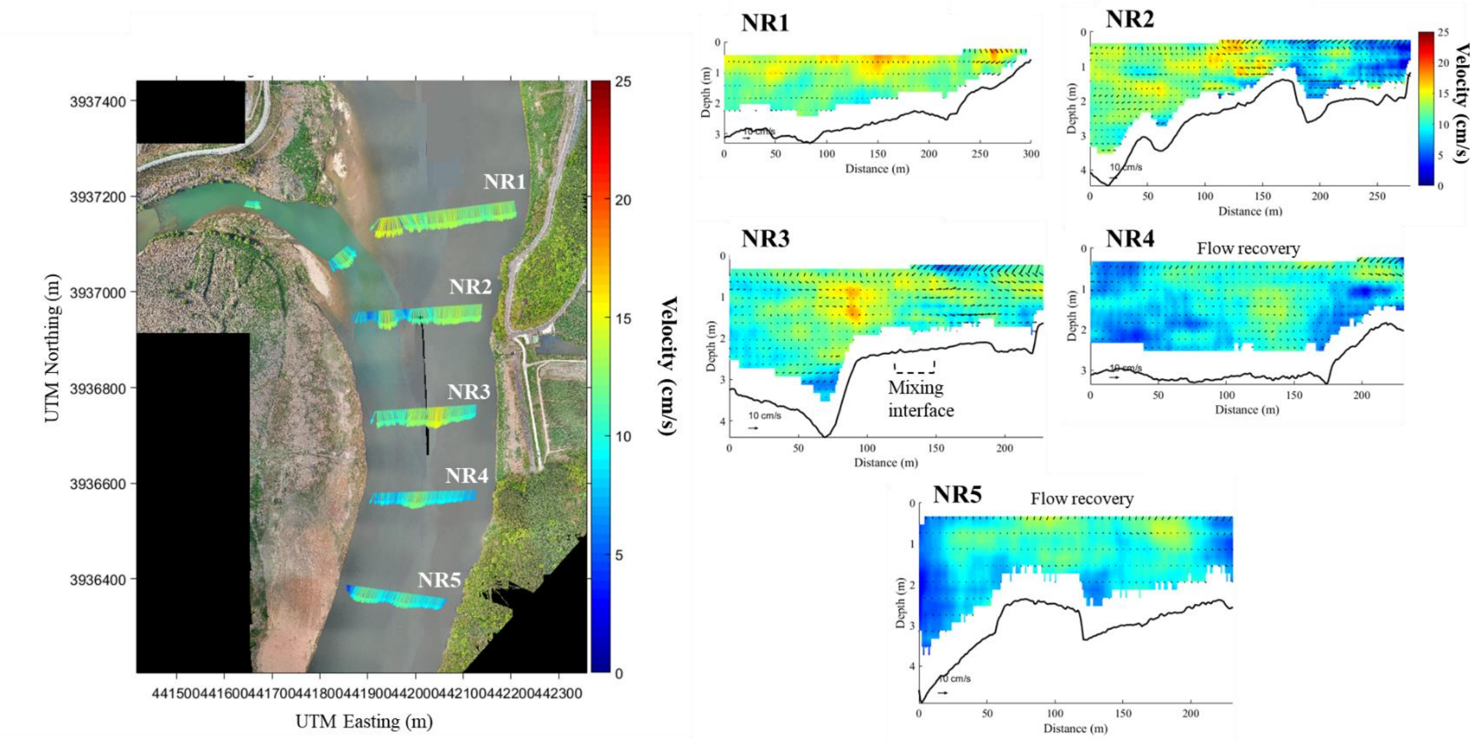

Fig. 3. 25. Flow measurement results at nine cross-sections upstream and downstream of the confluence of Nakdong and Hwnag Rivers in Exp. 4-3 (left bank on the right hand).

NR 3 in Exp. 4-3 was in the same location as NR 5 in Exp. 4-1. The mixing interface and secondary current developed in this section. Therefore, the vertical SSC_V distributions near the mixing layer showed irregular profiles (Fig. 3.26 (a)). At the point where the mixing layer was less affected, it appeared close to the Rouse profiles, in which the concentration increased relatively near the river bed. Especially, the point near the right bank, which was entrained from the Hwang River, showed a substantial concentration difference between the water surface and the riverbed. It was induced by the discrepancy of PSD near the surface and riverbed (Fig. 3.26 (b)). The suspended fine matter ($d < 2$ μm) was distributed near the surface only near the left bank. This fine matter originated from the Hwang River. It is inferred that these particles floated on the surface, imparting the green color to the water body in the RGB image (Fig. 3.22 (c)) despite the low Chl-a and the Cyanobacteria cell count. This variability in suspended matters with sediment and various vertical SSC_V profiles substantially increased the spectral variability.

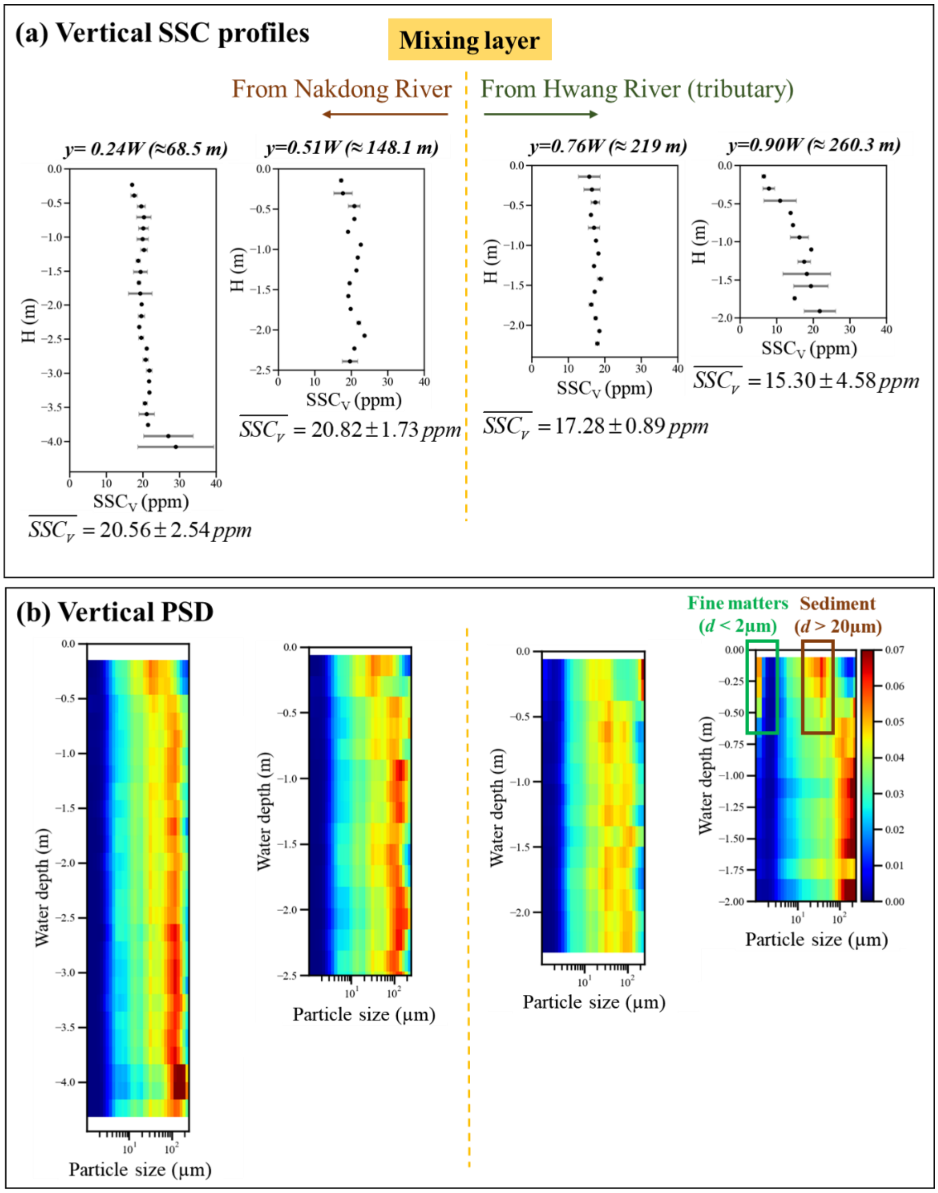

Fig. 3. 26. Vertical (a) SSC_V and (b) PSD profiles measured using LISST at NR5 in Exp. 4-3; y denotes the distance from the left bank.

3.5 Analysis of hyperspectral data of suspended sediment

In this subchapter, hyperspectral datasets of suspended sediment from lab-scale (Exp. 1) and field-scale (Exps. 2-1 and 2-2) experiments were used to investigate the confounding factors of spectral variability. As summarized in Table 3.12, the hyperspectral data and corresponding SSC data were collected under the various bottom, sediment, and stream conditions. These datasets were compared according to each experimental condition in the following subchapters. Additionally, the datasets from Exps. 2-1 and 2-2 were used for model development in Chapter 4.

Table 3. 12. Summary of hyperspectral datasets of suspended sediment collected in lab-scale and field-scale experiments.

Type	Exp.	Experimental condition	Case (sediment type)	No. of data
Lab-scale	Exp. 1	Non-bottom reflection; completely mixed state	1-1 (QS1)	18
			1-2 (QS2)	18
			1-3 (YL1)	18
			1-4 (YL2)	18
Field-scale	Exp. 2-1	Constant bottom reflection (sand); straight channel	2-1-1 (QS1)	234
			2-1-2 (YL1)	228
			2-1-3 (Mix.)	188
	Exp. 2-2	Different bottom reflections (vegetation and sand); meandering channel	2-2-1 (QS1)	356
			2-2-2 (YL1)	309
			2-2-3 (Mix.)	278
			2-2-4 (QS1)	228
			2-2-5 (YL1)	437
			2-2-6 (YL2)	397
			2-2-7 (Mix.)	420

3.5.1 Hyperspectral data of laboratory experiment

According to increased SSC_W, the intrinsic optical properties were measured under completely mixed and non-bottom reflection conditions in the laboratory experiment (Exp. 1). Scattered signals from the suspended sediment showed different reflectance spectra according to sediment type, and the reflectance values were much lower than that of yellow loess at 400 to 1,000 nm at the same SSC_W range (Fig. 3.27). In addition, when the particle size was fine, both quartz sand and yellow loess showed high reflectance values while maintaining the spectral shape. This result implies that reflectance at the same SSC can differ according to the PSD. In general, the intensity of the back-scattering signal increased depending on the increased size of a single particle, as reported in Koestner et al. (2020). However, the increased number of fine sediment particles at the same concentration reduced the effective volume through which light can transmit in terms of decreased voids between sediment particles.

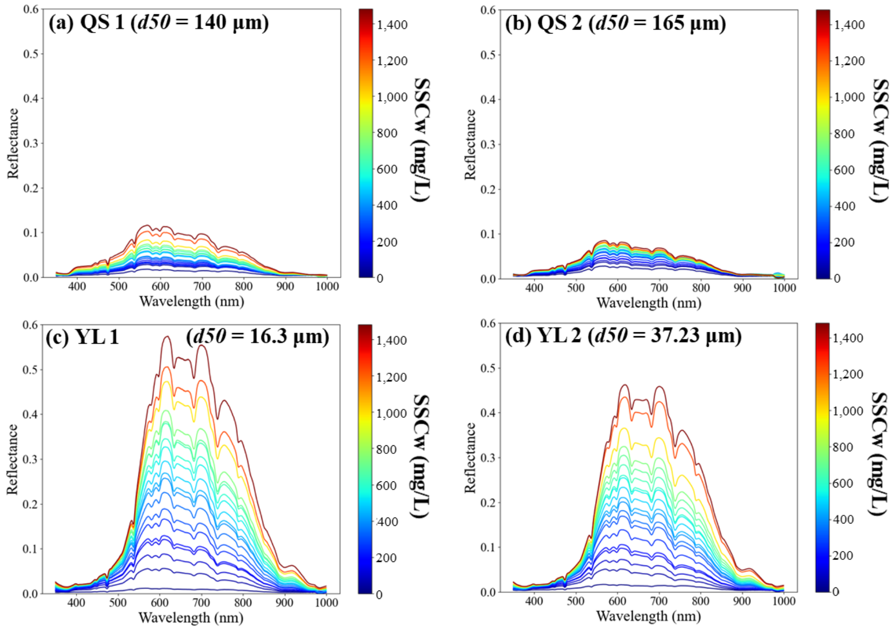

Fig. 3. 27. Hyperspectral spectrum according to SSC_W under non-bottom reflectance condition (Exp. 1): (a) QS 1, (b)QS 2, (c) YL 1, and (d) YL 2.

To estimate the effective wavelength of each sediment, linear OBRA was employed (Fig. 3.28). The range over 0.5 of R^2 differed according to sediment type irrespective of particle size. The effective wavelength of quartz sand was included in NIR (770–1,000 nm); the yellow loess was highly proportional to red-edge (600–700 nm). This result is in accordance with the difference in visibility between quartz sand and yellow loess. In addition, each sediment had strong linearity resulting in 0.88 and 0.98 R^2 with a single band ratio. This result demonstrates that if there is no bottom reflection and the suspended sediment is well mixed, the effective wavelengths of each sediment were precisely extracted. However, in rivers, the various sediments are mixed. The bottom reflectance critically affects the hyperspectral spectrum when the water depth is less than 2 m, as described in Chapter 2.1. Therefore, spectral variability occurs from sediment mixing and bottom type difference. The confounding factors of spectral variability were investigated in detail by comparing results from the laboratory experiment (Exp. 1) and field-scale experiments (Exps. 2-1 and 2-2).

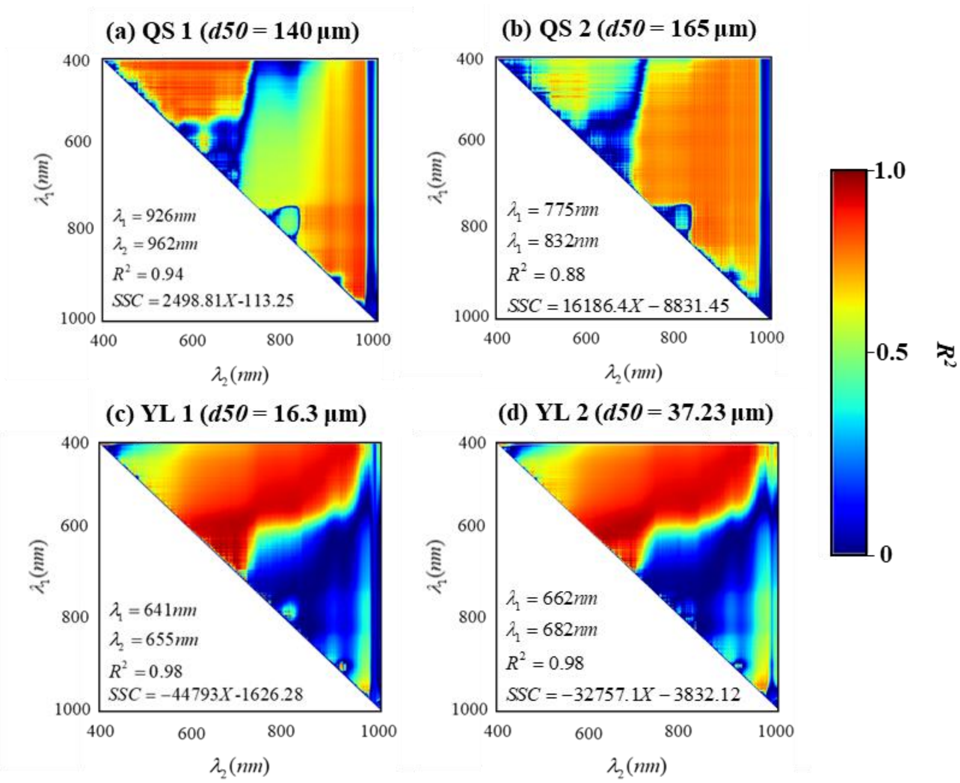

Fig. 3. 28. R^2 distribution of OBRA with a single-band ratio under non-bottom reflectance condition: (a) QS 1, (b)QS 2, (c) YL 1, and (d) YL 2.

3.5.2 Hyperspectral data of field-scale experiments

3.5.2.1 Effect of bottom reflectance

The effect of bottom reflectance was investigated using the results of field-scale experiments (Exp. 2-1 and 2-2). Fig. 3.29 shows the spectral reflectance under the constant bottom condition along with the entire measured wavelength range (400–1,000 nm) according to SSC_V variation for each case in Exp. 2-1. In the spectral profiles of all sediment types, the highest reflectance values appeared near red wavelengths (~650 nm). In addition, apparent variation due to an increase in SSC_V was observed near the red (650 nm) and NIR (750 nm) wavelengths; these were in line with the results from the laboratory experiment and these wavelengths were identified as sensitive ranges in earlier studies (Doxaran et al., 2003; Gebreslassie et al., 2020; Kabir and Ahmari, 2020). The difference in reflectance values occurred over 550 nm according to sediment type. However, contrary to the laboratory experiment (Exp. 1) result, the hyperspectral spectrum of all sediment types had similar tendencies under a constant bottom reflectance in Exp. 2-1. This result implied that the bottom reflectance makes the overall shape similar in the shallow waters even when the concentration is high. In particular, the reflectance values were substantially increased from bottom reflectance in the case of quartz sand compared to that in yellow loess. It can be explained by the particle size of quartz sand, which was 4 to 10 times larger than that of loess; therefore, the transmission of light was higher in quartz sand.

The result of OBRA in Exp. 2-1 shows the critical effect of bottom reflectance on the signals of suspended sediment. Fig. 3.30 (a) shows that the wavelengths of the selected optimal bands for quartz sand were near the red wavelength range (582.93 and 663.02 nm). The yellow loess was regressed by the red-edge and NIR bands (703.06 and 883.25 nm) with the highest value of R^2, as shown in Fig. 3.30 (b). Fig. 3.30 (c) shows that the wavelengths of the selected optimal bands for the mixture ranged between red and red-edge (747.11 and 703.06 nm). These selected spectral bands were one of the sensitive bands for SSC under non-bottom reflectance (Fig. 3.28); however, the wavelengths of optimal bands changed under the constant bottom condition.

In terms of accuracy, OBRA showed an R^2 of over 0.80 for yellow loess and mixture; however, it showed relatively poor performance for quartz sand, with an R^2 of 0.57 (Fig. 3.30). These results indicate that the linear OBRA is limited in its ability to retrieve the characteristics of suspended sediment with a high settling property and low visibility, like quartz sand (Fig. 3.8 (d)) (Kwon et al., 2022b). The correlation between the hyperspectral reflectance and the SSC is substantially reduced when the sediment and bottom properties are complicated.

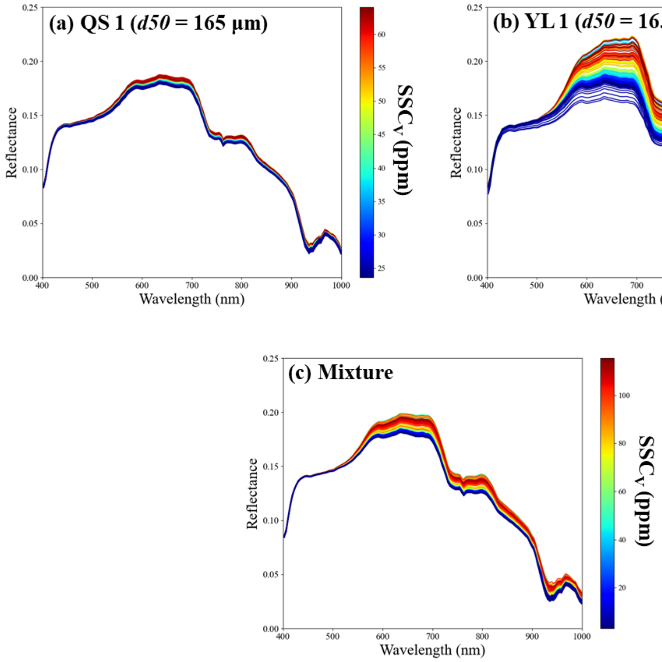

Fig. 3. 29. Acquired hyperspectral spectrum at the corresponding point of SSC_V in-situ measurement: (a) Quartz sand, (b) Yellow loess, (c) Mixture.

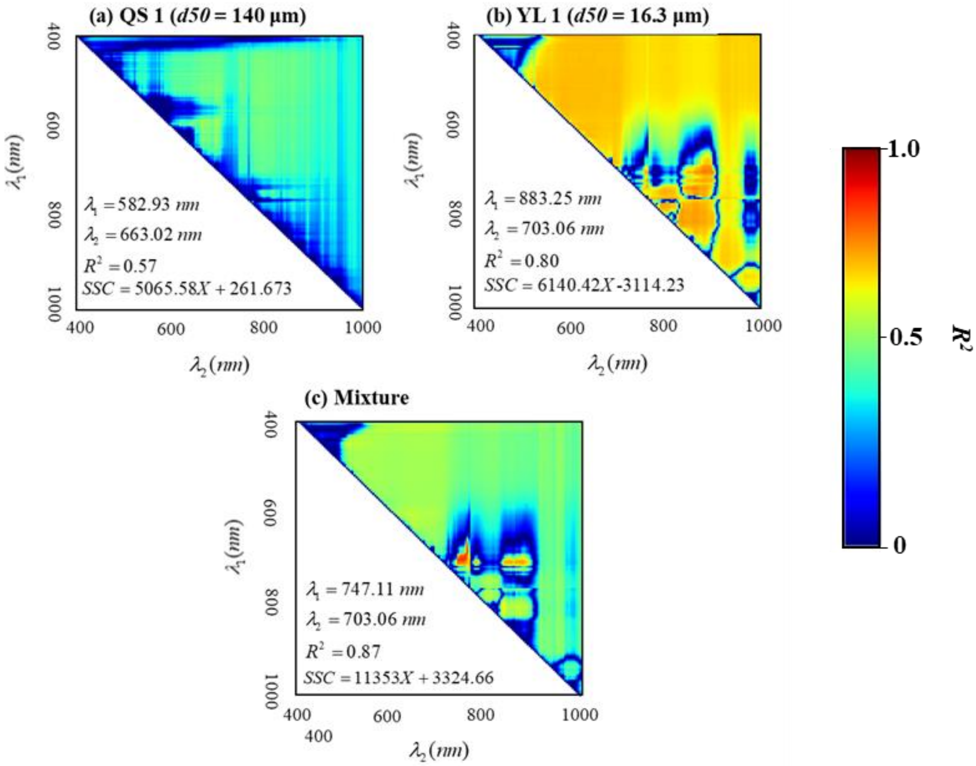

Fig. 3. 30. Results of OBRA with a single-band ratio under a constant bottom reflectance condition: (a) QS 1, (b) YL 1, and (c) mixture.

In this study, to investigate the dominance between the suspended sediment signal and the bottom reflectance to the spectral variability, experiments were conducted under the background water without sediment injection. Fig. 3.31 presents the hyperspectral spectrum of Exp. 2-2 under background water without sediment injection for different bottom conditions in each section. The effect of velocity (secondary currents) and bottom type on the hyperspectral spectrum is shown in this figure. All hyperspectral spectra had large reflectance values within the NIR range (800–1,000 nm), while deep water conditions generally showed low reflectance values within this range (Doxaran et al., 2009; Vanhellemont and Ruddick, 2015). Therefore, the bottom reflectance highly influenced the hyperspectral spectrum due to shallow depth. Furthermore, compared to that in the sand bottom, the noises and variation in the NIR range were substantially high when the bottom was covered by vegetation (Fig. 3.31 (a)). This high variation in the NIR range was due to the spectral characteristics of green grass, which has the first peak near the green band (500 nm) and high reflectance over NIR (800 nm) (Adjorlolo et al., 2012; He and Mui, 2010). The vegetated bottom showed a higher bottom reflectance than the sand bottom, in line with Albert and Mobley (2003). Accordingly, the bright bottom condition induced a high variation of the hyperspectral spectrum because the high bottom albedo increases L_b, and the noises were generated by the movement of vegetation with the flow. These spectral characteristics of the vegetation bottom in shallow water induced the optically complex condition.

The effect of secondary currents on the hyperspectral spectrum was insignificant compared with the bottom effect. As shown in Figs. 3.31 (a) and (b), in the other sections with the same bottom type, the intensity of the secondary flow was different; however, there was no significant changes in the hyperspectral spectrum. The NIR region is sensitive to the vegetation moving with the flow (Fig. 3.31 (a)). Therefore, the flow indirectly affects the spectral characteristics if there is no wake on the surface, which induces the surface reflection.

Fig. 3.32 presents the hyperspectral spectrum of Exp. 2-2 under the different bottom conditions at Sec. C2 according to SSCv values. The hyperspectral spectrum showed different profiles according to the bottom type and mineral content of the sediment. In terms of bottom type, Figs. 3.32 (a, c, and e) were hyperspectral spectrums of Sec. C2 with the arid sand bottom in Exp. 2-2-1~2-2-3, while Figs. 3.32 (b, d, and f) showed the hyperspectral spectrums of Section 2 with covered vegetation in Case. 2-2-4~2-2-7. Compared to that in the background water without sediment injection, all spectra increased according to SSCv values irrespective of bottom type. The overall value of the spectrum tended to increase as the SSCv increased. However, the noises and variation in the NIR range were still significantly high when the SSCv increased in Sec. C2 with the vegetated bottom. Therefore, the bottom reflectance influenced the hyperspectral spectrum when the bottom was vegetated despite high SSCv.

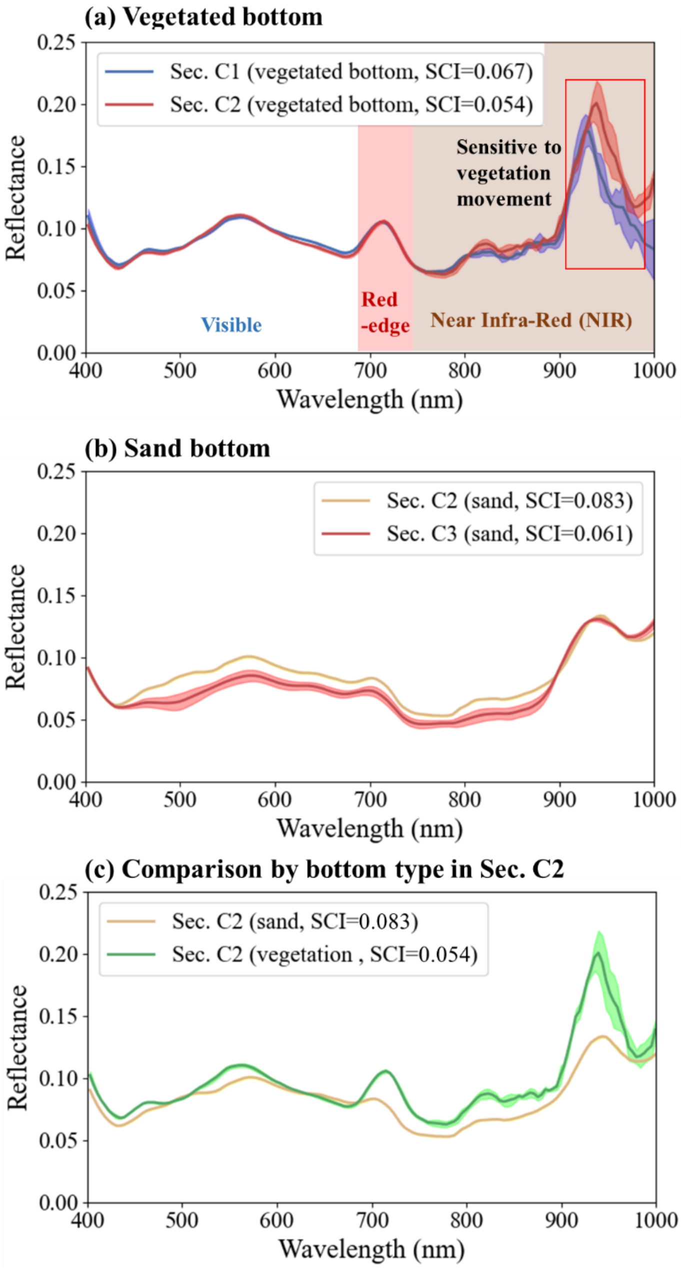

Fig. 3. 31. Hyperspectral spectrum collected in background water without sediment injection at each section of Exp. 2-2: (a) vegetation bottom, (b) sand bottom. (c) comparison by bottom type in Sec. C2; shaded area indicates the standard deviation of the time-averaged spectrum.

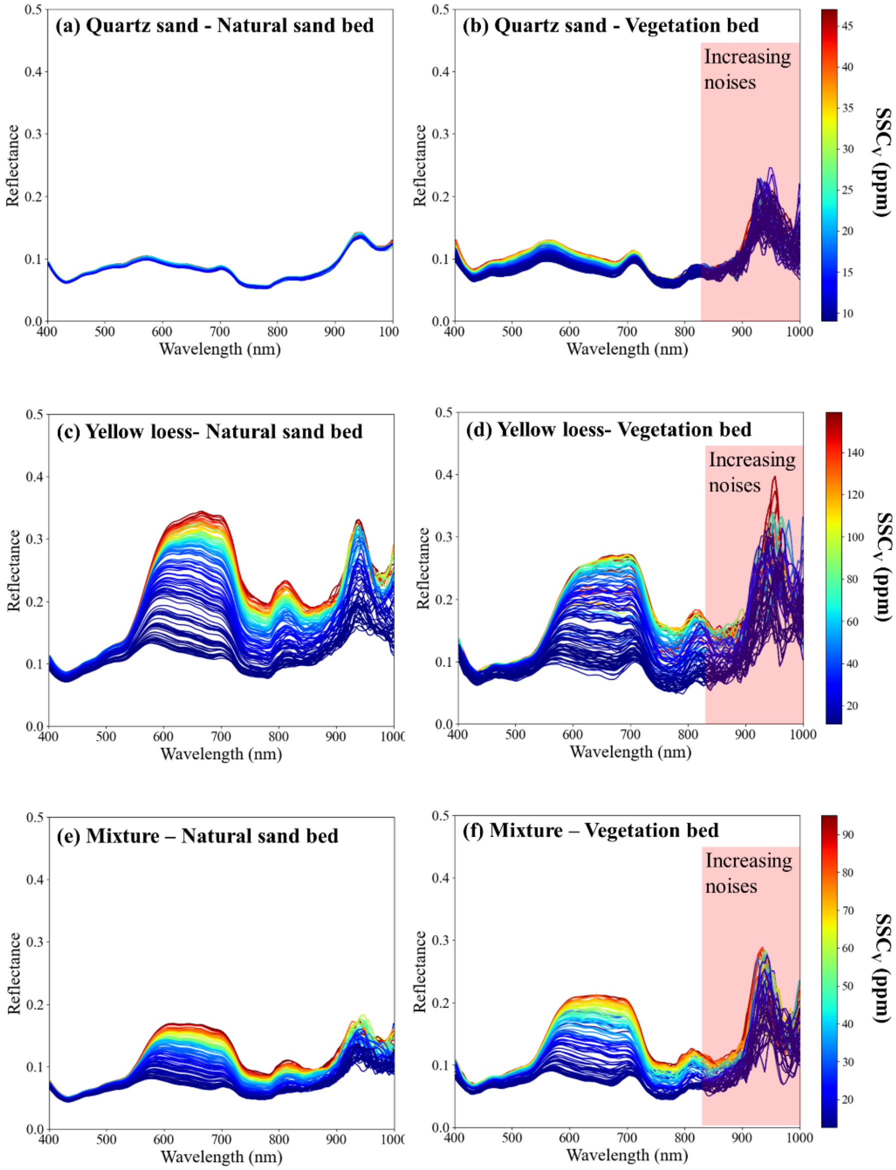

Fig. 3. 32. Hyperspectral spectrum according to SSCv at Sec. C2 of Exp. 2-2 with natural sand (a, c, and e) and vegetated bottom (b, d, and f).

In all sediment types, reflectance increased with increasing SSC_V values, especially in the range of 600–750 nm. Based on sediment type, the reflectance values showed a discrepancy over 550 nm. The quartz sand showed a negligible effect of increasing SSC_V on spectrum variation than the yellow loess, due to its mineral characteristics and high transmissivity from large particle size. For the same reason, the quartz sand was more affected by the bottom reflectance than the yellow loess as the bottom irradiance reflectance was more transmitted when the quartz sand was suspended in the water column.

3.5.2.2 Principal component analysis of the effect of suspended sediment properties

In order to evaluate the effect of certain properties (sediment type, PSD, sampling depth, and temperature) of suspended sediment on the hyperspectral spectrum, principal component analysis (PCA) was applied to the acquired hyperspectral images. PCA reduced the hyperspectral images with 150 spectral bands into a few orthogonally transformed variables, which retained the maximum variation of the original data. This dimensional reduction technique has been widely used for feature extraction of hyperspectral images in various fields (Kim et al., 2020; Qin et al., 2013; Sváb et al., 2005; Whetton et al., 2017). In this study, the condensed spectral characteristics of hyperspectral images acquired by PCA and the properties of suspended sediment were compared to identify the dominant properties. Each point in Fig. 3.33 represents a hyperspectral spectrum corresponding to the in-situ measured SSC_V, projected into the principal component (PC) 1 and PC 2. Defined by the eigenvectors of the covariance matrix, these two components showed that 80% of PC 1 and 16% of PC 2 of variance were retained. In the space defined by PC 1 and PC 2, there was little difference in the reflectance characteristics of each case in background water. However, as PC 1 increased, each case changed in a different direction, and the cases were clearly distinguished from each other. PC 1 showed a strong correlation with SSC_V, as noted in Table 3.12, which indicates that the spectral characteristics of the three types of sediments differed. Moreover, the lower the settling velocity and visibility, the more parallel the spectrum data was with the PC 1 axis. Therefore, if PC 2 is less affected, the spectral characteristics are more related to SSC_V.

PCA was applied to spatial hyperspectral images acquired by the drone. Fig. 3.31 shows the original RGB, PC 1, and PC 2 images. PC 1 successfully captured the distribution of suspended sediment in all cases; both the yellow loess and mixture, which had high visibility even in the RGB image and quartz sand, which had low visibility. The correlation between PC 1, which condenses the optical characteristics of the hyperspectral spectrum, and the properties of the suspended sediment was calculated to elucidate the relationship between the physical and spectral properties. SSC_V showed a high correlation with PC 1 (Table 3.13). The fine sand and *d50* showed a positive correlation with PC 1 in the aspect of PSD. These correlations indicate that the concentration and particle size of suspended sediment affected the L_c reaching the hyperspectral sensor. Therefore, reflectance at the same SSC_V can differ according to the PSD. Moreover, the reflectance values of quartz were lower than that of yellow loess, due to its high settling velocity and the invisibility of the mineral.

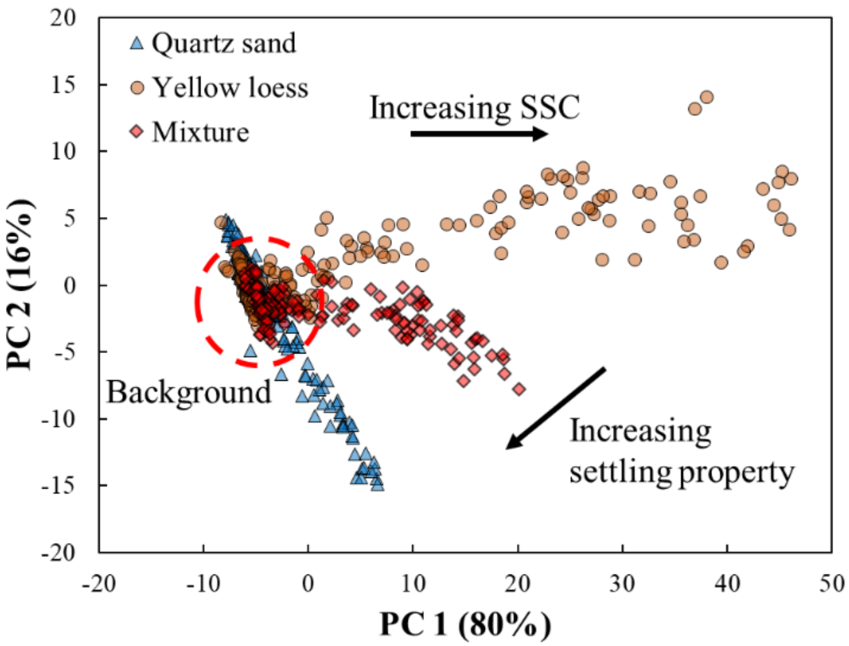

Fig. 3. 33. Hyperspectral spectrum under constant bottom condition (Exp. 2-1) in the space of the principal component (PC) 1 and 2.

Table 3. 13. Correlation between principal component 1 (PC 1) and sediment properties for Exp. 2-1

Sediment type	Sampling depth	Correlation coefficient					
		SSC_V	**Clay**	**Silt**	**Fine sand**	***d_{50}***	**Temp.**
Quartz sand (Case 2-1-1)	**0.75H**	**0.796**	-0.445	-0.441	**0.445**	**0.441**	0.298
	0.25H	**0.678**	-0.329	-0.352	**0.351**	**0.365**	-0.602
Yellow loess (Case 2-1-2)	**0.75H**	**0.844**	-0.359	-0.221	**0.361**	**0.365**	-0.395
	0.25H	**0.755**	-0.214	0.019	**0.277**	**0.255**	-0.171
Mixture (Case 2-1-3)	**0.75H**	**0.784**	-0.321	-0.382	**0.375**	**0.349**	-0.040
	0.25H	**0.698**	-0.109	-0.407	**0.291**	**0.194**	-0.044

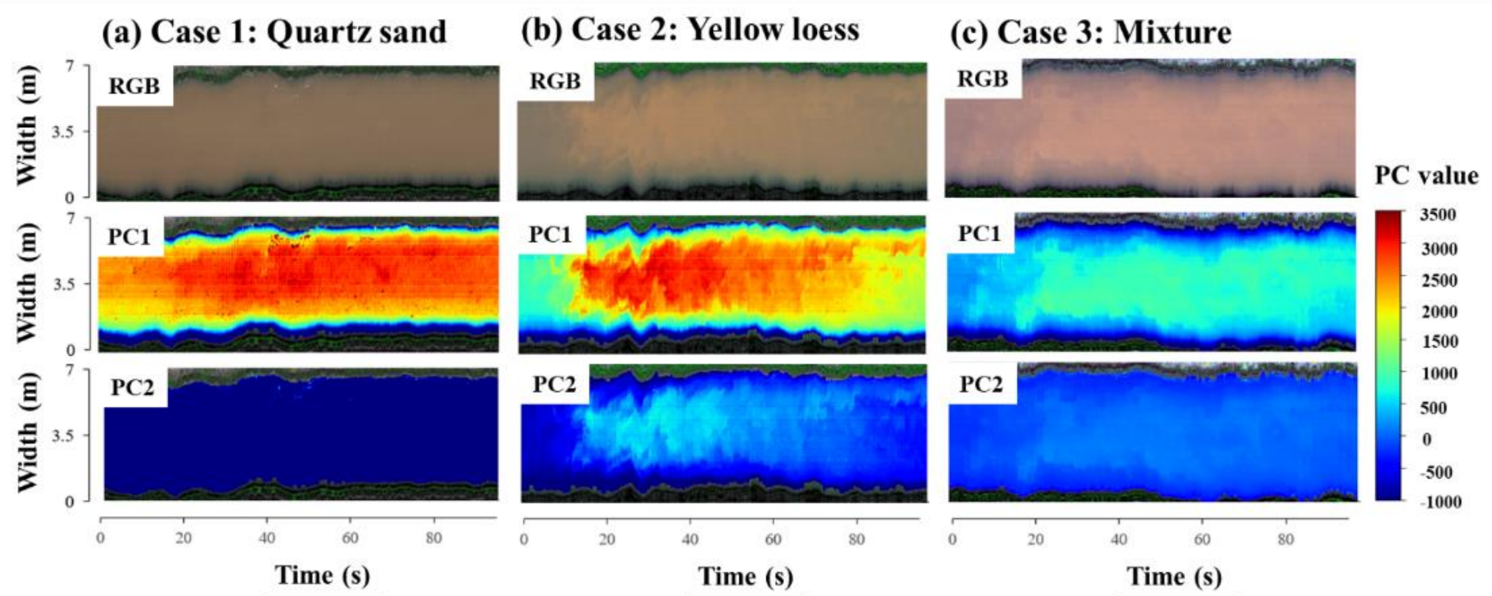

Fig. 3. 34. The comparison of RGB image, PC 1, and PC 2: (a) Case 2-1-1 (Quartz sand), (b) Case 2-1-2 (Yellow loess), (c) Case 2-1-3 (Quartz sand+ Yellow loess).

The PCA results of Exp. 2-2 demonstrated that PC 1 with eigenvalues accounted for 85% of the total variance in the whole dataset, implying that one loading can retain almost all portions of the spectral variance. Each point in Fig. 3.35 describes condensed hyperspectral band values corresponding to the SSC_V of each sediment type, projected into dimensions of PC 1 and PC 2. The result of Exp. 2-1 was different from that of Exp. 2-1 owing to different conditions of bottom and background water. In Exp. 2-2, quartz sand was linearly depicted, while yellow loess and mixture showed a non-linear behavior. The quartz sand and yellow loess had different spectral characteristics, and the mixture was significantly affected by the yellow loess in terms of shape, although all data were variated to the direction of PC1 irrespective of sediment type. Regarding the variability from the bottom type, the discrepancy in the optical characteristics of the bottom resulted in different spectral profiles. The trend was similar to when the bottom type is vegetation irrespective of sediment type; however, the data were highly scattered in general. This result was attributed to the noisy hyperspectral spectrum, which was induced by the bright bottom albedo of vegetation and the movement of submerged vegetation driven by the flow, as illustrated in Fig. 3.32 (b, d, and f). In addition, the effect of PSD difference was observed in PCA results. The fine yellow loess and coarse yellow loess had different shapes in the space of PCs 1 and 2 (Fig. 3.35 (b)). However, the difference was not as apparent as the sediment type difference and the bottom type difference.

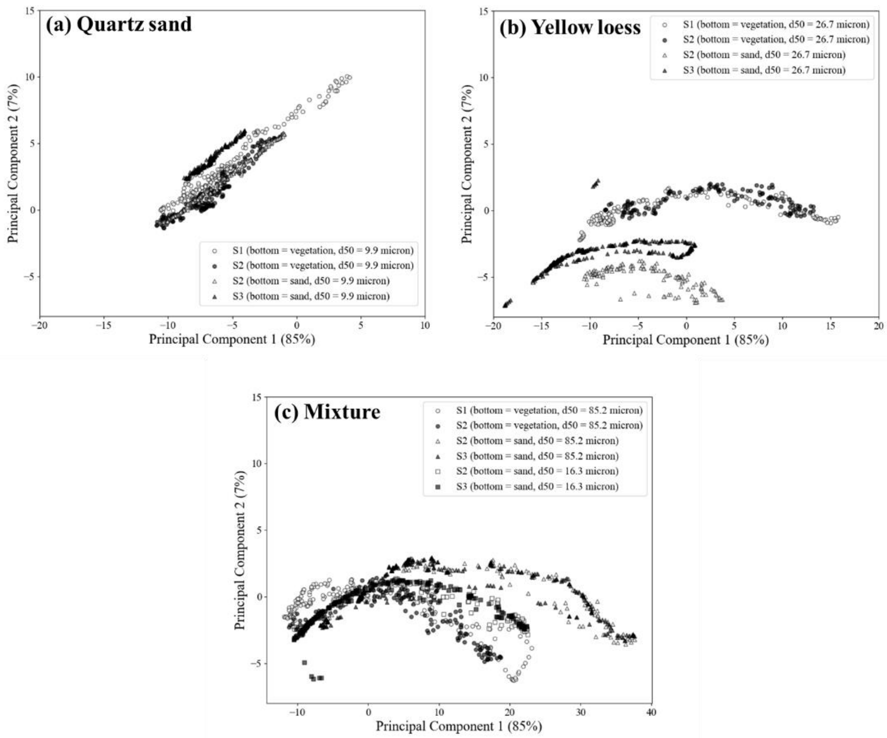

Fig. 3. 35. Hyperspectral spectrum in the space of the PCs 1 and 2 for Exp. 2-2: (a) quartz sand, (b) yellow loess, and (c) mixture.

The relationship between PCs of combined Exp. 2-2 datasets and physical factors appropriately explains the contribution of physical factors to spectral variation. To estimate the correlation of sediment type and bottom type with PCs, sediment types were indexed as 1, 2, and 3, indicating quartz sand, yellow loess, and mixture, respectively, while the presence and absence of vegetation at the bottom were indexed as 0 and 1. Table 3.14 describes the estimated correlation between each PC and physical factors, where the most significant variation condensed in PC1, accounting for 85% variance, is positively correlated with SSC_V and fractions of sand and clay. Among them, the clay fraction showed the highest correlation value at 0.997. Yellow loess with a relatively large proportion of clay and a large variation in SSC_V was closely related to PC1. However, d_{50} showed a fairly high correlation with PC2, explaining the 5% variation, and sediment type represented a considerably negative correlation with PC2. The quartz sand with a relatively large particle size was more affected by PC2 than yellow loess, as indicated in Fig. 3.33 (a). While the sediment properties were explained by PC1 and PC2 with a variance of over 90%, the bottom type is not related to large variance of PCs. The bottom type showed correlations of over 0.5 with PC 4, which accounted for 2% of the variance. Therefore, the spectral variance was mainly affected by the sediment properties, such as SSC_V, d_{50}, particle size distribution, and sediment type.

Table 3. 14. Correlation between PCs and physical variables for Exp. 2-2; the highlighted panels indicate an absolute value of correlation over 0.5.

	Sediment Property						Temp.	Bottom type
	SSC_V	d_{50}	Grain Size			Sediment type		
			Clay	Silt	Sand			
PC 1 (85%)	**0.621**	**-0.572**	**0.977**	0.324	**0.695**	0.077	0.141	-0.075
PC 2 (5.3%)	-0.189	**0.538**	-0.059	-0.453	-0.059	**-0.652**	-0.399	0.146
PC 3 (2.3%)	0.148	0.086	0.018	-0.079	0.176	-0.059	-0.323	0.026
PC 4 (2.0%)	0.274	-0.066	0.005	-0.039	0.240	-0.003	-0.259	**0.572**
PC 5 (1.4 %)	0.150	0.135	0.017	-0.220	0.122	-0.102	0.097	0.194

4. Development of suspended sediment concentration estimator using UAV-based hyperspectral imagery

4.1 Outline of Cluster-based Machine learning Regression with Optical Variability (CMR-OV)

In this chapter, a clustered machine learning regression for optical variability (CMR-OV) combining hyperspectral clustering and machine learning regression (MLR) was constructed to build a robust model for estimating SSC from hyperspectral images in rivers. The concept of this framework is based on multiple estimators for heterogeneous fields, which were proposed earlier on bathymetry and biophysical parameters (Bi et al., 2021; Bruzzone and Melgani, 2005; Niroumand-Jadidi et al., 2020). However, this study aimed to estimate the suspended sediment in rivers, focusing on resolving the complex optical variability caused by sediment types and bottom reflectance using hyperspectral clustering. In this section, the proposed framework for the estimation of SSC from hyperspectral images is outlined briefly, and the details of the algorithms developed for the framework are described in the subsequent sections.

The proposed framework consists of two main modules: real-time updating and application (Fig. 4.1). The real-time updating module includes a function to develop the model by learning the relationship between the SSC and the corresponding hyperspectral spectrum. Additionally, this module includes a function to upgrade the model through real-time learning of new data when applied to the untrained field later. This module consists of three main algorithms: Gaussian Mixture Model (GMM) clustering, Recursive Feature Elimination (RFE), and Machine Learning Regressor (MLR). These algorithms were sequentially operated to build the multiple estimators according to spectral similarity. Based on these algorithms, the CMR-OV process is as follows (Fig. 4.2): (a) spatiotemporally matching the hyperspectral images acquired using UAVs with in-situ measured SSC data; (b) dividing the matched dataset into training and validation data group; (c) hyperspectral clustering of the training data using GMM; (d) selecting the relevant spectral bands of the clustered training data for each cluster through RFE using the MLR for each cluster; (e) verifying the trained MLR by repeating Step (d) to minimize the total error score evaluated by the test dataset; (f) selecting trained clustered MLR models whose total error scores were minimally verified in Step (e) as a final estimator.

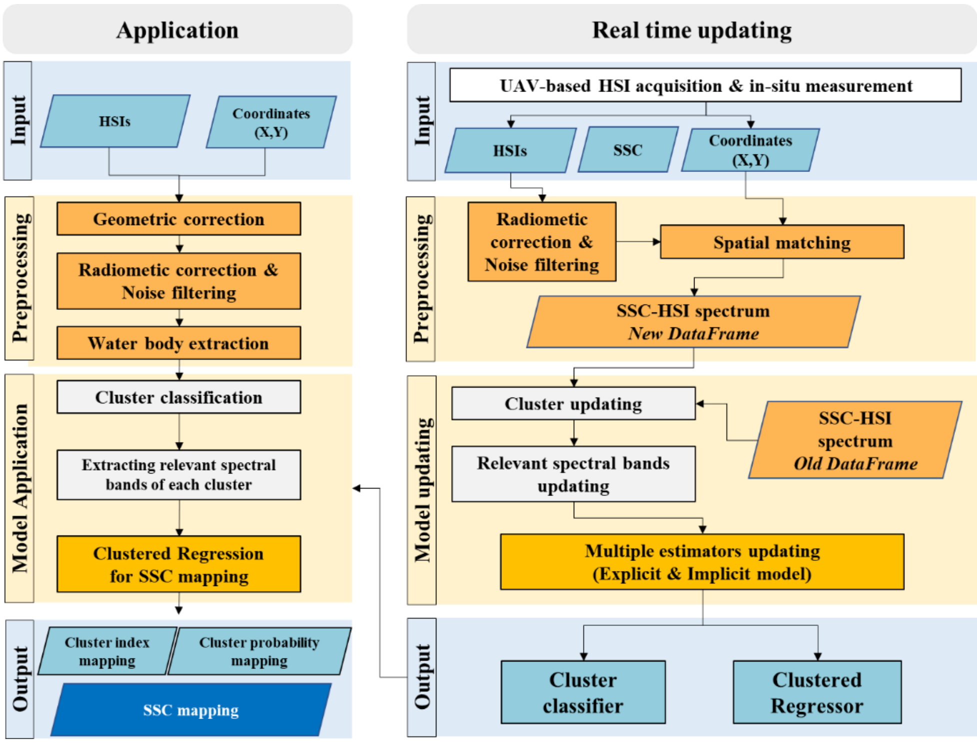

Fig. 4. 1. Flowchart of CMR-OV with two modules: real-time updating and application.

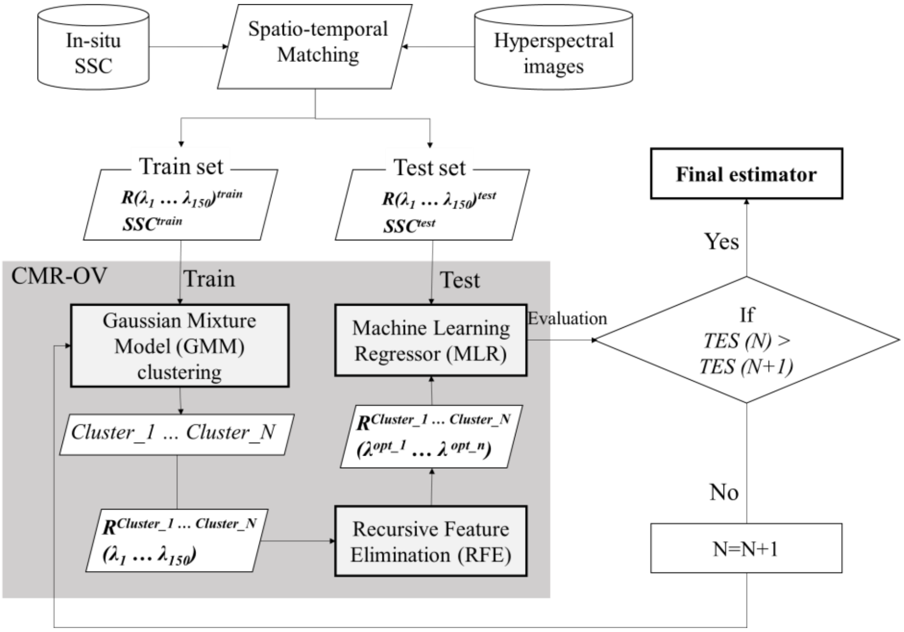

Fig. 4. 2. Flowchart of the process of developing multiple estimators based on three main algorithms: RFE, MLR, and GMM.

The application module aims to convert the hyperspectral images into the SSC distribution using the trained multiple estimators of CMR-OV (Fig. 4.1). After preprocessing hyperspectral images (radiometric correction and noise filtering), the estimators can be applied to the waterbody region extracted from the hyperspectral image. CMR-OV provides the SSC map and the clustered index with the probability of belonging to each cluster as the output data. Notably, the probability of belonging to each cluster can be seen as the reliability of trained estimators when applied to the untrained region.

From the final hyperspectral clusters determined from CMR-OV, the critical physical factors of optical similarity were analyzed using the Mann–Whitney U test, which is used to compare the means of independent samples based on a nonparametric test with ranked sums (Helsel, 1987; Kim et al., 2014). This test verified the discrepancy in physical factors according to the cluster types.

4.2 Pre-processing of hyperspectral images

In this study, the digital number (*DN*), recorded integer values of the radiance, were first converted to radiance (*L*) units using the nonuniformity corrections (NUC) (Leathers et al., 2005). The NUC is a scene-based correction for both radiance conversion and inhomogeneity of individual pixels in the hyperspectral image. Using scene-based correction, NUC can convert *DN* to radiance directly from a scene. Due to these advantages, this method is broadly used in the push-broom type hyperspectral approach (Hu et al., 2017; Leathers et al., 2005; Li et al., 2009; Rakwatin et al., 2007). In this study, the median-spatial ratio-based NUC method is used. This method assumes that the median value over the ratio of the radiance of neighboring pixels is approximately unity as follows:

$$median(L_{n+1,b} / L_{n,b}) = 1 \tag{4.1}$$

where $L_{n+1,b} = Gain_{n+1,b} \times (DN_{n+1,b} - Offset_{n+1,b})$ and $L_{n,b} = Gain_{n,b} \times (DN_{n,b} - Offset_{n,b})$, which assumes the *DN* and *L* have a linear relation, can be used to solve Eq. 4.1; *n+1* and *n* are the indexes of the pixel in cross line; b is the index of the spectral band. Therefore, the *Gain* and *offset* can be solved by optimization of minimizing the following loss function ($loss_{s,b}$) (Hu et al., 2017):

$$loss_{n,b} = \left| 1 - \frac{Gain_{n+1,b} \times (DN_{n+1,b} - Offset_{n+1,b})}{Gain_{n,b} \times (DN_{n,b} - Offset_{n,b})} \right| \tag{4.2}$$

After conversion of *DN* to radiance using NUC, calibration tarps offering Lambertian reflectance of 0.84, 0.56, 0.24, and 0.03 were used to convert the radiance to normalized reflectance. The reference reflectance values were obtained before each experiment by placing the tarp on a flat plate. From the reference values, the radiance was normalized to relative reflectance using Eq. (4.3):

$$R(\lambda) = Gain \cdot L(\lambda) + offset \tag{4.3}$$

where $R(\lambda)$ is relative reflectance.

For noise filtering, the pixel-based spectral de-noising was implemented using SAVGOL filter by a 5-point window with quadratic polynomial filter, as described earlier (Cimoli et al., 2020; de Almeida et al., 2019; Kwon et al., 2020; Mishra et al., 2019; Pyo et al., 2020b, 2019). By applying this filter to a hyperspectral spectrum where a bubble passed on the water surface, the high noise value was attenuated, and the spectrum was smoothed overall. Fig. 4.3 shows the results of hyperspectral image preprocessing using time series data of the radiance measured in Section 2 of Exp. 2-2. Values without radiometric correction and spectral de-noising included a few noises (Fig. 4.3 (a)). In addition, they was a difference in the value in the background water before the suspended sediment arrived due to the differences in the radiation conditions in each experiment. However, the normalized reflectance values had almost the same values as that in the background water after radiometric correction (Fig. 4.3 (b)). In addition, SAVGOL filtering with a second-order polynomial and a window size of 5 considerably removed the noises in the spectra (Fig. 4.3 (c)).

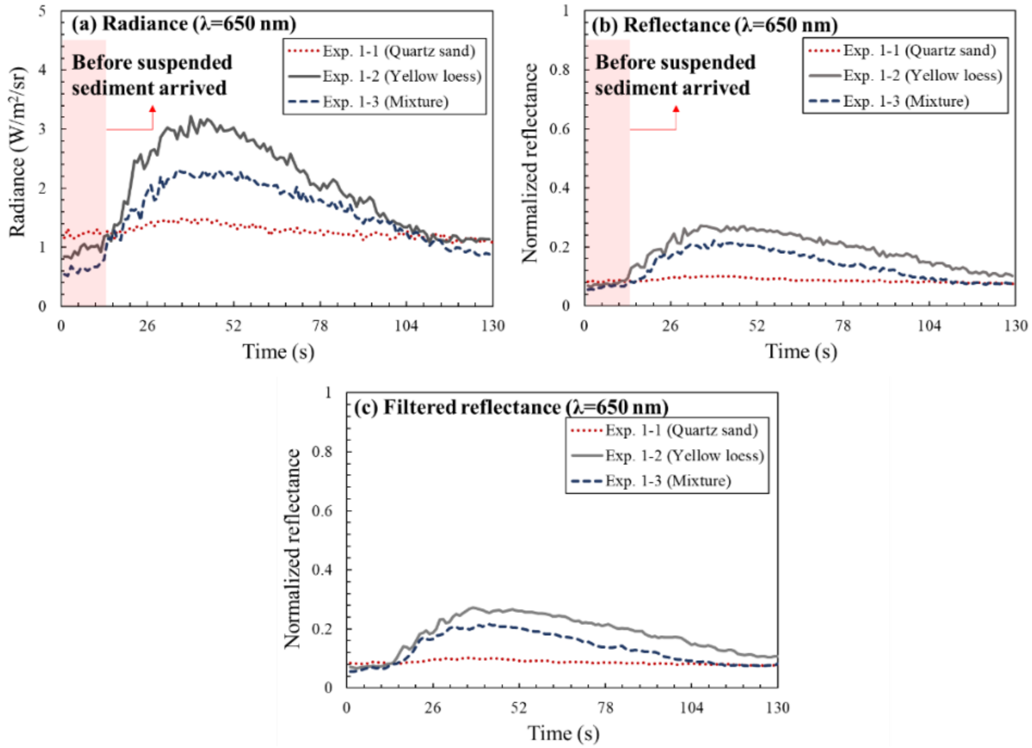

Fig. 4. 3. Times series data of (a) radiance, (b) normalized reflectance, and (c) filtered reflectance in the 650 nm wavelength

Subsequently, the pixels corresponding to the SSCv measurement points of each case were extracted from the corrected hyperspectral images. The spatial resolution of acquired hyperspectral images was 1.8 cm due to the 25 m flight of the drone with 29.5 degrees FOV of the hyperspectral camera. The hyperspectral spectrum corresponding to the measurement point of LISST-200X was obtained by spatially averaging 5 pixels near the measurement point. The extracted hyperspectral spectrum was temporally averaged at a 1.5-s interval, which is an equal measurement interval of LISST-200X; it was matched with the SSC dataset. The matched datasets were extracted for the effective range, a range over 1 % of maximum SSC, to extract the points where the SSCv changes from the background SSC.

4.3 Regression models and clustering technique

4.3.1 Index-based regression models

In order to retrieve the SSC using the regression approach with hyperspectral images, this study employed optimal band ratio analysis (OBRA)-based linear regression (LR) and symbolic regression (SR) as explicit regression approaches. OBRA, the most popular algorithm for retrieval of water depth and water quality parameters, uses the ratio of spectral bands to isolate the $L_c(\lambda)$ back-scattered by the suspended sediment in water bodies

(Legleiter et al., 2019, 2004; Legleiter and Harrison, 2019; Niroumand-Jadidi et al., 2020, 2019a, 2018). The optimal band ratio in OBRA was determined by calculating the band ratio according to all pairs of bands (λ_1, λ_2); it yields the highest accuracy of regression of SSC on band ratio. In this study, the log-transformed single band ratio (Eq. 4.4) and normalized difference ratio (Eq. 4.5) were used as the LR and SR input variables, respectively.

$$X \propto \ln\left[\frac{R(\lambda_1)}{R(\lambda_2)}\right] \tag{4.4}$$

$$X \propto \ln\left[\frac{R(\lambda_1)-R(\lambda_2)}{R(\lambda_1)+R(\lambda_2)}\right] \tag{4.5}$$

The relationship between hyperspectral radiance and SSC in the open channel flows is complicated because the radiance of SSC is influenced by many factors, such as the existence of various types of substrate in the water, varying water depth according to discharge, and surface scattering effect of glinting sunlight. Therefore, in this study, nonlinear regression was additionally employed to represent the optical complexity in shallow open channel waters (Baek et al., 2019a; Binding et al., 2005; Fraser, 1998; Legleiter and Harrison, 2019; Schiebe et al., 1992). SR was chosen from various nonlinear regression approaches. SR does not require the fixed functional form as prior knowledge since it aims to identify the optimal functional form using an evolutionary optimization algorithm, the genetic algorithm (GA) (Hristov et al., 2020; Searson et al., 2010; Weng et al., 2019). In the SR optimization process, the functional form evolved continuously through the operators in GA, such as mutation, recombination, and selection, until the mean squared error (MSE) reached the termination criteria. The input variable was selected in the same manner as the LR; these are the two types of optimal band ratio with the forms shown in Eqs. (4-4 and 4-5). In this study, only simple operators, +, −, ×, ÷, $-X$, $\sqrt{X}$, $\ln(X)$ were selected to avoid overcomplicating the functional form and overfitting. The SR was implemented using the *gplearn* library in Python 3.7.

4.3.2 Machine learning regression models

In this study, among the various ML-based regression models, random forest (RF) and support vector regression (SVR) were employed and compared to the band ratio-based explicit regression models. These two ML models, which are the most popular ML-based regression models, show superior performance when the given dataset is highly nonlinear and complicated due to high dimensionality (Choi and Seo, 2018; Kwon et al., 2021a). Therefore, unlike explicit regression, which makes the equation more complex and causes overfitting in the presence of many variables, the ML models have an advantage in analyzing high-dimensional data like hyperspectral images. In this study, RF and SVR models were developed to predict the SSC based on the reflectance values of several bands.

RF is an advanced decision tree model that minimizes the variance of predictions (Breiman, 2001). This model has the following advantages as a regression model in CMR-OV: (a) insensitivity to the hyperparameter and a short time requirement for model development in iterative training (Li et al., 2017; Probst et al., 2019; Sun et al., 2008); (b) insensitivity to the noisy data acquired by the experiment (Kwon et al., 2021a). With respect to the structure of RF, each decision tree in RF divides the space of the input variable into multiple hierarchies according to the value of the output variable based on the tree structure. Specifically, this model selects samples and variables randomly, then divides the input variable into each node of decision trees according to the value of the output variable. In the training process of this model, the split for each node is determined by maximizing the reduction in the overall impurity in nodes. The impurity can be estimated by mean square error (MSE) when the decision tree is used for regression, as given in Eq. 4.6.

$$\mathrm{MSE} = \frac{1}{n}\sum_{i}(y_i - \widehat{y_i})^2 \tag{4.6}$$

where n is a number of the dataset; y_i is the in-situ measured SSC; $\widehat{y_i}$ is predicted SSC. Based on these criteria, the example of a single decision tree with three depth and two sample splits is illustrated in Fig. 4.4. The overall process can be known through the constructed model structure, unlike black-box machine learning models such as Artificial Neural Network (ANN) and kernel-based models. In addition, the importance of a variable, which is used as a criteria for relevant spectral band selection in RFE, can be estimated by the normalized total reduction of MSE by each variable. For each spectral band (i) in the spectrum, the band importance (I) averaged number of trees (NT) of decision trees in RF is calculated as:

$$I_i = \sum_{NT} \Delta MSE_i(NT) \tag{4.7}$$

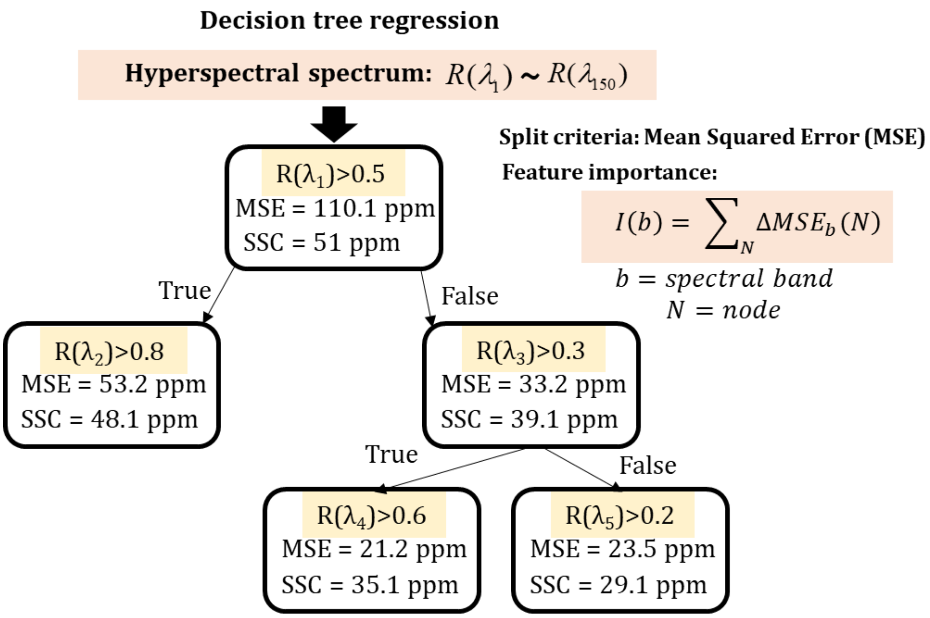

Fig. 4. 4. Structure of single decision tree for HSI-based SSC estimation.

In RF, a large number of decision tree models were combined by averaging in a process called ensemble learning (Fig. 4.5). Each decision tree in RF was developed from a random selection of samples and variables based on the bagging method proposed by Breiman (1996). The sample was generated by bootstrap sampling with random replacement in the bagging process. Due to this randomization, the bagging process reduces the variance and the correlation between decision trees. The final prediction result is calculated by aggregating predicted SSC in each decision tree model. In this stage, the final SSC values and uncertainty can be obtained by the average and the standard deviation of predicted SSC values.

When applying CMR-OV, RF models were tuned by estimating the optimal features randomly sampled at each split, which is the most sensitive hyperparameter in RF (Li et al., 2017; Probst et al., 2019). The RF was less sensitive to hyperparameters than other models as it is based on ensemble learning; it showed good performance with default values in Scikit-learns packages (Díaz-Uriarte and Alvarez de Andrés, 2006). Therefore, the optimal number of features randomly sampled at each split was determined by the grid-search, and the other hyperparameters were set to default values in Scikit-learns (Pedregosa et al., 2011). To prevent overfitting and to determine robust parameters in grid-search, 5-folds cross-validation was employed in hyperparameter tuning, which randomly resplit the whole dataset into 80% training dataset and 20% test dataset five times as different partitions.

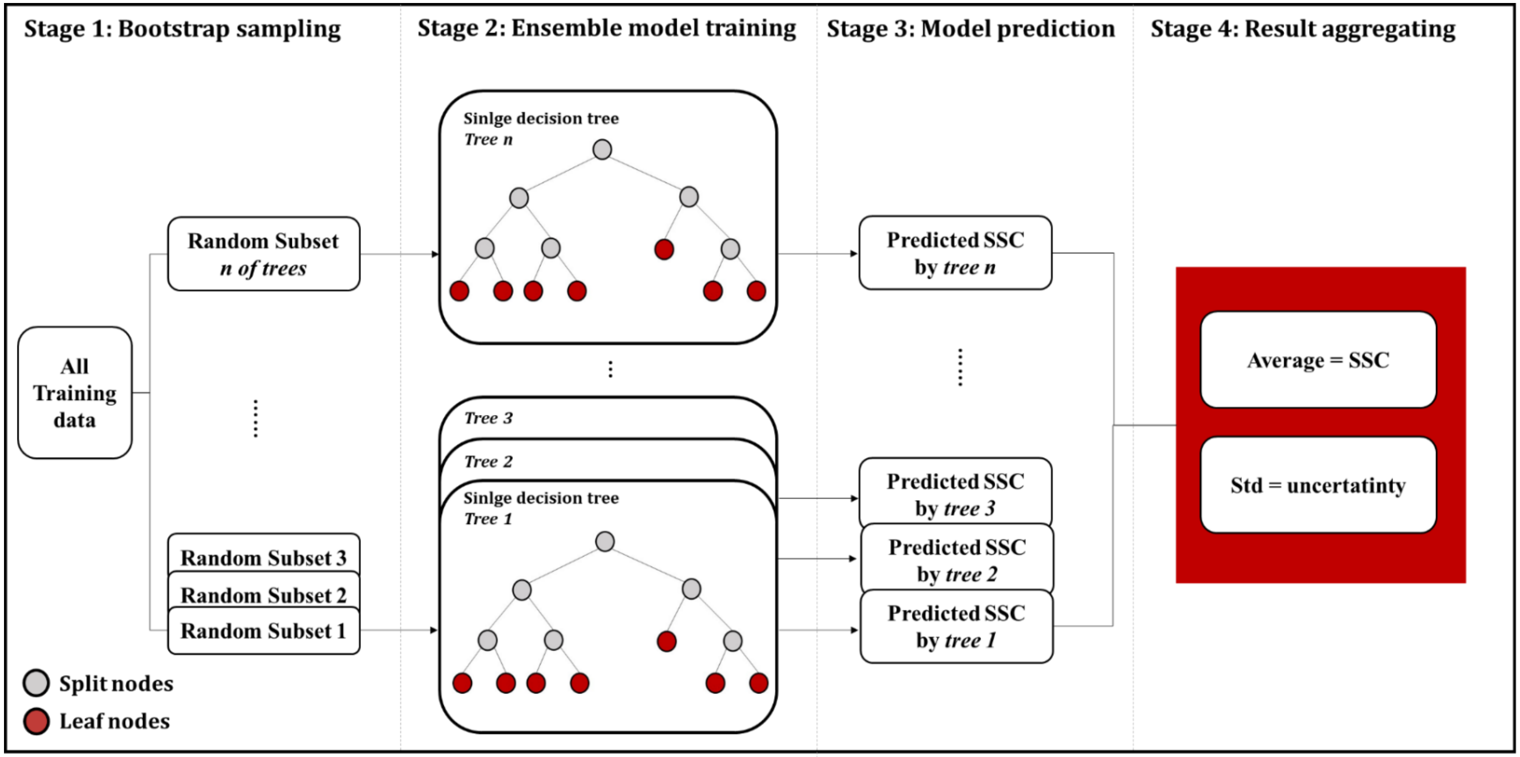

Fig. 4. 5. Training and prediction processes in RF.

SVR was proposed by Vapnik et al. (1997) and extended to a regression problem through the application of a support vector machine (SVM), which is a machine learning algorithm that is widely used for classification problems. SVR has the advantage of finding a globally optimal solution because it uses convex optimization to generate a function for the relationship between data inputs and outputs. This yields more accurate prediction results than other ML algorithms when the amount of available data is insufficient (Chi et al., 2008; Pal and Foody, 2010). In this study, the relationship between SSC and the reflectance value, which is defined by Eq. 4.8, was derived by solving the optimization problem with Eq. 4.9 as the objective function and Eq. 4.10 as the constraint to solve for the $f(x_{ij})$ that is distributed within one deviation ε. Eq. 4.8 was derived as the flattest regression function that was less than one deviation ε from the actual SSC values (y_i) for all reflectance values of each band (x_{ij}).

$$f(x_{ij}) = \sum_{i=1}^{n} \omega_i g(x_{ij}) + b_i \tag{4.8}$$

$$\min \frac{1}{2}|\omega|^2 + \Gamma \sum_{i=1}^{n} (\xi + \xi_i^*) \tag{4.9}$$

$$\begin{cases} y_i - f(x_{ij}) - b_i \le \varepsilon + \xi_i^* \\ f(x_{ij}) + b_i - y_i \le \varepsilon + \xi_i \\ \xi_i, \xi_i^* \ge 0 \end{cases} \tag{4.10}$$

where $f(x_{ij})$ is the convex function; j is the number of data; n is the number of spectral bands; ω_i are weight coefficients; b_i is the bias; $g(x_{ij})$ is the kernel function for nonlinear transformation; Γ is the penalty factor; and ξ_i and ξ_i^* are slack variables that determine the degree of penalty if the error exceeds ε. Among these parameters, Γ and ε are important to determine overfitting, underfitting, and the accuracy of models. A grid-search algorithm was used to search the optimal parameter values among all parameter combinations in the hyper-parameter range according to the best cross-validation score. The range of grid-search from an earlier study was adopted (Akhtar et al., 2019). The i_{th} band importance (I_i) can be estimated using the w_i, which indicates the effect of the reflectance value of the i_{th} band on the prediction by the finally trained SVR of Eq. 4.8.

4.3.3 Relevant band selection

In this study, to build the ML models with the relevant spectral bands for SSC, recursive feature elimination (RFE), a thorough feature selection method based on model performance, was employed (Guyon et al., 2002). RFE eliminates the least important band based on the particular feature importance criteria of each model (Fig. 4.6). This algorithm first trains the model using all of the spectral bands in the hyperspectral image. It then repeatedly removes any redundant bands until the performance of the continuously trained model is reduced. The remaining bands are finally selected as the relevant spectral bands for SSC. The root mean square error (RMSE) (Eq. 4.11) was adopted as the performance criteria, with 5-fold cross-validation at each step to reduce bias.

$$RMSE = \sqrt{\frac{1}{n}\sum\nolimits_i (y_i - y_i)^2} \tag{4.11}$$

where y_i is the in-situ measured SSC, and y_i is the remotely sensed SSC. Using the band importance (*I*) of the RF and SVR models, the optimal band subsets selected by RFE served as the input variables for each model. To be more robust in the selection, RFECV improves RFE with N-fold cross-validation to decrease the bias of selection.

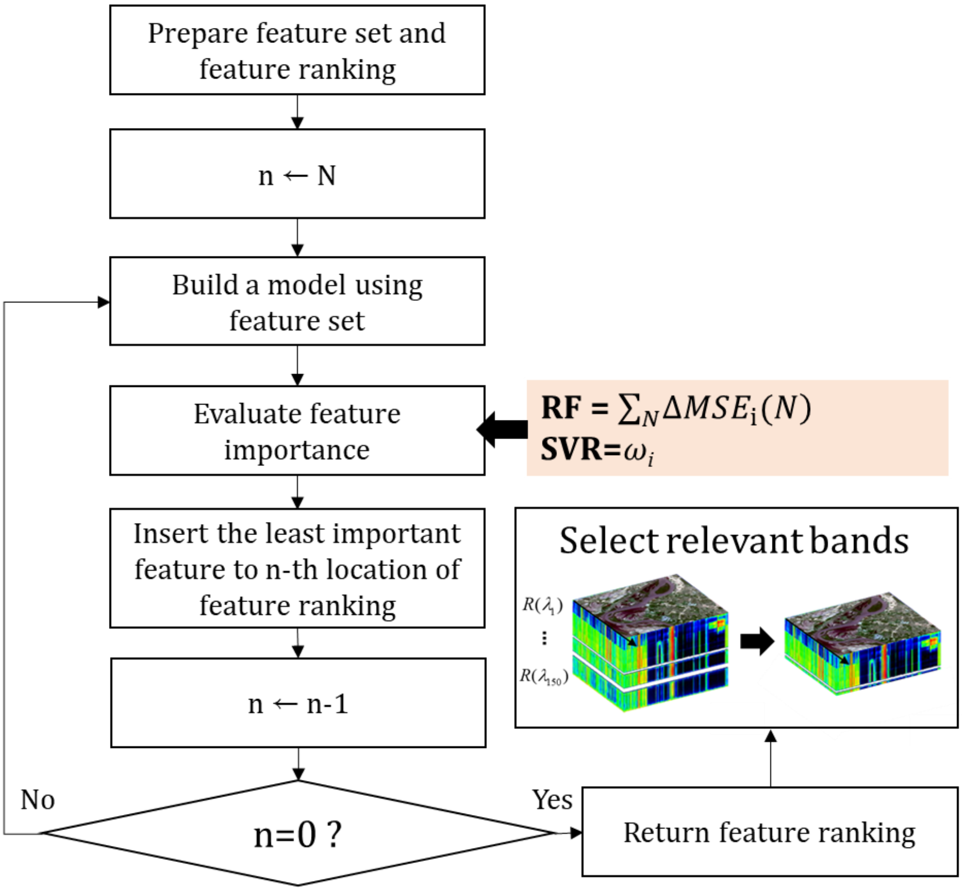

Fig. 4. 6. Flowchart of selecting relevant spectral bands using RFE

4.3.4 Gaussian mixture model for clustering

To maximize the performance of each RF model in CMR-OV, GMM clustering was applied to group a number of spectra recorded as pixel values from the HSI into various optically homogeneous clusters (Löffler et al., 2019; Zhou et al., 2018). In addition, the optically clustered dataset was used to investigate the dominant physical factors affecting the optical similarities between sediment properties and bottom properties.

GMM is a probability-based clustering method that statistically splits clusters based on a Gaussian distribution (Bouveyron and Brunet-Saumard, 2014; Herms et al., 2021; Kim et al., 2014). Compared to heuristic-based clustering, such as k-means and hierarchical clustering, GMM has several advantages. First, unlike heuristic-based clustering, GMM accounts for variance; therefore, the stretched structure dataset can be clustered. Second, the probability of belonging to each cluster is obtained from the fitted probability density function (PDF). Therefore, the multivariate dataset is fit using a weighted combination of heterogeneous Gaussian distributions in GMM. The fitted mixture of Gaussian distributions represents the PDF of the entire dataset as a non-Gaussian distribution. From this PDF, the clusters can be split using a decomposed single Gaussian distribution, ensuring the statistical homogeneity of each cluster. In this study, n independent dataset of the hyperspectral spectrum (x_i) was clustered using GMM. The Gaussian mixture PDF (N_{mix}) of the given spectrum (x_i) can be written as:

$$N_{mix}(x_i) = \sum_{j=1}^{J} \pi_j N_j(x|\mu_j, \Sigma_j) \tag{4.12}$$

where J is the number of clusters, π_k denotes mixture coefficient, ranging from 0 to 1 and $\sum_1^J \pi_j = 1$, N_k is single Gaussian distribution of j_{th} cluster with a mean (μ_j) and covariance matrix (Σ_k). Each single multivariate Gaussian distribution of j_{th} cluster is defined as:

$$N_j(x_i|\mu_j, \Sigma_k) = \frac{1}{(2\pi)^{\frac{d}{2}}|\Sigma|^{1/2}} \exp(-\frac{1}{2}(x_j - \mu)^T \Sigma^{-1}(x_j - \mu)) \tag{4.13}$$

where i is index of data, d is the dimension of the matrix, T denotes the transpose of the matrix, and $|\Sigma|$ is the determinant of Σ. The parameters to estimate in GMM are defined as $\theta = \{\pi, \mu, \Sigma\}$; $\pi \equiv \{\pi_1, \cdots, \pi_k\}, \mu \equiv \{\mu_1, \cdots, \mu_k\}, \Sigma \equiv \{\Sigma_1, \cdots, \Sigma_k\}$. The log-likelihood of the parameters (θ) can be expressed as:

$$l(\theta|x_i) = \sum_{i=1}^{n} ln\left\{\sum_{k=1}^{J} \pi_j N_j(x_i|\mu_j, \Sigma_j)\right\} \quad (4.14)$$

In this study, to estimate θ, the expectation-maximization (EM) algorithm was applied to maximize the log-likelihood in Eq. (3.14). First, the EM algorithm initialized each parameter and evaluated the log-likelihood (Eq. (3.14)). Then, as the expectation (E) step, the probability of each data point belonging to the k^{th} cluster was estimated from the responsibility (γ) with the current θ value (Eq. 4.15).

$$\gamma_j(x_i) = \frac{\pi_j N(x_i|\mu_j, \Sigma_j)}{\sum_{m=1}^{J} \pi_m N(x_i|\mu_m, \Sigma_m)} \quad (4.15)$$

Subsequently, the θ values were updated by the maximization (M) step, which re-estimates the θ values based on current responsibility. The updated θ values were evaluated by the log-likelihood, and E and M steps were iterated until the θ values converged at the maximum likelihood (Bishop, 2006).

4.3.5 Performance criteria

To evaluate the clustered regression models, R^2 (coefficient of determination), root mean square error percentage (RMSEP), and mean absolute percentage error (MAPE) were used. These metrics were adopted since they give normalized values. The formulae of these error metrics are listed in Eqs. (4.16)–(4.18):

$$R^2 = 1 - \sum_i \frac{(y_i - \hat{y_i})^2}{(y_i - \bar{y})^2} \tag{4.16}$$

$$RMSEP = \frac{\sqrt{\sum_i \frac{(y_i - \hat{y_i})^2}{n}}}{\bar{y}} \tag{4.17}$$

$$MAPE = \frac{1}{n}\sum_i \left|\frac{y_i - \hat{y_i}}{y_i}\right| \tag{4.18}$$

where $\bar{y}$ is the mean of the *y* values. The total error score (TSE) is calculated by averaging three error metrics to adopt the best trained clustered RF. In this process, R^2 is averaged as 1- R^2 to represent an error like other metrics.

4.4 Model development and evaluation

4.4.1 Comparison of regression models

4.4.1.1 OBRA-based explicit models

The explicit regression models, OBRA-based LR and SR were applied to the entire dataset that combined all three cases in a field-scale experiment (Exp. 2-1). In Chapter 3.5, spectral variability analysis shows that the relationship between the hyperspectral reflectance and the SSC can be complex owing to the variability in the sediment and bottom properties. In such optically complex conditions, the linear OBRA with a single band ratio showed low accuracy and high locality (Fig. 3.29).

To overcome this limitation, this study implemented two other approaches: the OBRA-based LR approach with a normalized difference ratio, and SR, as described in Section 4.3.1. These two approaches were applied only to the combined dataset (Case 2-1-1~2-1-3), which was split into training data (80%) and testing data (20%) (Table 4.1). The *'train_test_split'* function in the Scikit-learn package in Python was utilized to split the datasets randomly, and the statistical properties of training and test data are given in Table 4.1. Validation of the trained regression models was carried out using the test dataset. To measure the quantitative error of each model, R^2, RMSE, and mean absolute percentage error (MAPE) were utilized.

Table 4. 1. Statistical properties of the training and test datasets.

	SSCv (ppm)				
	No. of data	**Mean**	**SD**	**Min**	**Max**
Training dataset	520	55.76	54.55	23.10	270.9
Test dataset	130	55.66	55.79	23.45	266.2

The OBRA model selected the optimal bands for the normalized difference ratio, Eq. (4.3 and 4.4). The wavelengths of the spectral bands selected by OBRA and the relevant formulas are listed in Table 4.2. SR was employed with both the single band ratio and normalized difference ratio. The same bands selected by OBRA were used as the optimal bands for SR. The formulas derived using the training dataset was used to validate the four models using the test dataset, and the results are plotted in Fig. 4.7. LR and SR based on the single band ratio yielded similar results (Fig. 4.7 (a)). The LR 1 model underestimated the values at high concentrations, while the SR 1 model provided slightly better predictions for high concentrations and showed a lower MAPE than LR 1. Fig. 4.7 (b) shows that the SR 2 model produced the best performance for the prediction of high concentrations among the OBRA-based models. The LR 2 model underestimated the results at high concentrations, similar to the LR 1 model. This tendency of linear models to underestimate the results at high concentrations was also reported in earlier studies that obtained the concentration of fluorescent tracer and water depth based on remote sensing in shallow water (Baek et al., 2019, Legleiter and Harrison, 2019). Therefore, the nonlinear models can retrieve the SSC more accurately using the spectral characteristics of suspended sediment compared to the linear models. In addition, the normalized difference ratio was more appropriate for the independent variable of nonlinear models than the single band ratio.

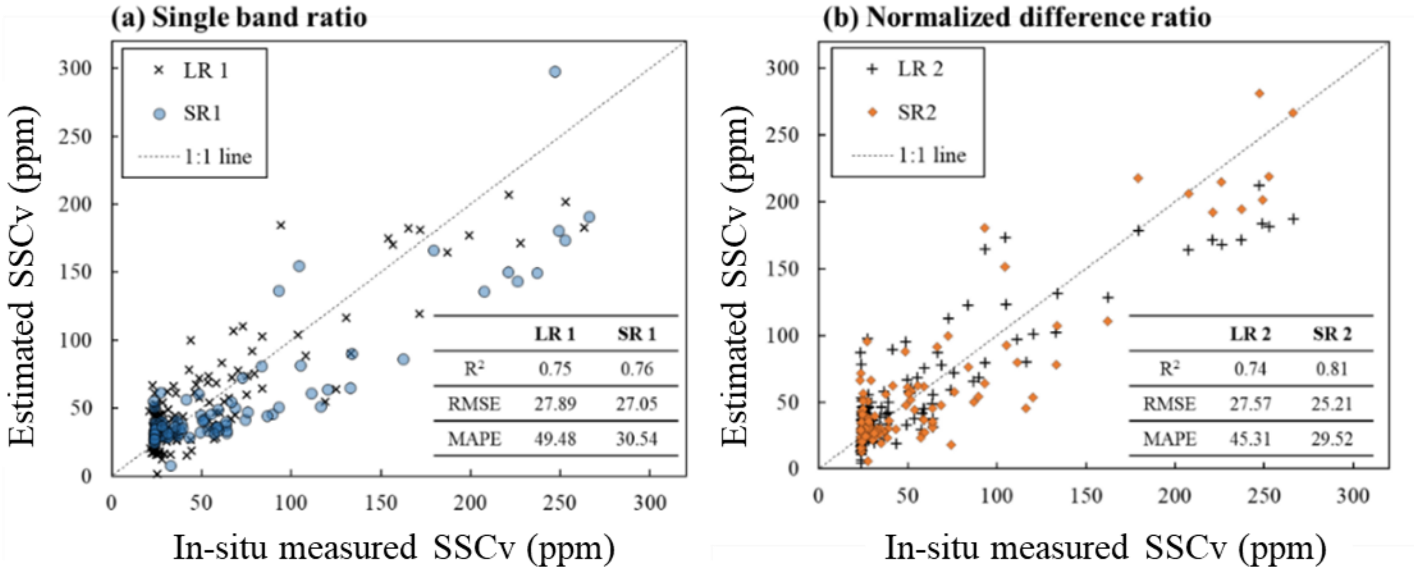

	LR 1	SR 1
R^2	0.75	0.76
RMSE	27.89	27.05
MAPE	49.48	30.54

	LR 2	SR 2
R^2	0.74	0.81
RMSE	27.57	25.21
MAPE	45.31	29.52

Fig. 4. 7. Comparison of in-situ measure SSCv and remote sensed SSCv from linear regression (LR) and symbolic regression (SR); The independent variables are (a) single band ratio and (b) normalized difference ratio.

Table 4. 2. Equations of index-based explicit regression models and their independent variable with optimal wavelength.

Model	Formula	Independent variable (X)	Optimal wavelength
LR 1	$SSC_V = 6021.12X + 1476.06$	$\ln\left[\frac{R(\lambda_1)}{R(\lambda_2)}\right]$	855.22 nm 791.15 nm
LR 2	$SSC_V = 122.99X + 633.47$	$\ln\left[\frac{R(\lambda_1)-R(\lambda_2)}{R(\lambda_1)+R(\lambda_2)}\right]$	651 nm 590.94 nm
SR 1	$SSC_V = X^3\left(-\ln(X-0.32)^3 + \ln(-0.924\ln(18402.35X^6)^3 + \frac{0.34}{X}\right)^3 - \frac{0.47}{X} - 1.57$	$\ln\left[\frac{R(\lambda_1)}{R(\lambda_2)}\right]$	855.22 nm 791.15 nm
SR 2	$SSC_V = 277.78\left(0.009X(-X^2 + X + 10.57) - 0.14 - \frac{X+0.079}{X}\right)^2$	$\ln\left[\frac{R(\lambda_1)-R(\lambda_2)}{R(\lambda_1)+R(\lambda_2)}\right]$	651 nm 590.94 nm

4.4.1.2 Machine learning-based implicit models

In this study, the RF and SVR models were developed to estimate the SSC_V using the optimal bands selected by RFE. Fig. 4.8 (a) shows the number of bands selected by RFE for each model. RF selected 62 bands with the lowest RMSE, while SVR selected 120 bands out of 150 bands. In terms of the wavelength of the selected bands, the wavelength frequency selected by each model is presented in Fig. 4.8 (b) and (c). The RF model identified particularly important wavelength ranges, violet (400–440 nm), red (640–680 nm), and NIR (920–960 nm). Among these ranges, the red band was the only one that overlapped with the spectral bands, indicating a high correlation with OBRA-based LR. RF additionally selected spectral bands with low variability according to the sediment type. However, in SVR, the wavelength of the selected band was evenly distributed throughout the spectrum, except violet (400–420 nm). Therefore, the SVR model is powerful in that high-dimensional input data becomes simpler in the feature space, as demonstrated in the earlier studies on SVR (Kwon et al., 2021a; Raghavendra and Deka, 2014; Yao et al., 2008). For SVR, the highest accuracy was obtained when 120 out of the 150 spectral bands were used, as shown in Fig. 4.8 (a).

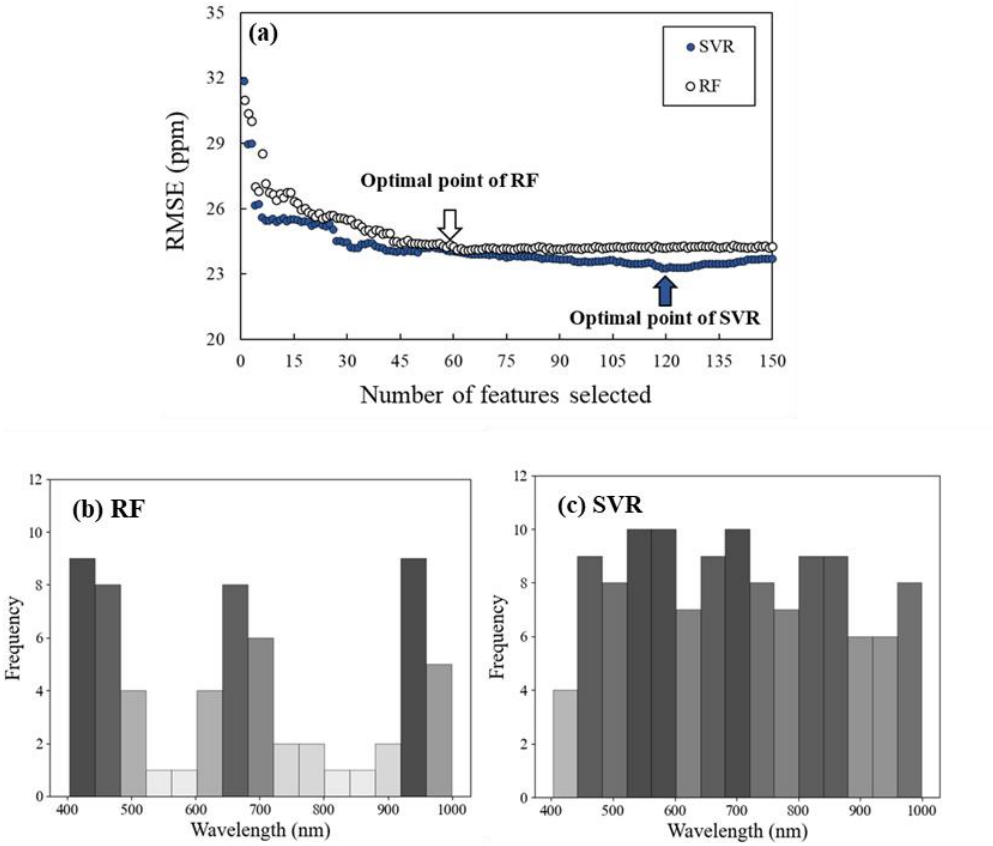

Fig. 4. 8. (a) Results of RFE and optimal point of RF and SVR; Frequency of a selected band from RFE according to wavelength: (b) RF, (c) SVR.

The RF and SVR models were trained and validated using the training and test datasets that were LR and SR. The validation results are plotted in Fig. 4.9, which shows that the implicit regression models (RF and SVR) yielded higher accuracy than the explicit regression models (LR and SR), especially in terms of MAPE. Among the two implicit regression models, SVR showed better performance, with an R^2 of 0.90, RMSE of 17.07 ppm, and MAPE of 14.18%, while RF showed an R^2 of 0.79 and RMSE of 25.37 ppm. Therefore, SVR was the most accurate model for the retrieval of SSC_V using hyperspectral images due to its outstanding performance in simplification of high-dimensional data.

In addition, to evaluate the sensitivity to spectral variability due to sediment types, both models were separately trained and validated according for each sediment type. The accuracy of validation using 20% of each dataset was increased significantly by both models (Table 4.3). In particular, the performance of RF was worse than that of SVR when a combined dataset was used, but RF showed a noticeable increase when it was separately trained according to each sediment type. RF used spectral bands smaller than SVR, as shown in Fig. 4.9; therefore, it was more efficient when a separate estimator is developed after dividing the dataset based on the optical characteristics as in this assessment. Therefore, there is a necessity of hyperspectral clustering because it is hard to classify the dataset according to optical similarities, such as sediment types, bottom types, and mixing state of sediment, in natural rivers.

RF was adopted as a final regressor in CMR-OV, and the improvement with hyperspectral clustering was evaluated in the following section.

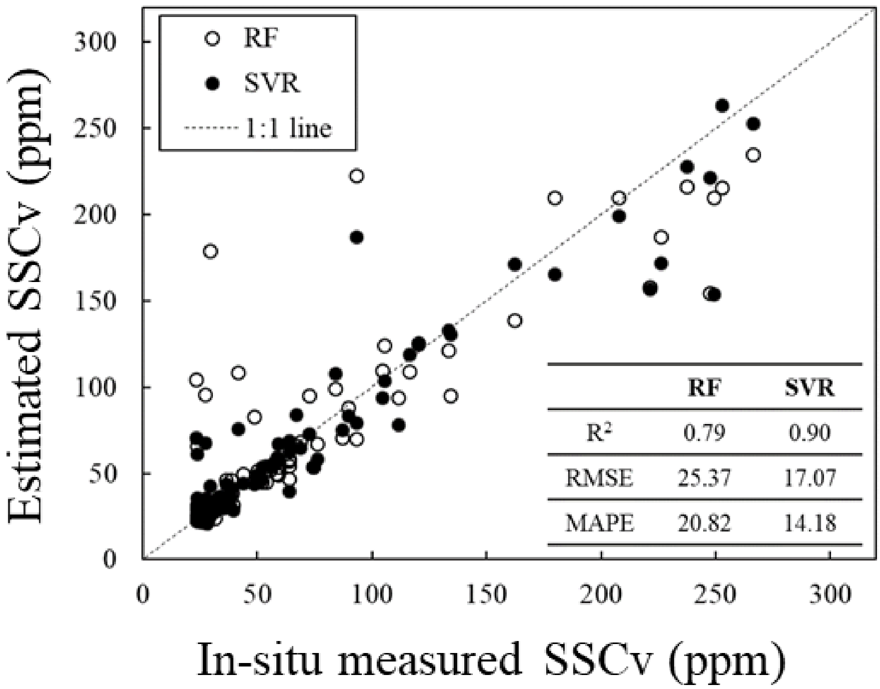

Fig. 4. 9. Comparison of in-situ measured SSC and remote sensed SSC from RF and SVR.

Table 4. 3. Validation results of separately trained models according to sediment type of Exp. 2-1.

	RF			**SVR**		
	Quartz sand	**Yellow loess**	**Mixture**	**Quartz sand**	**Yellow loess**	**Mixture**
R^2	0.81	0.93	0.93	0.83	0.97	0.91
RMSE	4.07	10.20	9.86	4.29	12.85	8.60
MAPE	7.36	9.26	9.25	7.21	8.68	16.89

4.4.2 Assessment of hyperspectral clustering

To evaluate the hyperspectral clustering for improving the model performance, the CMR-OV was trained and validated using the spatiotemporally matched dataset using the hyperspectral images and SSC data measured in Exps. 2-1 and 2-2, respectively. Exp. 2-1 was conducted under the constant bottom condition with various sediment injections, whereas Exp. 2-2 was conducted under different bottom conditions. Therefore, the effect of sediment and bottom property can be investigated for different experimental conditions.

Table 4.4 shows the evaluation results of the RF model with the dataset collected in Exp. 2-1 according to the number of clusters. In this process, the optimal spectral bands in each model were selected by RFECV with five-fold cross-validation. The RF model exhibited the most accurate performance when the dataset was split into two clusters. The clustered RF showed an improvement of up to 8.78% in R^2, 11.35% in RMSEP, 7.79% in MAPE, and 9.30 % in TES compared to that in the non-clustering case. The wavelengths of the selected bands and the number of selected spectral bands from non-clustered and clustered models are summarized in Table 4.5. The numbers of selected bands for each cluster were 4 and 7, which were reduced by six folds from hyperspectral clustering compared to the single RF model (62 bands) (Fig. 4.8). The relative importance of spectral bands from RFE can be seen in Fig.

4.10. Both hyperspectral clusters were spectrally distinct as two wavelength ranges: UV-Blue (410 ~ 500 nm) and near red-edge (685 ~ 810 nm). The red-edge was sensitive to SSC in the laboratory experiment (Chapter 3) and in earlier studies using satellite-based multispectral imagery (Doxaran et al., 2003; Kwon et al., 2021b; Pereira et al., 2019; Pham et al., 2018). The hyperspectral clusters were separated according to SSCv values; the clustered datasets were compared with the original dataset in the PC domain (Fig. 3.33), as shown in Fig. 4.11. At high concentration, the intrinsic spectral characteristics of suspended sediment were dominant; therefore, the 685 ~ 810 nm, near Red-edge, was important. In contrast, at low concentrations, the spectral bands within the low wavelength range were significant because of the strong effect of bottom reflectance. Therefore, quartz sand was included in group 1 due to the low concentration and high transmittance. Only hyperspectral clustering could determine the approximate suspended sediment characteristics when the bottom characteristics are constant.

Table 4. 4. Evaluation of RF according to number of clusters in Exp. 2-1; the values with highest accuracy are indicated in bold.

Number of clusters	R^2 (%)	RMSEP (%)	MAPE (%)	TES (%)
1	79.02	44.89	21.23	29.04
2	**87.78**	**33.54**	**13.44**	**19.73**
3	68.77	52.18	19.18	34.20
4	63.38	56.94	23.64	39.07

Table 4. 5. Wavelength of selected bands in each cluster.

Cluster	No. of data (training; test)	No. of selected bands	Wavelength of selected bands (nm)
Cluster 1	411; 103	4	696, 700, 760, 796
Cluster 2	69; 18	7	404, 420, 452, 472, 476, 480, 988

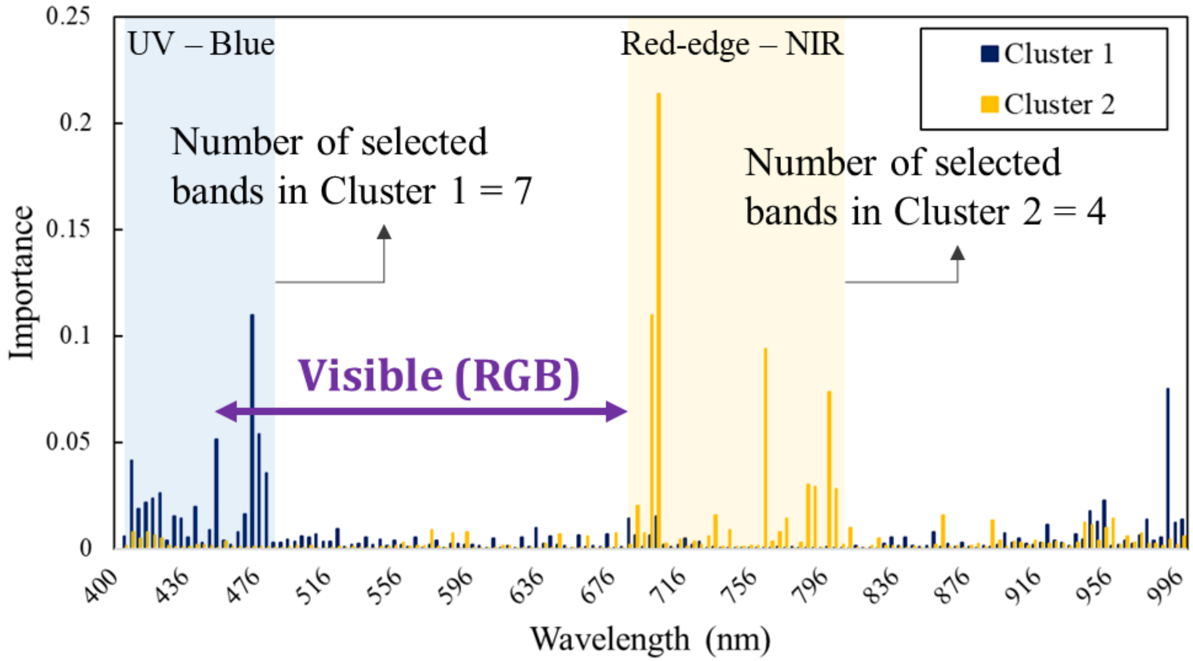

Fig. 4. 10. Relative band importance calculated using RFE according to cluster type in Exp. 2-1 (constant bottom condition).

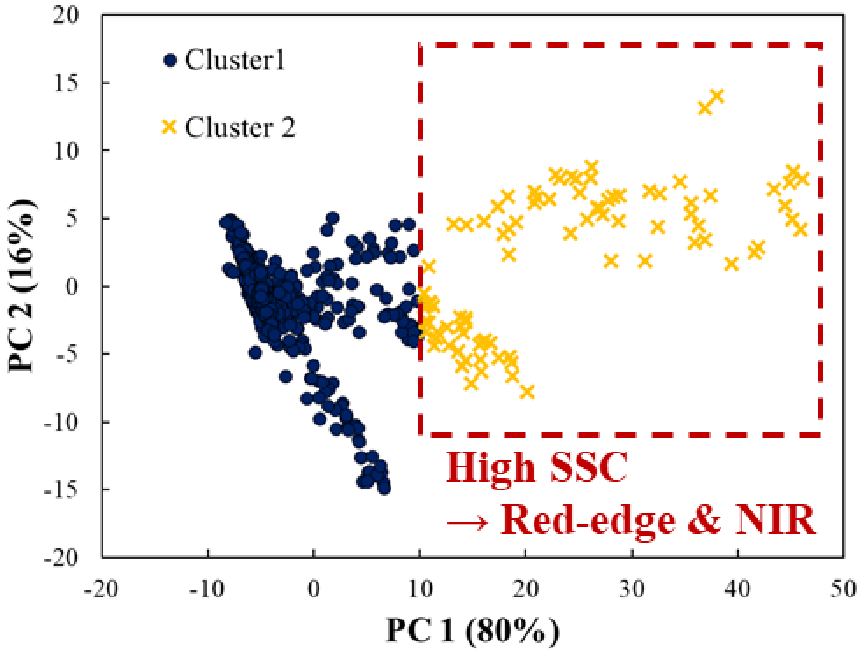

Fig. 4. 11. Result of the clustered dataset (Exp. 2-1) in the PCs domain.

The results of hyperspectral clustering for various suspended sediment characteristics were analyzed using the dataset of Exp. 2-1 when the bottom characteristics were constant. In addition to this variability of suspended sediment, the bottom effect can be investigated in detail through the dataset of Exp. 2-2, which was conducted in both vegetated and sand bottoms.

Table 4.6 summarizes the evaluation results of the RF model based on the number of clusters using the dataset collected in Exp. 2-2. The RF model showed the most accurate performance when the dataset was split into two clusters, as indicated by an evaluation using a dataset from Exp. 2-1. The clustered RF showed an improvement of up to 10.82% in R^2, 18.57% in RMSEP, 3.03% in MAPE, and 10.81 in TES compared to that in the non-clustering case. Fig. 4.12 compares the predicted SSC from the RF model before and after clustering and the non-clustered RF using selected spectral bands from the clustered RF, in comparison to the in situ measured SSC_V. Hyperspectral clustering improved the prediction performance in the overall SSC_V range. In addition, the non-clustered model had a limitation: accounting for various spectral bands selected by combining the spectral bands of clustered RF (Clusters 1 and 2).

Table 4. 6. Evaluation of RF according to number of clusters in Exp. 2-2; the values with the highest accuracy are indicated in bold.

Number of clusters	R^2 (%)	RMSEP (%)	MAPE (%)	TES (%)
1	82.62	45.87	18.07	27.11
2	**93.44**	**27.30**	**15.04**	**16.30**
3	90.10	37.42	18.15	21.82
4	89.68	39.34	15.16	21.61
5	87.35	44.64	15.68	24.32

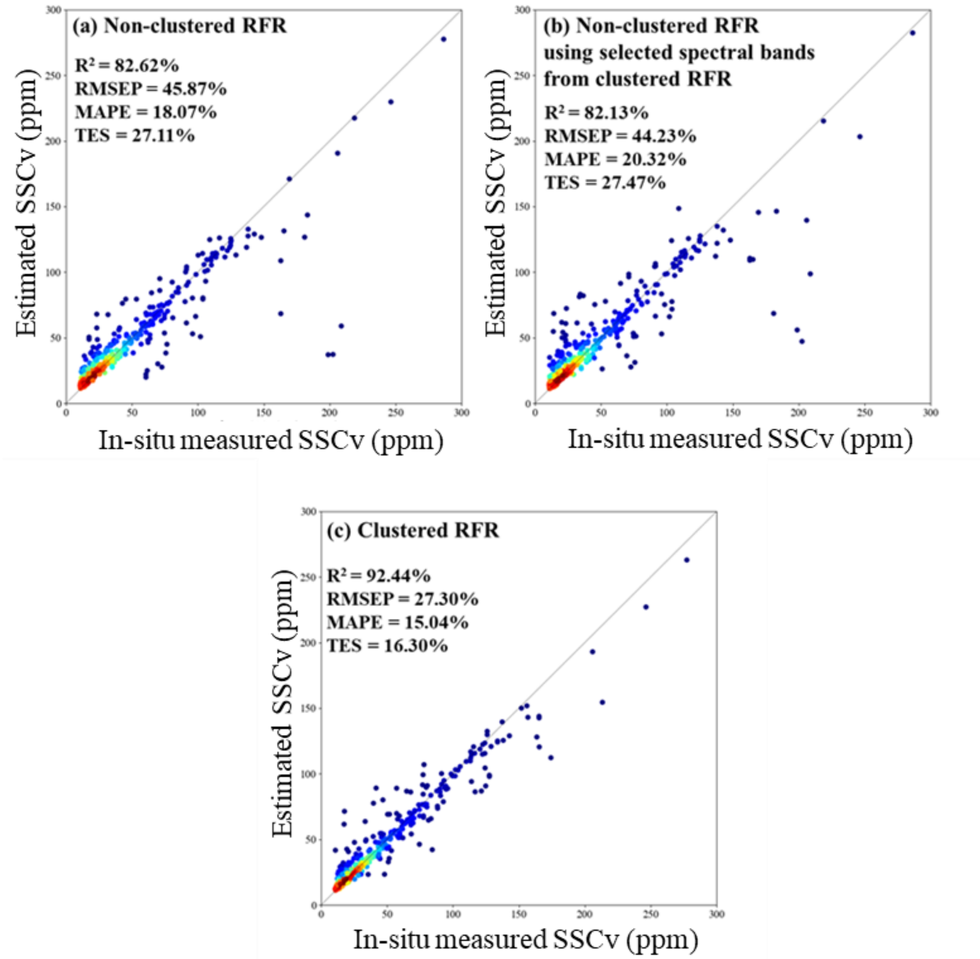

Fig. 4. 12. Comparison of in-situ measured SSC_V and predicted SSC_V (a) before and (b) after clustering.

However, the wavelength ranges of the selected bands and the number of selected spectral bands differed with Exp. 2-1, as shown in Table 4.7. In terms of the relevant bands in each cluster, Fig. 4.13 presents the relative band importance of each cluster from RFECV; the grey bar indicates the relative band importance without clustering. GMM split the dataset into two clusters with apparently different optical properties. Each cluster identified particularly important wavelength ranges: red-edge (650–700 nm) and NIR (780–1000 nm). Similarly, as shown in the measured hyperspectral spectrum according to the SSC_V in Fig. 3.32, the increased SSC_V induced a high reflectance variation within the red-edge range in all cases. Cluster 1, which relied on the red-edge range, was strongly associated with the spectral characteristics of suspended sediment. In contrast, the reflectance within the NIR range was dominant in Cluster 2. Therefore, factors other than the intrinsic optical properties of suspended sediment, such as bottom reflectance from submerged vegetation, substantially contribute to Cluster 2. The effect of the bottom reflectance varies depending on the bottom type, even for the same sediment type, as shown in the complex spectral variation in a vegetation area within the NIR range (Fig. 3.32 (b), (d), and (f)).

Table 4. 7. Wavelength of selected bands in each cluster and the non-clustered dataset.

Cluster	No. of data (training; test)	No. of selected bands	Wavelength of selected bands (nm)
Cluster 1	1,040; 260	10	451, 483, 635, 651, 659, 675, 679, 683, 687, 691
Cluster 2	645; 161	15	407, 411, 415, 419, 783, 787, 791, 795, 891, 903, 939, 967, 979, 983, 1,000
Non-clustered	1,685; 421	15	411, 487, 499, 643, 647, 683, 687, 691, 699, 707, 783, 927, 939, 979, 1,000

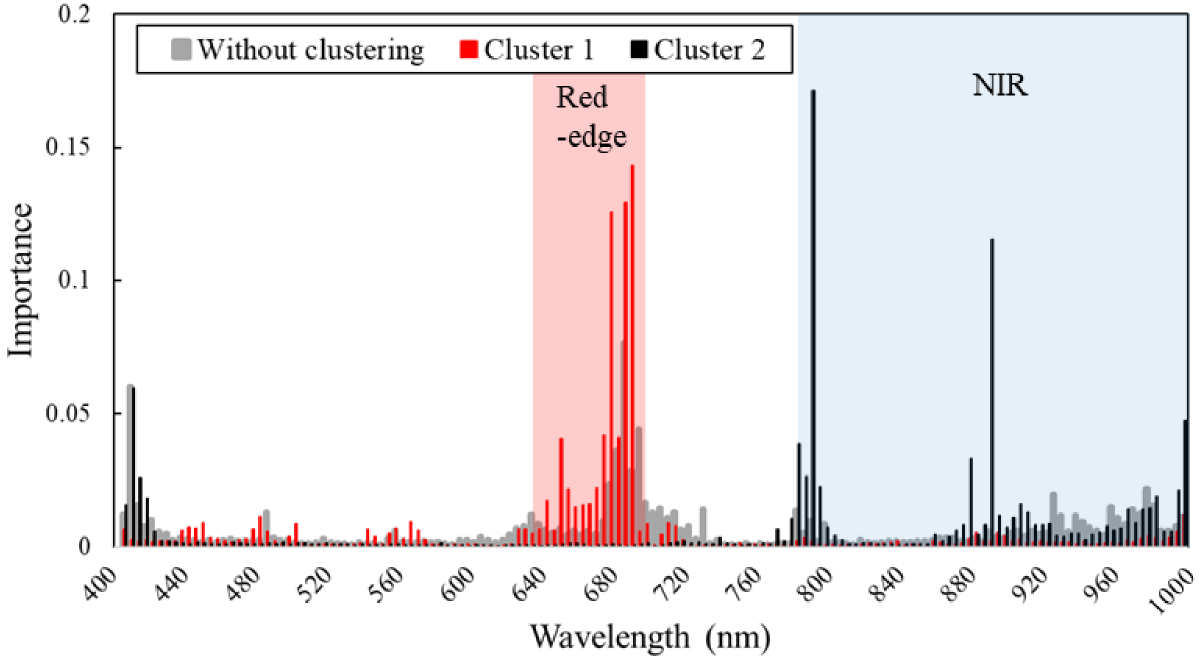

Fig. 4. 13. Relative band importance calculated by RFE according to the cluster type in Exp. 2-2.

The selected range of wavelengths without clustering covered the same range as Clusters 1 and 2. However, it is challenging to accurately predict the optically complex conditions with a non-clustered model, even though spectral bands with a wide range of wavelengths can be considered in the non-clustered model with a machine learning approach. Each clustered RF of the CMR-OV can be trained accurately from the clustered dataset because of the de-concentration of the spectral variability.

In terms of spectral similarity, Fig. 4.14 (a) and (b) depict the mean and standard deviation of the hyperspectral spectrum according to the cluster type. The std was larger in Cluster 2 than in Cluster 1, particularly in the NIR range (850–1000 nm), where variations were more prominent when the bottom was vegetated. Box plots of the physical factors according to the cluster type are shown in Fig. 4.14 (c); all physical factors except for the bottom type slightly differed between the two clusters. Additionally, this difference in physical factors with cluster types was evaluated statistically using the Mann-Whitney U test (Helsel, 1987), which is a nonparametric test of a null hypothesis based on a ranked sum, verifying the statistical difference of the significant variables in the clustered dataset (Kim et al., 2014; Rosner and Grove, 1999). The mean, *SD*, and U-test p-value of all physical factors in each cluster are listed in Table 4.6. For the bottom type and temperature, the hypothesis of statistical similarity (p-value = 0) was entirely rejected. The bottom type was the most important factor affecting spectral similarity, whereas the temperature difference was affected by the dates of Exps. 2-2-1~2-2-3 and 2-2-4~2-2-7. The sediment type had a slight effect on the optical similarity because the average sediment type index of both clusters was approximately 2 with a *SD* of 0.7~0.8, which indicated an even distribution of sediment type. In addition, the silt fraction, which was the dominant fraction in the yellow loess and mixture, had the highest p-value in the U test. Therefore, the sediment properties, such as sediment type, particle size, and fraction, strongly influenced the optical variation, as described in the PCA results (Chapter 3.5). However, the spectral similarity, which determined the cluster type, was principally affected by the bottom type.

Table 4. 8. Physical variables of each cluster and differences in each variable as measured using the Mann-Whitney U test; sand and vegetated bottom were indexed as 0 and 1, respectively.

Variables	Cluster 1		Cluster 2		p-value
	Mean	***SD***	**Mean**	***SD***	
Sediment type	1.987	0.729	1.929	0.784	0.022
Bottom type	0.008	0.089	0.924	0.266	0.000
d_{50} (µm)	18.00	2.963	17.88	3.590	0.026
Clay fraction	0.020	0.025	0.030	0.041	0.002
Silt fraction	0.809	0.116	0.792	0.147	0.165
Sand fraction	0.171	0.127	0.179	0.163	0.022
Temperature (°C)	18.53	2.255	17.22	1.652	0.000

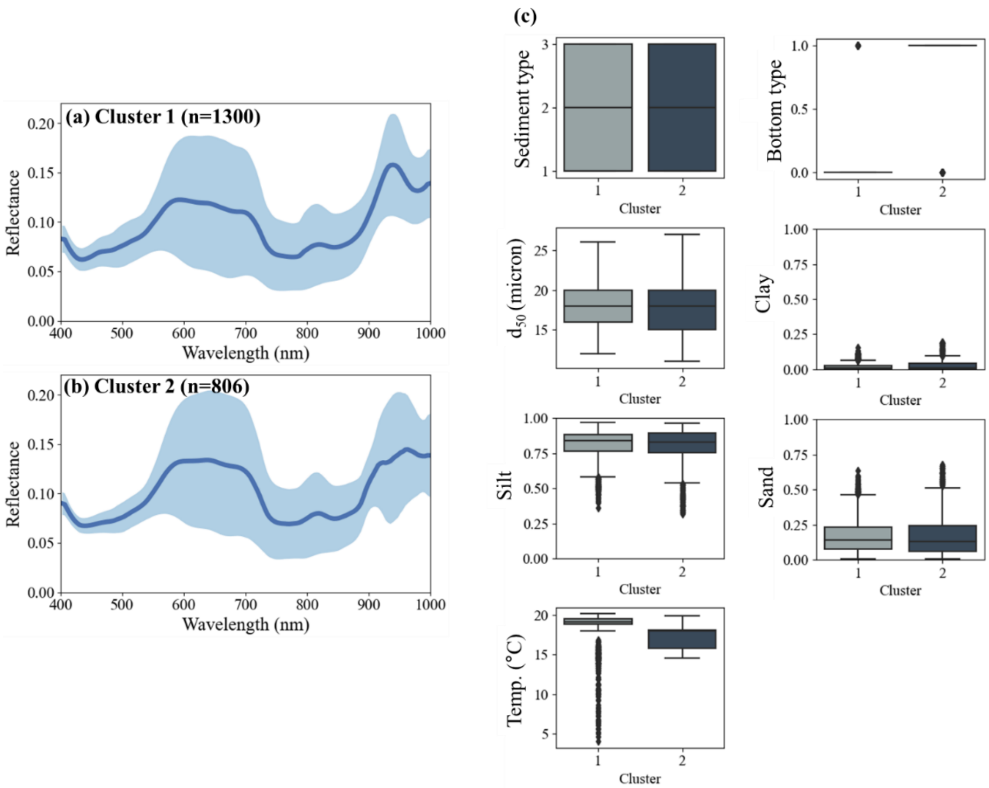

Fig. 4. 14. Hyperspectral spectrum of (a) Cluster 1 and (b) Cluster 2, with the mean of the spectrum indicated as a bold line and the standard deviation as shade; (c) boxplot of physical factors according to the cluster type: sediment type, bottom type, d_{50}, the fraction of clay, silt and sand, and temperature.

4.4.3 Spatio-temporal SSC_V mapping using CMR-OV

Using the CMR-OV developed in this study, the spatio-temporal SSC_V distributions of Exp. 2-1 in the straight channel were retrieved. In order to map the SSC_V distribution in the water area, the water body of the acquired hyperspectral images was extracted using the HDWI (Xie et al., 2014). Fig. 4.15 shows the spatial SSC_V variation in each case in the transverse direction over time. The range of mapped SSC_V distribution over time was similar to the in-situ measured SSC_V in all cases. The mapped results of the CMR-OV clearly delineate the transverse distribution of SSC_V over time for all cases, even though the cloud of quartz sand was invisible in the RGB image due to the high settling velocity and invisibility of the mineral (Fig. 3.34 (a)). In addition, a comparison of this result with the PCA result (Fig. 3.34) reveals that the transverse distribution of SSC_V over time according to the CMR-OV was quite similar to the distribution of PC 1 in all three cases. Fig. 4.15 (b) shows that the transverse distribution of SSC_V for yellow loess swung from the right bank to the left over time, while the cloud of SSC_V for quartz sand did not migrate transversely over time. Regarding the tails of the BTCs, Fig. 4.15 shows that the suspended sediment was completely mixed in the transverse direction near the peak of the BTC, the SSC_V gradually decreased after the peak, and a tail appeared. The proportion of the tail in the overall SSC distribution was larger in Cases 2-1-1 (quartz sand) and 2-1-3 (mixture), in which the tailing effect was caused by the friction at the channel bed. The quartz sand has a high propensity to settle and the concentration of quartz was greater near the channel bed than the water surface; therefore, the bottom friction forced quartz sand particles to be retained longer inside channel irregularities, which induced the longer tail in the BTCs.

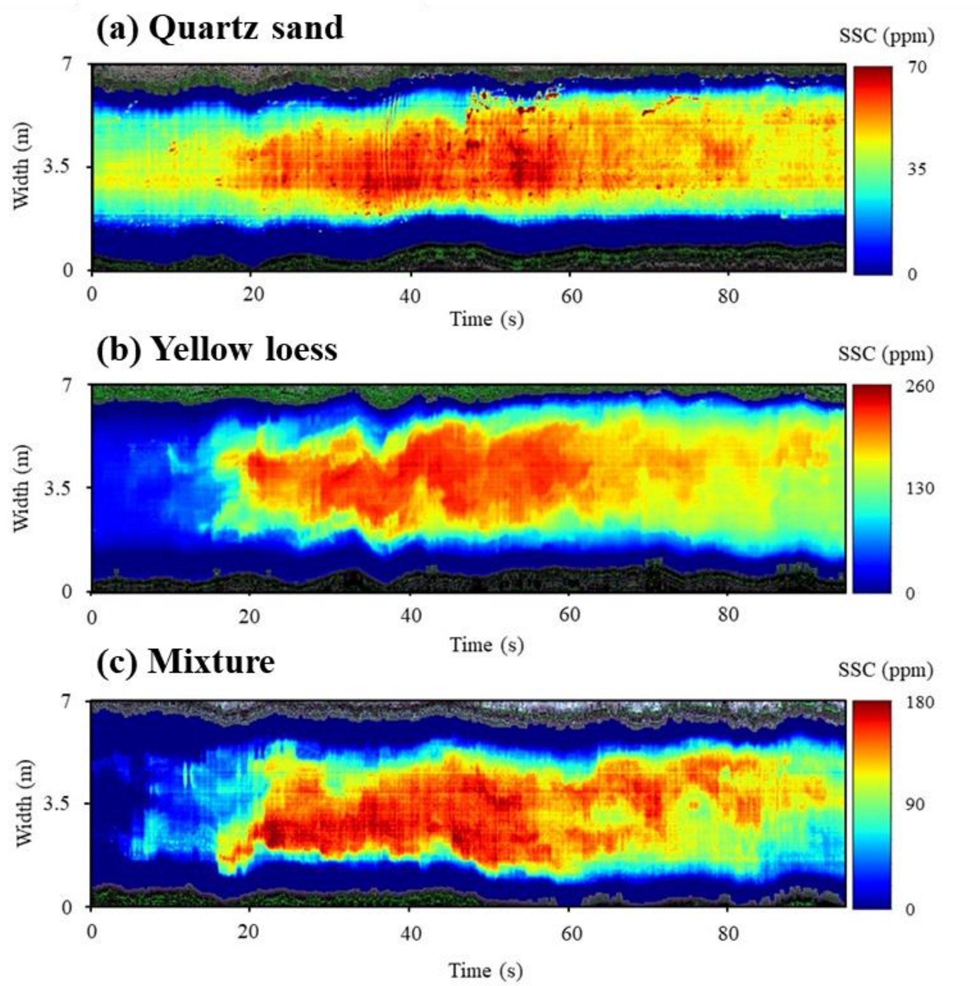

Fig. 4. 15. Spatiotemporal SSCv distribution retrieved from CMR-OV in Exp. 2-1: (a) quartz sand, (b) yellow loess, and (c) mixture.

Fig. 4.16 depicts a comparison of the retrieved BTCs of SSC_V using CMR-OV with the in-situ measured BTCs. The estimated SSC_V from both the training and test datasets yielded good agreement with the in-situ measured SSC_V. Different segments of the retrieved BTCs were assessed: rising limb, falling limb, and tail (Choi et al., 2020; Kwon et al., 2021a). Using these segmented BTCs, the influence of the concentration gradient on SSC error was assessed. The results are summarized in Table 4.7; the MAPE of the rising limb was the largest in all cases. In particular, Exp. 2-1-3 (mixture) showed the poorest performance for a rising limb, with a MAPE of 7.76% and 27.76% for the training and test dataset, respectively. Therefore, the spectral reflectance is unstable when the SSC_V changes rapidly. In terms of sediment type, the lowest MAPE (1.11% and 7.01% for the training and test dataset) were obtained for quartz sand (Exp. 2-1-1) even though the OBRA with quartz sand showed the lowest accuracy (Fig. 3.30).

Table 4. 9. Evaluation of estimated BTC from CMR-OV according to parts of BTC.

Case	MAPE (%)					
	Rising limb		Falling limb		Tail	
	Training	Test	Training	Test	Training	Test
Case 2-1-1 (quartz sand)	1.11	7.01	0.87	2.32	0.88	6.80
Case 2-1-2 (yellow loess)	3.02	18.89	1.29	15.31	1.27	8.94
Case 2-1-3 (mixture)	7.76	27.76	2.18	9.62	1.59	11.11

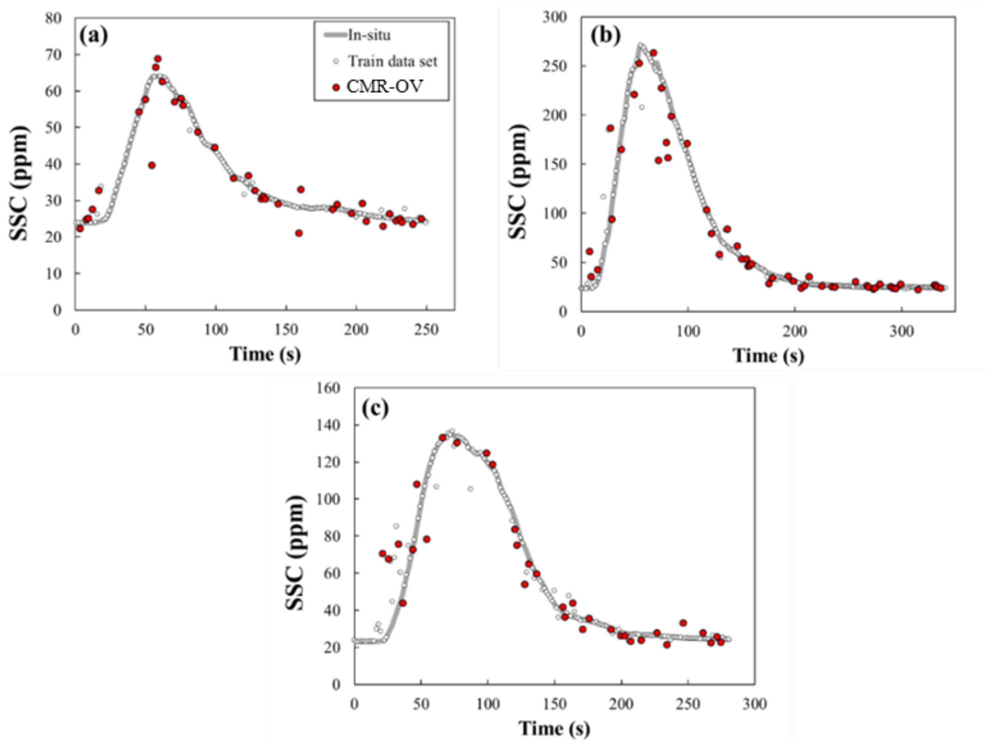

Fig. 4. 16. Comparison of in-situ measured BTC of SSC_V and retrieved BTC of SSC_V using CMR-OV with training data set and test data set: (a) quartz sand, (b) yellow loess, (c) mixture.

The spatiotemporal SSC_V distribution of Exp 2-2, conducted in a meandering channel, was mapped from the hyperspectral images of Exp. 2-2-3~2-2-7. Figs. 4.17 and 4.18 show the retrieved spatiotemporal SSC_V distributions that show the SSC_V variation in the transverse direction over time in water Sections 2 and 3 for each injected sediment type, along with the RGB images. These SSC_V distributions had cloud shapes, similar to those in the RGB images in all cases. However, for the quartz sand, the cloud shapes had abnormal visibility in the RGB images with a low SSC_V range. Even in this challenging case, the correct concentration field could be extracted using the CMR-OV. The concentration range of the entire field was estimated to be similar to the in-situ measurements. The SSC_V cloud showed significantly different behavior in each section according to the sediment type (Figs. 4.17 and 4.18). The higher the density of each sediment, the higher the sedimentation rate, which induces lower SSC_V and movement of suspended sediment against the flow. The proportion of trapped sediment near the side of the channel, induced by the wall friction that traps the sediment particles, was larger in quartz sand and mixture than that in yellow loess. Using the conventional in-situ measurements, such SSC_V distribution near the wall was hard to be measured accurately, and this unmeasured SSC_V would cause the underestimation of sediment load. Yellow loess showed more conservative behavior than the quartz sand; the discrepancy in SSC_V distribution varied with the particle size and sediment density. The tail of the SSC_V distribution of yellow loess was predominantly generated in the mainstream, implying that the fine and light sediments were more affected by the secondary flow induced by channel meandering through Sections 2 to 3. In the case of quartz sand and mixture, despite the sophisticated retrievals of SSC_V by CMR-OV, considerable noises were noticed at the tail of the SSC_V distribution. This is because the suspended sediment behaved irregularly due to turbulent diffusion, and the bottom reflection was more dominant in the low than that in the high SSC_V range.

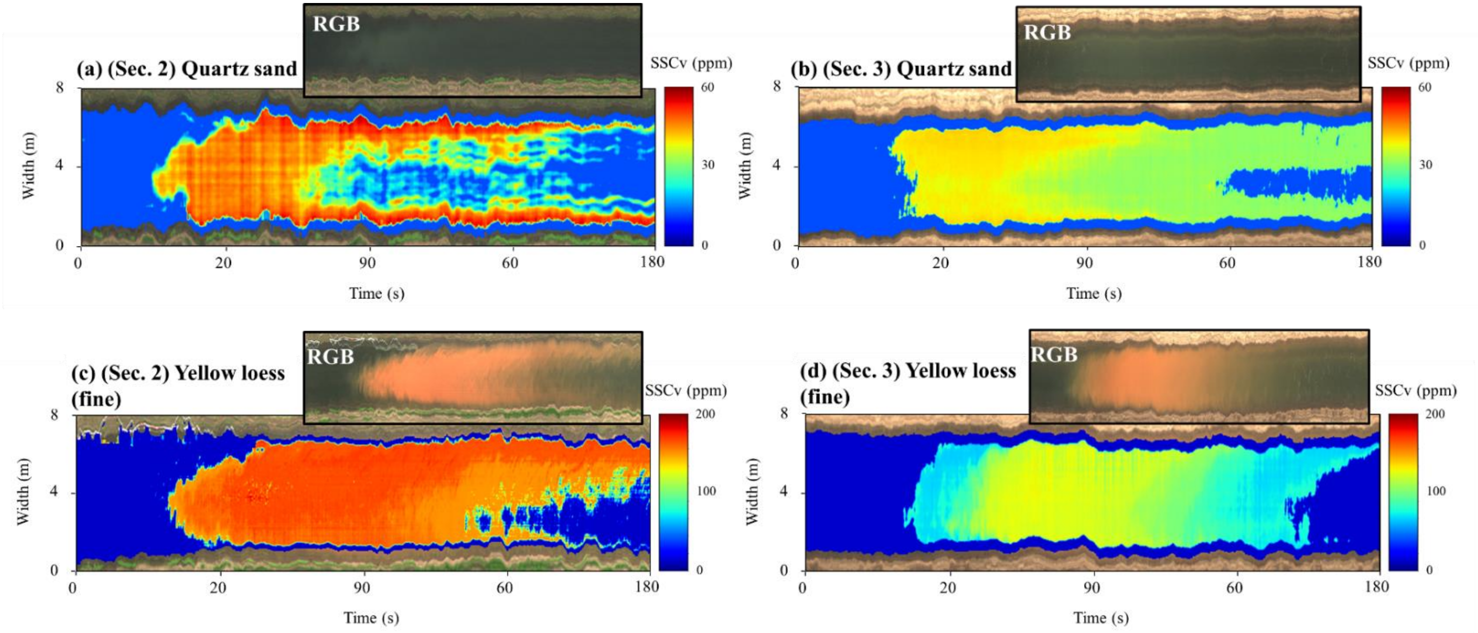

Fig. 4. 17. Spatiotemporal SSC_V distribution retrieved from CMR-OV in Exp. 2-2: (a and b) quartz sand, (c and d) fine yellow loess.

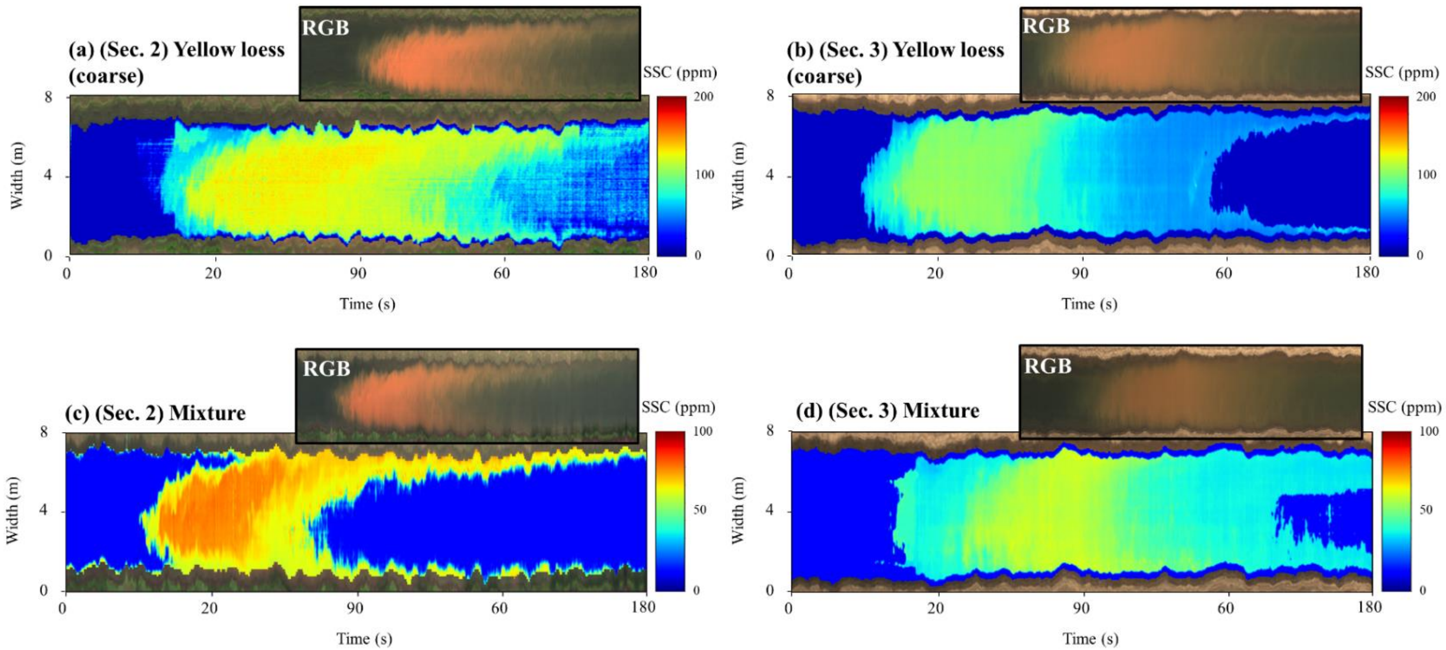

Fig. 4. 18. Spatiotemporal SSC_V distribution retrieved from CMR-OV in Exp. 2-2: (a and b) coarse yellow loess, (c and b) mixture.

5. Evaluation of field applicability of CMR-OV

5.1 Outline of field applicability test

In this chapter, the field applicability of CMR-OV was evaluated using experimental datasets, detailed in Chapter 3. The evaluation was performed in four respects: (1) Cross-applicability; (2) Uncalibrated dataset applicability; (3) Classification of river regions using hyperspectral clustering; (4) Reproducibility of mapping SSC distribution by CMR-OV. Field-scale experiments (Exps. 2-1 and 2-2) were used for model training (Table 5.1). The datasets from field surveys were used to evaluate cross-applicability and uncalibrated dataset applicability. All HSIs acquired from each field were retrieved as SSC maps using CMR-OV. All processes are detailed in the following subchapters.

Table 5. 1. Summary of datasets for field applicability test.

Test type	Experiment Type	Experi -ment	Stream type	SSC_V range (ppm)	No. of data
Training	Field-scale	Exp. 2-1	Straight channel	24.08 ~52.96	650
		Exp. 2-2	Meandering channel	22.52 ~30.32	2,106
Uncalibrated dataset applicability test	Field (straight and meandering rivers)	Exp. 3-1	Hwang river (upstream)	24.08 ~52.96	10; 4 (vertical)
		Exp. 3-2	Hwang river (downstream)	22.52 ~30.32	49
Cross-applicability and merged learning	Field (river confluence)	Exp. 4-1	Confluence of Nakdong and Hwang Rivers	22.25 ~40.01	2,369; 5 (vertical)
		Exp. 4-2		7.73 ~13.74	1,283
Uncalibrated dataset applicability test		Exp. 4-3		5.99 ~24.04	4 (vertical)

5.2 Cross-applicability validation of CMR-OV

The cross-applicability of the remote sensing-based estimator was a critical limitation; this is attributed to the locality of the estimator (Baek et al., 2019; Dethier et al., 2020; Kwon et al., 2022b). This reduces the field applicability of the remote sensing estimator because a single estimator cannot accurately learn various datasets, and it must re-learn in the uncalibrated area. Therefore, local learning, which independently trained the CMR-OV using each survey data, and merged learning, using the combined dataset of field-scale experiments and field surveys, were compared to evaluate the field applicability of CMR-OV. To assess the cross-applicability of CMR-OV, the 5-folds cross-validation was conducted using a merged dataset. All independent datasets in this study had high locality because each measurement was independently implemented and included crucial factors of spectral variability, as detailed in Chapter 2. Therefore, these tests can evaluate whether CMR-OV can be extended to various fields.

The field-scale experiments (Exps. 2-1 and 2-2) and field surveys (Exps. 4-1 and 4-2) were used to evaluate the cross-applicability of CMR-OV in this chapter. These datasets were independently collected under various sediment and stream conditions; therefore, they are suitable for verifying cross-applicability. Other datasets from field surveys (Exps. 3-1, 3-2, and 4-3) were used to verify the applicability of CMR-OV using uncalibrated datasets, and this issue is elaborated in Chapters 5.2 and 5.3.

To compare local and merged learnings, this study trained each model by randomly sampling 80% of its dataset and evaluated it using the residual data in each training. CMR-OV could accurately learn all the data acquired from the confluence in local learning, even the bimodal distributed dataset of Exp. 4-1 (Fig. 5.1). When CMR-OV was trained by combining all experimental and field survey data under various conditions, both training and test accuracy improved substantially. Although CMR-OV learned various datasets, the effective wavelength ranges were similar in the case of field-scale experiment results. UV, red, red-edge, and NIR indicated high relative band importance (Fig. 5.2). NIR and UV controlled the spectral variability of other physical properties (i.e., bottom, water depth, suspended matter), along with Red and Red-edge, which are closely related to the intrinsic spectral properties of the suspended sediment. Therefore, the CMR-OV can complement the locality using various wavelength ranges, which was the most critical limitation in earlier studies (Dethier et al., 2020; Kwon et al., 2022a). Therefore, CMR-OV could be a robust model as it learns more datasets under various conditions.

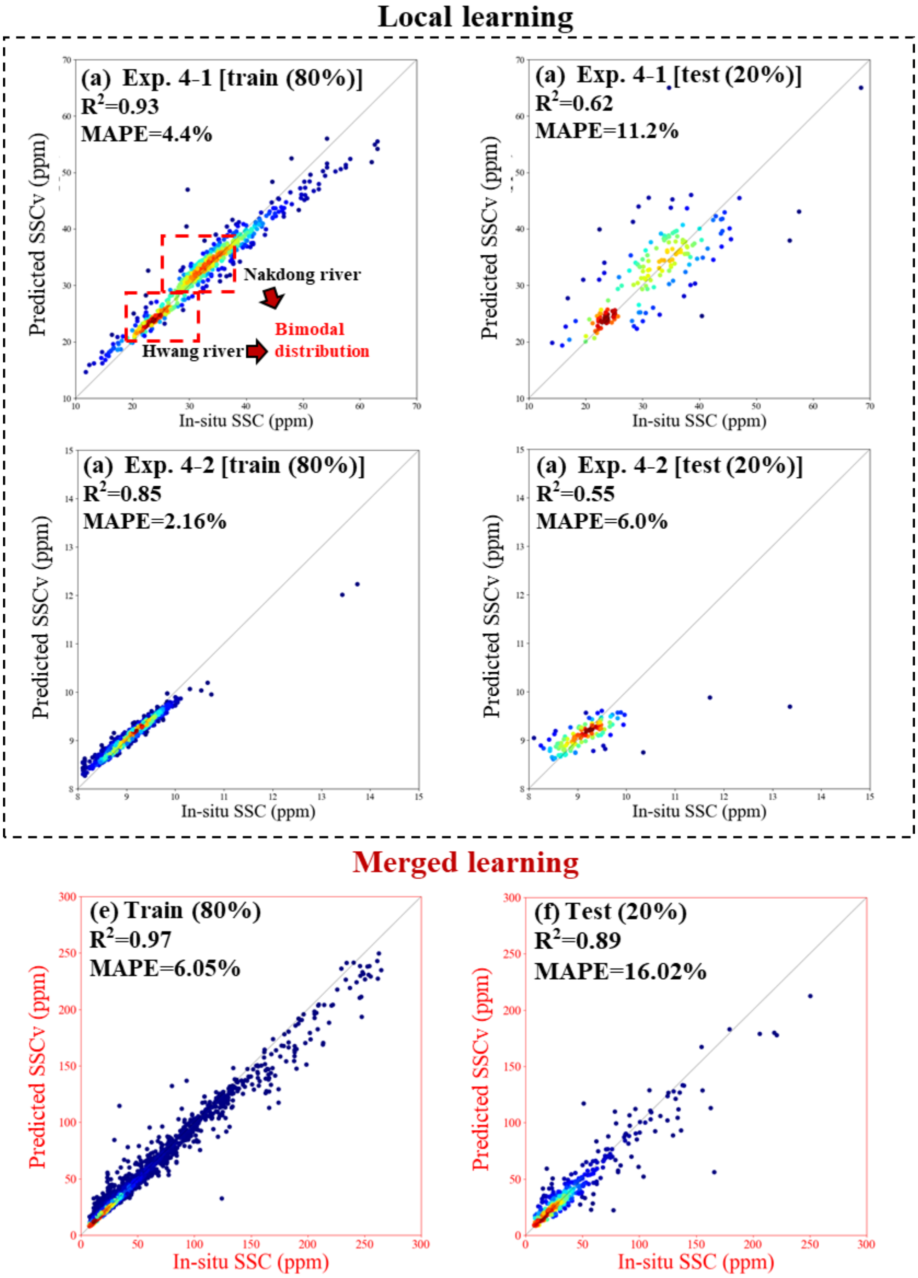

Fig. 5. 1. Comparison between in-situ measurement and prediction of local learning and merged learning.

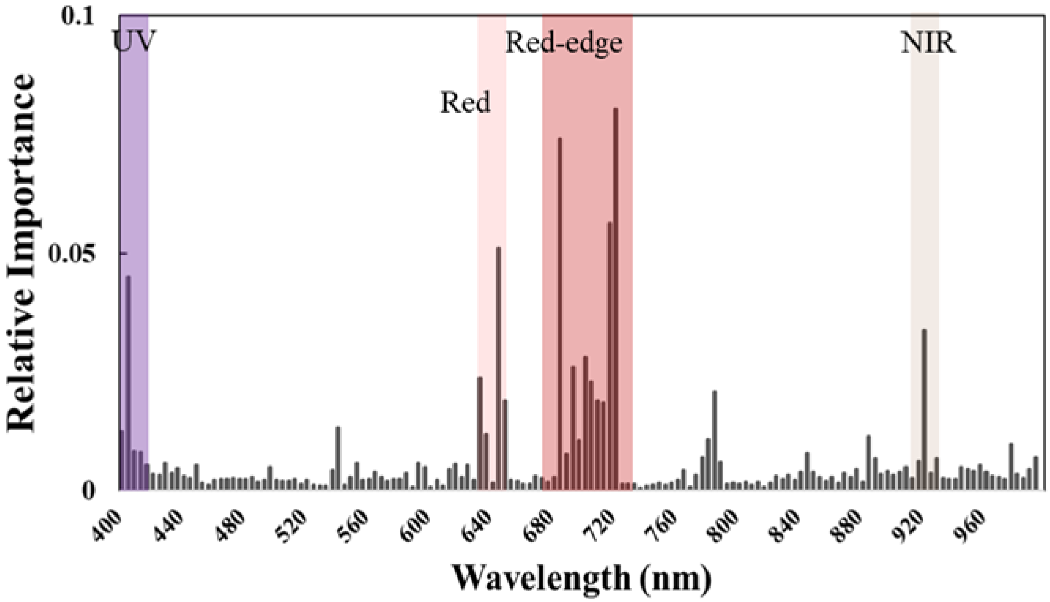

Fig. 5. 2. Relative band importance from CMR-OV by merged learning.

Cross-validation is a resampling procedure used to evaluate cross-applicability (Probst et al., 2019). To evaluate cross-applicability of CMR-OV, 5-folds cross-validation was implemented to split the test and training dataset in the ratio of 80 % and 20 %, respectively. Evaluation using the dataset under various conditions indicated how the estimator should perform in general when applied to predict under independent conditions with the training of the estimator. The dataset in this validation was randomly shuffled, then split into five unique groups. Each group was taken as a test dataset, and the remaining groups were used for the training dataset. Fig. 5.3 shows the randomly shuffled test and train dataset of 5-folds, which indicates the training and test dataset in white and black. Using these datasets, the training and test scores of R^2, and their standard deviation were estimated according to the number of clusters, as shown in Fig. 5.4 (a). Both the training and test performance were best with two clusters with 1 % of the standard deviation of cross-applicability. The evaluation using RMSE showed a similar result; the test score was best with 2 ~ 4 clusters, and the averaged RMSE was 12 ppm with 2 ppm of standard deviation (Fig. 5.4 (b)). In addition, the learning rate of CMR-OV was more rapid with increased clusters (Fig. 5.4 (c)). Therefore, the number of training data for each model is dominant in the learning rate rather than in the number of clusters. Consequently, CMR-OV showed competent performance in the cross-applicability test. However, the dataset in this study was insufficient in the range of SSC_V over 300 ppm. To improve CMR-OV as a more robust estimator, this range of SSC_V should be added with the additional survey in future studies.

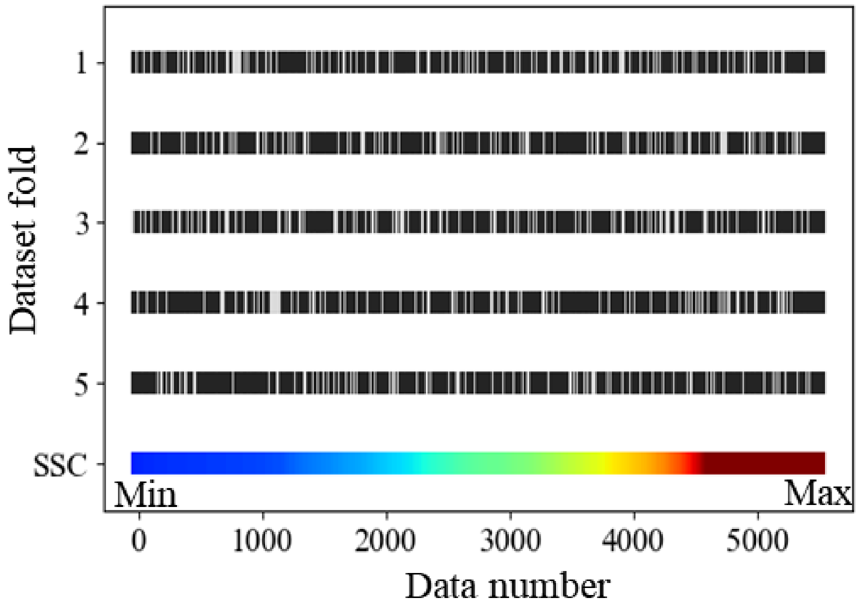

Fig. 5. 3. Shuffled dataset of 5 folds cross-validation; training dataset is in black, and test dataset is in white.

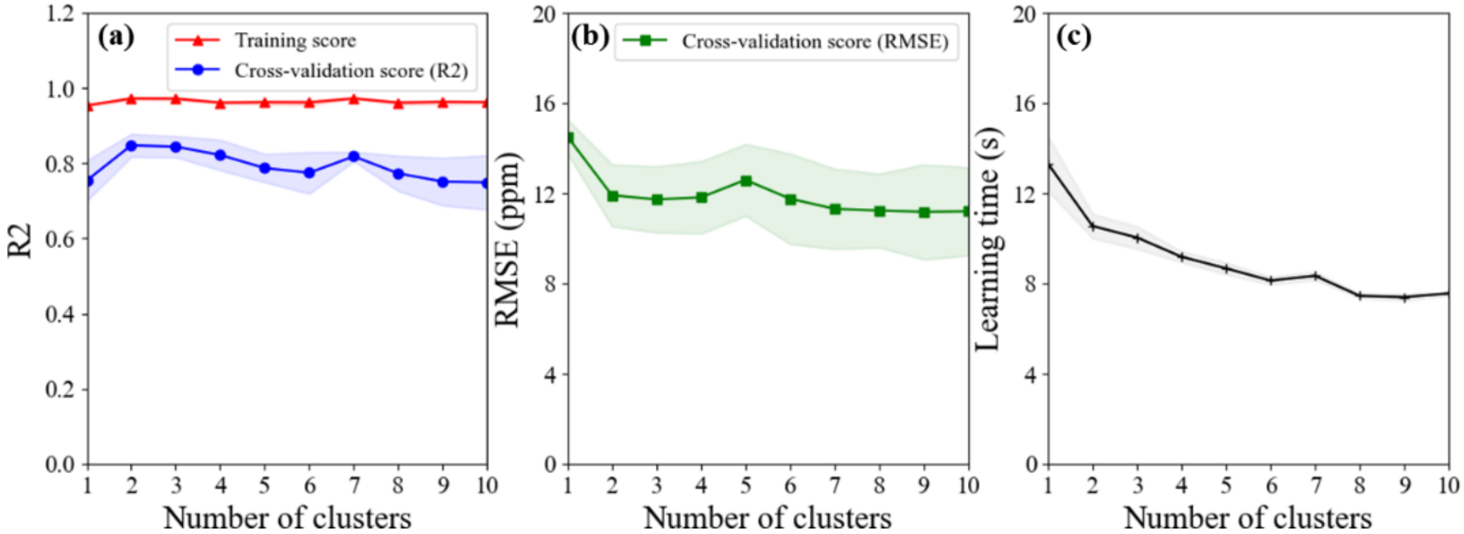

Fig. 5. 4. Cross-validation results according to the number of clusters: (a) training score and a test score of R^2, (b) test score of RMSE, and (c) learning rate.

5.3 Assessment of field applicability in rivers with simple geometry

In order to assess the field applicability of CMR-OV in uncalibrated datasets, it was validated using datasets collected from a straight reach upstream of the Hwang River (Exp. 3-1) and a weak meandering reach downstream of the Hwang River (Exp. 3-2). Ten points of hyperspectral spectrum and corresponding in-situ measured SSC_V were used to validate CMR-OV. The SSC_V was measured for 1 min at each point as described in Chapter 3.4.1. The time-averaged SSC_V and its *SD* were plotted in Fig. 5.5. The concentration values at the measured points were generally similar; however, the concentrations were relatively high in Points 5 and 6, and the standard deviation was also high owing to the temporary movement of bedload. In these two points, CMR-OV underestimated the SSCv because it is difficult to reflect unsteady concentration changes from instantaneous images acquired by UAVs. Nevertheless, CMR-OV gave an accurate estimation with an RMSE of 8.69 ppm and a MAPE of 18.43%, while the explicit model highly overestimated in the uncalibrated area, resulting in an RMSE of 304.77 ppm and a MAPE of 84.29% (Fig. 5.5). Fig. 5.6 shows the spatial SSCv distributions retrieved by both models. CMR-OV reproduced the concentration distribution clearly, but the explicit model overestimated the concentration by ten times except for some areas and the noise could not be controlled either. Therefore, CMR-OV could successfully account for the different bottom and sediment properties from the training dataset, and it was more globally applicable than the explicit model.

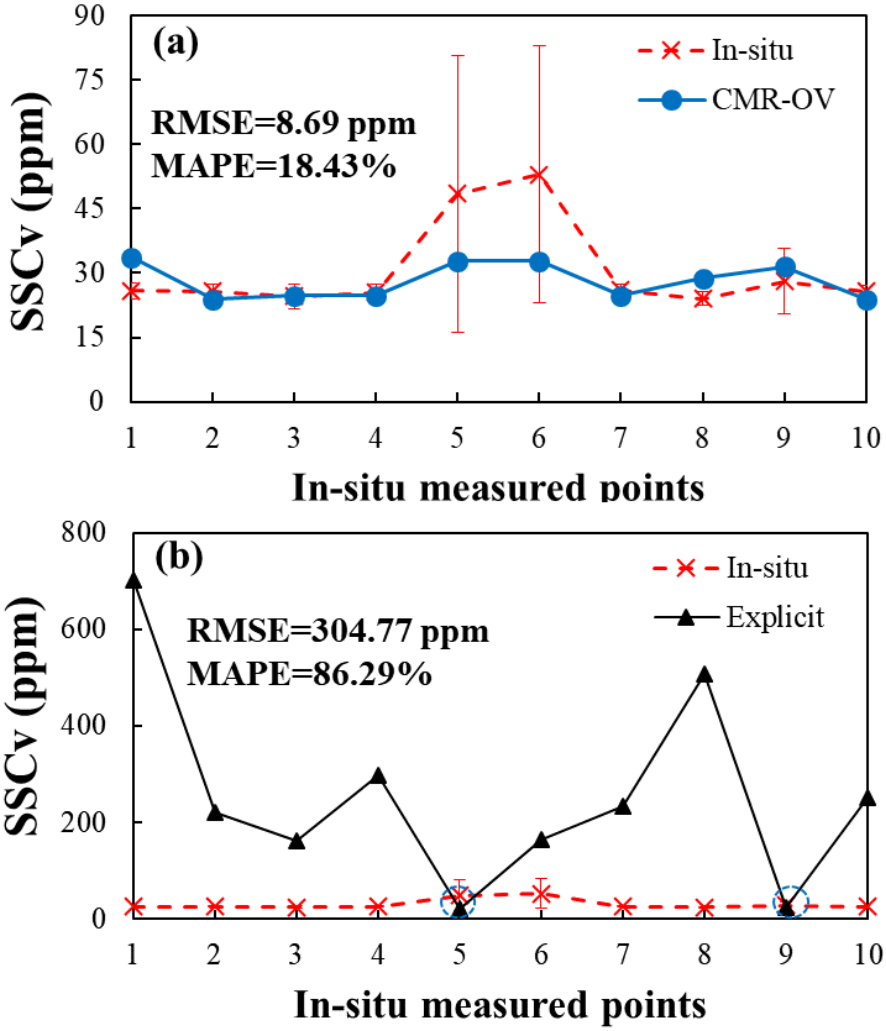

Fig. 5. 5. Comparison of in-situ measured time-averaged SSCv and SSCv estimated using (a) CMR-OV and (b) explicit model (SR 2) in Exp. 4-1.

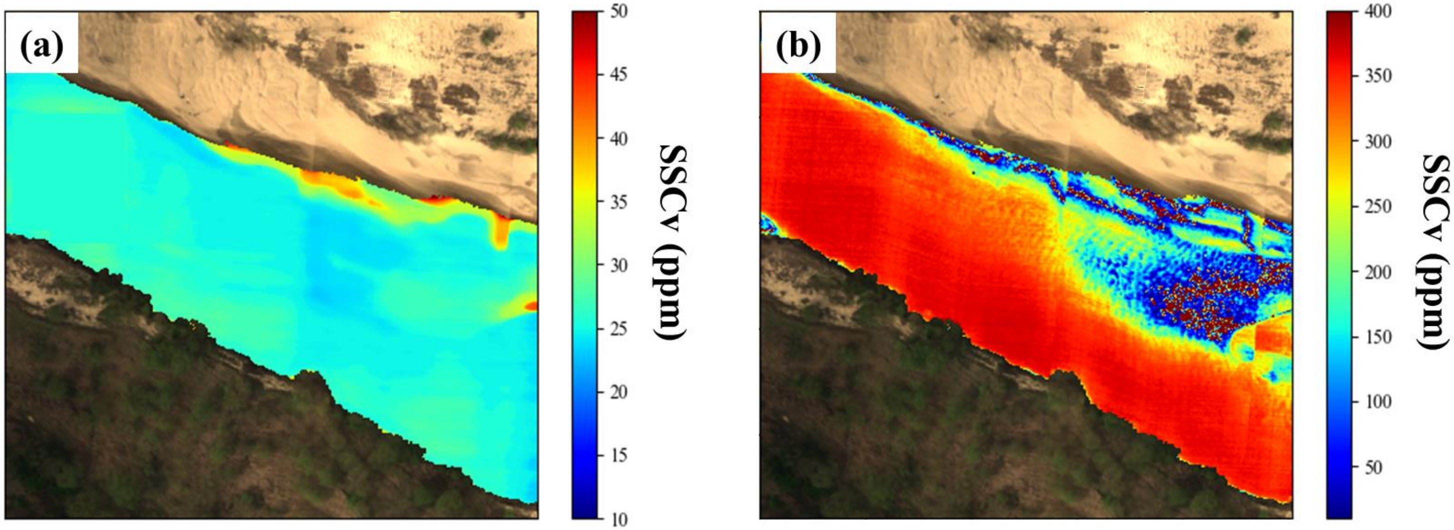

Fig. 5. 6. Spatial SSCv distributions in Exp. 3-1 retrieved using (a) CMR and (b) explicit model (SR 2).

Forty-nine points of hyperspectral spectrum and corresponding in situ measured SSC_V were collected at a downstream reach of Hwang River during Exp. 3-2, as described in Chapter 3.4.2. The validation results using a dataset of Exp. 3-2 are shown in Fig. 5.7, which compares the in situ measured SSC_V and the estimated SSC_V from each model at sampling points shown in Fig. 3.18 (b). The in-situ measurement showed that the SSCv around 25 ppm was uniformly distributed at all points. Nevertheless, it was difficult to accurately predict SSC_V in this area since the water depth of the measurement points varied considerably. This difference in water depth caused a discrepancy in the effect of the bottom reflectance. This depth variation might cause significant uncertainty in remote sensing-based SSC prediction (Baek et al., 2019; Ma et al., 2011; Tolk et al., 2000; Volpe et al., 2011). Therefore, the explicit model yielded highly overestimated results except for two shallow points, as shown in Fig. 5.7 (a); CMR-OV agreed with the in situ measured SSC_V. The CMR-OV exhibited an accurate performance with an RMSE of 1.06 ppm and a MAPE of 3.67%. Therefore, CMR-OV could successfully account for water depth differences and was more globally applicable than the explicit regression model. The reason for this is that the ML regression models learned spectral bands in wider wavelength ranges, which represented the effects of variability of suspended sediment and bottom properties with water depth difference. Fig. 5.8 shows the SSCv distribution map retrieved by each model. The SSCv spatial distribution map estimated from the CMR-OV was reproduced clearly compared to the results of the explicit model, similar to the validation results using a dataset from Exp. 3-1. The CMR-OV generated less noises than the explicit model, as shown in the retrieved map.

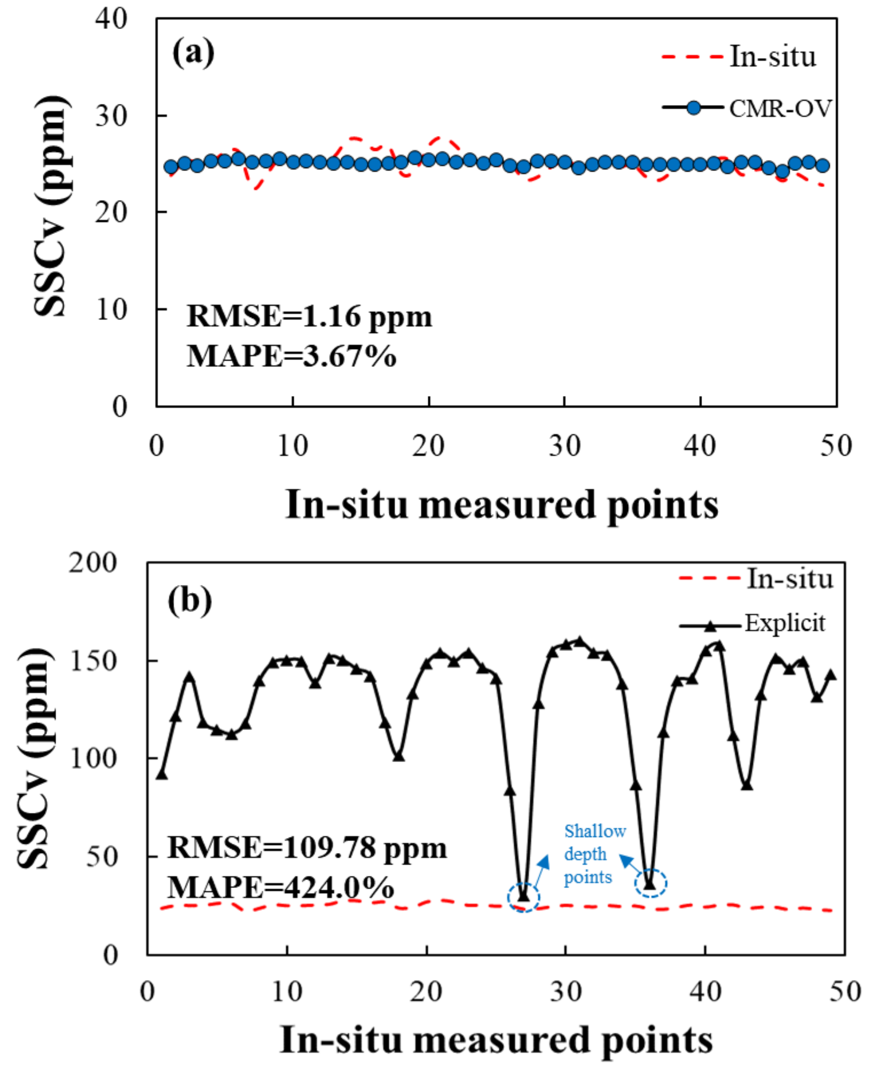

Fig. 5. 7. Comparison of in-situ measured time-averaged SSCv and SSCv estimated using (a) CMR-OV and (b) explicit model (SR 2) in Exp. 3-1.

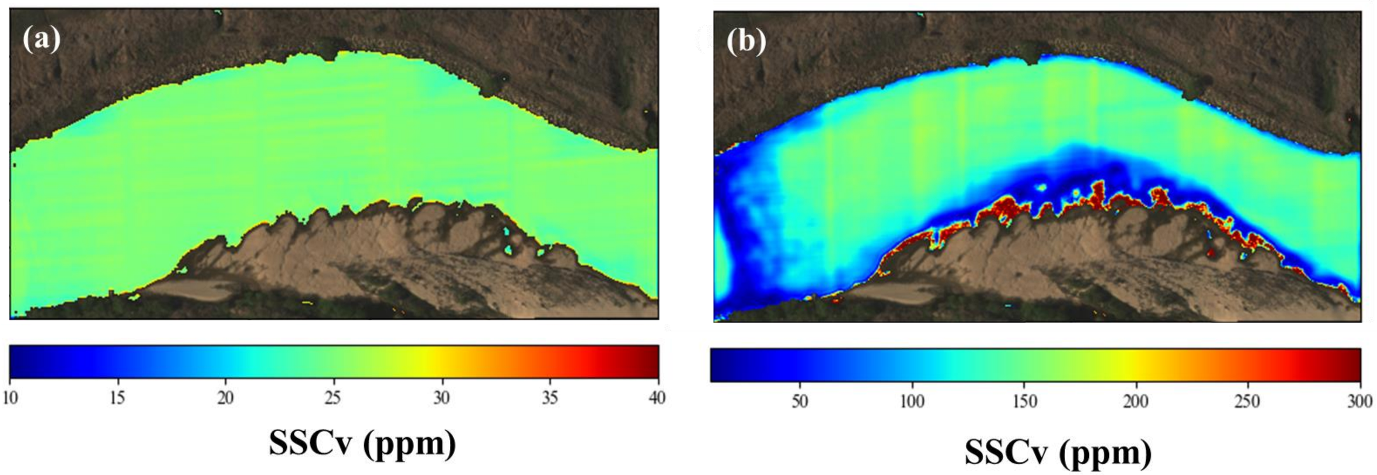

Fig. 5. 8. Spatial SSCv distributions in Exp. 3-2 retrieved using (a) CMR and (b) explicit model (SR 2).

5.4 Assessment of field applicability in river confluences

5.4.1 Classification of river regions using hyperspectral clustering

Using the HSI in three surveys (Exp. 4-1 ~ 4-3), the hyperspectral clustering in CMR-OV was assessed for classifying the two water bodies in a river confluence. HSI acquired in Exp. 4-1 was separated into two clusters (Fig. 5.9 (a)). These clusters were precisely classified as the water body of Nakdong and Hwang Rivers, with a mixing layer in between. However, the sandbar area located at the stagnation zone near the confluence junction was included in Cluster 2. It can be inferred that the optical characteristic of this area was similar to that of the Hwang River since the reflectance of the sand bottom was dominant, and the water column effect was negligible by shallow water depth ($H < 1$ m). In addition, the result of apparent classification demonstrated that both rivers have distinct optical characteristics, and confluent flows from both rivers at near-field confluence did not mix well. The averaged hyperspectral spectrum of each cluster also had different profiles, as shown in Fig. 5.9 (b) and (c). Although the SSC_V of Nakdong River was higher than that of the Hwang River, the reflectance was the opposite, owing to the high contribution of scattering effect from fine sediment particles and bottom reflectance by shallow water depth (Table 5.1). This result is contrary to the notion that the SSC and reflectance have a positive correlation (Binding et al., 2005; Montanher et al., 2014; Pereira et al., 2019; Qu et al., 2016; Umar et al., 2018). The optical variability from sediment particle size and bottom reflectance is critical in river confluences, as discussed in Chapter 3.5. Fig. 5. 10 (a) is the hyperspectral spectrum of both clusters in PC 1 and PC 2 domains. PC 1 occupied 93% of the variance ratio, and Cluster 2 is widely spread compared to Cluster 1, which is mainly concentrated at low values in this domain. In addition, as represented in the distribution of PC 1 (Fig. 5. 10 (b)), both rivers have apparently different optical characteristics. Overlapping bins of this histogram were mainly distributed around zero value, and the frequency was slightly low. This indicates poor effect of mixing after confluence.

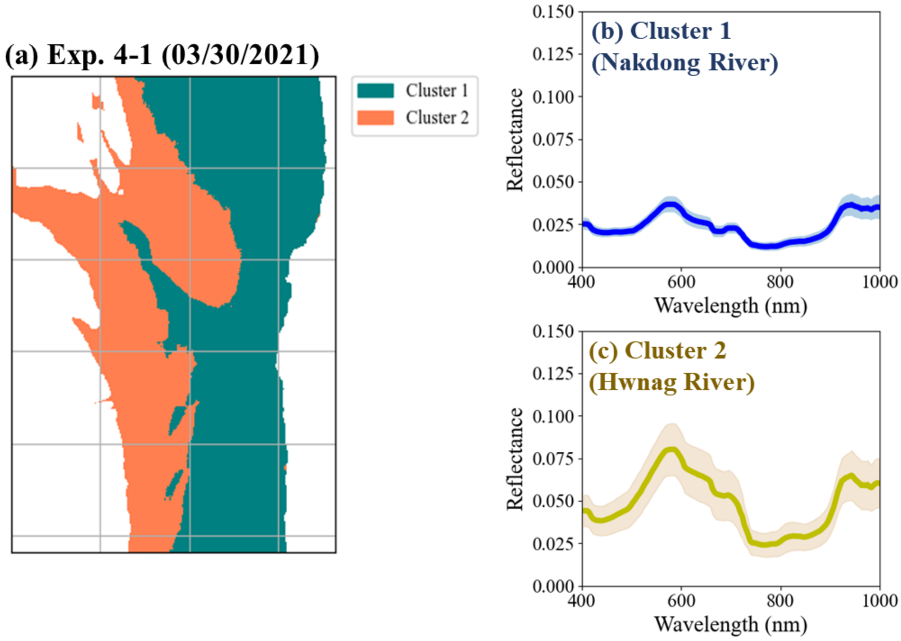

Fig. 5. 9. (a) Cluster mapping result of HSI acquired in Exp. 4-1 and averaged hyperspectral spectrum of (b) Cluster 1 and (c) Cluster 2.

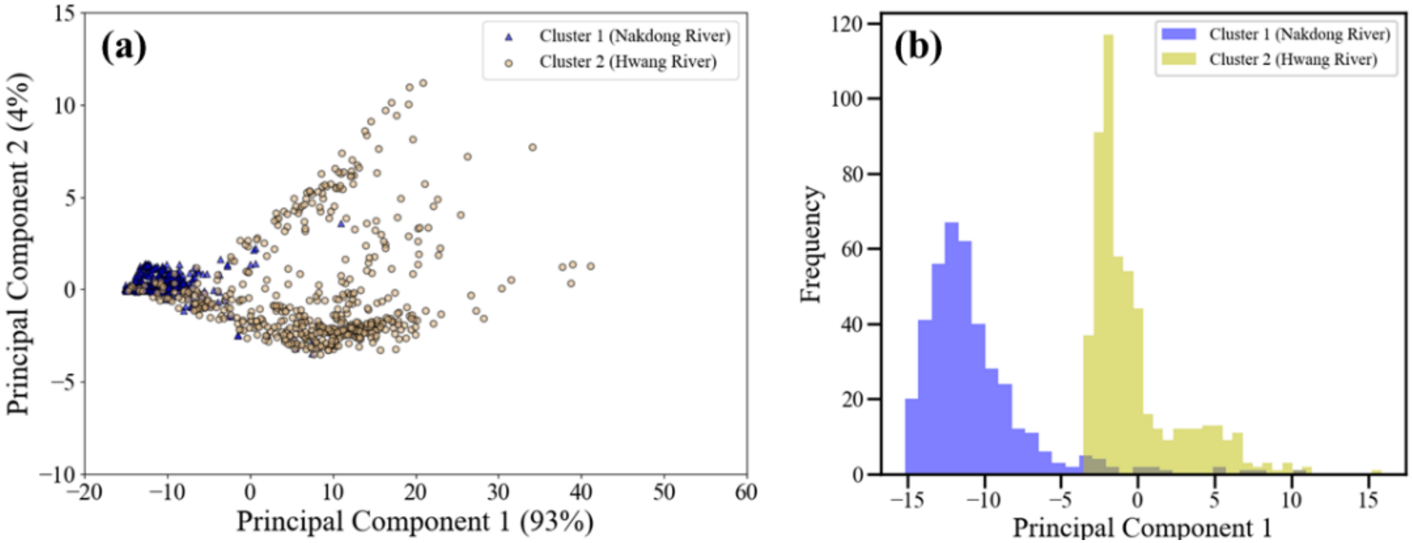

Fig. 5. 10. PCA results of Survey 1: (a) Hyperspectral spectrum in PC 1 - PC 2 domain and (b) histogram of PC 1.

Fig. 5.11 shows the values of SSC_V, *d50*, and water quality parameters (turbidity, water temperature, pH, and electronic conductivity (EC)) from hyperspectral clusters. Both clusters showed apparently different characteristics, and these values were almost similar to the in-situ measured values, (Table 4.1). In addition, the hyperspectral clustering result was compared to the clustering using in-situ measured suspended sediment and water quality parameters. When the in-situ measured data was divided into two clusters (Fig. 5.12 (b)), the patterns of the two clusters were almost identical with the hyperspectral clustering results except for the sand bar area (Fig. 5.12 (a)). Even when these clusters were divided into three and four, the result was more finely divided within the two hyperspectral clusters, as indicated in Figs. 5.12 (c) and (d). This result demonstrates that the hyperspectral clustering can classify differences in water characteristics without water quality information; it can simplify the variability of optical and sediment-water characteristics of river confluences using hyperspectral imagery.

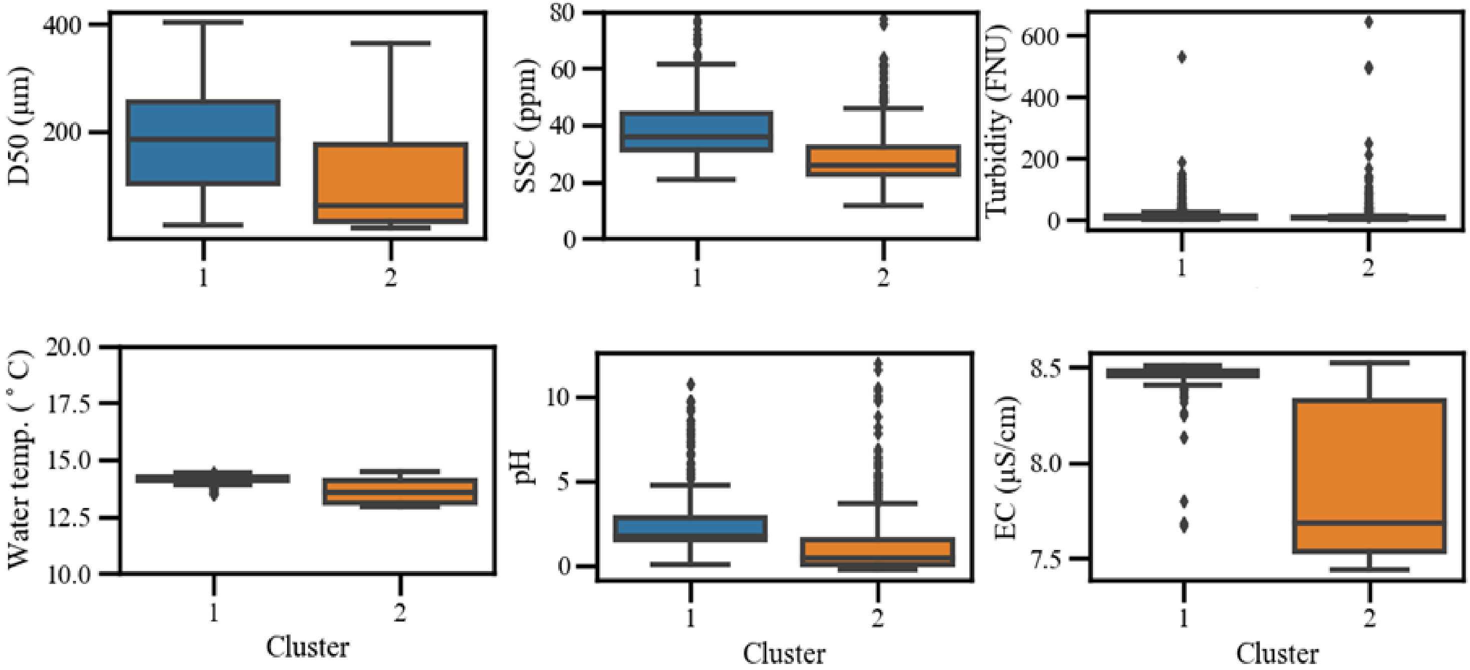

Fig. 5. 11. Sediment-water quality parameters of hyperspectral clusters in Exp. 4-1.

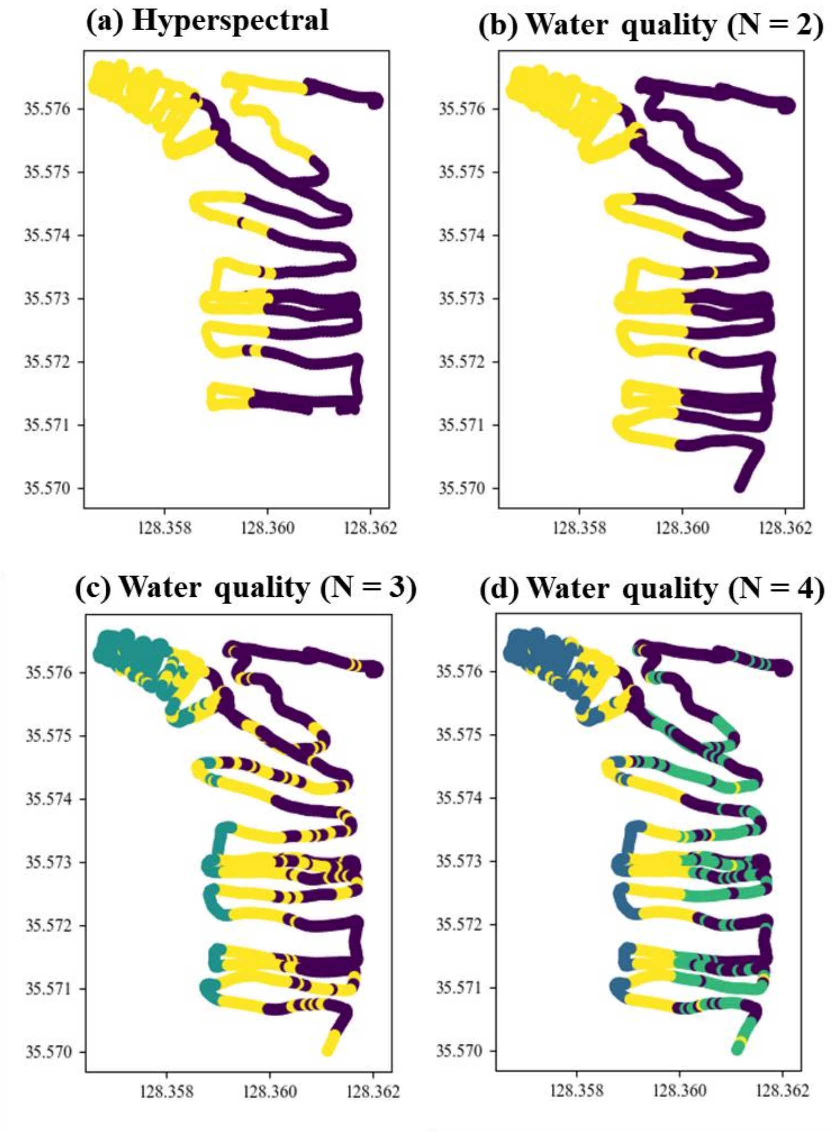

Fig. 5. 12. Comparison between hyperspectral clustering and in-situ measured clustering.

In Exp. 4-2, the SSC_V and its contrast between both rivers were very low (Chapter 3.4). Although this condition is challenging in classifying the water body of both rivers, the hyperspectral clustering assigned three clusters: the Nakdong River, upstream and downstream of the confluence, and the Hwang River (Fig. 5.13 (a)). In this case, the bottom reflectance mainly contributed to the classification result since both rivers had clear water and shallow depth ($H < 2$ m). The contribution of bottom reflectance is vastly increased under 2 m of water depth (Chapter 2.1.2.3). Therefore, the reflectance values of the three clusters had similar magnitudes with that of Exp. 4-1, despite low SSC_V. Accordingly, due to the effect of these bottom reflections, the classification of the Nakdong River into upstream and downstream was induced by the dynamic change in geometry from the confluent flows.

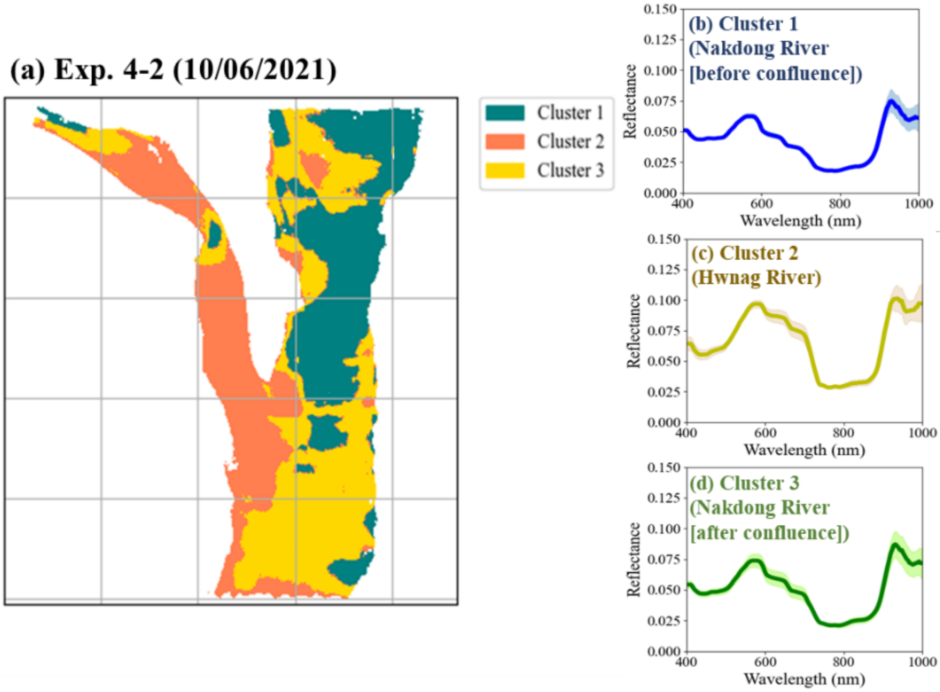

Fig. 5. 13. (a) Cluster mapping result of HSI acquired in Exp. 4-2 and averaged hyperspectral spectrum of (b) Cluster 1, (c) Cluster 2, and (c) Cluster 3.

The PCA result of Exp. 4-2 was also different from that of Exp. 4-1. The variation ratio of PC 1 of Exp. 4-2 was relatively lower than that of PC 1 of Exp. 4-1, at 76 %. The Nakdong River in Exp. 4-1 had a high SSC_V owing to the relatively deep water. PC 1 was less affected by bottom reflection. However, the low SSC_V and water depth caused the scattering of PC 1. The upstream showed a bimodal distribution, and the downstream appeared close to a Gaussian distribution; Fig. 5.13 (b) shows that the upstream and downstream distributions are apparently different. In addition, the Hwang River showed values close to the downstream of the Nakdong River, indicating that the waterbody and bottom characteristics after confluence were dominated by the Hwang River. Unlike in Exp. 4-1, the sediment-water quality values of each hyperspectral cluster were estimated with slight differences. This result is also similar to the in-situ measured values (Table 3.10). The distinct optical characteristics of each hyperspectral cluster in Exp. 4-2 were not induced by the sediment-water quality characteristics; instead, it can be attributed to the bottom reflectance.

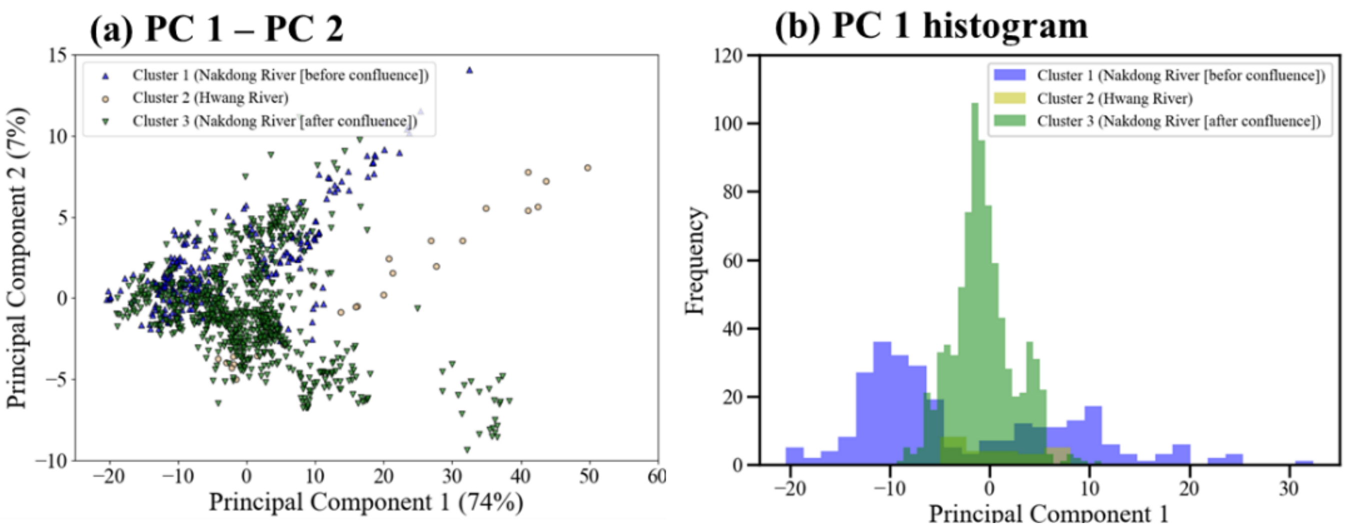

Fig. 5. 14. PCA results of Exp.4.2: (a) Hyperspectral spectrum in PC 1 - PC 2 domain and (b) histogram of PC 1.

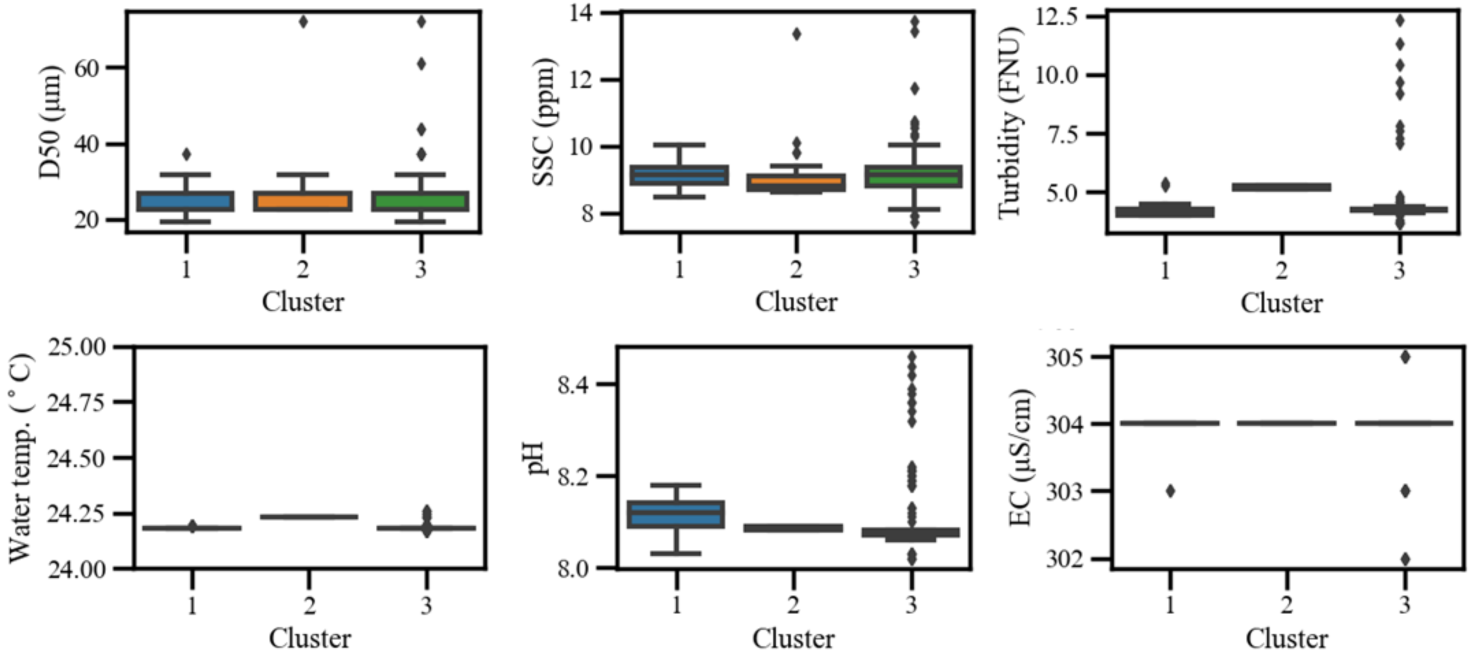

Fig. 5. 15. Sediment-water quality parameters of hyperspectral clusters in Exp. 4-2.

In Exp. 4-3, the contrast in the SSCv and turbidity between the two rivers was 5.39 ppm and 1.02 NTU (Table. 3.10); there was an apparent color difference between both rivers (Fig. 3. 21 (c)). Owing to these differences, hyperspectral clustering apparently divided the HSI of river confluence into two water bodies corresponding to the two rivers as two clusters (Fig. 5.16 (a)). Likewise, the averaged wavelength of the divided clusters had significantly different values. However, the wavelength in the red-edge region (700–800 nm), which is highly correlated with the intrinsic spectral characteristics of the sediment, showed similar reflectance for both rivers. Spectral bands in other wavelength regions showed rather high values in the Hwang River with low SSC_V. These results were identical to those of Exp. 4-1. The downstream part of the confluence in Exp. 4-1 was divided based on the mixing layer; however, the area of the Hwang River after the confluence point in Exp. 4-3 was more minor than that in Exp. 4-1. The two clusters were divided without such a clear mixing layer as in Exp. 4-1 because mixing occurred actively after confluence, and the tributary inflow did not majorly affect the spectral characteristics of the mainstream. This tendency is indicated in Fig. 5.17, which shows the hyperspectral spectrum of both clusters in PC 1 and PC 2 domains (Fig. 5.17). Therefore, the spectral characteristics were more clearly divided than in other cases, indicating the degree of mixing of the confluence to some extent. Fig. 5.18 presents the values of water quality parameters from both hyperspectral clusters. The differences in water quality can be well classified from the hyperspectral clusters, as corroborated by the analysis results of Exp. 4-1 and 4-2. Therefore, hyperspectral clustering was a competent method to classify the river confluence, irrespective of the information on sediment-water quality characteristics. Therefore, it can be a practical process to resolve the spectral variability of the river confluence.

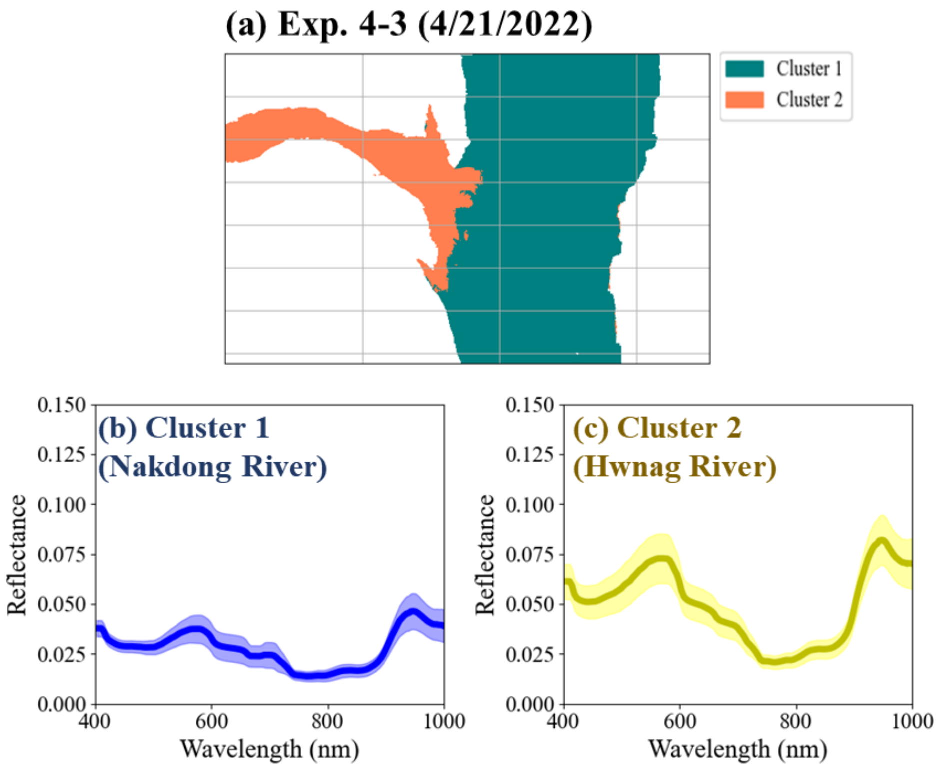

Fig. 5. 16. (a) Cluster mapping result of HSI acquired in Exp. 4-3 and averaged hyperspectral spectrum of (b) Cluster 1 and (c) Cluster 2.

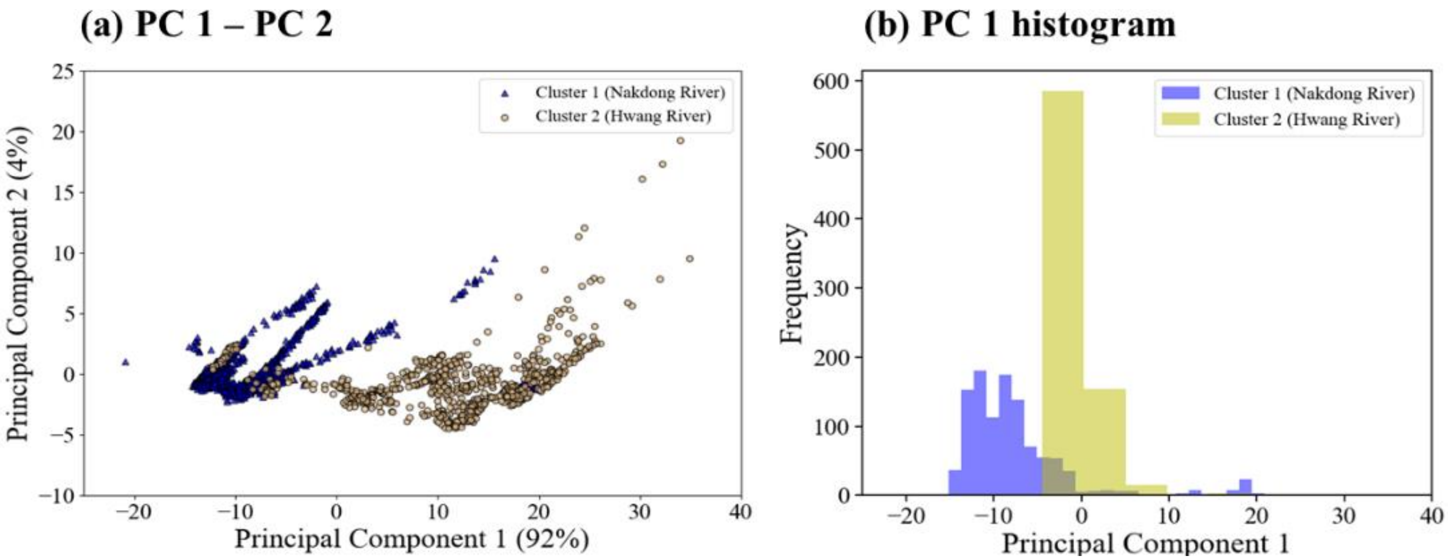

Fig. 5. 17. PCA results of Exp.4-2: (a) Hyperspectral spectrum in PC 1 - PC 2 domain and (b) histogram of PC 1.

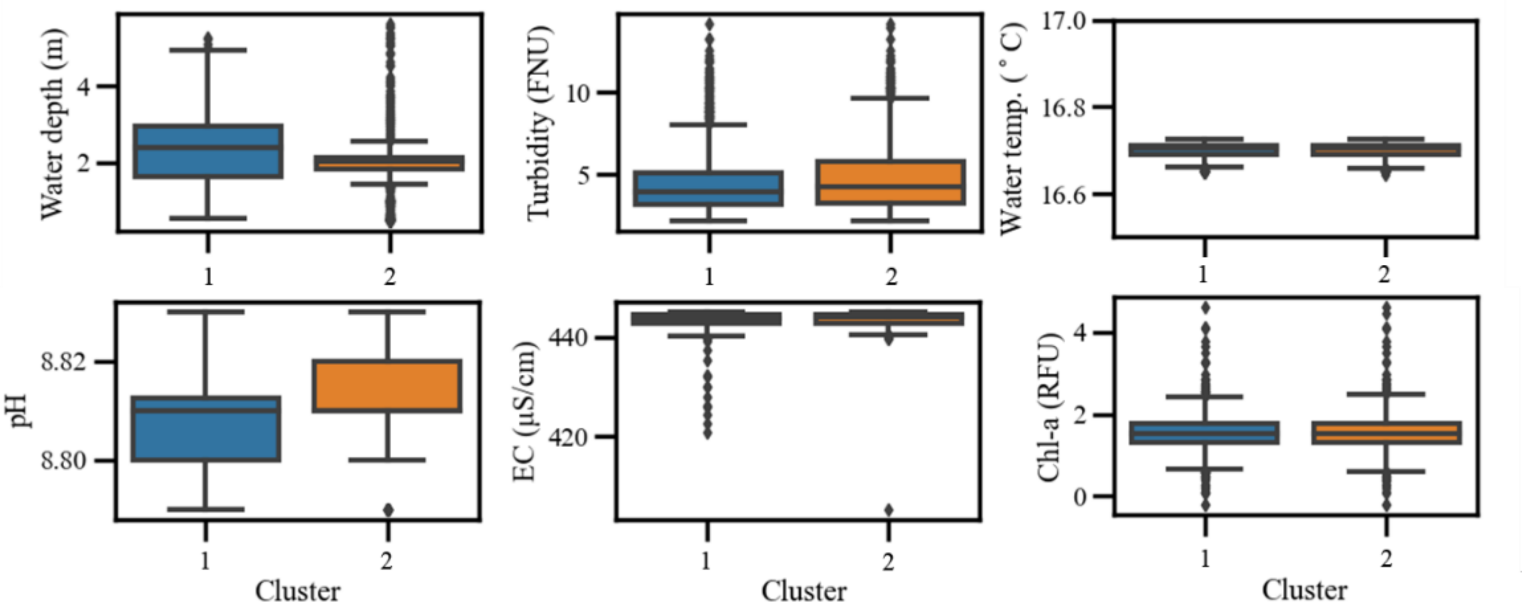

Fig. 5. 18. Sediment-water quality parameters of hyperspectral clusters in Exp. 4-3.

5.4.2 Retrievals of SSC_V map

(1) Exp. 4-1

The trained CMR-OV was applied to retrieve the SSC_V distribution of the confluence of the Hwang and Nakdong Rivers under three different conditions (Exp. 4-1 ~ 4-3). Fig.5.19 presents the mapping result for Exp. 4-1. CMR-OV produced more accurate mapping results than single RF. A concentration reversal with a high concentration occurred in the Nakdong River, unlike the tendency of the tributary to look more turbid in the actual RGB image (Fig. 5.20 (a)). Therefore, this phenomenon caused low reflectance of the hyperspectral spectrum in the Nakdong River with high SSC_V and high reflectivity in the tributary with low SSC_V owing to spectral variability. Therefore, the RF model without clustering overestimated the SSC_V of the tributary, while the CMR-OV precisely reproduced the concentration reversal in Survey 1. The single RF generated a SSC_V map with more noise than CMR-OV. In addition, there was a discrepancy between the results from CMR-OV and single RF in the sandbar area at the stagnation zone near the confluence point. Although this area is located in the Nakdong River, its water depth was under 1 m, which induced a large contribution of bottom reflectance. Despite this bottom effect, CMR-OV could control the effects by delineating this area from hyperspectral clustering, as detailed in Chapter 5.3.1.

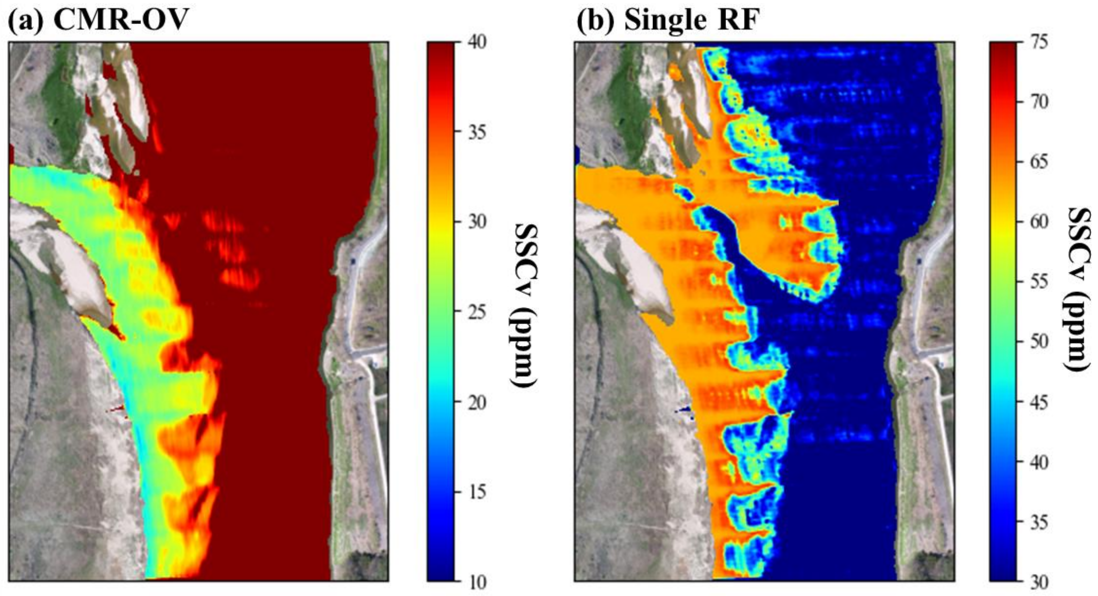

Fig. 5. 19. Comparison of SSC_V mapping results of Survey 1: (a) CMR-OV and (b) single RF.

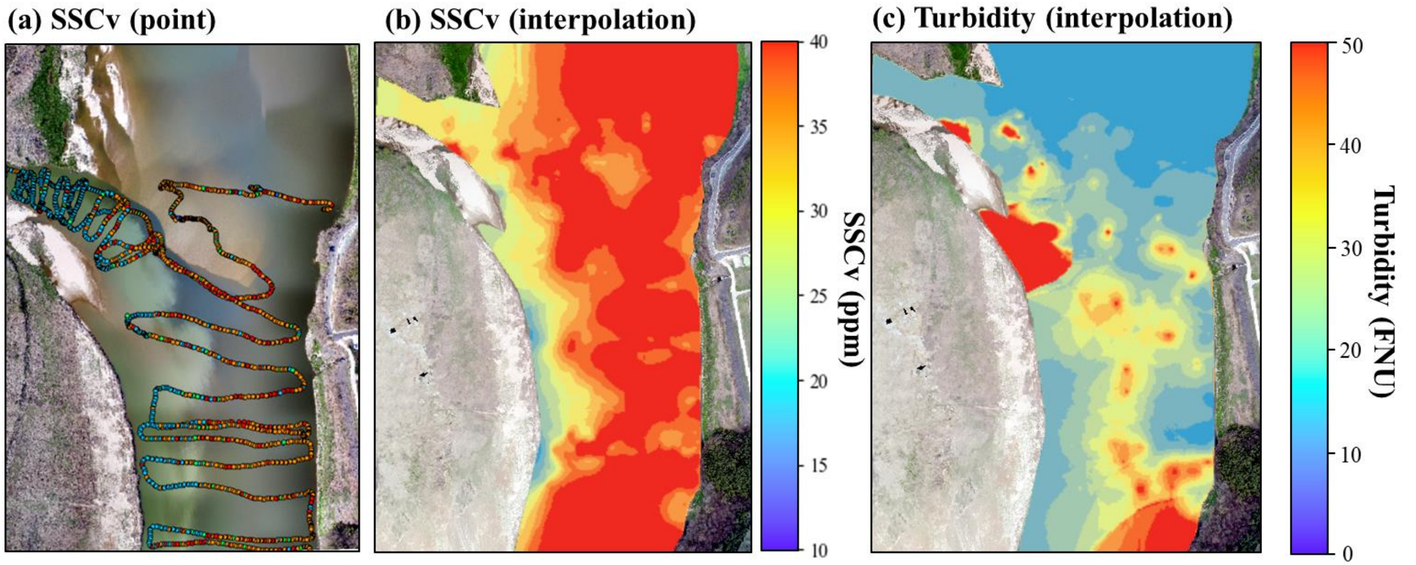

Fig. 5. 20. In-situ measurement-based mapping results of Exp. 4-1: (a) raw SSC_V data, (b) interpolated SSC_V data, and (c) interpolated turbidity data.

In terms of the mixing layer retrievals, unstable interfacial billows were generated at the mixing layer in Exp. 4-1 owing to the complex flow condition at the near-field of confluence. Compared to the RGB image, the CMR-OV reproduced the mixing layer more clearly than the moving boat method using in-situ SSCv and turbidity measurement techniques (Fig. 5.20). The detailed measured data from CMR-OV at the mixing layer could enhance the analysis of the confluence dynamics.

The remote sensing technique generally retrieves the surface concentration based on the strong absorbance of light in the water column, as detailed in Chapter 2.1.2. However, as elaborated in the theoretical research (Chapter 2.1.2), a value close to the average concentration could be obtained in shallow water. The signals of suspended sediment can be received up to the riverbed at depths of 2 m or less, if the bottom signal is well controlled. The SSCv retrieved from CMR-OV showed good agreement with the depth-averaged SSCv profile from in-situ measurements in the NR 5 section (Fig. 5. 21). The estimated transverse profile of SSCv revealed a large concentration gradient within the mixing layer. During the general mixing phenomenon at the confluence, the concentration gradient within the mixing tends to decrease owing to the shear effect (Jung et al., 2019; Lewis and Rhoads, 2015; Pouchoulin et al., 2020). However, in this case, a poor mixing pattern was observed in the SSCv map (Fig. 5.19 (a)) due to the wake effect described in Chapter 3.4.3.

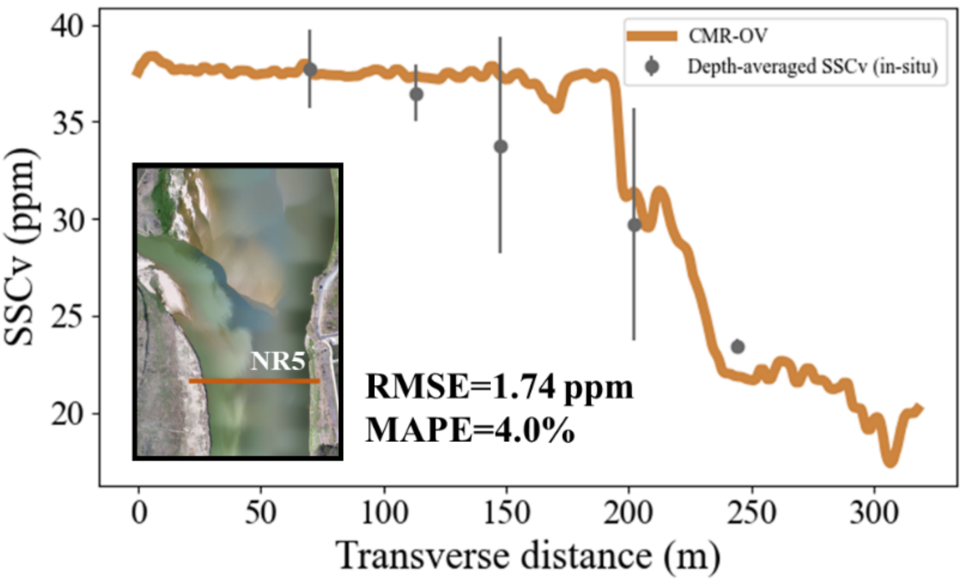

Fig. 5. 21. Comparison of depth-averaged SSCv and estimated SSCv along with the transverse distance from the left bank at NR5 section in Exp. 4-1.

(2) Exp. 4-2

The SSCv was uniformly distributed in both rivers under shallow water depth in Exp. 4-2, as described in the hyperspectral clustering result. Therefore, the transverse distribution of in-situ measured SSCv at the NR 5 section was more uniform than that in Exps. 4-1 and 4-3 (Fig.5.22). In this case, it is challenging to reproduce a uniform SSCv distribution because the geometry and water depth conditions are complicated after confluence. Despite this challenging condition, CMR-OV yielded an accurate result with a MAPE of 1.15 and an RMSE of 0.12 ppm compared with in-situ measured SSCv in the NR 5 section (Fig. 5.22). In addition, the CMR-OV improved the SSCv mapping performance compared to that of single RF. During Exp. 4-2, the overall water depth was less than 2 m with low SSC_V ($SSC_V < 10$ ppm) in both Nakdong and Hwang Rivers. Therefore, the bottom effect in this survey was more critical than that in other surveys. CMR-OV reproduced the clear concentration field (Fig. 5.23 (a)). However, the results were substantially overestimated in a single RF in the shallow areas (Fig. 5. 23 (b)). This discrepancy between the models demonstrates that the spectral variability owing to the differences in bottom reflectance can be well controlled in CMR-OV.

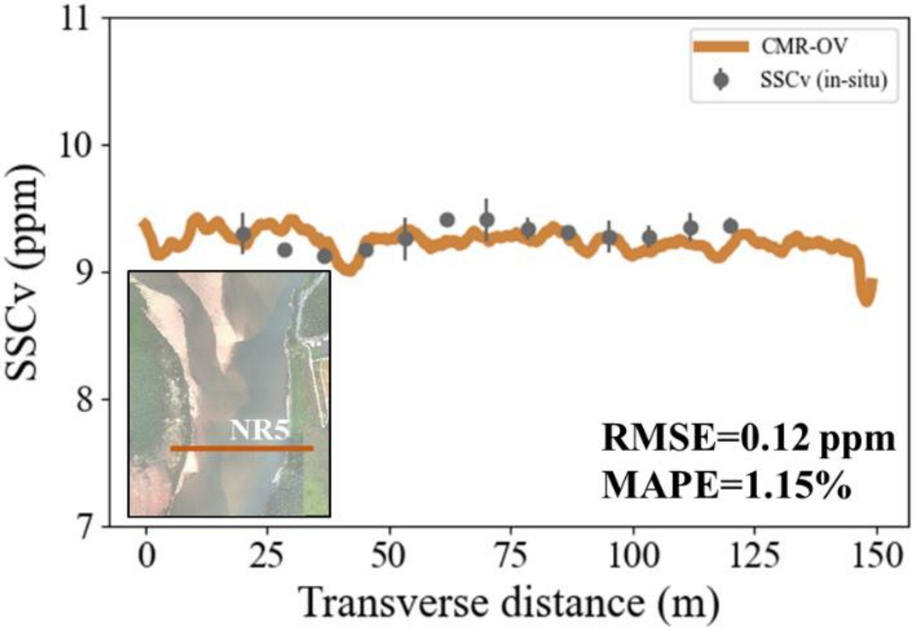

Fig. 5. 22. Comparison of in-situ measured SSCv and estimated SSCv along with the transverse distance from the left bank in the NR5 section in Exp. 4-2.

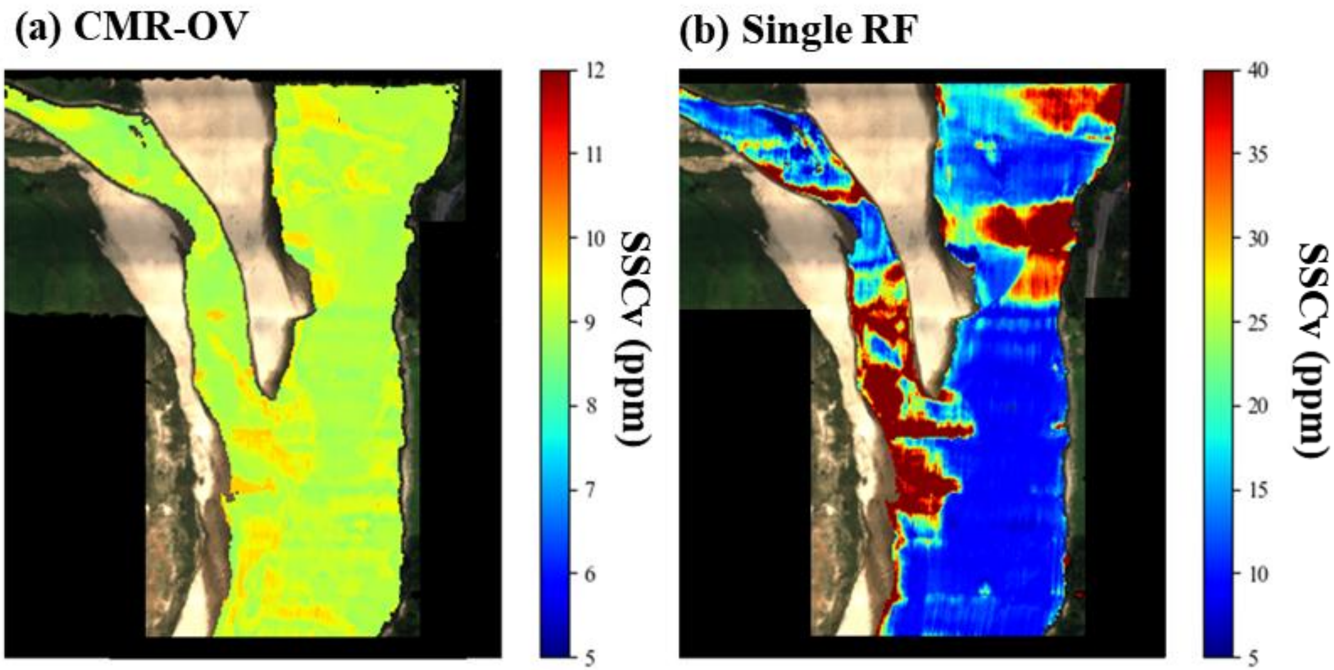

Fig. 5. 23. Comparison of SSCv mapping results of Exp. 4-2: (a) CMR-OV and (b) single RF

(3) Exp. 4-3

The site-specific problem of remote sensing in the water environment is the most critical problem (Dethier et al., 2020; Kabir and Ahmari, 2020; Liu et al., 2003; Montanher et al., 2014; Pyo et al., 2019). The dataset collected at Exp. 4-3 was not used as the training dataset. Therefore, the performance of CMR-OV in the uncalibrated case was evaluated using this dataset, as performed in Chapter 5.2. Fig. 5.24 presents the comparison between depth-averaged in-situ-measured SSCv and estimated SSCv. CMR-OV correctly reproduced the similar transverse distribution of depth-averaged SSCv in the NR 3 section in Exp. 4-3. Fine suspended matter was distributed in the water from Hwang River (tributary) on the surface (Fig. 3.26 (b)); however, it detected the suspended sediment below the surface and the result was close to the depth-averaged SSC_V.

The spatial distribution of SSCv retrieved by CMR-OV shows the mixing pattern of suspended sediment with SSCv contrast (Fig. 5. 25). The contrast of SSCv between the two rivers before confluence was apparently seen in the retrieved map; however, the mixing layer became unclear after confluence. The mixing layer disappeared rapidly. This phenomenon is the opposite of that in Exp. 4-1, in which mixing was suppressed because the wake effect and SSCv contrast were low.

It was challenging to observe this mixing pattern in the interpolation result of point data from a turbidity sensor based on the moving boat method (Fig. 5.26). CMR-OV substantially improved the reproducibility of mapping compared to that in the moving boat method. However, the hyperspectral camera used in this study is a line scanning type; therefore, there is a limit to measuring phenomena that occur in an unsteady state while the drone is flying. Despite this limitation, the CMR-OV with hyperspectral imagery improved reproducibility compared to that in existing measurement methods. In future studies, this could be extended to acquire more comprehensive spatiotemporal data using the snapshot hyperspectral camera, which can acquire an image of a wide area.

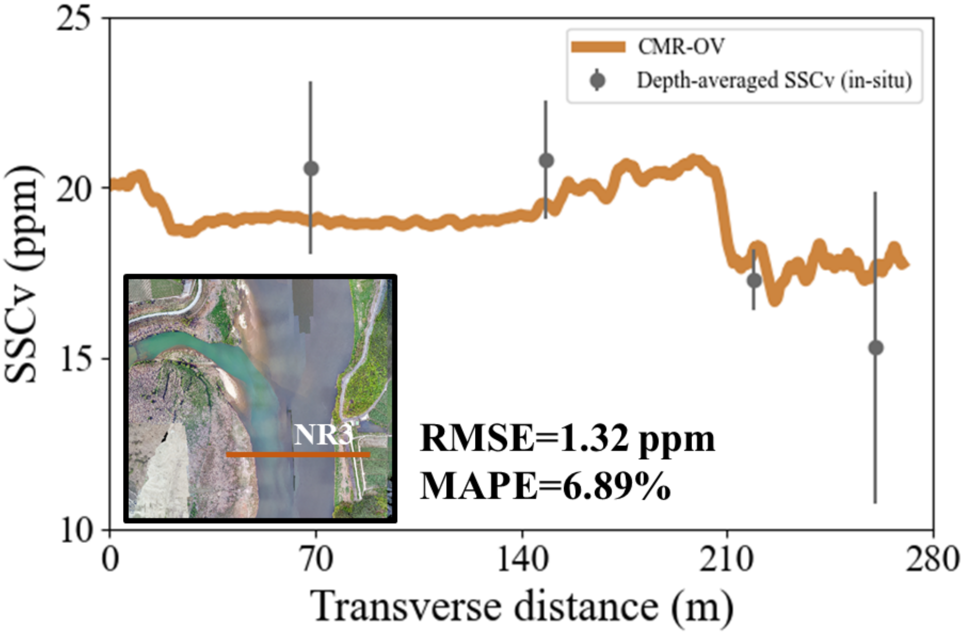

Fig. 5. 24. Comparison of depth-averaged in-situ measured SSCv and estimated SSCv along with the transverse distance from the left bank at NR3 section in Exp. 4-3.

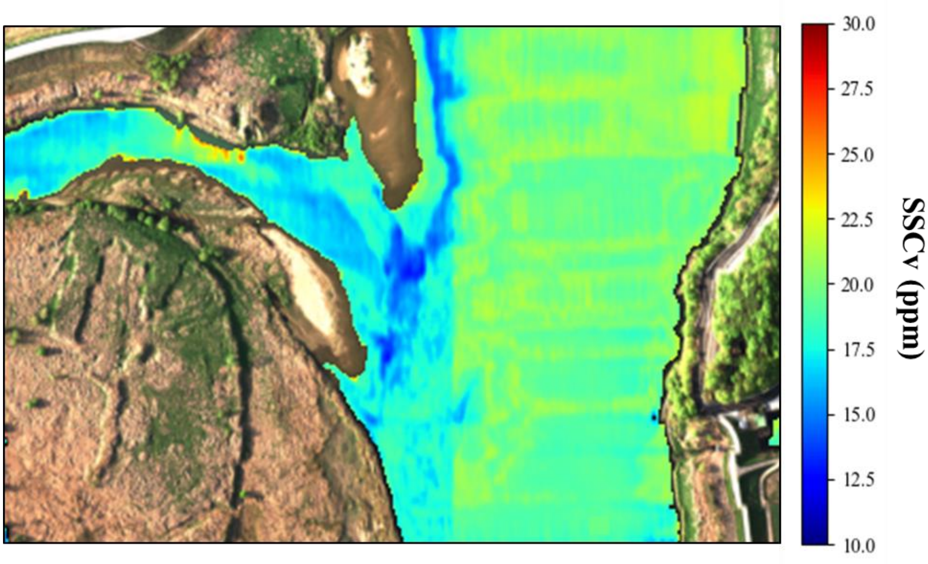

Fig. 5. 25. SSCv mapping results from CMR-OV in Exp. 4-3.

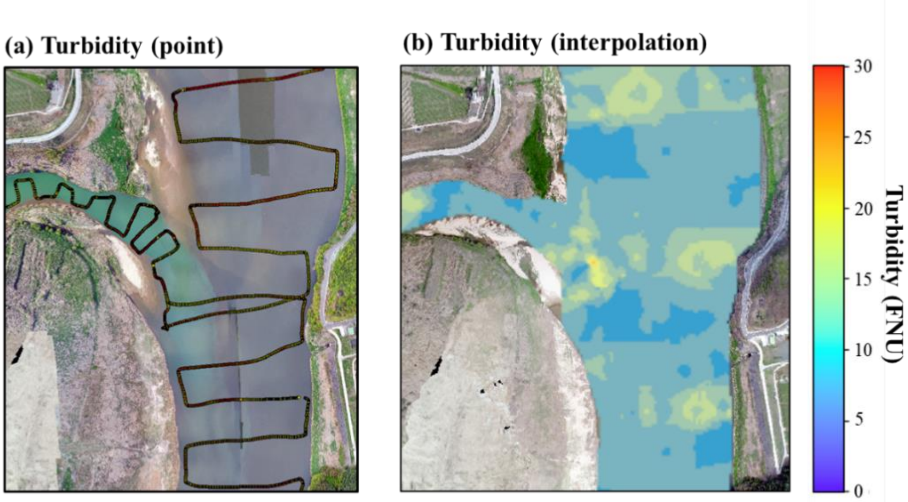

Fig. 5. 26. In-situ measurement-based mapping results of Exp. 4-3: (a) raw turbidity data and (b) interpolated turbidity data.

5.4.3 Mixing pattern extraction from SSCv map

Using mixing metric (σ_{mixing}) with SSCv map from CMR-OV, detailed mixing patterns at the river confluence can be evaluated. σ_{mixing} represents the degree of transverse mixing of each cross-section using a standard deviation of SSC for the downstream cross-sections (Lewis et al., 2020; Lewis and Rhoads, 2015). To quantify mixing metric at downstream cross-sections of confluence, the standard deviation of both upstream cross-sections of the main river and tributary was used to normalize the downstream standard deviation (σ_{yx}), as follows:

$$\sigma_{mixing} = 1 - \sigma_{yx} / \sigma_{upstream} \tag{5.1}$$

$\sigma_{upstream}$ is calculated using randomly sampled SSC data of both upstream Nakdong and Hwang River sections, which apportioned the samples according to the discharge ratio. Therefore, σ_{mixing} is 1 if the mixing is completely done and 0 when mixing does not occur (Lewis et al., 2020).

Owing to the high-resolution SSCv map from CMR-OV, the detailed mixing pattern can be evaluated by the continuous mixing metric distribution. Fig. 5.27 reveals the mixing metric distribution along with the longitudinal distance in Exps. 4-1 and 4-3, in which there were SSCv contrasts between the tributary and main river. In both surveys, the mixing metric increased with longitudinal distance. However, irregular billows in the mixing layer of Exp. 4-1, as shown in Fig. 5. 20 (a), resulted in the oscillated mixing metric profile in the longitudinal direction (Fig. 5.27). In addition, the mixing metric in Exp. 4-1 had negative values, indicating limited mixing owing to the strong wake effect. In contrast, the mixing metric distribution in Exp. 4-3 gradually increased in the positive range; the suspended sediment was almost completely mixed within the near-field.

Consequently, CMR-OV substantially improved the accuracy of SSC estimation and retrieved the SSC mixing pattern of river confluence in greater detail than the conventional measurement method. Due to the difficulty in measuring detailed SSC distribution, CMR-OV with hyperspectral imagery may benefit in determining the patterns of sediment mixing, at least in shallow waters or near the surface, as revealed in this chapter. However, measurements of three-dimensional distribution can improve the prediction and understanding of suspended sediment dynamics. This limitation could be substantially overcome by integrating the use of vertical measurement sensors.

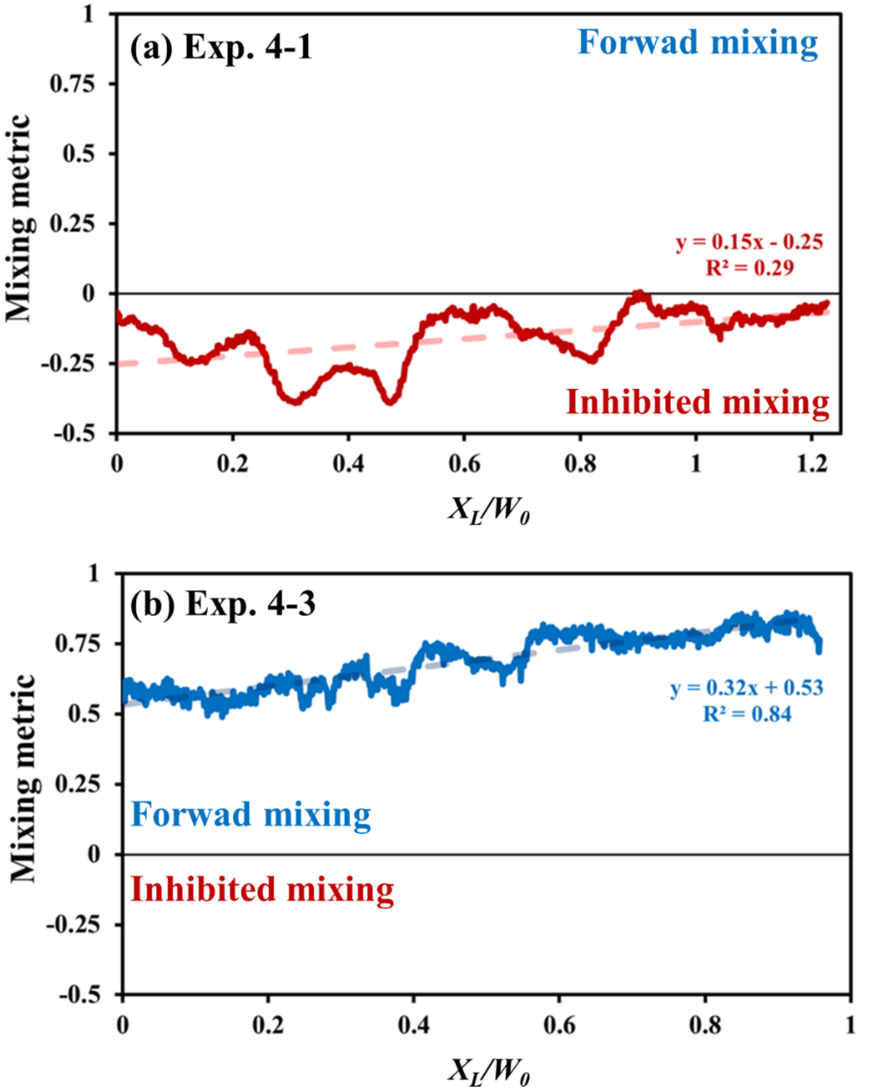

Fig. 5. 27. Mixing metric distribution along with longitudinal distance normalized by upstream width (X_L/W_0): (a) Exp. 4-1 and (b) Exp. 4-3.

6. Conclusions and future study

6.1 Conclusions

This study developed a robust method to estimate the suspended sediment concentration using UAV-based hyperspectral imagery. To apply such a method to various river conditions., this study focused on the spectral variability arising from the heterogeneity of sediment and streambed properties in rivers. Various experiments were conducted in the laboratory, field-scale channels, and field to figure out confounding factors of spectral variability. Based on the datasets for spectral variability collected from experimental studies, a CMR-OV was developed combining machine learning regression using RF and hyperspectral clustering using GMM. Finally, the CMR-OV successfully retrieved high-resolution spatial distributions of suspended sediment in various fields in the riverine system. The detailed achievements in this study are summarized below:

1. The result of the laboratory experiments showed that the suspended sediment has its own spectral characteristics that varies with the mineral contents. The effective spectral bands of each sediment had strong linearity with SSC, even though the variation of the hyperspectral spectrum increased when the particle size of suspended sediment decreased. However, in field-scale experiments, the hyperspectral spectrum and SSC were only weakly associated due to bottom reflectance. The shape of the

hyperspectral spectrum, related to spectral similarity, was dominated by the streambed type under shallow water depth (H<1m), irrespective of sediment properties. In particular, when the channel bottom was vegetated, the variance and the noise of the hyperspectral spectrum in the NIR region increased considerably. Specifically, the reflectance in the NIR region changed dynamically owing to the vegetation movement from the flow. However, the results of PCA showed that the dimension-reduced hyperspectral image revealed substantial heterogeneity based on the sediment type. The SSC and *d50* showed a strong correlation with the first or second principal components of the hyperspectral spectrum. This result implied that the concentration and size of suspended sediment complexly induced back-scattering in the water column. Spectral variability depends on the bottom and sediment properties; however, it is challenging to classify these characteristics in natural rivers deterministically. Therefore, it is necessary to deal with the optically complex dataset of suspended sediment by classifying them into spectrally similar groups through hyperspectral clustering.

2. In CMR-OV, the hyperspectral clustering separated the complex dataset into several homogeneous datasets based on spectral characteristics. The separated RF models corresponding to the clusters were built to construct the relationship between the spectrum in hyperspectral imagery and SSC. Hyperspectral clustering, through GMM in CMR-OV, clustered two

spectrally distinct clusters under constant and different bottom conditions with various suspended sediment properties. The red-edge (650–700 nm), related to the intrinsic characteristics of the sediment, was the most significant wavelength range in all cases. In addition to this, the wavelength range of UV (400–450 nm) and NIR (780–1,000 nm) controlled the other effects, including the bottom effect. Therefore, hyperspectral clustering could classify spectral characteristics, even without prior information on sediment properties and bottom type. Finally, CMR-OV outperformed the other regression models (explicit and implicit models) in terms of accuracy of SSC estimation. Moreover, CMR-OV yielded robust estimation results in the uncalibrated region, including a straight river, a meandering river, and a river confluence.

3. CMR-OV could retrieve the spatiotemporal SSC distribution of the open channel flow in detail, irrespective of the sediment type. A distinct feature of the mapped suspended sediment distribution is that CMR-OV could estimate up to invisibly suspended sediment and the tail part of the suspended sediment cloud. This part is difficult to obtain when using conventional point measurement because it mainly occurs at low concentrations near the sidewall of a stream. Therefore, CMR-OV could retrieve a different spatial pattern of suspended sediment according to the sediment particle size. In the straight and meandering channel (Exps. 2-1 and 2-2), yellow loess (d_{50}=16.3 μm) presented more conservative behavior

than the quartz sand (d_{50}= 140 μm). Therefore, quartz sand was retained longer inside channel irregularities; the tail of the sediment cloud was longer than that in yellow loess. However, in the meandering channel, the tail of yellow loess distribution was generated predominantly compared to that of quartz sand, implying that the fine and light sediments were more influenced by the secondary flow induced by channel meandering.

4. Through CMR-OV, the spatial distributions of SSCv for both rapid and inhibited mixing cases at the confluence of the Hwang and Nakdong Rivers were accurately reproduced. In addition, CMR-OV could retrieve the highly optically complex phenomenon in which turbidity and SSC were inversely proportional because a high turbid flow with fine matters and a sediment-laden flow with large sand particles merged at the confluence. Therefore, the complex spatial distribution of SSC can be estimated in greater detail; this is difficult to be reproduced by conventional measurements.

6.2 Future directions

In this study, the spectral variability from sediment and river bed properties was intensively investigated in a laboratory experiment, several field-scale experiments, and field surveys. Nevertheless, in future studies, researchers should consider additional spectral variability-related factors in rivers.

First, other constituents within the water column, such as colored organic matter (CDOM), algal blooms, and pollutants, should be investigated in conjunction with suspended sediment and bottom type. These constituents have been investigated in several previous studies (Baek et al., 2019; Niroumand-Jadidi et al., 2019a; Olmanson et al., 2013; Zeng et al., 2017). Although these constituents coexist in most rivers, their combined effects have not been investigated. Retrieving each constituent is easy because of their distinct optical characteristics, but measuring the exact contribution of each component is a challenging task owing to the nature of the coexistence characteristics. Therefore, CMR-OV can be extended to solve this problem using hyperspectral clustering.

Second, a more comprehensive range of SSC than those applied in this study should be considered. When a flood induces a highly turbid flow, or debris flow is injected into deep rivers, a high concentration of suspended sand is distributed. This substantially affects the morphology, ecosystem, and water quality of rivers. In this case of large SSC with deep water depth, the bottom reflectance is negligible owing to the high scattering effect from the suspended sediment. Therefore, hyperspectral clustering results in the division of clusters based on sediment properties. The result of Exp. 2-1 exhibited this tendency due to its high turbid background water and constant bottom condition. Compared to other conditions, the reflectance within the NIR range had relatively low values in Exp 2-1 because the bottom reflectance was relatively insignificant compared to that in Exp. 2-2. Accordingly, classifying the dataset into sediment properties and learning it increased the accuracy of model substantially. However, investigation in field surveys under such sediment dominant conditions in deep waters is necessary because the sediment and river characteristics can be more complex in natural rivers.

To develop a global estimator, various factors that were presented above need to be investigated. However, CMR-OV would possibly clarify the contribution of these various factors to SSC estimation and could be used to determine spectral variability. In terms of application in river management, the CMR-OV can be used in many problems requiring high-resolution SSC data, at least in shallow waters or waters near the surface. It could substantially contribute to river management tasks as it enables extensive and accurate river monitoring.

Reference

Adjorlolo, C., Cho, M.A., Mutanga, O., Ismail, R., 2012. Optimizing spectral resolutions for the classification of C3 and C4 grass species, using wavelengths of known absorption features. J. Appl. Remote Sens. 6, 063560–1. https://doi.org/10.1117/1.jrs.6.063560

Aggarwal, Y.., Mikkelsen, O.A., Pottsmith, H.., 2011. Sediment monitoring technology for turbine erosion and reservoir siltation applications. Proc. HYDRO 2011 Conf.

Akhtar, F., Li, J., Pei, Y., Imran, A., Rajput, A., Azeem, M., Wang, Q., 2019. Diagnosis and prediction of Large-for-Gestational-Age fetus using the stacked generalization method. Appl. Sci. 9, 1–18. https://doi.org/10.3390/app9204317

Albert, A., Mobley, C., 2003. An analytical model for subsurface irradiance and remote sensing reflectance in deep and shallow case-2 waters. Opt. Express 11, 2873. https://doi.org/10.1364/oe.11.002873

Aquino, T., Aubeneau, A., Bolster, D., 2015. Peak and tail scaling of breakthrough curves in hydrologic tracer tests. Adv. Water Resour. 78, 1–8. https://doi.org/10.1016/j.advwatres.2015.01.016

Ardabili, S., Mosavi, A., Dehghani, M., Várkonyi-Kóczy, A.R., 2020. Deep Learning and Machine Learning in Hydrological Processes Climate Change and Earth Systems a Systematic Review. Lect. Notes Networks Syst. 101, 52–62. https://doi.org/10.1007/978-3-030-36841-8_5

Arisanty, D., Nur Saputra, A., 2017. Remote Sensing Studies of Suspended Sediment Concentration Variation in Barito Delta. IOP Conf. Ser. Earth Environ. Sci. 98, 0–6. https://doi.org/10.1088/1755-1315/98/1/012058

Baek, D., Seo, I.W., Kim, J.S., Nelson, J.M., 2019a. UAV-based measurements of spatio-temporal concentration distributions of fluorescent tracers in open channel flows. Adv. Water Resour. 127, 76–88. https://doi.org/10.1016/j.advwatres.2019.03.007

Baek, D., Seo, I.W., Kim, J.S., Nelson, J.M., 2019b. UAV-based measurements of spatio-temporal concentration distributions of fluorescent tracers in open channel flows. Adv. Water Resour. 127, 76–88. https://doi.org/10.1016/j.advwatres.2019.03.007

Bhargava, D.S., Mariam, D.W., 1991. Light penetration depth, turbidity and reflectance related relationships and models. ISPRS J. Photogramm. Remote Sens. 46, 217–230.

Bhargava, D.S., Mariam, D.W., 1990. Spectral reflectance relationships to turbidity generated by different clay materials. Photogramm. Eng. Remote Sens. 56, 225–229.

Bi, S., Li, Y., Liu, G., Song, K., Xu, J., Dong, X., Cai, X., Mu, M., Miao, S., Lyu, H., 2021. Assessment of Algorithms for Estimating Chlorophyll-a Concentration in Inland Waters: A Round-Robin Scoring Method Based on the Optically Fuzzy Clustering. IEEE Trans. Geosci. Remote Sens. 1–17. https://doi.org/10.1109/TGRS.2021.3058556

Binding, C.E., Bowers, D.G., Mitchelson-Jacob, E.G., 2005. Estimating suspended sediment concentrations from ocean colour measurements in moderately turbid waters; The impact of variable particle scattering properties. Remote Sens. Environ. 94, 373–383. https://doi.org/10.1016/j.rse.2004.11.002

Bishop, C., 2006. Pattern recognition and machine learning. Springer-Verlag, Berlin, Heidelberg. https://doi.org/10.1198/tech.2007.s518

Booysen, R., Jackisch, R., Lorenz, S., Zimmermann, R., Kirsch, M., Nex, P.A.M., Gloaguen, R., 2020. Detection of REEs with lightweight UAV-based hyperspectral imaging. Sci. Rep. 10, 1–12. https://doi.org/10.1038/s41598-020-74422-0

Bouveyron, C., Brunet-Saumard, C., 2014. Model-based clustering of high-dimensional data: A review. Comput. Stat. Data Anal. 71, 52–78. https://doi.org/10.1016/j.csda.2012.12.008

Breiman, L., 2001. Random forests. Mach. Learn. 45, 5–32.

Breiman, L., 1996. Bagging predictors. Mach. Learn. 24, 123–140.

Bruzzone, L., Melgani, F., 2005. Robust multiple estimator systems for the analysis of biophysical parameters from remotely sensed data. IEEE Trans. Geosci. Remote Sens. 43, 159–173. https://doi.org/10.1109/TGRS.2004.839818

Caballero, I., Steinmetz, F., Navarro, G., 2018. Evaluation of the first year of operational Sentinel-2A data for retrieval of suspended solids in medium- to high-turbiditywaters. Remote Sens. 10. https://doi.org/10.3390/rs10070982

Chen, Z., Hanson, J.D., Curran, P.J., 1991. The form of the relationship between suspended sediment concentration and spectral reflectance: its implications for the use of Daedalus 1268 data. Int. J. Remote Sens. 12, 215–222. https://doi.org/10.1080/01431169108929647

Chen, Z.M., Hanson, J.D., Curran, P.J., 1991. The form of the relationship between suspended sediment concentration and spectral reflectance–Its implications for the use of Daedalus 1268 data. Int. J. Remote Sens. 12, 215–222.

Cheng, Z., Constantinescu, G., 2021. Shallow mixing layers between nonparallel streams in a flat-bed wide channel. J. Fluid Mech. 916, 1–37. https://doi.org/10.1017/jfm.2021.254

Cheng, Z., Constantinescu, G., 2020. Near-and far-field structure of shallow mixing layers between parallel streams. J. Fluid Mech. 904. https://doi.org/10.1017/jfm.2020.638

Chi, M., Feng, R., Bruzzone, L., 2008. Classification of hyperspectral remote-sensing data with primal SVM for small-sized training dataset problem. Adv. Sp. Res. 41, 1793–1799. https://doi.org/10.1016/j.asr.2008.02.012

Choi, S.Y., Seo, I.W., 2018. Prediction of fecal coliform using logistic regression and tree-based classification models in the North Han River, South Korea. J. Hydro-Environment Res. 21, 96–108. https://doi.org/10.1016/j.jher.2018.09.002

Choi, S.Y., Seo, I.W., Kim, Y.O., 2020. Parameter uncertainty estimation of transient storage model using Bayesian inference with formal likelihood based on breakthrough curve segmentation. Environ. Model. Softw. 123, 104558. https://doi.org/10.1016/j.envsoft.2019.104558

Cimoli, E., Lucieer, V., Meiners, K.M., Chennu, A., Castrisios, K., Ryan, K.G., Lund-Hansen, L.C., Martin, A., Kennedy, F., Lucieer, A., 2020. Mapping the in situ microspatial distribution of ice algal biomass through hyperspectral imaging of sea-ice cores. Sci. Rep. 10, 21848. https://doi.org/10.1038/s41598-020-79084-6

Constantinescu, G., Miyawaki, S., Rhoads, B., Sukhodolov, A., 2014. Numerical evaluation of the effects of planform geometry and inflow conditions on flow, turbulence structure, and bed shear velocity at a stream confluence with a concordant bed George. J. Geophys. Res. Earth Surf. 119, 2079–2097. https://doi.org/10.1002/2014JF003244

Constantinescu, G., Miyawaki, S., Rhoads, B., Sukhodolov, A., 2012. Numerical analysis of the effect of momentum ratio on the dynamics and sediment-entrainment capacity of coherent flow structures at a stream confluence. J. Geophys. Res. Earth Surf. 117, n/a-n/a. https://doi.org/10.1029/2012jf002452

de Almeida, C.T., Galvão, L.S., Aragão, L.E. de O.C. e., Ometto, J.P.H.B., Jacon, A.D., Pereira, F.R. de S., Sato, L.Y., Lopes, A.P., Graça, P.M.L. de A., Silva, C.V. de J., Ferreira-Ferreira, J., Longo, M., 2019. Combining LiDAR and hyperspectral data for aboveground biomass modeling in the Brazilian Amazon using different regression algorithms. Remote Sens. Environ. 232, 111323. https://doi.org/10.1016/j.rse.2019.111323

de Rooij, W.A., van der Stap, C.C.A.H., 1984. Expansion of Mie scattering matrices in generalized spherical functions. Astron. Astrophys. 131, 237–248.

Dekker, A.G., 1993. Detection of Optical Water Quality Parameters for Eutrophic Waters by High Resolution Remote Sensing.

Dekker, A.G., Vos, R.J., Peters, S.W.M., 2001. Comparison of remote sensing data, model results and in situ data for total suspended matter (TSM) in the southern Frisian lakes. Sci. Total Environ. 268, 197–214. https://doi.org/10.1016/S0048-9697(00)00679-3

Dethier, E.N., Renshaw, C.E., Magilligan, F.J., 2020. Toward Improved Accuracy of Remote Sensing Approaches for Quantifying Suspended Sediment: Implications for Suspended-Sediment Monitoring. J. Geophys. Res. Earth Surf. 125. https://doi.org/10.1029/2019JF005033

Díaz-Uriarte, R., Alvarez de Andrés, S., 2006. Gene selection and classification of microarray data using random forest. BMC

Bioinformatics 7, 1–13. https://doi.org/10.1186/1471-2105-7-3

Doxaran, D., Froidefond, J.-M., Castaing, P., 2003. Remote-sensing reflectance of turbid sediment-dominated waters Reduction of sediment type variations and changing illumination conditions effects by use of reflectance ratios. Appl. Opt. 42, 2623. https://doi.org/10.1364/ao.42.002623

Doxaran, D., Ruddick, K., McKee, D., Gentili, B., Tailliez, D., Chami, M., Babin, M., 2009. Spectral variations of light scattering by marine particles in coastal waters, from visible to near infrared. Limnol. Oceanogr. 54, 1257–1271. https://doi.org/10.4319/lo.2009.54.4.1257

Edwards, T.K., Glysson, G.D., 1999. Field Methods for Measurement of Fluvial Sediment: U.S. geological survey techniques of water-resources investigations. In: Book 3, Applications of Hydraulics.

Eon, R.S., Bachmann, C.M., 2021. Mapping barrier island soil moisture using a radiative transfer model of hyperspectral imagery from an unmanned aerial system. Sci. Rep. 1–11. https://doi.org/10.1038/s41598-021-82783-3

Fan, Y., Li, W., Calzado, V.S., Trees, C., Stamnes, S., Fournier, G., McKee, D., Stamnes, K., 2015. Inferring inherent optical properties and water constituent profiles from apparent optical properties. Opt. Express 23, A987. https://doi.org/10.1364/oe.23.00a987

Fonstad, M.A., Marcus, W.A., 2005. Remote sensing of stream depths with hydraulically assisted bathymetry (HAB) models. Geomorphology 72, 320–339. https://doi.org/10.1016/j.geomorph.2005.06.005

Ford, D.E., Johnson, M.C., 1983. An Assessment of Reservoir Density Currents and Inflow Processes, Tech. Rep. E–83–7. Mississippi, USA.

Fraser, R.N., 1998. Multispectral remote sensing of turbidity among Nebraska Sand Hills lakes. Int. J. Remote Sens. 19, 3011–3016. https://doi.org/10.1080/014311698214406

Gebreslassie, H.G., Melesse, A.M., Bishop, K., Gebremariam, A.G., 2020. Linear spectral unmixing algorithm for modelling suspended sediment concentration of flash floods, upper Tekeze River, Ethiopia. Int. J. Sediment Res. 35, 79–90. https://doi.org/10.1016/j.ijsrc.2019.07.007

Gualtieri, C., Filizola, N., de Oliveira, M., Santos, A.M., Ianniruberto, M., 2018. A field study of the confluence between Negro and Solimões Rivers. Part 1: Hydrodynamics and sediment transport. Comptes Rendus - Geosci. 350, 31–42. https://doi.org/10.1016/j.crte.2017.09.015

Gualtieri, C., Ianniruberto, M., Filizola, N., 2019. On the mixing of rivers with a difference in density: The case of the Negro/Solimões confluence, Brazil. J. Hydrol. 578. https://doi.org/10.1016/j.jhydrol.2019.124029

Guyon, I., Weston, J., Barnhil, l S., Vapnik, V., 2002. Gene selection for cancer classification using support vector machines. Mach. Learn. 46, 389–422.

Hafeez, S., Sing Wong, M., Abbas, S., Y. T. Kwok, C., Nichol, J., Ho Lee, K., Tang, D., Pun, L., 2019. Detection and Monitoring of Marine Pollution Using Remote Sensing Technologies. Monit. Mar. Pollut. https://doi.org/10.5772/intechopen.81657

Haggerty, R., Wondzell, S.M., Johnson, M.A., 2002. Power-law residence time distribution in the hyporheic zone of a 2nd-order mountain stream. Geophys. Res. Lett. 29, 1–4. https://doi.org/10.1029/2002GL014743

Haun, S., Kjærås, H., Løvfall, S., Olsen, N.R.B., 2013. Three-dimensional measurements and numerical modelling of suspended sediments in a hydropower reservoir. J. Hydrol. 479, 180–188. https://doi.org/10.1016/j.jhydrol.2012.11.060

He, Y., Mui, A., 2010. Scaling up semi-arid grassland biochemical content from the leaf to the canopy level: Challenges and opportunities. Sensors 10, 11072–11087. https://doi.org/10.3390/s101211072

Helsel, D.R., 1987. Advantages of nonparametric procedures for analysis of water quality data. Hydrol. Sci. J. 32, 179–190. https://doi.org/10.1080/02626668709491176

Herms, I., Jódar, J., Soler, A., Lambán, L.J., Custodio, E., Núñez, J.A., Arnó, G., Ortego, M.I., Parcerisa, D., Jorge, J., 2021. Evaluation of natural background levels of high mountain karst aquifers in complex hydrogeological settings. A Gaussian mixture model approach in the Port del Comte (SE, Pyrenees) case study. Sci. Total Environ. 756, 143864. https://doi.org/10.1016/j.scitotenv.2020.143864

Horna-Munoz, D., Constantinescu, G., Rhoads, B., Lewis, Q., Sukhodolov, A., 2020. Density Effects at a Concordant Bed Natural River Confluence. Water Resour. Res. 56. https://doi.org/10.1029/2019WR026217

Hristov, A., Bosman, J.W., Bhulai, S., Van Der Mei, R.D., 2020. Deriving Explicit Control Policies for Markov Decision Processes Using Symbolic Regression. ACM Int. Conf. Proceeding Ser. 41–47. https://doi.org/10.1145/3388831.3388840

Hu, B.L., Hao, S.J., Sun, D.X., Liu, Y.N., 2017. A novel scene-based non-uniformity correction method for SWIR push-broom hyperspectral sensors. ISPRS J. Photogramm. Remote Sens. 131, 160–169. https://doi.org/10.1016/j.isprsjprs.2017.08.004

Islam, M.R., Yamaguchi, Y., Ogawa, K., 2001. Suspended sediment in the Ganges and Brahmaputra Rivers in Bangladesh: Observation from TM and AVHRR data. Hydrol. Process. 15, 493–509. https://doi.org/10.1002/hyp.165

Ismail, K., Boudhar, A., Abdelkrim, A., Mohammed, H., Mouatassime, S., Kamal, A., Driss, E., Idrissi, E., Nouaim, W., 2019. Evaluating the potential of Sentinel-2 satellite images for water quality characterization of artificial reservoirs: The Bin El Ouidane Reservoir case study (Morocco). Meteorol. Hydrol. Water Manag. 7. https://doi.org/10.26491/mhwm/95087

Jakob, S., Zimmermann, R., Gloaguen, R., 2017. The Need for Accurate Geometric and Radiometric Corrections of Drone-Borne Hyperspectral Data for Mineral Exploration: MEPHySTo-A Toolbox for Pre-Processing Drone-Borne Hyperspectral Data. Remote Sens. 9. https://doi.org/10.3390/rs9010088

Jaud, M., Le Dantec, N., Ammann, J., Grandjean, P., Constantin, D., Akhtman, Y., Barbieux, K., Allemand, P., Delacourt, C., Merminod, B., 2018. Direct georeferencing of a pushbroom, lightweight hyperspectral system for mini-UAV applications. Remote Sens. 10, 1–15. https://doi.org/10.3390/rs10020204

Jeon, E., Kim, K., Cho, S., Kim, S., 2019. A Comparative Study of Absolute Radiometric Correction Methods for Drone-borne Hyperspectral Imagery. Korean J. Remote Sens. 35, 203–215. https://doi.org/doi.org/10.7780/kjrs.2019.35.2.1

Jiang, D., Matsushita, B., Pahlevan, N., Gurlin, D., Lehmann, M.K., Fichot, C.G., Schalles, J., Loisel, H., Binding, C., Zhang, Y., Alikas, K., Kangro, K., Uusõue, M., Ondrusek, M., Greb, S., Moses, W.J., Lohrenz, S., O'Donnell, D., 2021. Remotely estimating total suspended solids concentration in clear to extremely turbid waters using a novel semi-analytical method. Remote Sens. Environ. 258. https://doi.org/10.1016/j.rse.2021.112386

Kabir, S.M.I., Ahmari, H., 2020. Evaluating the effect of sediment color on water radiance and suspended sediment concentration using digital imagery. J. Hydrol. 589, 125189. https://doi.org/10.1016/j.jhydrol.2020.125189

Kilham, N.E., Roberts, D., Singer, M.B., 2012. Remote sensing of suspended sediment concentration during turbid flood conditions on the Feather River, CaliforniaA modeling approach. Water Resour. Res. 48, 1–18. https://doi.org/10.1029/2011WR010391

Kim, G., Baek, I., Stocker, M.D., Smith, J.E., Van Tassell, A.L., Qin, J., Chan, D.E., Pachepsky, Y., Kim, M.S., 2020. Hyperspectral imaging from a multipurpose floating platform to estimate chlorophyll-a concentrations in irrigation pond water. Remote Sens. 12. https://doi.org/10.3390/rs12132070

Kim, J.S., Baek, D., Seo, I.W., Shin, J., 2019. Retrieving shallow stream bathymetry from UAV-assisted RGB imagery using a geospatial regression method. Geomorphology 341, 102–114. https://doi.org/10.1016/j.geomorph.2019.05.016

Kim, K.H., Yun, S.T., Park, S.S., Joo, Y., Kim, T.S., 2014. Model-based clustering of hydrochemical data to demarcate natural versus human impacts on bedrock groundwater quality in rural areas, South Korea. J. Hydrol. 519, 626–636. https://doi.org/10.1016/j.jhydrol.2014.07.055

Kirk, J.T.O., 1994. Light and Photosynthesis in Aquatic Ecosystems, 2nd ed. Cambridge University Press, Canberra.

Koestner, D., Stramski, D., Reynolds, R.A., 2020. Assessing the effects of particle size and composition on light scattering through measurements of size-fractionated seawater samples. Limnol. Oceanogr. 65, 173–190. https://doi.org/10.1002/lno.11259

Konsoer, K.M., Rhoads, B.L., 2014. Spatial–temporal structure of mixing interface turbulence at two large river confluences. Environ. Fluid Mech. 14, 1043–1070. https://doi.org/10.1007/s10652-013-9304-5

Kwak, S., Lyu, S., Kim, Y. Do, Kim, D., 2020. Field Measurement of Spatiotemporal Algae Distribution Using In Situ Optical Particle Size Sensor. Water Resour. Res. 56, 1–16. https://doi.org/10.1029/2019WR026825

Kwon, S., Noh, H., Seo, I.W., Jung, S.H., Baek, D., 2021a. Identification framework of contaminant spill in rivers using machine learning with breakthrough curve analysis. Int. J. Environ. Res. Public Health 18, 1–28. https://doi.org/10.3390/ijerph18031023

Kwon, S., Seo, I.W., Beak, D., 2021b. Development of suspended solid concentration measurement technique based on multi-spectral satellite imagery in Nakdong River using machine learning model. J. Korea Water Resour. Assoc. 54, 121–133. https://doi.org/10.3741/JKWRA.2021.54.2.121

Kwon, S., Seo, I.W., Noh, H., Kim, B., 2022a. Hyperspectral retrievals of suspended sediment using cluster-based machine learning regression in shallow waters. Sci. Total Environ. 833, 155168. https://doi.org/10.1016/j.scitotenv.2022.155168

Kwon, S., Shin, J., Seo, I.W., Noh, H., Jung, S.H., You, H., 2022b. Measurement of suspended sediment concentration in open channel flows based on hyperspectral imagery from UAVs. Adv. Water Resour.

159, 104076. https://doi.org/10.1016/j.advwatres.2021.104076

Kwon, S., Shin, J., Seo, I.W., Noh, H., Jung, S.H., You, H., 2021c. Measurement of Suspended Sediment Concentration in Open Channel Flows Based on Hyperspectral Imagery from UAVs. Adv. Water Resour. 159, 104076. https://doi.org/10.1016/j.advwatres.2021.104076

Kwon, Y.S., Pyo, J.C., Kwon, Y.H., Duan, H., Cho, K.H., Park, Y., 2020. Drone-based hyperspectral remote sensing of cyanobacteria using vertical cumulative pigment concentration in a deep reservoir. Remote Sens. Environ. 236, 111517. https://doi.org/10.1016/j.rse.2019.111517

Latosinski, F.G., Szupiany, R.N., García, C.M., Guerrero, M., Amsler, M.L., 2014. Estimation of Concentration and Load of Suspended Bed Sediment in a Large River by Means of Acoustic Doppler Technology. J. Hydraul. Eng. 140, 04014023. https://doi.org/10.1061/(asce)hy.1943-7900.0000859

Leathers, R.A., Downes, T.V., Priest, R.G., 2005. Scene-based nonuniformity corrections for optical and SWIR pushbroom sensors. Opt. Express 13, 5136. https://doi.org/10.1364/opex.13.005136

Lee, Z., Carder, K.L., Arnone, R.A., 2002. Deriving inherent optical properties from water color: a multiband quasi-analytical algorithm for optically deep waters. Appl. Opt. 41, 5755. https://doi.org/10.1364/ao.41.005755

Lee, Z., Carder, K.L., Mobley, C.D., Steward, R.G., Patch, J.S., 1999. Hyperspectral remote sensing for shallow waters: 2 Deriving bottom depths and water properties by optimization. Appl. Opt. 38, 3831. https://doi.org/10.1364/ao.38.003831

Legleiter, C.J., 2021. The optical river bathymetry toolkit. River Res. Appl.

37, 555–568. https://doi.org/10.1002/rra.3773

Legleiter, C.J., Harrison, L.R., 2019. Remote Sensing of River Bathymetry: Evaluating a Range of Sensors, Platforms, and Algorithms on the Upper Sacramento River, California, USA. Water Resour. Res. 55, 2142–2169. https://doi.org/10.1029/2018WR023586

Legleiter, C.J., Manley, P. V., Erwin, S.O., Bulliner, E.A., 2019. An Experimental Evaluation of the Feasibility of Inferring Concentrations of a Visible Tracer Dye from Remotely Sensed Data in Turbid Rivers. Remote Sens. 12, 57. https://doi.org/10.3390/rs12010057

Legleiter, C.J., Mobley, C.D., Overstreet, B.T., 2017. A framework for modeling connections between hydraulics, water surface roughness, and surface reflectance in open channel flows. J. Geophys. Res. Earth Surf. 122, 1715–1741. https://doi.org/10.1002/2017JF004323

Legleiter, C.J., Roberts, D.A., Marcus, W.A., Fonstad, M.A., 2004. Passive optical remote sensing of river channel morphology and in-stream habitat: Physical basis and feasibility. Remote Sens. Environ. 93, 493–510. https://doi.org/10.1016/j.rse.2004.07.019

Leite Ribeiro, M., Blanckaert, K., Roy, A.G., Schleiss, A.J., 2012. Flow and sediment dynamics in channel confluences. J. Geophys. Res. Earth Surf. 117. https://doi.org/10.1029/2011JF002171

Lewis, Q., Rhoads, B., Sukhodolov, A., Constantinescu, G., 2020. Advective Lateral Transport of Streamwise Momentum Governs Mixing at Small River Confluences. Water Resour. Res. 56, 1–20. https://doi.org/10.1029/2019WR026817

Lewis, Q.W., Rhoads, B.L., 2018. LSPIV Measurements of Two-Dimensional Flow Structure in Streams Using Small Unmanned Aerial Systems: 2.

Hydrodynamic Mapping at River Confluences. Water Resour. Res. 54, 7981–7999. https://doi.org/10.1029/2018WR022551

Lewis, Q.W., Rhoads, B.L., 2015. Rates and patterns of thermal mixing at a small stream confluence under variable incoming flow conditions. Hydrol. Process. 29, 4442–4456. https://doi.org/10.1002/hyp.10496

Li, E., Liu, S., Yin, S., Fu, X., 2009. Nonuniformity correction algorithms of IRFPA based on radiation source scaling. 5th Int. Conf. Inf. Assur. Secur. IAS 2009 1, 317–321. https://doi.org/10.1109/IAS.2009.110

Li, J., Alvarez, B., Siwabessy, J., Tran, M., Huang, Z., Przeslawski, R., Radke, L., Howard, F., Nichol, S., 2017. Application of random forest and generalised linear model and their hybrid methods with geostatistical techniques to count data: Predicting sponge species richness. Environ. Model. Softw. 97, 112–129. https://doi.org/10.1016/j.envsoft.2017.07.016

Liu, H., Li, Q., Shi, T., Hu, S., Wu, G., Zhou, Q., 2017. Application of Sentinel 2 MSI Images to Retrieve Suspended Particulate Matter Concentrations in Poyang Lake. Remote Sens. 9, 761. https://doi.org/10.3390/rs9070761

Liu, Y., Huang, H., Yan, L., Yang, X., Bi, H., Zhang, Z., 2020. Particle size parameters of particulate matter suspended in coastal waters and their use as indicators of typhoon influence. Remote Sens. 12. https://doi.org/10.3390/SU12166405

Löffler, M., Zhang, A.Y., Zhou, H.H., 2019. Optimality of Spectral Clustering for Gaussian Mixture Model.

Lokhov, A.S., Kravchishina, M.D., Klyuvitkin, A.A., Kochenkova, A.I., 2020. In situ Measurements of the Characteristics of Suspended Particles in the Barents Sea by the LISST-Deep Laser Diffractometer. Oceanology 60, 650–663. https://doi.org/10.1134/S0001437020050148

Luo, J., Cirpka, O.A., Kitanidis, P.K., 2006. Temporal-moment matching for truncated breakthrough curves for step or step-pulse injection. Adv. Water Resour. 29, 1306–1313. https://doi.org/10.1016/j.advwatres.2005.10.005

Ma, R., Dai, J., 2005. Investigation of chlorophyll-a and total suspended matter concentrations using landsat ETM and field spectral measurement in Taihu Lake, China. Int. J. Remote Sens. 26, 2779–2795. https://doi.org/10.1080/01431160512331326648

Merten, G.H., Capel, P.D., Minella, J.P.G., 2014. Effects of suspended sediment concentration and grain size on three optical turbidity sensors. J. Soils Sediments 14, 1235–1241. https://doi.org/10.1007/s11368-013-0813-0

Meyer, P., Itten, K.I., Kellenberger, T., Sandmeier, S., Sandmeier, R., 1993. Radiometric corrections of topographically induced effects on Landsat TM data in an alpine environment. ISPRS J. Photogramm. Remote Sens. 48, 17–28. https://doi.org/10.1016/0924-2716(93)90028-L

Mishra, P., Karami, A., Nordon, A., Rutledge, D.N., Roger, J.M., 2019. Automatic de-noising of close-range hyperspectral images with a wavelength-specific shearlet-based image noise reduction method. Sensors Actuators, B Chem. 281, 1034–1044. https://doi.org/10.1016/j.snb.2018.11.034

Mobley, C.D., 1999. Estimation of the remote-sensing reflectance from above-surface measurements. Appl. Opt. 38, 7442. https://doi.org/10.1364/ao.38.007442

Montanher, O.C., Novo, E.M.L.M., Barbosa, C.C.F., Rennó, C.D., Silva, T.S.F., 2014. Empirical models for estimating the suspended sediment concentration in Amazonian white water rivers using Landsat 5/TM. Int. J. Appl. Earth Obs. Geoinf. 29, 67–77. https://doi.org/10.1016/j.jag.2014.01.001

Ni, L., Wang, D., Wu, J., Wang, Y., Tao, Y., Zhang, J., Liu, J., 2020. Streamflow forecasting using extreme gradient boosting model coupled with Gaussian mixture model. J. Hydrol. 586, 124901. https://doi.org/10.1016/j.jhydrol.2020.124901

Niroumand-Jadidi, M., Bovolo, F., Bruzzone, L., 2020. SMART-SDB: Sample-specific multiple band ratio technique for satellite-derived bathymetry. Remote Sens. Environ. 251, 112091. https://doi.org/10.1016/j.rse.2020.112091

Niroumand-Jadidi, M., Bovolo, F., Bruzzone, L., 2019a. Novel spectra-derived features for empirical retrieval of water quality parameters: Demonstrations for OLI, MSI, and OLCI sensors. IEEE Trans. Geosci. Remote Sens. 57, 10285–10300. https://doi.org/10.1109/TGRS.2019.2933251

Niroumand-Jadidi, M., Pahlevan, N., Vitti, A., 2019b. Mapping substrate types and compositions in shallow streams. Remote Sens. 11. https://doi.org/10.3390/rs11030262

Niroumand-Jadidi, M., Vitti, A., Lyzenga, D.R., 2018. Multiple Optimal Depth Predictors Analysis (MODPA) for river bathymetry: Findings from spectroradiometry, simulations, and satellite imagery. Remote Sens. Environ. 218, 132–147. https://doi.org/10.1016/j.rse.2018.09.022

Novo, E.M.M., Hansom, J.D., Curran, P.J., 1989. The effect of sediment type on the relationship between reflectance and suspended sediment concentration. Int. J. Remote Sens. 10, 1283–1289. https://doi.org/10.1080/ 01431168908903967

Okyay, Ü., Khan, S.D., Lakshmikantha, M.R., Sarmiento, S., 2016. Ground-based hyperspectral image analysis of the lower Mississippian (Osagean) reeds spring formation rocks in southwestern Missouri. Remote Sens. 8. https://doi.org/10.3390/rs8121018

Olmanson, L.G., Brezonik, P.L., Bauer, M.E., 2013. Airborne hyperspectral remote sensing to assess spatial distribution of water quality characteristics in large rivers: The Mississippi River and its tributaries in Minnesota. Remote Sens. Environ. 130, 254–265. https://doi.org/10.1016/j.rse.2012.11.023

Overstreet, B.T., Legleiter, C.J., 2017. Removing sun glint from optical remote sensing images of shallow rivers. Earth Surf. Process. Landforms 42, 318–333. https://doi.org/10.1002/esp.4063

Pal, M., Foody, G.M., 2010. Feature selection for classification of hyperspectral data by SVM. IEEE Trans. Geosci. Remote Sens. 48, 2297–2307. https://doi.org/10.1109/TGRS.2009.2039484

Parsons, D.R., Jackson, P.R., Czuba, J.A., Engel, F.L., Rhoads, B.L., Oberg, K.A., Best, J.L., Mueller, D.S., Johnson, K.K., Riley, J.D., 2013. Velocity Mapping Toolbox (VMT): A processing and visualization suite for moving-vessel ADCP measurements. Earth Surf. Process. Landforms 38, 1244–1260. https://doi.org/10.1002/esp.3367

Patel, E., Kushwaha, D.S., 2020. Clustering Cloud Workloads: K-Means vs Gaussian Mixture Model. Procedia Comput. Sci. 171, 158–167. https://doi.org/10.1016/j.procs.2020.04.017

Pedocchi, F., García, M.H., 2006. Evaluation of the LISST-ST instrument for suspended particle size distribution and settling velocity measurements. Cont. Shelf Res. 26, 943–958. https://doi.org/10.1016/j.csr.2006.03.006

Pedregosa, F., Varoquaux, G., Gramfort, A., Michel, V., Thirion, B., Grisel, O., Blondel, M., Prettenhofer, P., Weiss, R., Dubourg, V., Vanderplas, J., Passos, A., Cournapeau, D., Brucher, M., Perrot, M., Duchesnay, É., 2011. Scikit-learn: Machine learning in Python. J. Mach. Learn. Res. 12, 2825–2830.

Penney, J., Morel, Y., Haynes, P., Auclair, F., Nguyen, C., 2020. Diapycnal mixing of passive tracers by Kelvin-Helmholtz instabilities. J. Fluid Mech. https://doi.org/10.1017/jfm.2020.483

Pereira, F.J.S., Costa, C.A.G., Foerster, S., Brosinsky, A., de Araújo, J.C., 2019a. Estimation of suspended sediment concentration in an intermittent river using multi-temporal high-resolution satellite imagery. Int. J. Appl. Earth Obs. Geoinf. 79, 153–161. https://doi.org/10.1016/j.jag.2019.02.009

Pereira, F.J.S., Costa, C.A.G., Foerster, S., Brosinsky, A., de Araújo, J.C., 2019b. Estimation of suspended sediment concentration in an intermittent river using multi-temporal high-resolution satellite imagery. Int. J. Appl. Earth Obs. Geoinf. 79, 153–161. https://doi.org/10.1016/j.jag.2019.02.009

Peterson, K.T., Sagan, V., Sidike, P., Cox, A.L., Martinez, M., 2018. Suspended sediment concentration estimation from landsat imagery along the lower missouri and middle Mississippi Rivers using an extreme learning machine. Remote Sens. 10. https://doi.org/10.3390/rs10101503

Pham, Q.V., Ha, N.T.T., Pahlevan, N., Oanh, L.T., Nguyen, T.B., Nguyen, N.T., 2018. Using landsat-8 images for quantifying suspended sediment concentration in red river (Northern Vietnam). Remote Sens. 10. https://doi.org/10.3390/rs10111841

Pinet, S., Martinez, J.-M., Ouillon, S., Lartiges, B., Villar, R.E., 2017. Variability of apparent and inherent optical properties of sediment-laden waters in large river basins – lessons from in situ measurements and bio-optical modeling. Opt. Express 25, A283. https://doi.org/10.1364/oe.25.00a283

Pomázi, F., Baranya, S., 2020. Comparative assessment of fluvial suspended sediment concentration analysis methods. Water (Switzerland) 12. https://doi.org/10.3390/w12030873

Pouchoulin, S., Le Coz, J., Mignot, E., Gond, L., Riviere, N., 2020. Predicting Transverse Mixing Efficiency Downstream of a River Confluence. Water Resour. Res. 56, 1–23. https://doi.org/10.1029/2019WR026367

Probst, P., Wright, M.N., Boulesteix, A.L., 2019. Hyperparameters and tuning strategies for random forest. Wiley Interdiscip. Rev. Data Min. Knowl. Discov. 1–18. https://doi.org/10.1002/widm.1301

Pyo, J.C., Duan, H., Baek, S., Kim, M.S., Jeon, T., Kwon, Y.S., Lee, H., Cho, K.H., 2019. A convolutional neural network regression for quantifying cyanobacteria using hyperspectral imagery. Remote Sens. Environ. 233, 111350. https://doi.org/10.1016/j.rse.2019.111350

Pyo, J.C., Duan, H., Ligaray, M., Kim, M., Baek, S., Kwon, Y.S., Lee, H., Kang, T., Kim, K., Cha, Y.K., Cho, K.H., 2020a. An integrative remote sensing application of stacked autoencoder for atmospheric correction and cyanobacteria estimation using hyperspectral imagery. Remote Sens. 12. https://doi.org/10.3390/rs12071073

Pyo, J.C., Hong, S.M., Kwon, Y.S., Kim, M.S., Cho, K.H., 2020b. Estimation of heavy metals using deep neural network with visible and infrared spectroscopy of soil. Sci. Total Environ. 741, 140162. https://doi.org/10.1016/j.scitotenv.2020.140162

Pyo, J.C., Park, L.J., Pachepsky, Y., Baek, S.S., Kim, K., Cho, K.H., 2020c. Using convolutional neural network for predicting cyanobacteria concentrations in river water. Water Res. 186, 116349. https://doi.org/10.1016/j.watres.2020.116349

Qin, J., Chao, K., Kim, M.S., Lu, R., Burks, T.F., 2013. Hyperspectral and multispectral imaging for evaluating food safety and quality. J. Food Eng. 118, 157–171. https://doi.org/10.1016/j.jfoodeng.2013.04.001

Qu, L., Lei, T., Ning, D., Civco, D., Yang, X., 2016. A spectral mixing algorithm for quantifying suspended sediment concentration in the Yellow River: a simulation based on a controlled laboratory experiment. Int. J. Remote Sens. 37, 2560–2584. https://doi.org/10.1080/01431161.2016.1182662

Raghavendra, S., Deka, P.C., 2014. Support vector machine applications in the field of hydrology: A review. Appl. Soft Comput. J. 19, 372–386. https://doi.org/10.1016/j.asoc.2014.02.002

Rai, A.K., Kumar, A., 2015. Continuous measurement of suspended sediment concentration: Technological advancement and future outlook. Meas. J. Int. Meas. Confed. 76, 209–227. https://doi.org/10.1016/j.measurement.2015.08.013

Rakwatin, P., Takeuchi, W., Yasuoka, Y., 2007. Stripe noise reduction in MODIS data by combining histogram matching with facet filter. IEEE Trans. Geosci. Remote Sens. 45, 1844–1855. https://doi.org/10.1109/TGRS.2007.895841

Rhoads, B.L., Johnson, K.K., 2018. Three-dimensional flow structure, morphodynamics, suspended sediment, and thermal mixing at an asymmetrical river confluence of a straight tributary and curving main channel. Geomorphology 323, 51–69. https://doi.org/10.1016/j.geomorph.2018.09.009

Rhoads, B.L., Kenworthy, S.T., 1995. Flow structure at an asymmetrical stream confluence. Geomorphology 11, 273–293. https://doi.org/10.1016/0169-555X(94)00069-4

Rhoads, B.L., Sukhodolov, A.N., 2008. Lateral momentum flux and the spatial evolution of flow within a confluence mixing interface. Water Resour. Res. 44, 1–17. https://doi.org/10.1029/2007WR006634

Rosner, B., Grove, D., 1999. Use of the Mann-Whitney U-test for clustered data. Stat. Med. 18, 1387–1400. https://doi.org/10.1002/(SICI)1097-0258(19990615)18:11<1387::AID-SIM126>3.0.CO;2-V

Ross, M.R.V., Topp, S.N., Appling, A.P., Yang, X., Kuhn, C., Butman, D., Simard, M., Pavelsky, T.M., 2019. AquaSat: A Data Set to Enable Remote Sensing of Water Quality for Inland Waters. Water Resour. Res. 55, 10012–10025. https://doi.org/10.1029/2019WR024883

Rouse, H., 1937. Modern Conceptions of the Mechanics or Fluid Turbulence. Trans. Am. Soc. Civ. Eng. 102, 463–505.

Rozovskii, I.L., 1957. Flow of water in bendsof open channels. Acad. Sci. Ukr. SSR.

Sabrina, S., Lewis, Q., Rhoads, B., 2021. Large-Scale Particle Image Velocimetry Reveals Pulsing of Incoming Flow at a Stream Confluence. Water Resour. Res. 57, 1–21. https://doi.org/10.1029/2021WR029662

Savitzky, A.; Golay, M.J.E., 1964. Smoothing and Differentiation. Anal.

Chem 36, 1627–1639.

Schiebe, F.R., Harrington, J.A., Ritchie, J.C., 1992. Remote sensing of suspended sediments: The lake chicot, arkansas project. Int. J. Remote Sens. 13, 1487–1509. https://doi.org/10.1080/01431169208904204

Searson, D.P., Leahy, D.E., Willis, M.J., 2010. GPTIPS:An open source genetic programming toolbox for multigene symbolic regression. Proc. Int. MultiConference Eng. Comput. Sci. 2010, IMECS 2010 77–80. https://doi.org/10.1007/978-94-007-0286-8

Seo, I.W., Lee, K.W., Beak, K.O., 2006. Flow structure and turbulence characteristics in meandering channel. J. Korean Soc. Civ. Eng. 26, 469–479.

Shen, F., Zhou, Y.X., Li, J.F., Shen, F., Suhyb Salama, M.H.D., Su, Z., Kuang, D.B., 2010. Remote-sensing reflectance characteristics of highly turbid estuarine waters – a comparative experiment of the yangtze river and the yellow river. Int. J. Remote Sens. 31, 2639–2654. https://doi.org/10.1080/01431160903085610

Simmons, S.M., Azpiroz-Zabala, M., Cartigny, M.J.B., Clare, M.A., Cooper, C., Parsons, D.R., Pope, E.L., Sumner, E.J., Talling, P.J., 2020. Novel Acoustic Method Provides First Detailed Measurements of Sediment Concentration Structure Within Submarine Turbidity Currents. J. Geophys. Res. Ocean. 125, 1–24. https://doi.org/10.1029/2019JC015904

Smith, G.M., Milton, E.J., 1999. The use of the empirical line method to calibrate remotely sensed data to reflectance. Int. J. Remote Sens. 20, 2653–2662. https://doi.org/10.1080/014311699211994

Son, G., Kim, D., Kwak, S., Kim, Y. Do, Lyu, S., 2021. Characterizing three-dimensional mixing process in river confluence using acoustical backscatter as surrogate of suspended sediment 54, 167–179. https://doi.org/10.3741/JKWRA.2021.54.3.167

Spyrakos, E., O'Donnell, R., Hunter, P.D., Miller, C., Scott, M., Simis, S.G.H., Neil, C., Barbosa, C.C.F., Binding, C.E., Bradt, S., Bresciani, M., Dall'Olmo, G., Giardino, C., Gitelson, A.A., Kutser, T., Li, L., Matsushita, B., Martinez-Vicente, V., Matthews, M.W., Ogashawara, I., Ruiz-Verdú, A., Schalles, J.F., Tebbs, E., Zhang, Y., Tyler, A.N., 2018. Optical types of inland and coastal waters. Limnol. Oceanogr. 63, 846–870. https://doi.org/10.1002/lno.10674

Stanev, V.G., Iliev, F.L., Hansen, S., Vesselinov, V. V., Alexandrov, B.S., 2018. Identification of release sources in advection–diffusion system by machine learning combined with Green's function inverse method. Appl. Math. Model. 60, 64–76. https://doi.org/10.1016/j.apm.2018.03.006

Sukhodolov, A.N., Krick, J., Sukhodolova, T.A., Cheng, Z., Rhoads, B.L., Constantinescu, G.S., 2017. Turbulent flow structure at a discordant river confluence: Asymmetric jet dynamics with implications for channel morphology. J. Geophys. Res. Earth Surf. 122, 1278–1293. https://doi.org/10.1002/2016JF004126

Sun, Y. V., Bielak, L.F., Peyser, P.A., Turner, S.T., Sheedy, P.F., Boerwinkle, E., Kardia, S.L.R., 2008. Application of machine learning algorithms to predict coronary artery calcification with a sibship-based design. Genet. Epidemiol. 32, 350–360. https://doi.org/10.1002/gepi.20309

Sváb, E., Tyler, A.N., Preston, T., Présing, M., Balogh, K. V., 2005. Characterizing the spectral reflectance of algae in lake waters with high suspended sediment concentrations. Int. J. Remote Sens. 26, 919–928. https://doi.org/10.1080/0143116042000274087

Szupiany, R.N., Amsler, M.L., Parsons, D.R., Best, J.L., 2009. Morphology, flow structure, and suspended bed sediment transport at two large braid-bar confluences. Water Resour. Res. 45, 1–19. https://doi.org/10.1029/2008WR007428

Thorne, P.D., Hanes, D.M., 2002. A review of acoustic measurement of small-scale sediment processes. Cont. Shelf Res. 22, 603–632. https://doi.org/10.1016/S0278-4343(01)00101-7

Thorne, P.D., Hurther, D., 2014. An overview on the use of backscattered sound for measuring suspended particle size and concentration profiles in non-cohesive inorganic sediment transport studies. Cont. Shelf Res. 73, 97–118. https://doi.org/10.1016/j.csr.2013.10.017

Topliss, B.J., Almos, C.L., Hill, P.R., 1990. Algorithms for remote sensing of high concentration, inorganic suspended sediment. Int. J. Remote Sens. 11, 947–966. https://doi.org/10.1080/01431169008955069

Topp, S.N., Pavelsky, T.M., Jensen, D., Simard, M., Ross, M.R.V., 2020. Research trends in the use of remote sensing for inland water quality science: Moving towards multidisciplinary applications. Water (Switzerland) 12, 1–34. https://doi.org/10.3390/w12010169

Uijttewaal, W.S.J., Booij, R., 2000. Effects of shallowness on the development of free-surface mixing layers. Phys. Fluids 12, 392–402. https://doi.org/10.1063/1.870317

Umar, M., Rhoads, B.L., Greenberg, J.A., 2018a. Use of multispectral satellite remote sensing to assess mixing of suspended sediment downstream of large river confluences. J. Hydrol. 556, 325–338. https://doi.org/10.1016/j.jhydrol.2017.11.026

Umar, M., Rhoads, B.L., Greenberg, J.A., 2018b. Use of multispectral satellite remote sensing to assess mixing of suspended sediment downstream of large river confluences. J. Hydrol. 556, 325–338. https://doi.org/10.1016/j.jhydrol.2017.11.026

van Rooijen, E., Mosselman, E., Sloff, K., Uijttewaal, W., 2020. The effect of small density differences at river confluences. Water (Switzerland) 12, 1–18. https://doi.org/10.3390/w12113084

Vanhellemont, Q., Ruddick, K., 2015. Advantages of high quality SWIR bands for ocean colour processing: Examples from Landsat-8. Remote Sens. Environ. 161, 89–106. https://doi.org/10.1016/j.rse.2015.02.007

Vapnik, V., Golowich, S.E., Smola, A., 1997. Support vector method for function approximation, regression estimation, and signal processing. Adv. Neural Inf. Process. Syst. 281–287.

Vercruysse, K., Grabowski, R.C., Rickson, R.J., 2017. Suspended sediment transport dynamics in rivers: Multi-scale drivers of temporal variation. Earth-Science Rev. 166, 38–52. https://doi.org/10.1016/j.earscirev.2016.12.016

Volpe, V., Silvestri, S., Marani, M., 2011. Remote sensing retrieval of suspended sediment concentration in shallow waters. Remote Sens. Environ. 115, 44–54. https://doi.org/10.1016/j.rse.2010.07.013

Wang, C., Chen, S., Li, D., Wang, D., Liu, W., Yang, J., 2017. A Landsat-based model for retrieving total suspended solids concentration of estuaries and coasts in China. Geosci. Model Dev. 10, 4347–4365. https://doi.org/10.5194/gmd-10-4347-2017

Wang, F., Zhou, B., Xu, J., Song, L., Wang, X., 2009. Application of neural network and MODIS 250 m imagery for estimating suspended sediments concentration in Hangzhou Bay, China. Environ. Geol. 56, 1093–1101.

https://doi.org/10.1007/s00254-008-1209-0

Wang, J.-J., Lu, X.X., Liew, S.C., Zhou, Y., 2009. Retrieval of suspended sediment concentrations in large turbid rivers using Landsat ETM+: an example from the Yangtze River, China. Earth Surf. Process. Landforms 34, 1082–1092. https://doi.org/10.1002/esp.1795 2006

Wang, Q., Wang, Y., Niu, R., Peng, L., 2017. Integration of information theory, K-Means cluster analysis and the logistic regression model for landslide susceptibility mapping in the three gorges area, China. Remote Sens. 9. https://doi.org/10.3390/rs9090938

Wang, Y., Peng, Y., Du, Z., Lin, H., Yu, Q., 2020. Calibrations of suspended sediment concentrations in high-turbidity waters using different in situ optical instruments. Water (Switzerland) 12. https://doi.org/10.3390/w12113296

Wei, L., Huang, C., Zhong, Y., Wang, Z., Hu, X., Lin, L., 2019. Inland waters suspended solids concentration retrieval based on PSO-LSSVM for UAV-borne hyperspectral remote sensing imagery. Remote Sens. 11. https://doi.org/10.3390/rs11121455

Weng, B., Song, Z., Zhu, R., Yan, Q., Sun, Q., Grice, C.G., Yan, Y., Yin, W.J., 2019. Symbolic regression discovery of new perovskite catalysts with high oxygen evolution reaction activity. arXiv 1–27.

Whetton, R.L., Waine, T.W., Mouazen, A.M., 2017. Optimising configuration of a hyperspectral imager for on-line field measurement of wheat canopy. Biosyst. Eng. 155, 84–95. https://doi.org/10.1016/j.biosystemseng.2016.12.006

White, B.L., Helfrich, K.R., 2013. Rapid gravitational adjustment of horizontal shear flows. J. Fluid Mech. 721, 86–117.

https://doi.org/10.1017/jfm.2013.41

Wong, J., Liew, S.C., Wong, E., Lee, Z., 2019. Modeling the remote-sensing reflectance of highly turbid waters. Appl. Opt. 58, 2671. https://doi.org/10.1364/ao.58.002671

Wosiacki, L.F.K., Suekame, H.K., Wood, M.S., Gonçalves, F.V., Bleninger, T., 2021. Mapping of suspended sediment transport using acoustic methods in a Pantanal tributary. Environ. Monit. Assess. 193. https://doi.org/10.1007/s10661-021-09266-w

Woźniak, S.B., Stramski, D., 2004. Modeling the optical properties of mineral particles suspended in seawater and their influence on ocean reflectance and chlorophyll estimation from remote sensing algorithms. Appl. Opt. 43, 3489–3503. https://doi.org/10.1364/AO.43.003489

Wu, C., Li, H., Ren, J., 2021. Research on hierarchical clustering method based on partially-ordered Hasse graph. Futur. Gener. Comput. Syst. 125, 785–791. https://doi.org/10.1016/j.future.2021.07.025

Yang, C.Y., Julien, P.Y., 2019. The ratio of measured to total sediment discharge. Int. J. Sediment Res. 34, 262–269. https://doi.org/10.1016/j.ijsrc.2018.11.005

Yao, X., Tham, L.G., Dai, F.C., 2008. Landslide susceptibility mapping based on Support Vector Machine: A case study on natural slopes of Hong Kong, China. Geomorphology 101, 572–582. https://doi.org/10.1016/j.geomorph.2008.02.011

Yaseen, Z.M., Sulaiman, S.O., Deo, R.C., Chau, K.W., 2019. An enhanced extreme learning machine model for river flow forecasting: State-of-the-art, practical applications in water resource engineering area and future research direction. J. Hydrol. 569, 387–408.

https://doi.org/10.1016/j.jhydrol.2018.11.069

Yuan, S., Tang, H., Li, K., Xu, L., Xiao, Y., Gualtieri, C., Rennie, C., Melville, B., 2021. Hydrodynamics, Sediment Transport and Morphological Features at the Confluence Between the Yangtze River and the Poyang Lake. Water Resour. Res. 57. https://doi.org/10.1029/2020WR028284

Yuan, S., Tang, H., Xiao, Y., Xia, Y., Melching, C., Li, Z., 2019. Phosphorus contamination of the surface sediment at a river confluence. J. Hydrol. 573, 568–580. https://doi.org/10.1016/j.jhydrol.2019.02.036

Zeng, C., Richardson, M., King, D.J., 2017. The impacts of environmental variables on water reflectance measured using a lightweight unmanned aerial vehicle (UAV)-based spectrometer system. ISPRS J. Photogramm. Remote Sens. 130, 217–230. https://doi.org/10.1016/j.isprsjprs.2017.06.004

Zhang, X., Hu, L., Xiong, Y., Huot, Y., Gray, D., 2020. Experimental Estimates of Optical Backscattering Associated With Submicron Particles in Clear Oceanic Waters. Geophys. Res. Lett. 47. https://doi.org/10.1029/2020GL087100

Zhou, Y., Rangarajan, A., Gader, P.D., 2018. A Gaussian mixture model representation of endmember variability in hyperspectral unmixing. IEEE Trans. Image Process. 27, 2242–2256. https://doi.org/10.1109/TIP.2018.2795744

Zinger, J.A., Rhoads, B.L., Best, J.L., Johnson, K.K., 2013. Flow structure and channel morphodynamics of meander bend chute cutoffs: A case study of the Wabash River, USA. J. Geophys. Res. Earth Surf. 118, 2468–2487. https://doi.org/10.1002/jgrf.20155

Appendix

Appendix A. Breakthrough curve (BTC) analysis

The BTC features can be calculated from the temporal moment (Kwon et al., 2021a; Luo et al., 2006). The k_{th} degree temporal moment (m_k) at location (x) was calculated from Eq. B.1. Based on this equation, the first moment is related to the advection of the contaminant as a time to the centroid ($\bar{t}$), representing the mean travel time of the entire contaminant cloud (Eq. B.2). The second-moment temporal variance (σ) of the BTC indicates the degree of diffusion (Eq. B3). The third and fourth temporal moments are related to skewness (*SKNS*) and kurtosis (*KURT*), which represent the asymmetry and peak of the BTC (Eqs. B.4 and B.5).

$$m_k = \int_0^{\infty} t^k C(x,t)dt \qquad \text{(B.1)}$$

$$\bar{t} = \frac{m_1}{m_0} \qquad \text{(B.2)}$$

$$\sigma = m_2 / m_0 - \bar{t} \qquad \text{(B.3)}$$

$$SKNS = \frac{m_3}{m_2^{3/2}} \qquad \text{(B.4)}$$

$$KURT = \frac{m_4}{m_2^{\;2}} - 3 \tag{B.5}$$

where t is time, C is the concentration of the BTC.

The slope features were applied to the segments of BTC of rising limb, falling limb, and tail (Kwon et al., 2021a). The slope of the rising and falling limb can be calculated by dividing the maximum concentration by the time variation of each part. These features indicate how quickly the contaminant increases and decreases. Thus, if advection is more dominant than dispersion, the peak concentration is increased with high kurtosis, and the retention time is decreased, which is equivalent to the slope being increased. In particular, the magnitude of the storage zone effect from the contaminant retention is featured as the power-law shape (Aquino et al., 2015; Haggerty et al., 2002). The tail slope indicates how the concentration decrease from the storage zone effect, and it can be calculated by the power of the equation from the power-law regression.

Appendix B. Experimental data

Appendix B. 1. BTCs of in-situ measured SSC from field-scale experiments

a) Field-scale experiment in a straight channel (Exp. 2-1)

	SSCv (ppm)					
	Case2-1-1 (quart sand)		Case2-1-2 (yellow loess)		Case2-1-3 (mixture)	
h/H Time(s)	0.75	0.25	0.75	0.25	0.75	0.25
0	23.53	24.01	23.09	23.42	23.26	23.35
1.5	23.58	24.03	23.08	23.51	23.24	23.40
3	23.56	24.05	23.09	23.49	23.15	23.38
4.5	23.55	24.00	23.09	23.50	23.18	23.39
6	23.60	24.05	23.07	23.47	23.14	23.32
7.5	23.61	24.04	23.05	23.50	23.11	23.34
9	23.65	24.04	23.09	23.52	23.11	23.31
10.5	23.66	24.03	23.09	23.49	23.06	23.28
12	23.71	24.08	23.17	23.49	23.10	23.26
13.5	23.65	24.05	23.29	23.49	23.08	23.28
15	23.63	24.02	23.32	23.50	23.10	23.29
16.5	23.67	24.03	23.34	23.48	23.05	23.24
18	23.68	23.99	23.33	23.47	23.08	23.24
19.5	23.72	23.97	23.29	23.47	23.11	23.28
21	23.74	23.97	23.37	23.46	23.07	23.24
22.5	23.70	23.99	23.42	23.43	23.08	23.25
24	23.75	23.99	23.45	23.39	23.08	23.28
25.5	23.75	23.95	23.48	23.43	23.16	23.26
27	23.74	23.98	23.52	23.41	23.24	23.26
28.5	23.74	24.01	23.57	23.35	23.19	23.26
30	23.75	23.91	23.56	23.37	23.20	23.28
31.5	23.69	23.87	23.53	23.29	23.23	23.27
33	23.72	23.87	23.46	23.36	23.31	23.26
34.5	23.69	23.87	23.47	23.33	23.30	23.28
36	23.69	23.82	23.51	23.33	23.31	23.27
37.5	23.75	23.80	23.53	23.36	23.33	23.24
39	23.69	23.80	23.54	23.36	23.29	23.25
40.5	23.66	23.78	23.55	23.37	23.29	23.21
42	23.58	23.74	23.50	23.36	23.26	23.24
43.5	23.64	23.71	23.44	23.39	23.24	23.17
45	23.63	23.73	23.46	23.44	23.24	23.21
46.5	23.66	23.73	23.52	23.44	23.24	23.19
48	23.67	23.75	23.56	23.42	23.22	23.18
49.5	23.70	23.76	23.62	23.40	23.19	23.15
51	23.70	23.72	23.56	23.48	23.17	23.18
52.5	23.68	23.65	23.51	23.46	23.14	23.12
54	23.68	23.66	23.49	23.47	23.18	23.06
55.5	23.66	23.68	23.48	23.45	23.12	23.11

57	23.71	23.61	23.47	23.46	23.10	23.13
58.5	23.70	23.61	23.43	23.50	23.13	23.22
60	23.61	23.68	23.43	23.50	23.11	23.21
61.5	23.65	23.68	23.42	23.49	23.09	23.20
63	23.63	23.72	23.45	23.52	23.01	23.17
64.5	23.69	23.76	23.45	23.57	23.03	23.15
66	23.67	23.80	23.44	23.52	23.12	23.19
67.5	23.68	23.82	23.42	23.76	23.07	23.19
69	23.71	23.75	23.39	23.75	23.22	23.21
70.5	23.70	23.78	23.36	23.73	23.25	23.22
72	23.79	23.77	23.31	23.76	23.29	23.21
73.5	23.78	23.80	23.30	23.78	23.24	23.27
75	23.77	23.76	23.29	23.73	23.24	23.30
76.5	23.73	23.78	23.25	23.75	23.27	23.33
78	23.70	23.75	23.24	23.80	23.23	23.34
79.5	23.66	23.78	23.28	23.83	23.28	23.40
81	23.63	23.80	23.31	23.87	23.26	23.39
82.5	23.59	23.82	23.33	23.85	23.29	23.41
84	23.59	23.86	23.39	23.85	23.25	23.43
85.5	23.67	23.82	23.42	23.84	23.22	23.33
87	23.63	23.85	23.37	23.82	23.21	23.27
88.5	23.62	23.80	23.32	23.84	23.21	23.21
90	23.69	23.79	23.29	23.79	23.26	23.21
91.5	23.68	23.81	23.30	23.82	23.32	23.20
93	23.61	23.80	23.27	23.77	23.33	23.25
94.5	23.54	23.80	23.22	23.76	23.28	23.25
96	23.53	23.81	23.18	23.81	23.23	23.24
97.5	23.48	23.89	23.17	23.56	23.26	23.25
99	23.46	23.94	23.20	23.58	23.16	23.24
100.5	23.52	23.98	23.24	23.58	23.15	23.24
102	23.53	24.02	23.34	23.53	23.12	23.23
103.5	23.54	24.00	23.43	23.50	23.11	23.23
105	23.58	24.00	23.98	23.49	23.08	23.18
106.5	23.58	23.96	24.24	23.50	23.01	23.18
108	23.58	24.02	24.33	23.56	23.43	23.22
109.5	23.69	23.97	25.58	24.90	23.72	23.19
111	23.70	23.98	27.21	25.81	24.23	23.20
112.5	23.76	24.01	32.57	26.49	27.46	23.28
114	23.86	24.00	40.54	27.50	31.17	23.56
115.5	24.04	24.10	51.89	30.89	34.99	24.49
117	24.34	24.13	68.89	33.49	38.40	25.77
118.5	24.67	24.20	81.28	39.96	43.44	26.98
120	24.96	24.28	92.60	45.11	47.61	28.69
121.5	25.28	24.38	91.45	52.08	52.62	30.54
123	26.50	25.07	99.50	61.14	56.31	33.77
124.5	28.43	25.69	110.20	76.27	61.28	36.21
126	30.23	27.36	121.14	88.07	66.21	40.61
127.5	32.42	29.33	135.60	101.79	71.87	46.11
129	34.76	30.92	147.34	113.87	76.67	48.03
130.5	36.67	33.18	161.83	124.11	83.18	52.57
132	38.09	35.42	174.02	135.73	89.38	56.21
133.5	39.46	37.05	186.07	149.85	94.44	61.71
135	41.37	38.89	198.54	160.41	101.11	66.48
136.5	44.06	41.12	214.13	169.74	107.68	71.55
138	46.20	42.82	212.88	179.89	114.28	77.50
139.5	47.99	45.04	229.00	189.62	121.62	81.87
141	49.83	47.31	244.83	199.59	127.40	86.90

142.5	51.66	49.94	256.75	210.48	129.65	93.36
144	52.56	52.23	257.68	223.41	132.04	99.76
145.5	53.12	54.48	258.07	234.27	133.83	104.18
147	54.36	56.81	252.12	242.41	136.33	108.38
148.5	55.43	59.36	253.44	247.64	138.58	112.61
150	56.73	61.54	256.56	254.48	138.39	116.51
151.5	58.75	63.97	272.45	260.02	140.02	119.48
153	59.90	65.53	278.54	263.31	139.66	122.11
154.5	60.43	67.32	280.41	259.60	140.91	125.57
156	60.54	67.53	275.98	261.23	140.32	126.95
157.5	60.11	67.79	269.17	260.54	138.93	127.68
159	59.67	68.42	266.13	259.43	138.33	132.59
160.5	58.75	69.34	261.82	260.92	135.84	134.03
162	58.63	69.23	257.86	260.02	134.39	134.71
163.5	58.15	69.31	253.08	255.80	132.77	134.74
165	56.99	68.84	247.99	257.50	132.24	135.80
166.5	55.03	68.37	238.84	256.50	130.26	137.22
168	53.47	68.25	249.35	258.01	129.78	136.74
169.5	52.77	67.92	240.77	257.55	126.75	138.07
171	51.74	67.15	230.22	255.96	124.30	138.35
172.5	50.39	66.64	221.30	253.24	122.35	137.81
174	50.01	66.31	221.12	247.60	119.15	136.81
175.5	50.23	65.86	218.45	240.95	117.44	136.38
177	49.88	64.85	215.23	236.94	116.18	136.26
178.5	49.42	64.21	210.20	231.83	113.31	136.76
180	48.44	63.97	201.22	227.88	113.92	136.20
181.5	46.68	63.38	192.29	223.02	111.48	137.64
183	44.78	62.12	184.48	219.41	112.63	137.47
184.5	42.80	61.20	176.87	212.70	109.88	137.53
186	41.28	60.08	176.30	207.29	108.02	135.37
187.5	40.08	58.43	174.09	202.03	106.66	134.22
189	38.67	56.96	169.79	196.60	106.20	132.17
190.5	38.23	55.02	164.49	189.54	105.11	130.13
192	37.45	54.02	159.77	184.44	103.15	129.81
193.5	37.14	53.53	158.06	179.91	102.50	128.26
195	37.05	53.48	154.38	174.09	100.21	125.92
196.5	36.74	52.69	152.00	172.72	97.27	122.33
198	36.73	52.02	145.11	167.58	92.52	120.18
199.5	35.88	51.23	138.88	161.05	89.66	117.37
201	35.46	50.52	134.90	155.16	88.30	115.04
202.5	35.38	48.96	129.34	149.49	87.26	112.39
204	35.17	47.65	122.69	145.83	86.38	108.56
205.5	34.56	46.50	116.57	141.74	85.03	105.97
207	33.62	45.68	110.78	138.86	83.04	102.78
208.5	33.07	44.30	104.66	135.34	79.89	99.47
210	32.98	42.96	101.94	130.35	76.71	97.01
211.5	32.78	41.40	98.82	125.34	73.77	91.80
213	32.65	40.73	95.24	119.13	70.68	87.60
214.5	32.41	39.82	93.31	117.18	68.45	83.77
216	32.27	39.71	89.28	111.60	67.08	81.67
217.5	31.93	39.66	85.41	106.87	64.97	78.62
219	31.82	39.44	82.36	104.04	62.18	75.33
220.5	31.55	38.71	79.27	101.44	59.95	72.48
222	31.29	37.92	77.36	98.16	57.95	69.34
223.5	30.90	37.12	72.83	94.48	56.31	66.57
225	30.50	36.30	69.58	90.44	53.52	63.94
226.5	30.55	35.70	66.40	85.60	52.24	62.24

228	30.11	35.39	64.49	81.08	50.95	60.44
229.5	30.08	34.53	62.84	79.33	49.77	58.39
231	29.91	34.09	61.17	77.60	48.01	56.07
232.5	29.69	33.73	60.00	76.34	46.01	53.29
234	29.41	33.42	59.45	74.02	44.52	52.14
235.5	29.27	33.09	57.78	72.53	42.61	50.43
237	29.24	32.87	56.82	70.60	40.55	48.89
238.5	28.98	32.46	55.49	69.49	39.85	46.74
240	28.66	32.06	54.54	68.78	38.96	44.78
241.5	28.45	31.87	53.27	68.33	38.00	44.43
243	28.37	31.84	51.25	67.13	37.25	43.54
244.5	28.31	31.44	48.98	66.01	36.43	41.70
246	28.22	30.91	47.90	64.94	35.69	41.04
247.5	28.21	30.52	47.43	63.53	35.21	39.44
249	27.97	30.36	46.95	61.67	34.62	39.10
250.5	27.90	30.11	45.74	60.68	34.33	39.34
252	27.77	29.92	44.74	59.33	34.07	39.02
253.5	27.76	29.64	44.21	58.75	33.89	38.67
255	27.68	29.31	43.63	57.48	33.69	38.30
256.5	27.36	29.24	43.08	56.38	33.77	37.65
258	27.41	28.83	42.93	55.24	33.57	36.98
259.5	27.34	28.77	42.76	53.40	33.38	36.94
261	27.41	28.66	42.07	52.20	32.84	36.90
262.5	27.51	28.68	40.87	50.87	32.44	37.13
264	27.48	28.52	39.90	49.15	31.99	36.83
265.5	27.48	28.32	39.84	47.90	31.34	37.06
267	27.49	28.22	39.62	46.60	30.81	36.68
268.5	27.53	28.15	38.89	45.44	30.38	36.64
270	27.50	28.20	37.50	44.55	29.98	36.17
271.5	27.81	28.23	36.28	43.25	29.77	35.76
273	27.80	28.15	35.72	42.99	29.34	35.42
274.5	27.81	28.03	35.17	42.03	29.13	35.27
276	28.03	28.10	34.60	41.01	28.88	34.65
277.5	28.12	27.99	33.83	39.76	28.72	34.39
279	28.08	27.74	33.24	39.26	28.54	33.38
280.5	28.04	27.59	32.96	38.53	28.30	32.29
282	28.06	27.82	32.52	37.99	28.04	31.93
283.5	27.99	27.91	32.25	37.28	27.21	31.36
285	27.92	27.93	32.16	36.38	26.40	31.10
286.5	27.90	27.73	31.70	35.55	26.08	30.95
288	27.81	27.66	31.48	34.82	25.83	30.56
289.5	27.66	27.64	30.90	34.99	25.56	30.14
291	27.40	27.51	30.59	34.94	25.55	29.69
292.5	27.13	27.46	30.34	34.55	25.52	29.05
294	27.19	27.27	30.03	34.31	25.60	28.90
295.5	26.90	27.31	28.95	33.78	25.70	28.46
297	26.78	27.18	28.27	33.35	25.66	28.55
298.5	26.63	27.22	28.00	32.67	25.67	28.47
300	26.53	26.95	27.67	31.45	25.62	28.61
301.5	26.16	26.71	27.69	30.72	25.50	28.40
303	26.18	26.52	27.61	29.80	25.46	28.31
304.5	26.17	26.58	27.58	29.26	25.34	28.32
306	25.92	26.41	27.42	29.07	25.26	28.44
307.5	25.64	26.34	27.19	28.87	25.18	28.36
309	25.62	26.28	27.02	28.65	25.04	28.38
310.5	25.46	26.34	26.94	28.47	24.93	28.24
312	25.29	26.07	27.03	28.19	24.82	28.15

313.5	25.22	25.93	26.91	28.02	24.84	27.90
315	25.14	25.82	26.57	27.95	24.93	27.75
316.5	25.08	25.82	26.52	27.98	25.06	27.46
318	25.01	25.68	26.36	28.10	25.04	27.01
319.5	24.95	25.66	26.21	27.59	24.99	26.81
321	24.92	25.58	26.34	27.37	24.97	26.77
322.5	24.96	25.40	26.26	27.45	24.97	26.78
324	24.86	25.45	26.23	27.25	24.87	26.68
325.5	24.89	25.26	26.17	27.23	24.82	26.46
327	24.81	25.19	26.12	27.32	24.81	26.22
328.5	24.86	25.07	25.94	27.35	24.73	25.99
330	24.75	25.04	25.95	27.25	24.66	25.80
331.5	24.68	25.09	25.73	27.22	24.65	25.78
333	24.53	25.11	25.81	27.21	24.60	25.64
334.5	24.40	25.04	25.76	27.25	24.63	25.52
336	24.35	25.01	25.71	27.11	24.64	25.21
337.5	24.37	25.00	25.69	27.04	24.65	25.29
339	24.31	24.95	25.74	26.95	24.59	25.21
340.5	24.30	24.79	25.52	26.88	24.65	25.18
342	24.33	24.63	25.25	26.81	24.52	25.13
343.5	24.27	24.57	25.12	26.64	24.49	25.18
345	24.27	24.49	25.17	26.52	24.41	25.15
346.5	24.28	24.40	25.17	26.30	24.19	25.10
348	24.26	24.34	25.19	26.06	24.23	25.07
349.5	24.31	24.22	25.20	25.94	24.16	24.93
351			24.86	25.75	24.06	24.93
352.5			24.82	25.53	24.13	24.78
354			24.57	25.50	24.13	24.70
355.5			24.50	25.42	24.15	24.69
357			24.45	25.36	24.15	24.72
358.5			24.42	25.20	24.15	24.67
360			24.39	25.18	24.13	24.65
361.5			24.48	25.16	24.19	24.70
363			24.36	25.22	24.15	24.74
364.5			24.45	25.17	24.07	24.79
366			24.46	25.20	24.04	24.80
367.5			24.45	25.16	24.00	24.69
369			24.27	25.18	24.04	24.64
370.5			24.28	25.33		
372			24.26	25.41		
373.5			24.26	25.38		
375			24.33	25.44		
376.5			24.27	25.49		
378			24.25	25.49		
379.5			24.14	25.60		
381			24.07	25.69		
382.5			23.97	25.78		
384			24.04	25.71		
385.5			24.08	25.74		
387			24.09	25.60		
388.5			24.10	25.74		
390			24.14	25.67		
391.5			24.18	25.66		
393			24.15	25.46		
394.5			24.00	25.41		
396			23.98	25.34		
397.5			24.05	25.31		

399			24.18	25.33		
400.5			24.19	25.15		
402			24.22	25.11		
403.5			24.24	25.16		
405			24.14	25.15		
406.5			24.17	25.16		
408			24.18	25.10		
409.5			24.20	24.97		
411			24.25	24.91		
412.5			24.32	24.82		
414			24.30	24.79		
415.5			24.28	24.68		
417			24.28	24.62		
418.5			24.30	24.55		
420			24.26	24.54		
421.5			24.14	24.43		
423			24.14	24.39		
424.5			24.15	24.41		
426			24.16	24.41		
427.5			24.10	24.45		
429			24.00	24.36		
430.5			23.92	24.30		
432			23.88	24.19		
433.5			23.86	24.21		
435			23.87	24.19		
436.5			23.85	24.15		
438			23.83	24.17		

b) Field-scale experiment in a meandering channel (Exp. 2-2; Case 2-2-1~2-2-3)

	SSCv (ppm)					
	Case2-2-1 (quart sand)		**Case2-2-2 (yellow loess)**		**Case2-2-3 (mixture)**	
Section / Time (s)	**Sec. C1**	**Sec. C2**	**Sec. C1**	**Sec. C2**	**Sec. C1**	**Sec. C2**
1	10.29	9.81	10.53	10.93	11.93	11.42
2	10.29	9.81	10.53	11.04	11.93	11.42
3	10.29	9.81	10.66	11.04	11.93	11.42
4	10.29	9.83	10.66	11.04	11.79	11.42
5	10.29	9.83	10.71	11.04	11.79	11.83
6	10.29	9.83	11.40	11.04	11.77	11.83
7	10.29	10.10	11.44	11.09	11.77	11.42
8	10.29	10.10	11.56	11.09	11.77	11.69
9	10.29	10.24	11.44	10.93	11.68	11.83
10	10.15	10.10	11.44	11.01	11.65	11.95
11	10.15	10.45	11.40	11.09	11.65	12.12
12	10.06	10.60	11.30	11.09	11.68	12.12
13	10.06	10.60	11.30	11.09	11.68	12.12
14	10.15	10.60	11.25	11.23	11.65	11.95
15	10.15	10.65	11.30	11.23	11.65	11.69
16	10.06	10.65	11.25	11.23	11.76	11.69
17	10.61	10.65	11.00	11.19	11.65	11.88

18	9.93	10.45	11.00	11.23	11.76	11.88
19	10.61	10.45	11.00	11.23	11.76	11.66
20	10.61	10.59	11.00	11.23	11.76	11.66
21	10.43	10.65	11.00	11.23	11.47	11.66
22	10.66	10.59	11.63	11.19	11.47	11.66
23	10.66	10.59	11.66	11.18	11.45	11.61
24	10.59	10.50	11.66	11.18	11.45	11.68
25	10.52	10.44	11.63	11.19	11.47	11.71
26	10.52	10.44	11.66	11.18	11.47	11.68
27	10.43	10.43	11.77	11.18	11.83	11.61
28	10.43	10.50	11.77	10.79	11.83	11.61
29	10.43	10.43	11.63	10.79	11.83	11.61
30	10.52	10.43	11.53	10.79	11.87	11.61
31	10.52	10.43	11.53	10.79	11.87	11.61
32	10.42	10.43	11.36	10.94	11.87	11.71
33	10.16	10.43	11.36	11.03	11.88	11.71
34	10.16	10.43	11.53	11.03	11.88	11.46
35	10.16	10.51	11.56	10.94	11.87	11.35
36	10.16	10.51	11.53	10.94	11.26	11.46
37	10.16	10.53	11.36	11.03	11.26	11.46
38	10.39	10.53	11.53	11.03	11.18	11.46
39	10.39	10.53	11.56	11.04	11.26	11.35
40	10.39	10.68	11.68	11.04	11.18	11.35
41	10.39	10.68	11.68	11.23	11.18	11.35
42	10.39	10.82	12.04	11.04	11.44	11.34
43	10.39	10.95	12.04	10.96	11.20	11.34
44	10.39	10.95	12.04	10.96	11.40	11.34
45	10.46	10.68	11.68	10.99	11.40	11.80
46	10.46	10.68	11.71	10.99	11.40	11.17
47	10.46	11.00	11.71	10.96	11.40	11.63
48	10.50	10.68	11.68	10.96	11.41	11.80
49	10.46	10.68	11.45	10.96	11.41	11.80
50	10.45	10.52	11.01	10.99	11.44	11.63
51	10.45	10.31	10.96	10.99	11.44	11.63
52	10.45	10.27	10.74	10.99	11.47	11.67
53	10.45	10.27	10.87	10.99	11.52	12.05
54	10.45	10.18	10.87	11.12	11.76	11.67
55	10.21	10.18	10.87	11.12	11.81	11.63
56	10.21	10.18	10.87	11.12	11.81	11.63
57	10.14	10.18	10.74	11.12	11.92	11.60
58	10.14	10.27	10.87	11.15	11.92	11.52
59	10.14	10.27	10.87	11.12	11.81	11.52
60	10.21	10.39	10.87	10.74	11.81	11.52
61	10.21	10.39	10.87	10.65	11.92	11.40
62	10.21	10.45	10.87	10.58	11.92	11.38
63	10.24	10.39	10.94	10.65	11.81	11.38
64	10.24	10.53	10.94	10.65	11.67	11.38
65	10.24	10.53	10.94	10.65	11.37	11.40
66	10.24	10.60	10.94	10.80	11.67	11.38
67	10.24	10.60	11.53	10.80	11.67	11.40
68	10.24	10.53	11.62	10.58	11.47	11.40
69	10.24	10.53	11.62	10.80	11.53	11.52
70	10.29	10.31	11.62	10.80	11.67	11.52
71	10.15	10.31	11.62	11.23	11.67	11.52
72	10.13	10.31	11.62	11.23	11.83	11.52
73	10.13	10.60	11.53	11.18	11.83	11.45
74	10.31	10.61	11.53	11.18	11.83	11.42

75	10.20	10.66	11.53	11.11	11.83	11.39
76	10.31	10.61	11.40	10.90	11.53	11.42
77	10.38	10.31	11.32	11.02	11.53	11.42
78	10.41	10.31	11.15	11.11	11.83	11.45
79	10.43	10.31	11.15	11.02	11.83	11.45
80	10.43	10.31	11.15	11.02	11.71	11.80
81	10.75	10.11	11.32	11.02	11.71	12.04
82	10.75	10.10	11.32	11.11	11.71	12.04
83	10.54	10.10	11.39	11.11	11.71	12.59
84	10.75	10.08	11.32	11.32	11.75	13.55
85	10.75	10.08	11.32	11.54	11.75	15.86
86	10.75	10.05	11.39	11.66	11.80	17.68
87	10.54	10.08	11.39	12.40	11.80	17.87
88	10.33	10.05	11.39	12.69	11.80	19.39
89	10.33	10.08	11.39	12.83	12.57	20.80
90	10.27	10.08	11.39	14.71	12.58	22.61
91	10.02	10.17	11.32	15.35	13.62	28.39
92	9.99	10.22	11.32	16.74	17.41	29.11
93	9.99	10.44	11.32	17.39	24.21	32.95
94	9.88	10.46	11.62	18.71	27.36	52.10
95	9.99	10.46	11.64	35.65	28.22	60.59
96	9.99	10.61	11.64	37.90	34.31	62.02
97	9.88	10.68	12.09	46.10	40.77	62.23
98	10.02	11.49	12.65	50.70	44.16	68.23
99	9.88	13.06	13.40	58.57	46.68	69.72
100	9.88	14.26	13.42	61.09	50.16	72.39
101	9.88	15.25	14.95	63.57	65.25	76.65
102	10.02	15.56	15.11	88.24	83.05	77.39
103	10.05	19.24	15.15	98.66	94.27	77.39
104	10.10	20.54	17.10	124.85	96.02	84.32
105	10.31	22.24	23.78	142.93	99.90	89.18
106	11.29	22.31	43.03	152.57	119.10	93.72
107	11.29	28.20	51.75	156.88	123.06	93.72
108	11.59	30.26	63.51	156.88	127.76	93.72
109	11.76	32.50	70.66	162.48	162.25	84.25
110	11.76	39.54	71.92	162.93	169.13	84.25
111	11.84	40.24	72.50	165.33	175.83	84.25
112	13.31	43.02	108.94	165.49	175.83	79.89
113	14.00	44.85	122.54	165.49	183.22	79.89
114	14.03	46.63	139.54	167.59	184.97	79.19
115	17.40	49.89	145.96	167.59	195.83	72.17
116	19.78	51.92	192.86	166.03	197.36	72.06
117	19.83	55.38	240.81	166.03	203.65	70.97
118	20.51	59.19	256.80	166.03	203.65	69.12
119	22.50	59.74	270.57	166.03	203.65	68.75
120	23.08	59.74	281.45	165.49	203.65	67.91
121	27.08	59.74	284.31	152.02	197.36	65.54
122	33.25	59.74	284.31	141.54	197.36	64.17
123	36.16	57.72	284.31	136.08	193.69	63.72
124	36.19	57.72	292.19	129.93	189.93	58.02
125	37.94	56.96	292.19	125.71	183.34	54.84
126	47.50	56.96	284.31	124.37	177.99	54.09
127	47.91	53.30	281.45	123.53	174.39	53.99
128	49.27	51.62	272.39	121.56	173.72	47.26
129	57.34	50.93	243.24	116.82	170.65	45.88
130	63.66	50.67	241.41	105.93	166.13	45.58
131	76.11	47.68	217.88	94.74	158.44	43.54

132	76.52	45.81	213.78	92.63	152.48	41.24
133	80.03	44.99	213.78	90.64	142.97	40.81
134	81.51	41.05	204.80	80.43	132.92	40.09
135	86.43	39.59	201.00	80.22	128.12	36.23
136	91.10	39.59	200.89	77.20	128.04	36.13
137	97.07	38.10	188.16	76.62	125.12	36.13
138	97.07	36.67	184.24	72.38	124.69	35.16
139	97.34	34.86	164.40	69.83	123.72	34.61
140	97.34	33.59	156.93	63.90	107.38	34.05
141	97.34	32.61	156.70	61.09	96.75	33.21
142	97.34	31.79	156.48	57.56	96.57	31.73
143	91.10	29.94	141.83	57.26	96.57	29.47
144	91.05	29.57	130.59	54.68	93.40	27.99
145	91.01	26.58	129.35	52.96	93.01	26.71
146	74.15	26.58	127.20	50.41	93.01	25.55
147	74.15	26.58	126.31	50.41	88.56	24.59
148	72.56	24.40	113.34	48.47	81.06	23.87
149	69.79	23.02	108.98	45.85	75.36	23.27
150	69.65	23.01	107.92	45.75	71.18	23.26
151	61.56	22.33	104.44	45.04	70.75	22.09
152	64.66	22.11	104.11	42.89	69.72	22.09
153	64.66	21.40	103.96	36.58	65.31	22.08
154	64.66	21.40	95.14	36.56	63.59	22.08
155	56.36	20.87	93.06	34.72	63.59	21.72
156	55.12	20.08	86.41	34.26	63.01	20.38
157	53.76	19.30	83.94	33.78	61.15	18.95
158	53.76	19.30	82.62	32.33	54.18	18.63
159	53.76	18.81	80.15	30.82	52.37	18.60
160	50.77	18.81	77.00	30.39	52.37	17.45
161	49.71	16.09	75.57	29.40	46.31	17.45
162	48.97	15.70	74.42	29.38	46.02	17.38
163	47.85	15.49	72.27	28.07	44.91	17.21
164	47.20	15.34	71.75	27.91	44.41	17.21
165	46.67	14.72	65.00	26.22	41.39	17.00
166	46.20	14.72	62.75	26.05	40.68	16.55
167	42.82	14.72	61.87	25.99	39.94	15.89
168	38.14	14.38	61.33	24.40	39.25	15.13
169	35.74	14.35	61.33	24.40	38.72	15.13
170	35.61	14.00	60.80	24.01	38.55	15.13
171	35.37	13.74	54.80	23.88	37.00	14.88
172	31.31	13.74	53.64	23.88	36.65	14.87
173	29.03	13.66	52.93	23.75	34.62	14.87
174	26.64	13.66	52.91	23.75	34.50	14.88
175	26.40	13.66	52.93	22.92	33.95	14.88
176	26.40	13.34	52.10	22.62	32.06	14.88
177	25.50	13.16	50.06	20.80	31.75	15.54
178	24.63	13.16	49.54	20.54	28.18	15.54
179	24.47	13.12	48.48	20.52	27.98	15.46
180	24.20	12.75	45.29	19.83	26.96	14.52
181	24.47	13.12	44.82	19.35	26.69	14.52
182	24.47	12.75	42.19	19.02	24.85	14.52
183	24.28	12.73	38.79	18.61	24.71	14.52
184	24.28	12.53	38.66	18.57	24.53	14.32
185	24.28	12.39	37.46	17.87	23.69	14.52
186	22.18	12.39	36.75	17.45	23.07	14.52
187	22.18	12.39	36.64	16.90	23.07	14.17
188	22.18	12.39	36.15	16.70	23.07	14.09

189	20.97	12.34	35.75	16.34	23.07	14.09
190	20.97	12.31	33.79	16.21	22.15	14.01
191	20.97	11.93	32.66	16.21	22.10	13.89
192	19.04	11.93	32.03	16.09	21.90	13.71
193	18.34	11.93	31.35	15.93	20.81	13.62
194	17.85	11.93	31.00	15.21	20.81	13.62
195	17.85	11.54	30.41	15.21	20.81	13.15
196	17.52	11.93	30.38	15.13	20.81	13.13
197	17.85	11.54	30.25	14.99	20.54	13.02
198	17.52	11.54	29.89	14.90	20.24	13.13
199	17.34	11.54	29.24	14.82	20.24	12.89
200	16.86	11.49	29.09	14.67	20.15	12.89
201	17.34	11.33	26.69	14.73	19.65	13.02
202	16.86	11.49	26.53	14.73	19.27	13.02
203	16.86	11.33	25.84	14.67	18.17	12.89
204	16.44	11.59	25.79	14.48	18.12	13.02
205	16.51	11.59	25.58	14.22	17.82	13.02
206	15.47	11.52	25.79	14.22	17.82	13.02
207	15.23	11.52	25.58	14.22	17.82	13.02
208	15.03	11.50	24.04	14.09	17.82	12.88
209	15.03	11.31	24.04	13.89	17.82	12.87
210	15.23	11.31	23.86	13.87	17.83	12.31
211	15.03	11.35	23.61	13.74	17.83	12.30
212	15.06	11.35	22.72	13.41	17.68	12.30
213	15.10	11.35	22.11	13.41	17.83	12.31
214	15.06	11.33	21.90	13.41	17.83	12.30
215	15.03	11.31	21.70	13.18	17.83	12.18
216	15.03	10.83	21.09	13.18	17.83	12.18
217	15.03	10.83	20.51	13.18	17.83	12.18
218	14.80	11.31	20.42	13.74	17.38	12.18
219	14.52	11.10	20.42	13.18	17.28	12.50
220	14.17	11.10	19.64	13.18	16.95	12.99
221	14.10	11.10	19.58	13.16	16.72	12.99
222	13.60	11.10	19.58	13.16	16.10	12.99
223	13.50	11.10	19.55	13.38	15.85	12.96
224	13.60	10.95	19.30	13.38	15.85	12.96
225	13.60	10.95	19.30	13.38	15.73	12.96
226	13.40	11.10	19.30	13.37	15.63	12.96
227	13.33	11.20	18.87	12.83	15.63	12.73
228	13.33	11.10	18.83	12.78	15.63	12.23
229	13.33	11.06	18.76	12.76	15.61	12.03
230	13.12	11.06	18.76	12.70	15.37	12.03
231	13.12	11.06	18.76	12.70	15.37	12.03
232	13.14	10.95	18.55	12.70	15.37	12.03
233	13.12	10.95	17.76	12.70	15.28	12.06
234	13.12	11.06	17.76	12.70	15.02	12.06
235	12.78	11.15	17.41	12.97	14.71	12.00
236	12.78	11.15	16.91	12.70	14.71	12.06
237	12.78	11.06	16.89	12.97	14.56	12.06
238	12.40	11.06	16.59	12.97	14.56	12.06
239	12.34	10.95	16.26	12.97	14.56	12.06
240	12.40	11.15	15.94	12.97	14.30	11.96
241	12.40	10.69	15.81	12.97	14.25	11.84
242	12.34	10.99	15.77	12.97	14.25	11.84
243	12.34	10.99	15.77	12.97	14.18	11.84
244	11.84	10.78	15.77	12.30	14.17	11.84
245	11.84	10.78	15.77	12.30	14.17	11.96

246	11.84	10.78	15.77	13.03	14.17	11.96
247	11.84	10.78	15.66	13.03	14.07	12.62
248	11.84	10.99	15.61	13.03	14.07	12.62
249	11.98	11.08	15.66	13.03	13.68	12.62
250	11.88	10.99	15.71	13.03	13.68	12.62
251	11.88	10.99	15.71	13.03	13.68	12.62
252	11.98	11.04	15.71	12.61	13.61	12.46
253	12.09	11.04	15.71	12.61	13.61	12.15
254	12.16	11.08	15.57	12.61	13.46	12.15
255	12.16	11.08	14.85	12.50	13.19	12.08
256	12.09	11.04	14.57	12.43	13.19	12.05
257	12.09	11.04	14.57	12.43	13.46	11.94
258	12.16	11.04	14.85	12.43	13.19	12.05
259	12.24	11.04	14.48	12.43	13.46	12.05
260	12.36	11.04	14.13	12.43	13.58	11.95
261	12.24	11.21	14.13	12.26	13.72	11.95
262	12.24	11.21	14.13	12.18	13.73	11.95
263	12.46	11.21	14.05	12.13	13.73	11.94
264	12.46	11.08	14.05	12.13	13.73	11.95
265	12.46	10.70	14.07	12.09	14.04	12.08
266	12.46	10.99	14.13	12.05	13.73	12.25
267	12.46	10.99	14.13	11.87	13.72	12.35
268	12.46	10.99	14.13	11.87	13.72	12.25
269	12.46	10.70	14.45	11.87	13.73	12.25
270	12.45	10.70	14.80	11.84	13.73	12.25
271	12.45	10.70	14.56	11.84	13.53	12.29
272	12.02	10.91	14.80	11.84	13.46	12.29
273	11.81	10.74	14.91	11.87	13.13	12.29
274	11.58	10.91	15.41	11.87	13.13	12.29
275	11.53	10.91	15.57	11.87	13.06	12.29
276	11.58	10.74	15.57	11.84	13.12	11.98
277	11.53	10.74	15.41	11.65	13.13	11.98
278	11.54	10.74	15.57	11.55	13.13	12.29
279	11.54	10.91	15.57	11.27	13.13	11.98
280	11.54	10.91	15.71	11.55	13.12	11.98
281	11.54	10.86	15.71	11.27	13.12	11.98
282	11.58	10.86	15.66	11.24	13.12	
283	11.67	10.92	15.57	11.14	13.12	
284	11.67	10.86	15.56	11.14	13.12	
285	11.67	10.86	15.21	11.11	13.12	
286	11.67	10.92	15.56	11.14	13.12	
287	11.73		15.56	11.16	13.12	
288	11.82		15.56	11.24	12.58	
289	11.73		15.66	11.48	12.58	
290	11.73		15.56	11.37	12.82	
291	11.73		14.99	11.48	12.58	
292	11.64		14.99	11.48	12.82	
293	11.64		14.80	11.48	12.82	
294	11.57		14.46	11.48	13.19	
295	11.57		14.46	11.48	12.82	
296	10.81		14.22	11.48	12.82	
297	10.81		13.94	11.48	12.82	
298	10.78		13.94	11.39	12.99	
299	10.81		13.94	11.37	12.99	
300	10.81		13.94	11.35	12.99	
301	10.81		13.82	11.35	13.18	
302	11.02		13.94	11.35	12.99	

303	11.02		13.82	11.35	13.18	
304	11.02		13.82	11.39	12.99	
305	11.02		13.82	11.43	13.18	
306	11.02		13.82	11.43	13.62	
307	11.02		13.69	11.43	13.62	
308	11.02		13.58	11.43	13.62	
309	10.84		13.31		13.62	
310	10.71		13.27		13.62	
311	10.75		13.01		12.82	
312	10.71		12.81		12.82	
313	10.71		12.71		12.82	
314	10.71		12.68		12.99	
315	10.71		12.68		12.72	
316	10.71		12.68		12.72	
317	10.71		12.48		12.99	
318	10.75		12.48		12.99	
319	10.78		12.68		12.99	
320	10.86		12.68		12.99	
321	10.86		12.76		12.99	
322	11.25		12.76		13.13	
323	11.25		13.02		13.13	
324	10.78		13.02		13.04	
325	11.23		12.78		13.04	
326	11.30		12.78		13.00	
327	11.23		12.78		12.90	
328	10.80		12.76		12.80	
329	10.80		12.57		12.56	
330	10.80		12.63		12.80	
331	11.01		12.57		12.80	
332	10.80		12.63		12.80	
333	10.80		12.57		12.89	
334	10.80		12.53		12.87	
335	10.80		12.57		12.89	
336	10.80		12.57		12.87	
337	10.92		12.53		12.87	

c) Field-scale experiment in a meandering channel (Exp. 2-2; Case 2-2-4~2-2-7)

	SSCv (ppm)							
	Case2-2-4 (quart sand)		Case2-2-5 (yellow loess)		Case2-2-6 (coarse yellow loess)		Case2-2-7 (mixture)	
Section / Time (s)	Sec. C2	Sec. C3	Sec. C2	Sec. C3	Sec. C2	Sec. C3	Sec. C2	Sec. C3
1	7.86	8.86	9.81	9.43	10.59	10.28	10.17	10.89
2	7.86	8.86	9.81	9.48	10.59	10.41	10.17	10.89
3	7.86	7.97	9.81	9.43	10.59	10.41	10.18	10.89
4	7.86	7.97	9.74	9.43	10.59	10.41	10.17	10.89
5	7.9	7.97	9.72	9.48	10.59	10.41	10.17	10.73
6	8.02	7.97	9.74	9.48	10.64	10.54	10.18	10.52
7	8.02	7.96	9.74	9.73	10.64	10.59	10.18	10.28
8	8.72	8.45	9.72	9.73	10.59	10.54	10.17	9.91
9	8.06	8.45	9.61	9.48	10.64	10.54	10.16	10.28

10	8.64	8.24	9.57	9.72	10.64	10.54	10.16	9.96
11	8.43	8.15	9.57	9.73	10.32	10.54	10.27	9.91
12	8.43	8.24	9.61	9.73	10.32	10.54	10.27	9.78
13	8.52	8.45	9.72	10.14	10.32	10.59	10.21	9.78
14	8.52	8.24	9.61	9.73	10.64	10.59	10.21	9.81
15	8.43	8.24	9.9	9.73	10.62	10.75	10.21	9.81
16	8.5	8.46	9.61	9.86	10.32	10.52	10.21	9.92
17	8.5	8.46	9.9	10.15	10.36	10.52	10.22	9.92
18	8.5	8.24	9.9	10.16	10.62	10.41	10.27	9.96
19	8.52	8.24	9.9	10.16	10.36	10.62	10.27	9.96
20	8.5	8.24	9.9	10.16	10.36	10.62	10.27	10.01
21	8.5	8.24	9.4	10.16	10.62	10.75	10.22	10.25
22	8.5	8.24	9.4	10.16	10.36	10.62	10.22	10.27
23	8.5	7.99	9.4	10.16	10.36	10.41	10.27	10.27
24	8.49	7.99	9.69	10.16	10.36	10.43	10.27	10.27
25	8.5	7.99	9.69	10.16	10.28	10.43	10.27	10.36
26	8.5	7.99	9.97	10.16	10.36	10.43	9.88	10.27
27	8.5	7.99	9.69	9.77	10.66	10.43	9.73	10.27
28	8.49	7.99	9.69	9.77	10.73	10.43	9.73	10.25
29	8.36	7.99	9.69	9.56	10.78	10.43	9.73	10.25
30	8.36	8.33	9.7	9.77	10.95	10.48	9.88	10.25
31	8.36	8.33	9.7	9.86	10.95	10.48	9.88	10.12
32	8.36	7.99	9.7	9.86	11.07	10.78	9.95	10.12
33	8.36	8.3	9.7	9.86	11.19	10.78	9.88	10.12
34	8.58	8.33	9.66	9.86	11.15	10.78	9.88	10.12
35	8.58	8.36	9.66	9.86	11.15	10.9	9.83	10.12
36	8.58	8.36	9.49	10.34	11.15	10.9	9.95	10.19
37	8.58	8.36	9.56	10.34	11.15	10.92	10.03	10.39
38	8.58	8.3	9.66	10.34	11.15	10.92	9.95	10.39
39	8.6	8.26	9.66	10.41	11.15	10.9	9.95	10.41
40	8.6	7.92	9.64	10.34	11.15	10.9	9.83	10.41
41	8.6	8.26	9.66	10.34	10.73	10.76	10.17	10.41
42	8.58	8.26	9.64	10.27	10.44	10.42	9.83	10.39
43	8.31	8.08	9.64	10.34	10.44	10.42	10.17	10.39
44	8.26	8.08	9.56	10.27	10.44	10.42	10.17	10.33
45	8.26	7.92	9.5	10.27	10.41	10.42	10.17	10.33
46	8.23	8.08	9.5	10.19	10.48	10.44	9.97	10.55
47	8.1	8.08	9.5	10.27	10.55	10.44	9.83	10.37
48	8.1	7.84	9.45	10.05	10.55	10.44	9.97	10.55
49	8.07	8.08	9.37	9.99	10.55	10.44	9.97	10.37
50	8.1	8.14	9.45	9.99	10.48	10.44	10.13	10.37
51	8.23	8.14	9.37	10.05	10.55	10.44	10	10.37
52	8.23	8.16	9.36	9.99	10.55	10.44	10	10.37
53	8.2	8.16	9.25	9.99	10.48	10.05	9.97	10.37
54	8.2	8.16	9.36	10.35	10.25	10.05	9.73	10.74
55	8.2	8.16	9.36	10.35	10.25	10.05	9.73	10.37
56	8.2	8.14	9.93	10.35	10.25	10	9.73	10.21
57	8.21	8.16	9.93	10.11	10.25	10	10	10.21
58	8.45	8.16	9.93	10.11	10.25	10.05	10	10.21
59	8.47	8.21	9.93	10.35	10.17	10.25	9.72	10.21
60	8.63	8.21	9.96	10.11	10.25	10.25	9.72	10.21
61	8.47	8.21	9.96	10.11	10.25	10.53	9.72	10.38
62	8.47	8.17	9.96	10.11	10.28	10.6	9.72	10.38
63	8.47	8.17	9.96	10.11	10.28	10.6	9.72	10.38
64	8.46	8.17	9.96	10.11	10.28	10.6	9.83	10.35

65	8.47	8.17	9.96	10.11	10.42	10.6	10.1	10.35
66	8.47	8.17	9.88	10.11	10.42	10.62	10.21	10.35
67	8.46	8.17	9.79	10.11	10.47	10.6	10.1	10.35
68	8.45	8.17	9.88	10.66	10.47	10.62	9.99	10.35
69	8.45	8.17	9.96	10.11	10.47	10.68	9.99	10.36
70	8.45	8.17	9.88	10.05	10.47	10.62	9.83	10.35
71	8.45	8.2	9.96	10.05	10.86	10.97	9.74	10.35
72	8.41	8.22	10.08	10.05	10.86	10.62	9.99	10.36
73	8.41	8.94	10.08	9.84	10.93	10.61	10.03	10.36
74	8.45	8.38	9.96	9.84	10.99	10.62	10.03	10.36
75	8.45	8.38	10.08	9.84	11.01	10.79	10.03	10.4
76	8.45	8.38	10.08	9.75	11.01	10.79	10.03	10.4
77	8.45	8.42	10.14	9.48	11.28	10.97	10.03	10.4
78	8.51	8.77	10.14	9.48	12.83	10.91	10.28	10.4
79	8.56	8.92	10.62	9.92	13.1	10.91	10.89	10.21
80	8.56	8.77	10.74	9.48	13.27	10.91	11.14	10.4
81	8.56	8.68	11.51	9.59	13.85	10.89	11.71	10.4
82	8.56	8.68	13.22	9.5	14.32	10.89	12.43	10.41
83	8.59	8.42	15.11	9.59	14.39	10.89	13.84	10.41
84	9.02	8.68	20.05	9.59	20.75	10.89	13.85	10.53
85	9.04	8.68	21.14	9.59	22.06	10.89	14.42	10.58
86	9.21	8.68	25	9.63	23.31	10.89	15.78	10.58
87	9.76	8.68	25.65	9.91	27.1	10.89	20.05	10.58
88	9.77	8.14	39.68	9.63	31.85	10.83	24.94	10.41
89	10.85	8.14	46.85	9.63	52.35	10.83	30.26	10.41
90	12.22	8.11	51.11	9.91	56.61	10.83	31.96	10.33
91	13.07	8.06	52.8	10.26	58.4	10.83	33.88	10.33
92	13.51	8.06	64.87	10.26	59.88	10.83	38.29	10.3
93	14.65	8.06	71.11	9.91	78.64	10.37	47.87	10.3
94	20.22	8.04	75.32	10.26	80.02	10.37	62.55	10.3
95	23.16	8.06	81.42	10.26	90.72	10.34	62.55	10.3
96	25.51	8.11	86.12	10.26	103.58	10.47	62.93	10.3
97	25.51	8.11	118.86	9.85	109.43	10.34	65.45	10.3
98	30.87	8.11	136.97	9.85	122.32	10.47	67.73	10.51
99	31.13	8.04	138.19	9.76	122.32	10.34	68.19	10.51
100	31.33	8.11	154.62	9.76	125.99	10.33	75.15	10.81
101	34.29	8.39	155.7	9.76	136.85	10.32	76.41	10.81
102	36.28	8.39	155.7	9.76	136.85	10.32	76.77	10.81
103	40.46	8.39	155.7	9.76	136.85	10.26	88.5	10.81
104	41.95	8.39	155.7	9.76	138.15	10.26	90.28	10.62
105	42.14	8.39	156.08	9.85	138.15	10.26	92.38	10.62
106	45.72	8.39	156.08	9.76	138.15	10.26	92.38	10.52
107	45.72	8.48	154.62	10.07	133.81	10.32	92.38	10.62
108	45.72	8.76	151.95	10.43	133.81	10.32	90.28	10.52
109	43.9	8.76	147.85	10.43	133.81	10.32	88.5	10.62
110	43.9	8.55	146.55	10.43	132.06	10.52	87.92	10.52
111	46.51	8.55	137.36	10.09	123.31	10.68	81.77	10.43
112	46.51	8.72	124.11	10.09	118.64	10.68	81.77	10.52
113	43.9	8.72	122.51	10.43	117.91	10.68	79.98	10.43
114	43.9	8.72	122.37	10.66	117	10.68	76.35	10.73
115	42.26	8.69	119.29	10.66	113.73	10.68	75.56	10.26
116	41.3	8.58	115.64	10.72	113.39	10.68	74.67	10.47
117	39.16	8.55	114.44	10.66	113.39	10.68	74.38	10.26
118	38.14	8.51	110.24	10.09	110.47	10.7	73.04	10.47
119	38.13	8.36	108.22	10.72	110.24	10.7	69.49	10.47

120	37.73	8.36	99.55	10.06	105.46	10.68	64.53	10.47
121	33.08	8.36	91.46	10.56	97.92	10.66	62.05	10.47
122	32.4	8.15	91.33	10.72	91.71	10.7	61.71	10.47
123	31.86	8.15	87.09	10.56	83.39	10.81	61.52	10.7
124	31.57	8.15	79.68	10.2	83.34	10.81	59.26	10.7
125	31.57	8.15	78.03	10.2	77.64	10.92	55.09	10.7
126	29.52	8.15	76.58	10.06	77.64	10.81	51.72	10.7
127	27.26	7.99	72.26	10.2	77.2	10.81	50.21	10.7
128	27.15	7.9	72.07	10.48	77.2	10.81	49.89	10.22
129	26.86	7.9	70.5	10.2	73.13	10.92	49.69	9.96
130	25.3	7.9	68.25	10.26	66.02	10.92	45.71	10.22
131	23.34	7.88	60.61	10.26	66.02	11.01	45.07	10.22
132	22.72	7.88	60.46	10.2	63.83	11.01	43.53	10.19
133	22.4	7.88	60	10.2	52.29	11.01	41.2	10.19
134	22.31	7.88	59.67	10.26	51.46	11.01	37.99	10.19
135	21.35	7.88	57.11	10.36	51.46	11.01	37.26	10.19
136	21.29	7.88	53.4	10.36	51.31	11.01	37.2	10.19
137	19.2	7.88	50.39	10.26	50.4	11.13	36.92	10.07
138	17.34	8	49.33	10.15	49.16	11.13	34.45	10.19
139	17.18	8.27	45.31	10.26	48.72	11.01	33.59	10.32
140	16.88	8.27	42.98	10.36	44.84	10.97	31.08	10.19
141	15.75	8.49	42.79	10.37	44.84	10.97	30.47	10.32
142	15.25	8.27	42.69	10.37	43.75	10.97	30.47	10.36
143	15.25	8.27	41.16	10.96	40.36	10.85	30.28	10.36
144	15.15	8.18	40.64	10.37	40.04	10.38	29.67	10.18
145	14.79	8.07	40.26	10.37	38.33	10.85	29.53	10.36
146	14.74	8.07	39.04	10.96	36.49	10.85	28.53	10.36
147	14.47	8.18	36.56	10.96	36.28	10.21	28.53	10.36
148	14.05	8.18	35.06	11.2	35.62	10.85	25.59	10.47
149	14.05	8.18	34.34	11.2	35.17	10.21	25.37	10.47
150	14.05	8.19	33.57	10.96	35.16	10.21	25.12	10.47
151	14.05	8.18	33.15	10.52	35.16	10.75	24.73	10.47
152	13.65	8.18	30.5	10.52	31.6	10.75	23.98	10.22
153	13.64	8.19	28.66	10.36	30.47	10.75	23.98	10.22
154	13.37	8.19	27.72	10.36	30.32	10.75	22.95	10.45
155	13.37	8.19	27.43	10.23	29.74	10.44	21.81	10.45
156	12.9	8.19	26.54	10.11	27.72	10.44	21.76	10.45
157	12.78	8.14	26.06	10.23	26.97	10.44	21.56	10.45
158	12.08	8.14	25.53	10.23	26.52	10.34	21.55	10.28
159	12.08	8.01	25.17	10.23	26.44	10.34	20.69	10.22
160	11.41	7.85	24.4	10.36	25.25	10.09	19.94	10.15
161	11.33	7.91	23.33	10.36	24.94	10.09	19.49	10.15
162	10.87	8.01	23.24	10.11	23.08	10.09	17.47	10.15
163	10.8	8.01	23.07	10.48	23.08	10.07	17.21	10.11
164	10.8	8.01	22.81	10.48	22.97	10.07	16.68	10.11
165	10.78	8.01	21.37	10.57	22.47	10.07	16.62	10.11
166	10.78	8.01	19.19	10.57	22.97	10.58	16.13	10.24
167	10.74	8.11	18.94	10.62	22.97	10.93	16.13	10.11
168	10.3	8.11	18.94	10.57	22.97	11.39	15.95	10.24
169	10.29	8.18	18.1	10.57	22.62	11.54	15.95	10.81
170	10.3	8.26	18.1	10.57	22.47	11.54	15.22	10.81
171	10.29	8.26	17.87	10.57	21.49	11.54	15.22	10.81
172	10.29	8.18	17.67	10.57	21.49	11.39	15.22	10.81
173	10.29	8.18	17.67	10.3	20.51	11.39	15.08	10.81
174	10.37	8.26	17.62	10.3	20.17	11.54	15.08	10.5

175	10.37	8.4	16.39	10.16	19.5	11.54	14.72	10.5
176	10.29	8.4	15.87	10.14	19	11.39	14.69	10.4
177	10.12	8.26	15.83	10.14	18.75	11.36	14.59	10.5
178	10.12	8.4	15.8	10.16	18.24	10.85	14.56	10.4
179	9.91	8.4	15.8	10.14	17.89	10.85	14.36	10.4
180	9.91	8.4	15.8	10.02	17.89	10.95	14.36	10.4
181	9.91	8.4	15.36	10.14	17.38	10.95	14.16	10.37
182	9.82	8.4	15.1	10.14	17.01	11.13	14.16	10.37
183	9.91	8.4	15.1	10.15	16.81	11.36	14.08	10.67
184	9.91	8.45	14.73	10.67	16.73	11.36	13.51	11.2
185	9.82	8.34	14.1	10.7	16.56	11.36	13.29	11.2
186	9.82	8.39	14.08	10.73	16.54	11.37	13.04	11.32
187	9.82	8.73	14.02	10.73	16.45	12.74	12.98	11.32
188	9.59	8.42	14.08	10.98	16.36	12.89	12.74	11.37
189	9.53	8.42	14.08	11.88	16.45	13.61	12.56	11.4
190	9.28	8.42	14.02	12.48	16.36	13.77	12.56	11.57
191	9.23	8.52	14.02	12.81	14.78	13.88	12.28	11.57
192		8.52	14	13.04	14.78	13.97	12.19	11.57
193		8.52	13.77	13.45	14.78	14.75	12.17	11.81
194		8.52	13.61	14.25	14.78	16.38	12.14	11.99
195		8.73	13.61	14.36	14.27	17.73	12.14	12.78
196		9	13.18	14.71	14.17	19.96	12.14	13.78
197		9.58	12.58	17.43	14.13	20.07	12.13	13.93
198		9.72	12.57	18.8	14.13	22.64	11.81	14.61
199		9.72	12.36	19.17	13.85	26.41	11.61	14.87
200		10.01	12.36	19.7	13.78	27.98	11.61	16.68
201		10.05	12.28	20.77	13.78	30.4	11.52	18.63
202		10.44	12.28	20.93	13.59	30.97	11.61	19.75
203		10.67	12.04	24.99	13.56	32.71	11.61	20.48
204		10.67	12.02	30.92	13.17	34.84	11.81	22.35
205		11.32	11.98	31.9	12.97	38.11	12.12	23.55
206		11.53	11.87	33.05	12.86	42.64	12.12	23.98
207		11.85	11.87	34.17	12.74	42.74	12.12	27.19
208		12.28	11.76	36.23	12.69	46.06	12.12	27.24
209		14.08	11.76	37.91	12.66	46.07	12.12	27.36
210		14.08	11.56	42.28	12.47	48.26	11.92	27.51
211		14.29	11.41	43.53	12.47	54.06	12.3	28.78
212		15.36	11.41	44.5	12.47	57.69	11.93	30.69
213		15.66	11.56	49.68	12.47	66.22	11.92	31.91
214		16.37	11.76	53.98	12.25	68.97	11.83	32.24
215		16.44	11.76	57.55	12.21	71.69	11.76	34.53
216		17.56	11.82	58.23	12.21	74.24	11.76	40.95
217		17.78	11.46	59.17	12.21	78.7	11.17	43.53
218		18.49	11.46	64.36	12.18	80.4	11.03	44.93
219		19.94	11.46	67.22	12.05	85.42	11.03	45.22
220		20.75	11.46	70.29	11.93	87.61	11.07	45.32
221		21.36	11.46	73.6	11.92	88.13	11.03	50.4
222		23.54	11.34	74.16	11.92	88.52	10.77	50.66
223		23.93	11.26	80.08	11.92	89.87	10.83	54.43
224		25.96	11.23	82.15	11.92	90.21	11.03	54.43
225		26.77	11.26	84.38	11.9	92.02	11.03	55.51
226		27.14	11.23	90.29	11.8	92.48	11.03	56.01
227		27.48	11.19	92.28	11.71	93.72	11.07	56.83
228		28	11.19	94.49	11.8	102.86	11.12	57.98
229		28.23	11.23	95.92	11.8	103.79	11.07	62.86

230		28.76	11.23	99.71	11.9	106.83	11.04	65.4
231		30.11	11.19	101.46	12.2	106.94	11.27	66.59
232		30.47	11.07	107.52	12.38	107.9	11.27	66.79
233		30.95	10.81	114.08	12.2	109.56	11.27	67.63
234		30.95	10.81	118.01	12.51	110.47	11.04	68.52
235		31.47	10.81	118.13	12.51	110.47	10.66	68.53
236		31.47	10.82	119.39	12.51	110.47	10.66	71.35
237		31.67	10.82	120.18	12.51	111.1	10.66	71.35
238		31.67	10.82	121.24	12.2	111.1	10.5	71.35
239		31.67	10.81	121.24	11.71	110.47	10.24	71.98
240		31.57	10.82	121.24	11.42	110.47	10.24	72.07
241		32.64	10.82	122.55	11.4	110.4	10.24	72.32
242		31.57	10.85	122.89	11.4	110.26	10.43	72.49
243		31.57	10.85	122.89	11.33	107.17	10.5	72.32
244		32.64	10.85	122.89	11.33	107.17	10.5	72.32
245		32.64	10.82	122.89	11.21	107.17	10.5	71.35
246		31.86	10.79	122.89	11.33	107.1	10.5	70.8
247		31.86	10.7	122.89	11.33	106.89	10.5	70.8
248		32.17	10.7	121.78	11.77	106.5	10.43	70.8
249		32.17	10.7	121.78	11.77	101.74	10.67	70.01
250		32.99	10.5	121.78	11.77	101.6	10.67	69.68
251		32.3	10.5	116.92	11.77	98.94	10.67	67.2
252		32.3	10.5	113.99	11.52	98.94	10.67	67.13
253		32.99	10.67	111.33	11.52	98.82	10.67	66.29
254		32.99	10.38	111.33	11.16	98.82	10.76	67.13
255		32.3	10.38	111.23	11.14	98.69	10.76	67.1
256		32.37	10.33	111.07	11.01	97.72	10.76	65.85
257		32.3	10.33	111.07	10.93	96.86	10.78	65.59
258		32.3	10.33	111.07	10.88	96.79	10.78	65.59
259		32.3	10.38	108.71	10.88	95.96	10.76	65.38
260		32.29	10.33	108.23	10.88	95.1	10.78	64.92
261		32.29	10.33	107.22	10.93	94.26	10.78	64.1
262		32.29	10.33	107.19	10.93	91.58	10.73	62.63
263		30.88	10.33	105.03	10.93	90.81	10.67	61.5
264		30.88	10.46	102.88	10.93	90.26	10.54	60.18
265		30.57	10.46	98.32	10.93	88.23	10.67	59.57
266		29.39	10.46	97.14	10.93	87.27	10.54	58.78
267		29.39	10.73	94.55	10.78	87.09	10.45	57.66
268		29	10.46	94.3	10.88	85.33	10.33	57.56
269		29	10.22	89.59	10.78	83.57	9.97	57.22
270		29	10.46	88.98	10.7	82.03	9.97	55.23
271		28.1	10.73	88.97	10.7	80.23	10.23	54.23
272		28.1	10.71	88.31	10.7	79.06	10.28	53.46
273		26.76	10.71	85.39	10.65	76.48	10.28	52.42
274		26.25	10.28	85.17	10.7	73.18	10.23	51.91
275		24.58	10.69	82.77	10.87	71.56	10.19	51.33
276		26.25	10.69	80.5	10.88	71.09	10.23	51.26
277		26.25	10.57	77.32	10.88	70.38	10.23	50.66
278		24.58	10.57	76.38	10.87	67.91	10.28	49.31
279		24.58	10.57	76.32	10.87	67.66	10.28	48.17
280		23.99	10.42	76.31	11.09	67.43	10.75	48.17
281		23.99	10.42	76.12	10.87	67.43	10.75	47.93
282		23.78	10.28	75.03	10.85	67.04	10.75	47.11
283		23.31	10.19	73.49	10.87	65.41	10.75	46.3
284		23.64	10.19	72.58	11.09	65.41	10.8	46.3

285		23.31	10.19	72.35	11.16	65.35	10.8	45.71
286		22.62	9.84	71.62	10.85	62.07	10.8	45.33
287		22.55	10.19	68.08	10.85	60.91	10.76	42.47
288		22.37	10.19	65.5	11.16	60.64	10.55	42.36
289		22.37	10.15	64.99	11.19	58.91	10.76	41.66
290		21.72	10.15	64.65	11.19	58.53	10.55	41.52
291		20.17	9.99	63.69	11.19	56.51	10.38	41.36
292		20.17	9.99	63.34	11.23	53.29	10.38	41.33
293		19.47	10.15	63.17	11.44	52.69	10.38	39.85
294		18.88	10.45	62.23	11.44	52.54	10.3	39.85
295		18.48	10.15	61.55		51.95	10.14	39.55
296		18.76	10.2	60.73		51.43	10.1	38.66
297		18.48	10.19	58.96		51.04	10.14	38.17
298		17.97	10.19	55.81		48.84	10.3	38.17
299		17.97	10.19	55.65		48.38	10.3	38.17
300		17.97	10.19	55.32		47.98	10.16	37.79
301		17.97	10.2	53.79		46.99	10.16	36.54
302		17.97	10.2	53.44		44.6	10.14	35.31
303		17.2	10.2	52.23		44.6	10.16	34.15
304		17.2	10.2	50.18		44.6	10.45	34.14
305		17.14	10.2	49.94		44.6	10.45	33.64
306		16.99	10.19	48.34		44.42	10.45	33.64
307		16.43	10.3	47.14		44.29	10.44	33.33
308		16.42	10.11	47.07		43.93	10.16	31.42
309		16.05	9.99	46.56		43.01	10.13	30.73
310		15.94	10.3	45.82		42.8	10.01	30.21
311		15.47	9.79	44.64		42.44	10.13	30.11
312		15.2	9.79	43.85		42.19	10.13	29.93
313		14.99		42.55		39.54	10.01	29.93
314		14.99		41.63		39.54	10.01	28.73
315		14.99		41.46		39.54	10	28.33
316		14.99		40.88		39.23	10	28.07
317		14.95		40.66		39.23	10	27.87
318		14.95		40.34		36.78	9.92	26.37
319		14.23		38.73		36.21	10	25.83
320		14.83		37.63		35.97	10.05	25.83
321		14.83		37.54		35.07	10.05	25.34
322		14.83		37.22		35.07	10.29	25.19
323		14.83		37.22		34	10.29	25.15
324		14.23		36.41		33.5	10.05	25.12
325		13.92		36.24		32.57	10.05	25.12
326		13.34		33.63		31.8	9.97	25.12
327		13.24		33.37		31.73	9.97	25.12
328		13.24		32.62		31.59	9.97	24.95
329		13.34		32.49		31.59	9.97	24.3
330		13.31		32.49		31.19	9.97	23.29
331		13.31		31.73		30.86	9.97	23.16
332		12.87		31.4		30.86	9.97	23.09
333		12.86		30.34		29.3	9.93	22.89
334		12.86		29.86		28.75	10.1	22.69
335		12.53		28.46		28.53	10.1	21.98
336		12.5		28.24		27.83	10.1	21.98
337		12.5		27.71		27.83	10.1	21.41
338		12.47		27.71		26.92	10.39	21.41
339		12.47		26.73		26.33	10.39	20.98

340		12.39		26.73		26.09	10.59	20.92
341		12.39		26.47		25.67	10.51	20.86
342		12.39		26.39		25.67	10.05	20.14
343		11.97		26.47		25.54	10.42	19.83
344		12.39		26.47		25.04	10.42	19.68
345		11.97		26.47		24.91	10.42	19.68
346		11.92		26.47		24.69	10.42	19.52
347		11.45		26.25		24.63	10.42	19.05
348		11.92		25.03		24.63	10.42	18.75
349		11.45		24.81		24.27	10.42	18.97
350		11.45		24.39		24.27	10.2	18.75
351		11.39		24.39		23.69	10.2	18.47
352		11.45		24.33		22.97	10.2	18.47
353		11.45		23.84		22.78	10.02	18.47
354		11.39		23.43		22.78	9.93	18.46
355		11.26		23.29		22.78	10.02	18.21
356		11.1		23.01		22.46	9.93	18.21
357		10.97		22.51		21.9	9.93	18.07
358		10.85		22.48		21.9	9.93	17.51
359		10.97		22.25		21.9	9.82	17.51
360		10.85		22.25		21.9	9.88	17.51
361		10.69		22.06		21.16	9.88	17.18
362		10.58		22.06		20.7	9.97	16.95
363		10.69		22.05		20.46	9.97	17.6
364		10.58		21.38		20.46	10.16	17.6
365		10.58		21.01		20.46	10.16	16.47
366		10.58		21.01		20.46	10.16	16.47
367		10.55		21.01		20.46	10.16	16.47
368		10.55		20.77		20.46	10.18	16.47
369		10.55		19.82		19.78	10.18	16.45
370		10.58		19.62		19.73	10.18	16.45
371		10.62		19.44		18.98	10.18	15.46
372		10.62		19.16		18.97	10.18	16.42
373		10.55		18.87		18.97	10.18	15.65
374		10.55		18.71		18.91	10.07	15.65
375		10.26		18.59		18.76	9.99	15.46
376		10.24		18.27		18.5	10.07	14.97
377		10.24		18.15		18.5	10.07	14.92
378		10.24		18.15		18.44	10.07	14.84
379		10.21		18.1		18.44	10.07	14.92
380		10.09		17.98		18.09	10.07	14.92
381		10.01		17.98		18.09	10.19	15.06
382		10.09		17.98		18.06	10.07	14.92
383		9.91		17.98		18.09	10.07	14.78
384		9.91		17.95		18.06	10.07	14.78
385		10.09		17.31		16.99	10.07	14.78
386		10.39		16.81		16.99	9.98	14.78
387		9.88		16.81		16.79	9.98	14.86
388		9.88		16.81		16.6	9.98	14.86
389		9.88		16.22		16.6	9.98	14.79
390		9.88		16.22		16.6	9.98	14.78
391		9.88		16.01		15.98	9.75	14.76
392		9.75		16.01		15.98	9.75	14.76
393		9.69		16.03		15.18	9.89	14.73
394		9.61		16.01		15.18	9.89	14.53

395		9.18		15.99		15.32	9.89	13.86
396		9.15		15.99		15.18	9.89	13.7
397		9.15		15.99		15.09	10.07	13.5
398		9.2		15.94		15.09	9.89	13.7
399		9.2		15.94		15.09	9.89	13.5
400		9.2		15.8		15.32	9.86	13.5
401		9.2		15.79		15.32	9.86	13.5
402		9.2		15.79		14.96	9.63	13.5
403		9.5		15.62		14.87	9.55	13.5
404		9.77		15.47		14.58	9.63	13.5
405		10.02		15.3		14.58	9.63	13.38
406		10.02		15		14.48	9.83	13.26
407		10.02		15.3		14.58	9.83	13.26
408		9.77		14.89		14.58	9.83	13.26
409		9.64		14.38		14.58	9.83	13.26
410		9.64		14.38		14.58	10.02	13.38
411		9.63		14.38		14.78	10.02	13.38
412		9.63		14.38		14.79	10.05	13.25
413		9.56		14.38		14.79	10.05	13.38
414		9.56		14.65		14.79	10.02	13.25
415		9.45		14.65		14.78	10.02	13.43
416		9.45		14.65		14.78	10.16	13.43
417		9.38		14.65		14.65	10.02	13.43
418		9.32		14.65		14.65	10.02	13.11
419		9.38		14.65		14.65	10.06	12.84
420		9.32		14.65		14.41	10.06	12.84
421		9.38		14.35		13.99	10.06	12.76
422		9.38		13.79		13.91	9.57	12.71
423		9.42		13.5		13.7	9.57	12.71
424		9.42		13.5		13.7	9.61	12.71
425		9.52		13.5		13.56	9.57	12.71
426		9.42		13.66		13.56	9.57	12.71
427		9.42		13.66		13.77	9.61	12.45
428		9.52		12.97		13.71	10.06	12.45
429		9.42		13.66		13.56	9.61	12.3
430		9.54		13.72		13.71	9.57	12.2
431		9.76		13.73		13.56	9.61	12.16
432		10.33		13.72		13.71	9.61	12.04
433		10.33		13.72		13.71	9.95	12.04
434		10.33		13.72		13.71	10.23	12.04
435		10.03		13.72		14.03	10.28	12.01
436		10.33		13.73		14.03	10.28	11.65
437		10.33		13.77		13.71	10.44	11.65
438		10.03		13.77		13.59	10.41	11.66
439		10.03		13.77		13.59	10.51	11.66
440		9.66		13.23		13.59	10.51	11.65
441		9.56		13.23		14.03	10.51	11.58
442		9.56		13.23			10.51	11.66
443		9.56		13.23			10.41	11.66
444		9.56		12.98			10.41	11.66
445		9.56		12.98			10.18	12.19
446		9.52		12.88			10.07	12.19
447		9.52		12.44			9.99	12.2
448		9.24		12.88			9.99	12.2
449		8.98		12.88			9.99	12.2

Appendix B. 2. Dataset of spectra from hyperspectral images and corresponding SSC in rivers

From experimental studies in Chapter 3, 5,896 data of spectra from hyperspectral images and corresponding SSC were collected. This dataset can be obtained through the link below:

https://github.com/ksy92/Hyperspectral-dataset-Kwon-2022-

Appendix C. CMR-OV code

This code includes calculating the optimal number of hyperspectral clusters, selecting the optimal spectral band combination for each cluster, learning the final model with hyperspectral cluster, and mapping SSC as a TIFF file that can be visualized in the GIS program. To run this code, the dataset with the same format as the spectra-SSC dataset in Appendix B is nessecarily required as an input file.

```
# -*- coding: utf-8 -*-
"""
Created on Fri May 27 2022

@author: Siyoon Kwon
"""

import pandas as pd
import spectral.io.envi as envi
import numpy as np
from osgeo import gdal, osr

total_df= pd.read_csv('Spectra-SSC Dataset.csv')

#%%Data setting
from sklearn.model_selection import train_test_split
import sklearn.metrics as metrics
from sklearn import preprocessing

def regression_results(y_true, y_pred):

    errors = abs(np.array(y_true).reshape(-1) - np.array(y_pred).reshape(-1))
    explained_variance=metrics.explained_variance_score(y_true, y_pred)
    mean_absolute_error=metrics.mean_absolute_error(y_true, y_pred)
    mean_absolute_error=np.mean(errors**2)
    mse=metrics.mean_squared_error(y_true, y_pred)
    mean_squared_log_error=metrics.mean_squared_log_error(y_true, y_pred)
    mean_absolute_error=metrics.mean_absolute_error(y_true, y_pred)
    r2=metrics.r2_score(y_true, y_pred)
    mape = 100 * (errors / np.array(y_true).reshape(-1))
    mape = np.mean(mape)

    return round(explained_variance,4),   round(r2,4),
    round( mean_absolute_error,4),round(np.sqrt(mse),4),   round(mape,4)

con = total_df['SSC']
spectrum = total_df.iloc[:,34:184]
spectrum= spectrum.dropna()
con=con[spectrum.index]
```

```
X1 = spectrum.values
Y = con.values

#%% Clustering
from sklearn.feature_selection import RFECV
from sklearn.mixture import GaussianMixture
from sklearn.ensemble import RandomForestRegressor

n_clusters = 10
cluster=GaussianMixture(n_components=n_clusters,random_state=1000,
covariance_type='full').fit(X1)
C_INDEX = cluster.fit_predict(X1)

total_df2 = total_df.iloc[spectrum.index, :]
total_df2['Cluster'] = C_INDEX

case_for_cl = total_df2.copy()
model = RandomForestRegressor(n_estimators = 100, n_jobs=4, random_state=20)

#%%Learning curve
from sklearn.model_selection import ShuffleSplit
from sklearn.model_selection import learning_curve

total_len = len(case_for_cl)
for z in np.arange(n_clusters):
    X1 = spectrum[case_for_cl['Cluster']==z]
    globals()['por_x_{}'.format(z)]= len(X1)/total_len

for z in np.arange(n_clusters):
    X1 = spectrum[case_for_cl['Cluster']==z] #spectrum#
    Sc = preprocessing.StandardScaler().fit(X1)
    X= Sc.transform(X1)
    X = pd.DataFrame(X).dropna(axis=0)
    Y = con[case_for_cl['Cluster']==z]
    globals()['estimator_{}'.format(z)] =    model

    cv = ShuffleSplit(n_splits=5, test_size=0.2, random_state=0)
    train_sizes, train_scores, test_scores, fit_times, _ = learning_curve(
            globals()['estimator_{}'.format(z)],
            X,
            Y,
            cv=cv,
            n_jobs=-1,
            train_sizes=np.linspace(0.1, 1.0, 5),
            return_times=True,
        )
    globals()['CV_train_mean_{}'.format(z)] = np.mean(train_scores, axis=1)
    globals()['CV_train_std_{}'.format(z)] = np.std(train_scores, axis=1)
    globals()['CV_test_mean_{}'.format(z)] = np.mean(test_scores, axis=1)
    globals()['CV_test_std_{}'.format(z)] = np.std(test_scores, axis=1)
    globals()['CV_fit_times_mean_{}'.format(z)] = np.mean(fit_times, axis=1)
    globals()['CV_fit_times_std_{}'.format(z)] = np.std(fit_times, axis=1)

fin_train_mean= 0
fin_train_std = 0
fin_test_mean= 0
fin_test_std = 0
fin_time_mean= 0
fin_time_std = 0
```

```
for z in np.arange(n_clusters):
      fin_train_mean += globals()['CV_train_mean_{}'.format(z)][-
1]*globals()['por_x_{}'.format(z)]
      fin_train_std += globals()['CV_train_std_{}'.format(z)][-1]*globals()['por_x_{}'.format(z)]
      fin_test_mean += globals()['CV_test_mean_{}'.format(z)][-1]*globals()['por_x_{}'.format(z)]
      fin_test_std += globals()['CV_test_std_{}'.format(z)][-1]*globals()['por_x_{}'.format(z)]
      fin_time_mean += globals()['CV_fit_times_mean_{}'.format(z)][-1]
      fin_time_std += globals()['CV_fit_times_std_{}'.format(z)][-1]*globals()['por_x_{}'.format(z)]

#%%Cross-validation!
from sklearn.model_selection import cross_val_score
from sklearn.model_selection import ShuffleSplit

case_for_cl = total_df2.copy()
total_len = len(case_for_cl)
for z in np.arange(n_clusters):
      X1 = spectrum[case_for_cl['Cluster']==z]
      globals()['por_x_{}'.format(z)]= len(X1)/total_len

for z in np.arange(n_clusters):
      X1 = spectrum[case_for_cl['Cluster']==z] #spectrum#
      Sc = preprocessing.StandardScaler().fit(X1)
      #Sc = preprocessing.MinMaxScaler().fit(X1)
      X= Sc.transform(X1)
      #X = pd.DataFrame(X)
      X = pd.DataFrame(X).dropna(axis=0)
      Y = con[case_for_cl['Cluster']==z]#con#
      globals()['estimator_{}'.format(z)] =    model
      #globals()['X_train_{}'.format(z)], globals()['X_test_{}'.format(z)],
globals()['y_train_{}'.format(z)], globals()['y_test_{}'.format(z)] = train_test_split(X, Y,
test_size=test_size,    random_state=100)

      # globals()['estimator_{}'.format(z)].fit(X,Y)
      cv = ShuffleSplit(n_splits=5, test_size=0.2, random_state=0)
      globals()['CV_score_{}'.format(z)] = cross_val_score(globals()['estimator_{}'.format(z)], X,
Y,scoring='neg_mean_squared_error', cv=cv)
      globals()['CV_mean_{}'.format(z)] = np.mean(np.sqrt(-globals()['CV_score_{}'.format(z)]))
      globals()['CV_std_{}'.format(z)] = np.std(np.sqrt(-globals()['CV_score_{}'.format(z)]))

fin_mean= 0
fin_std = 0
for z in np.arange(n_clusters):
      fin_mean += globals()['CV_mean_{}'.format(z)]*globals()['por_x_{}'.format(z)]
      fin_std += globals()['CV_std_{}'.format(z)]*globals()['por_x_{}'.format(z)]

#%%Final training
start_t= time.time()
test_size = 0.2
y_test = pd.DataFrame([])
y_train = pd.DataFrame([])
y_pred = pd.DataFrame([])
y_pred2 = pd.DataFrame([])

for z in np.arange(n_clusters):
      X1 = spectrum[case_for_cl['Cluster']==z]
      Sc = preprocessing.StandardScaler().fit(X1)
      X = pd.DataFrame(X1).dropna(axis=0)
      Y = con[case_for_cl['Cluster']==z]
      globals()['estimator_{}'.format(z)] =    model
```

```
    globals()['X_train_{}'.format(z)], globals()['X_test_{}'.format(z)],
globals()['y_train_{}'.format(z)], globals()['y_test_{}'.format(z)] = train_test_split(X, Y,
test_size=test_size,   random_state=50)
    globals()['estimator_{}'.format(z)].fit(globals()['X_train_{}'.format(z)],
globals()['y_train_{}'.format(z)])

    globals()['dset_{}'.format(z)] = pd.DataFrame()
    globals()['dset_{}'.format(z)]['importance'] =
globals()['estimator_{}'.format(z)].feature_importances_

    rfecv = RFECV(estimator=model, step=2, cv=5, n_jobs = -1,
scoring="neg_mean_squared_error")
    rfecv.fit(X, Y)

    globals()['rfescore_{}'.format(z)] = rfecv.grid_scores_
    globals()['dset_{}'.format(z)]['attr'] = X.columns

    globals()['dset_{}'.format(z)]['selection'] = rfecv.support_
    X.drop(X.columns[np.where(rfecv.support_ == False)[0]], axis=1, inplace=True)
    globals()['rfeindex_{}'.format(z)] = np.where(rfecv.support_ == True)[0]
    globals()['X_train_{}'.format(z)], globals()['X_test_{}'.format(z)],
globals()['y_train_{}'.format(z)], globals()['y_test_{}'.format(z)] = train_test_split(X, Y,
test_size=test_size,   random_state=100)


    minmax_scale = preprocessing.StandardScaler().fit(globals()['X_train_{}'.format(z)])
    X_train = minmax_scale.transform(globals()['X_train_{}'.format(z)])
    X_test = minmax_scale.transform(globals()['X_test_{}'.format(z)])

    globals()['estimator_{}'.format(z)] =   model
    globals()['estimator_{}'.format(z)].fit(globals()['X_train_{}'.format(z)],
globals()['y_train_{}'.format(z)])
    globals()['y_pred_{}'.format(z)] =
pd.DataFrame(globals()['estimator_{}'.format(z)].predict(globals()['X_test_{}'.format(z)]))
    globals()['res_{}'.format(z)] = regression_results(globals()['y_test_{}'.format(z)],
globals()['y_pred_{}'.format(z)])
    globals()['y_pred2_{}'.format(z)] =
pd.DataFrame(globals()['estimator_{}'.format(z)].predict(globals()['X_train_{}'.format(z)]))

    y_test = pd.concat([y_test, globals()['y_test_{}'.format(z)]])
    y_pred = pd.concat([y_pred, globals()['y_pred_{}'.format(z)]])
    y_train = pd.concat([y_train, globals()['y_train_{}'.format(z)]])
    y_pred2 = pd.concat([y_pred2, globals()['y_pred2_{}'.format(z)]])

    globals()['res_fin_c1{}'.format(z)] = regression_results(globals()['y_test_{}'.format(z)],
globals()['y_pred_{}'.format(z)])
    globals()['res_fin_c2{}'.format(z)] = regression_results(globals()['y_train_{}'.format(z)],
globals()['y_pred2_{}'.format(z)])

Train_result = regression_results(y_train, y_pred2)
Test_result = regression_results(y_test, y_pred)

elapsed = time.time() - start_t

#%%Read HSI file
file = 'HSI.hdr'
file2 ='hsi'

test=envi.open(file, file2)
dataset = gdal.Open(file2, gdal.GA_Update)
```

```
gt = dataset.GetGeoTransform()
rows = dataset.RasterYSize
cols = dataset.RasterXSize

all_b = test.open_memmap(writeable=True)

MNDWI =   (all_b[:,:,31]-all_b[:,:,103])/(all_b[:,:,31]+all_b[:,:,103])


#%%Radiometric correction & filtering
from sklearn.linear_model import LinearRegression
from scipy import ndimage, misc

ref_db = pd.read_csv('Calibration tarps.csv')

# 1 point correction
rad2 = rad_84 = ref_db['84']
all_b_r = np.zeros([len(all_b[:,0,0]),len(all_b[0,:,0]),len(all_b[0,0,:])])
for zzz in np.arange(len(rad2)):
	all_b_r[:,:,zzz] = ((0.84)/rad2.iloc[zzz])*(all_b[:,:,zzz])


# 4 points correction
rf_ref = np.array([0.84,0.56,0.24,0.03])
rad_reg = LinearRegression()

all_b_r = np.zeros([len(all_b[:,0,0]),len(all_b[0,:,0]),len(all_b[0,0,:])])
for z in np.arange(len(all_b_r[:,0,0])):
	for i in np.arange(150):

		rad_reg.fit(ref_db.iloc[i,:].values.reshape(-1,1), rf_ref)
		all_b_r[:,z,i] = rad_reg.predict(all_b[:,z,i].reshape(-1,1))

all_b_r_fil = ndimage.median_filter(all_b_r, size=(3,3,10))

#%% Prediction
def extract_pixels(X):
   q = X.reshape(-1, X.shape[2])
   df = pd.DataFrame(data = q)
   df.columns= [f'band{i}' for i in range(1, 1+X.shape[2])]
   return df

df = extract_pixels(all_b_r_fil)
n = np.linspace(0,2,num=10)

C_INDEX2 = cluster.fit_predict(df)
clu_map = C_INDEX2.reshape(len(all_b_r_fil),len(all_b_r_fil[0,:,0]))

c1_ind = np.where(C_INDEX2==0)
c2_ind = np.where(C_INDEX2==1)

X1 = spectrum[case_for_cl['Cluster']==0]
Sc1 = preprocessing.StandardScaler().fit(X1)
X2 = spectrum[case_for_cl['Cluster']==1]
Sc2 = preprocessing.StandardScaler().fit(X2)

df3_1 = Sc1.transform(df.iloc[:,:])
df3_2 = Sc2.transform(df.iloc[:,:])

mapp_pred_c1 = estimator_0.predict(df3_1[c1_ind,:][0])
```

```
mapp_pred_c2 = estimator_1.predict(df3_2[c2_ind,:][0])
mapp_pred_l = df.iloc[:,0].copy()
mapp_pred_l.iloc[c1_ind] = mapp_pred_c1
mapp_pred_l.iloc[c2_ind] = mapp_pred_c2
mapp_pred_l = np.array(mapp_pred_l)

#%% Mapping
mapp_pred_fin = mapp_pred_l.reshape(len(all_b_r_fil),len(all_b_r_fil[0,:,0]))
mapp_pred_mask = np.ma.masked_where((MNDWI<0), mapp_pred_fin )

ds = gdal.Open(file2)
cols = ds.RasterXSize
rows = ds.RasterYSize
myarray = mapp_pred_mask
geotransform = ds.GetGeoTransform()
wkt = ds.GetProjection()
driver = gdal.GetDriverByName("GTiff")
output_file = "SSC_map from CMR_OV.tif"
dst_ds = driver.Create(output_file,
                                cols,
                                rows,
                                1,
                                gdal.GDT_Float32)

new_array = mapp_pred_mask
where_are_NaNs = np.isnan(new_array)
new_array[where_are_NaNs] = 0
dst_ds.GetRasterBand(1).WriteArray( new_array )
dst_ds.GetRasterBand(1).SetNoDataValue(0)
dst_ds.SetGeoTransform(geotransform)
srs = osr.SpatialReference()
srs.ImportFromWkt(wkt)
dst_ds.SetProjection( srs.ExportToWkt() )
ds = None
dst_ds = None
```

국문초록

고해상도 초분광영상을 활용한 하천 부유사농도 계측기법 개발

서울대학교 대학원
건설환경공학부
권 시 윤

기존의 하천 부유사 농도 계측은 샘플링 기반 직접계측 방식에 의존하여 시공간적 고해상도 자료 취득이 어려운 실정이다. 이러한 한계점을 극복하기 위해 최근 위성과 드론을 활용하여 촬영된 다분광 혹은 초분광 영상을 통해 고해상도의 부유사농도 시공간분포를 계측하는 기법에 대한 연구가 활발히 진행되고 있다. 하지만, 다른 하천 물리량 계측에 비해 부유사 계측 연구는 하천에 따라 부유사가 다양하게 분포하고 다른 부유물질 혹은 하상에 의한 바닥 반사의 영향 때문에 분광 자료를 통해 정확한 부유사농도 분포를 재현하기 어려운 실정이다. 특히, 부유사 분광 특성에 영향을 미치는 입도분포, 광물특성, 침강성 등이 하천에 따라 강한

지역성을 나타내기에 이러한 요인에서 야기되는 분광다양성으로 인해 특정 시기와 지역에만 적합한 원격탐사 기반 계측 모형들이 개발되어 왔다.

본 연구에서는 이러한 분광다양성을 반영하여 다양한 하천 및 유사 조건에서 적용 가능한 고해상도 초분광영상을 활용한 하천 부유사농도 계측방법을 개발하기 위해 초분광 군집화 기법과 다양한 파장대의 분광 밴드를 학습할 수 있는 기계학습 회귀 모형을 결합하여 CMR-OV라는 방법론을 제시하였다.

CMR-OV 개발 및 검증은 1) 실험적 연구를 통한 하천 부유사 분광 특성의 주요 교란 요인 분석, 2) 최적 회귀모형 선정 및 초분광 클러스터링과의 결합, 3) 현장적용성 평가의 과정을 거쳐 수행되었다. 실험적 연구에서는 우선 실내 실험실에서 횡방향 혼합기를 활용하여 바닥 반사를 제거하고 완전 혼합된 상태에서 부유사의 고유 초분광 스펙트럼 자료를 수집하였다. 이를 바탕으로 실제 하천과 유사한 조건의 실규모 옥외 수로 실험에서 다양한 유사 특성(입도 및 광물)과 하상 특성(식생 및 모래)에 대한 초분광 자료를 수집하여 고유 초분광 스펙트럼과 비교하였다. 그 결과, 부유사의 분광 특성은 유사의 종류 및 입도에 따라 농도 증가에 따른 초분광 스펙트럼의 반사율 변화가 상이하게 나타났다. 또한, 1 m 이하의 얕은 수심 조건에서는 바닥 반사의 영향으로 하상 종류에 따라 초분광 스펙트럼의 개형이 크게 변화하였으며, 고농도의 부유사가 분포할 때도 바닥 반사가 크게 영향을 미치는 것을

확인하였다.

이러한 분광다양성이 반영된 부유사농도와 초분광 자료의 관계를 구축하기 위하여 기계학습 기반 랜덤포레스트 회귀 모형과 가우시안 혼합 모형 기반 초분광 군집 기법을 결합한 CMR-OV를 적용한 결과, 기존 연구들에서 주로 활용된 밴드비 기반의 모형과 단일 기계학습모형에 비해 정확도가 크게 향상하였다. 특히, 기존 최적 밴드비 분석 (OBRA) 방법은 비선형성을 고려해도 좁은 영역의 파장대만을 고려하는 한계점으로 인해 분광다양성을 반영하지 못하는 것으로 밝혀졌다. 하지만, CMR-OV는 폭 넓은 파장대 영역을 고려함과 동시에 높은 정확도를 산출하였다.

최종적으로 CMR-OV를 황강의 직선구간 및 사행구간과 낙동강과 황강의 합류부에 적용하여 현장검증을 수행한 결과, 기존 모형 대비 정확도와 부유사 농도 맵핑의 정밀성에서 큰 개선이 있었으며, 비학습지역에서도 높은 정확도를 산출하였다. 특히, 하천 합류부에서는 초분광 군집을 통해 두 하천 흐름의 경계층을 명확히 구별하였으며, 이를 바탕으로 지류와 본류에 대해 각각 분리된 회귀모형을 구축하여 복잡한 합류부 근역 경계층에서의 부유사 분포를 보다 정확하게 재현하였다. 또한, 나아가서 재현된 고해상도의 부유사 공간분포를 바탕으로 혼합도를 산정한 결과, 기존 점계측 대비 상세하게 부유사 혼합에 대한 정량적 평가가 가능한 것으로 나타났다. 따라서, 본 연구에서 개발한 초분광영상 기반 부유사 계측 기술을 통해 추후 하천 조사 및 관리 실무의

정확성 및 효율성을 크게 증진할 수 있을 것으로 기대된다.

주요어: 하천부유사 계측, 원격탐사, 초분광영상, 분광 다양성, 기계학습모형, 공간분포 맵핑

학번: 2018-28430